

Autorul tezei de abilitare: **CS II Dr. Ing. Pop Mihai Alin**

Titlul tezei de abilitare: **Cercetări privind aplicarea tehnologiilor inovative în ingineria materialelor avansate**

Domeniul: **Ingineria materialelor**

Portofoliu de lucrari

1. **Pop, M. A.**, Croitoru, C., Matei, S., Zaharia, S. M., Coșniță, M., & Spîrchez, C. (2024). Thermal and Sound Insulation Properties of Organic Biocomposite Mixtures. *Polymers*, 16(5), 672. WOS:001182946900001 (**FI=4.7**) **Q1**, [link](#)
2. Matei, S., **Pop, M. A.**, Zaharia, S. M., Coșniță, M., Croitoru, C., Spîrchez, C., & Cazan, C. (2024). Investigation into the Acoustic Properties of Polylactic Acid Sound-Absorbing Panels Manufactured by 3D Printing Technology: The Influence of Nozzle Diameters and Internal Configurations. *Materials*, 17(3), 580. WOS:001160043000001 (**Autor corespondent**) (**FI=3.1**) **Q2**, [link](#)
3. Blaj, M. I., Zaharia, S. M., Morariu, C. O., **Pop, M. A.**, Cosnita, M., & Oancea, G. (2024). Tensile Behavior of Parts Manufactured Using a Material Extrusion Process from a Filament with Short Carbon Fibers and PET Matrix. *Processes*, 12(2). WOS:001172605600001 (**FI=2.8**) **Q2**, [link](#)
4. Zaharia, S. M., Pascariu, I. S., Chicos, L. A., Buican, G. R., **Pop, M. A.**, Lancea, C., & Stamate, V. M. (2023). Material extrusion additive manufacturing of the composite UAV used for search-and-rescue missions. *Drones*, 7(10), 602. WOS:001092500000001 (**FI=4.4**) **Q1**, [link](#)
5. Zaharia, S. M., **Pop, M. A.**, Cosnita, M., Croitoru, C., Matei, S., & Spîrchez, C. (2023). Sound Absorption Performance and Mechanical Properties of the 3D-Printed Bio-Degradable Panels. *Polymers*, 15(18), 3695. WOS:001072568300001 (**Autor corespondent**) (**FI=4.7**) **Q1**, [link](#)
6. **Pop, M. A.**, Cosnita, M., Croitoru, C., Zaharia, S. M., Matei, S., & Spîrchez, C. (2023). 3D-Printed PLA Molds for Natural Composites: Mechanical Properties of Green Wax-Based Composites. *Polymers*, 15(11), 2487. WOS:001005765300001 (**FI=4.7**) **Q1**, [link](#)
7. Zaharia, S. M., **Pop, M. A.**, Buican, G. R., Chicos, L. A., Stamate, V. M., Pascariu, I. S., & Lancea, C. (2023). Design and testing of brushless DC motor components of A6 steel additively manufactured by selective laser sintering. *Aerospace*, 10(1), 60. WOS:000916773600001 (**FI=2.1**) **Q2**, [link](#)

- 8. Pop, M. A.,** Croitoru, C., Bedo, T., Geamăn, V., Radomir, I., Crișan, A., ... & Chicoș, L. A. (2022). The Influence of Solar Sintering on Copper Heat Exchanger Parts with Controlled 3D-Printed Morphology. *Materials*, 15(9), 3324. (FI=3.748) Q2, [link](#)
- 9. Pop, M. A.,** Croitoru, C., Bedó, T., Geamăn, V., Radomir, I., Cos, nit, ă, M., ... & Milos, an, I. (2019). Structural changes during 3D printing of bioderived and synthetic thermoplastic materials. *Journal of Applied Polymer Science*, 136(17), 47382. WOS:000456861100001 (FI=2.7) Q2, [link](#)
- 10. Catana, D. and Pop, M.A.,** 2021. Studies regarding simulation process to static loading of the structures obtained from polylactic acid, 3D printed. *Journal of Applied Polymer Science*, 138(6), p.50036. WOS:000575801800001 (FI=2.7) Q2, [link](#)

Data

CS II dr. ing. Pop Mihai Alin

04.02.2025

Article

Thermal and Sound Insulation Properties of Organic Biocomposite Mixtures

Mihai Alin Pop ¹, Cătălin Croitoru ^{2,*}, Simona Matei ¹, Sebastian-Marian Zaharia ³, Mihaela Coșniță ⁴
and Cosmin Spîrchez ⁵

¹ Department of Materials Science, Transilvania University of Brasov, 500036 Brasov, Romania; mihai.pop@unitbv.ro (M.A.P.); simona.matei@unitbv.ro (S.M.)

² Materials Engineering and Welding Department, Transilvania University of Brasov, 500036 Brasov, Romania

³ Department of Manufacturing Engineering, Transilvania University of Brasov, 500036 Brasov, Romania; zaharia_sebastian@unitbv.ro

⁴ Department of Product Design, Mechatronics and Environment, Transilvania University of Brasov, 500036 Brasov, Romania; mihaela.cosnita@unitbv.ro

⁵ Wood Processing and Design Wooden Product Department, Transilvania University of Brasov, 500036 Brasov, Romania; cosmin.spirchez@unitbv.ro

* Correspondence: c.croitoru@unitbv.ro

Abstract: Sustainable building materials with excellent thermal stability and sound insulation are crucial for eco-friendly construction. This study investigates biocomposites made from cellulose pulp reinforced with beeswax, fir resin, and natural fillers like horsetail, rice flour, and fir needles. Eight formulations were obtained, and their thermal resistance, oxidation temperature, and acoustic properties were evaluated. Biocomposites exhibited significant improvements compared to conventional materials. Oxidation temperature onset increased by 60–70 °C compared to polyurethane foam or recycled textiles, reaching 280–290 °C. Sound absorption coefficients ranged from 0.15 to 0.78, with some formulations exceeding 0.5 across mid-frequencies, indicating good sound-dampening potential. These findings demonstrate the promise of these biocomposites for sustainable construction, offering a balance of thermal and acoustic performance alongside environmental and health benefits.

Keywords: thermal properties; sound insulation; biocomposites; paper pulp; internal architectures



Citation: Pop, M.A.; Croitoru, C.; Matei, S.; Zaharia, S.-M.; Coșniță, M.; Spîrchez, C. Thermal and Sound Insulation Properties of Organic Biocomposite Mixtures. *Polymers* **2024**, *16*, 672. <https://doi.org/10.3390/polym16050672>

Academic Editor: Luis Alves

Received: 9 February 2024

Revised: 26 February 2024

Accepted: 28 February 2024

Published: 1 March 2024



Copyright: © 2024 by the authors. Licensee MDPI, Basel, Switzerland. This article is an open access article distributed under the terms and conditions of the Creative Commons Attribution (CC BY) license (<https://creativecommons.org/licenses/by/4.0/>).

1. Introduction

A balance between energy, performance, and cost efficiency are critical issues in all engineering fields. Nearly 40% of energy consumption and 36% of greenhouse gas emissions are caused by residential and commercial buildings. Therefore, there are initiatives to reduce these emissions and energy consumption while increasing the sustainability of the built environment through the concept of near-zero energy (NZE) buildings [1]. One of the key aspects of NZE buildings is the use of sustainable and energy-efficient materials for construction. In response to this challenge, one ongoing research direction is aimed at developing new eco-friendly, non-structural multipurpose materials with sound- or thermal-insulating properties [2]. In this context, all-natural composite materials have emerged as a promising alternative to synthetic polymer composites for various applications, including sound insulation and non-structural panels.

This paper focuses on the thermal stability and sound insulation properties of all-natural composites, as these are crucial factors in determining their suitability for use in various applications, such as building insulation, acoustic panels, packaging, and furniture. Thermal stability is crucial for ensuring the long-term performance and durability of the materials used in construction, while sound insulation is vital for maintaining a comfortable and quiet living environment. By understanding the thermal and acoustic properties of all-natural composites, their performance can be optimized and sustainable, and alternatives can be designed.

The benefits of using ecological materials instead of synthetic ones as insulation include lower energy and carbon usage, as well as esthetic perks like unique textures, colors, and patterns [3,4]. These ecological materials could also promote a healthier indoor environment, including the elimination of volatile organic compounds [5–8]. In some cases, it has been found that, for example, natural composites have lower thermal conductivity and higher thermal diffusivity than synthetic composites, which means they can better resist heat transfer and thermal shocks [7]. Also, natural composites can have higher sound absorption coefficients than synthetic composites, which means they can better absorb and dissipate sound energy [8].

Natural formulations, such as paper, natural fibers, waxes, and natural resins, have been widely used as components of composite materials due to their availability, cost, renewability, biodegradability, and compatibility with each other. However, the sound performance and thermal properties of hybrid all-organic composites with natural resources as both matrix and filler have not been extensively studied.

Therefore, this work aims to assess the evaluation of the thermal properties (first-order transitions, glass transitions, degradation, and stability against cyclic thermal aging) and acoustic properties (sound absorption coefficient—SAC, sound transmission loss—STL) of several tailor-made all-organic composites from natural resources. The composites present an organic matrix (beeswax, fir resin) and biomass fillers (horsetail powder, rice flour, ground fir needles, recycled cellulose fibers from paper) in varying amounts. In this assembly, paper and fibers can provide structural reinforcement and thermal insulation, while wax and natural resins can act as binders and modifiers of the composite properties [9].

The advantage of using beeswax and fir resin as the matrix could be their improved compatibility with the filler, as they contain a wide range of compounds in their structure, including hydrocarbons with a chain length of C27–C33, free fatty acids with a chain length of C24–C32, and fatty acid esters in the case of beeswax [10] and terpenes and rosin acids in the case of fir resin [10], as well as other compounds. Also, among the advantages, the easy processing may be mentioned (due to their relatively lower melting/softening points compared to synthetic thermoplastics, for example). According to Neto et al. [9], the thermal stability of beeswax and its composites with different fillers was investigated by TGA and DSC. The results showed that beeswax had a melting point of about 65 °C and a degradation temperature of about 300 °C. The addition of fillers, such as wood flour or rice husk, increased the thermal stability of the composites by delaying the onset of degradation and reducing weight loss [11]. Beeswax can be used as a matrix or a modifier in composites with different fillers, such as wood, rice husk, calcium carbonate, glass fiber, carbon fiber, and clay. Beeswax composites showed good thermal, mechanical, and electrical properties, but their sound absorption properties have not been widely studied [12].

According to [13], the thermal stability of coniferous resin and its composites with different fillers was studied by TGA and DSC. The results showed that fir resin had a softening point of about 80 °C and a degradation temperature of about 350 °C, which means that it can withstand moderate heating without significant changes to its properties [14]. The melting point depends on the type and purity of the resin and can vary from 60 to 120 °C. Coniferous resins can be used as matrices or modifiers in composites with different fillers, such as wood, cellulose, glass fiber, carbon fiber, and clay, which generally improve thermal stability by increasing the onset of degradation and decreasing weight loss. Coniferous resin composites also showed good mechanical and electrical properties, but their sound absorption properties have not been reported [15].

Natural fibers and ground plant material, in general, and their polymer composites with synthetic matrices (polyesters, thermosets) have different thermal degradation temperatures depending on their chemical composition, morphology, molecular structure, and interfacial interactions. Generally, cellulose degrades at around 300 °C, hemicellulose degrades at around 200 °C, and lignin degrades at around 400 °C [16]. The addition of plant fibers, bacterial cellulose fibers, or ground plant-based material to thermoplastic matrices, such as polypropylene, polyethylene, and polylactic acid, enhanced the thermal stability of

the composites by increasing the char residue and decreasing the weight loss [17]. Biomass-derived fillers can influence the thermal conductivity, thermal expansion, and thermal degradation of the natural composites by altering the heat transfer and thermal stability of the matrix. The thermal properties depend on the thermal conductivity, specific heat, and thermal degradation temperature of the fillers, as well as the thermal contact resistance and thermal mismatch between the fillers and the matrix [18].

Horsetail and fir needles used in this study contain, in addition to the lignocellulosic part, phenolic compounds, resin acids, or silicon dioxide (horsetail), which have a strengthening and thermal stabilizing effect on wax and/or resin. Rice flour contains starch, waxes, and proteins that are compatible with the chosen matrices, and ground paper (recycled cellulose) has a high specific surface area and a high degree of absorption/wicking for wax and resin.

Fiber and paper composites have been extensively studied for their sound absorption properties. Various factors, such as composite structure, fiber-based thickness, and surface treatment, were investigated to optimize the sound absorption coefficient [19]. Generally, natural plant-derived fillers have lower density and higher porosity than synthetic fillers, which is beneficial for sound insulation applications. Also, natural plant-derived fillers have more irregular shapes than synthetic fillers, which can increase the overall irregularity of the composites, helping with sound wave scattering, diffraction, or reflection [20–22].

Chen et al. developed multi-layer gradient fiber-based composites with porous, resonant, and damping structures, achieving a broadband sound absorption coefficient (SAC) of 0.42 [23]. Khem et al. studied the sound absorption capability of oil palm frond (OPF) composites and found that the sound absorption coefficient was proportional to density and improved with alkali treatment [24]. Haghghat et al. evaluated the impact of fiber size on the sound absorption values of sugarcane bagasse (SCB) waste fiber composites and found that smaller fiber sizes resulted in higher absorption performance [25]. The sound absorbing coefficient for paper pulp composites can vary between 0.2 and 0.6, depending on factors such as fiber density and composition [26].

This study explores the synergy between natural components (beeswax, fir resin, rice flour, and horsetail) and recycled paper pulp to create fully bio-based composites with superior thermal stability and sound insulation. While previous research examined these components individually, their combined acoustic insulation potential remains largely unexplored. This study addresses this issue by evaluating how formulation adjustments and internal composite geometry (patterned voids) affect sound absorption, transmission, and reflection characteristics.

Compared to synthetic polymer composites, these fully bio-based materials could offer significant environmental and economic advantages, including lower environmental impact and, potentially, lower cost. However, a comprehensive understanding of their sound absorption and thermal degradation properties is lacking. This study aims to fill this knowledge gap by investigating the influence of composition, structure, and natural component properties on composite performance, ultimately paving the way for optimized materials for diverse applications.

2. Experimental

2.1. Materials

The natural beeswax was of the type of artificial combs used in beekeeping. The horsetail (*Equisetum arvense*) plant, rice, fir resin, and fir needles were purchased from a store specializing in natural products (Paradisul Verde, Brasov, Romania). The recycled paper used was obtained by grinding waste document fragments (usual A4 paper with a specific weight of 80 g/m²).

2.2. Mixtures Obtaining

A total of 8 materials recipes were obtained by melting beeswax and fir resin and mixing it with horsetail/fir needles and ground powder/rice flour, respectively, in pre-

determined proportions and pouring it into circular silicone rubber molds, resulting in specimens with a diameter of 18 mm and a height between 15 and 20 mm. The composite recipes expressed in Table 1 represent the composition of wax, resin, and ground biomass fillers that were poured over the cellulose fiber pulp base to obtain the sound insulation composites, as detailed in Section 2.5.

Table 1. Material recipes used in this study.

Crt. No.	Material	Sample Code
1	Beeswax (100%)	Pr-1
2	Fir resin (100%)	Pr-2
3	Cellulose pulp (100%)	Hr
4	Beeswax (50%) + fir resin (50%)	Pr-9
5	Beeswax (62.5%) + horsetail powder (37.5%)	Pr-4
6	Beeswax (45.5%) + rice flour (54.5%)	Pr-6
7	Beeswax (61.5%) + ground fir needles (38.5%)	Pr-7
8	Beeswax (31.25%) + fir resin (31.25%) + horsetail powder (37.5%)	Pr-8

The recipes mentioned in Table 1 were chosen based on our preliminary experimentation. The filler integration and spreading behavior of each component (fir resin, beeswax, and their mixture) was evaluated with increasing filler(s) content. This iterative process aimed to identify the maximum filler incorporation possible while maintaining good processability and uniform spreading on the paper pulp core.

The miscibility of hydrophilic and hydrophobic materials at the filler–matrix interface is crucial in controlling dispersion and determining the final composite properties. Poor compatibility could lead to phase separation or weak interfacial bonding.

Several factors help mediate the hydrophilicity discrepancy in our formulations. First, waxes and resins contain ester, acid, and alcohol groups, making them moderately polar and capable of hydrogen bonding with cellulose. This increases interfacial interaction. Secondly, fillers like horsetail and rice contain various polar extractives and surface-active compounds that can plasticize the interface. Heating the mixtures above the melting points enhances molecular mobility and mixing, and strong mechanical processes like grinding disrupt filler particle agglomeration, increasing surface area for interaction.

2.3. Thermal Analysis

The thermal analysis (TA) of the compositions corresponding to Table 1 was conducted using a Differential Scanning Calorimetry (DSC) technique with a DSC-200 F3 Maia/STA 449F3 Jupiter (Netzsch, Selb, Germany) instrument. The thermal protocol consisted of a heating and cooling rate of 10 °C/min, with the following steps: (1) cooling from room temperature (25 °C) to −80 °C; (2) heating from −80 °C to 300 °C; (3) cooling from 300 °C back to room temperature.

The composite samples underwent cyclic thermal aging by being subjected to five consecutive cooling/heating cycles between −70 °C and 70 °C using the same DSC instrument and 10 °C/min heating/cooling rate as previously described.

The simultaneous thermal analysis (STA) combines Thermogravimetry (TG) and Differential Scanning Calorimetry (DSC) into a single instrument. The sample analysis was conducted in a temperature range of 20 to 300 °C under a nitrogen atmosphere, with a heating rate of 10 °C/min using the STA 449F3 Jupiter (Netzsch, Selb, Germany) instrument.

Thermogravimetric analysis (TG) was conducted using the following heating program (heating rate: 10 °C/min): heating from 20 °C to 300 °C.

2.4. Microstructure Analysis

The cross-section of the fractured composite samples was analyzed using a digital optical microscope Emspira 3 (Leica Microsystems GmbH, Wetzlar, Germany) at specified magnifications as indicated on each micrograph.

2.5. Acoustic Properties Determination

To prepare the natural composite samples, two different methods were used: direct pouring and molding. The direct pouring method involved pouring the heated wax, resin, and filler mixture onto ground cellulose paper pulp in 3D-printed poly (lactic acid) cylindrical molds with 50 mm internal diameter. This method produced filled samples, which were expected to have higher density and lower porosity than the unfilled samples. The molding method involved placing the paper pulp inside cylindrical molds with 50 mm internal diameter, particularly in the interior part composed of a disk with pins with different geometric configurations: circular, undulated, and triangular. The positive pins on the interior disk conferred the desired geometry into the paper core. On the molded pulp, the composite formulation was poured and later extracted after cooling. This method produced samples with different shapes and sizes of voids, which were expected to affect the acoustic properties of the samples. The samples were coded as Pr-x-filled, Pr-x-circ, Pr-x-tri, and Pr-x-und, where “x” denotes the number of the formulation corresponding to Table 1. The use of 3D printing and molding techniques allowed us to create various natural composite samples with controlled and reproducible geometries, which enabled us to investigate the effect of the composition and void shape on the acoustic properties of the samples.

To evaluate the acoustic properties of the molded composite materials, an acoustic impedance tube (Holmarc HO-ED-A-03, Holmarc Opto-Mechatronics Ltd., Kochi, India) was used. This device consisted of an anodized aluminum tube with an inner diameter of 50 mm, which could measure the sound absorption coefficient (α), the sound transmission loss (TLn), and the reflection coefficient (R) of the samples in the frequency range of 500 Hz–3150 Hz. The device also included two pairs of microphones, sample holders, a data acquisition system, and measurement software. The transfer function method was applied according to the current standards to analyze the frequency dependencies of the acoustic properties of the composite samples. For each sample, several parameters were measured, such as the sample diameter (50 mm), the microphone spacing (30 mm), the temperature, and the humidity. Then, the sample was inserted into the impedance tube between the two sets of microphones in a fixed position.

3. Results and Discussion

In Figures S1–S7 (presented in the Supplementary Materials section), the thermal DSC and TG/DTA thermograms are presented for the beeswax, fir resin, their mixture, and various compositions with ground fir needles, horsetail powder, and rice flour, corresponding to Table 1. Additionally, Figure S8 illustrates the thermograms for the paper pulp.

The thermal transitions in the negative temp domain and the positive temp domain with low amplitude were not considered in this study for further analysis because they do not affect significant processing or servicing temperatures of natural composites [27,28]. Negative temperature transitions are usually due to the freezing of the traces of bonded and unbonded water within these natural materials [29], and they were not comprehensively considered any further.

The following aspects were observed from the DSC, DTA, and TG thermograms:

- During stage I (cooling), the crystallization of certain compounds (possibly small molecular) from the studied matrices (beeswax, fir resin) was observed at temperatures of approximately -20 °C. Mixing the two matrices, as well as mixing them with the filler agent (horsetail powder, fir needles, rice flour, recycled paper), leads to a decrease in this crystallization point by approximately $1-3$ °C.

- During stage II (heating), beeswax melting was observed at 69.8 °C, and fir resin melting started at 58 °C and continued until 293.5 °C, corresponding to different fractions thereof. Mixtures of the two matrices melt at temperatures 1–2 °C lower than the pure components, and mixing matrices with the filler agent has, essentially, the same effect. Fir resin also exhibits a softening point at 30.4 °C (glass transition temperature, T_g); the mixture of the two matrices (wax and resin) lowers this point to 15.8 °C. No softening point was detected for pure wax.
- During stage III (cooling), beeswax oxidation begins at 291.4 °C, and fir resin oxidation at 181.3 °C. The mixture of the two matrices (wax and resin) is thermally stable under the analysis conditions, with no exothermic peak corresponding to the oxidation observed. This aspect may be favorable for obtaining composite materials with this type of matrix. The addition of horsetail powder and fir needle powder to wax leads to a slight decrease in the onset temperature of oxidation (288 °C and 285 °C), while in the case of rice flour, the decrease is insignificant (around 1 °C).
- The solidification of melts (wax + fillers, fir resin) always occurs with undercooling, with solidification temperatures lower than those corresponding to melting at stage II.

The data from Figures S1–S8 are summarized in Table 2 for the second and/or third TA regimes, where significant changes occur in the thermograms. Also, the mass loss (expressed in %) is given for the thermal regime end value of 300 °C.

The thermal stability of the composites is influenced by the type and amount of the matrix and the filler materials. Fir resin has a higher thermal stability than beeswax or plant-based materials, as it can withstand higher temperatures without degradation. Therefore, composites with higher fir resin content show higher thermal stability than those with lower fir resin content. Also, fir resin shifts the onsets for oxidation to higher temperatures. Horsetail (*Equisetum*) is a natural filler that contains a high percentage of inorganic silicate-based compounds, such as silica and phytoliths. These compounds can enhance the thermal stability of the composites by increasing the char formation and reducing the mass loss during thermal decomposition [17,30]. Hence, the composites with horsetail addition exhibit higher thermal stability than those with fir needles or rice flour.

For comparison, the relevant thermal parameters for two of the most used insulation materials in buildings and the automotive domain, namely, polyurethane foam and textile rags, are also presented in Table 2. The textile rags present the second-highest mass loss evidenced from T_g , after the composites with rice flour, while the polyurethane foam presented the lowest thermal degradation in the studied temperature interval. The textile rags start to degrade at around 250 °C, about the same as polyurethane, which is 30 °C lower than beeswax and the composites with beeswax matrix, implying that the composites used in this study have the potential to be used in a wider temperature interval. Also, paper pulp presented good thermal stability until 200 °C, which is the onset of oxidation for this material. By adding different natural formulations to paper pulp, its thermal stability can be improved.

Studying cyclic heating–cooling regimes can help optimize the design and selection of natural composites for various applications that require thermal stability and resistance. By analyzing the thermal properties, such as melting point or onset of oxidation of different natural composites and their combinations under cyclic heating–cooling regimes, the best natural composites and compositions can be identified and improved [31]. The thermal cyclic performance for the matrices and composite mixtures from this study being subjected to five consecutive cooling/heating cycles between -70 °C and 70 °C is illustrated in Table 3. Only the major peaks with the highest enthalpy were selected for each formulation.

Table 2. Thermal transitions, oxidation, and mass loss for the analyzed composite mixtures.

Thermal Analysis		DSC/DTA			TG	
Sample Code	TA Stage	Peak Temperature (°C)	ΔH (J/g)	Observations	Mass Loss at 300 °C (%)	Observations
Pr-1	II—heating	68.5	−15.53	Melting	1.27	Highest onset of oxidation
	III—cooling	292.6	3.32	Onset of oxidation		
Pr-2	II—heating	30.4	-	Tg—softening	6.24	
		58.1...293.5	−0.91...−0.97	Melting		
Pr-9	II—heating	181.3	−0.003	Onset of oxidation	5.09	Intermediary thermal stability between wax and fir resin
		15.8	-	Tg—softening		
Pr-4	III—cooling	58.4...291	−3.21	Melting	14.60	Highest onset of oxidation from all composites
		-	-	No oxidation was observed		
Pr-6	II—heating	70.6	−26.21	melting	25.53	Lowest thermal stability from all wax matrix composites
		288.8	0.29	Onset of oxidation		
Pr-7	III—cooling	292.6	3.32	Onset of oxidation	14.09	Intermediary thermal stability
		71.2	−8.11	Melting		
Pr-8	II—heating	143.3...282.7	−11.09...−0.77	Melting of rice compounds (waxes)	7.61	Highest thermal stability from the studied composite mixtures
		290.6	4.83	Onset of oxidation		
Hr	III—cooling	68.2	−10.89	Melting of wax	20.90	
		140.3	−4.03	Melting of compounds from fir needles		
Polyurethane foam	II—heating	285.9	10.90	Onset of oxidation	0.56	
		58.4...291	−3.21	Melting		
Textile rags	II—heating	65.6	−16.87	Melting of wax	16.78	
		174.6...290	−0.35...−0.95	Melting of resin components		
Textile rags	III—cooling	284.7	0.04	Onset of oxidation	16.78	
		284.1	13.95	Onset of oxidation		
Textile rags	DTA	73.1	−18.65	Free water vaporisation	16.78	
		−12.2	−0.428	Free water freezing		
Textile rags	DTA	205.2	−19.7	Onset of oxidation	16.78	
		160.7	0.015	Melting		
Textile rags	II—heating	246.2	−0.12	Onset of oxidation	16.78	
		249.8	−4.94	Onset of cellulose oxidation		

Minitab v.19 software was used to compare the peak temperatures for the different compositions and test if the observed changes were statistically significant. The significance level was set at 0.05. The null hypothesis is that there is no difference in the peak temperatures for the different compositions. The alternative hypothesis is that there is a difference in the peak temperatures for the different compositions. In the cases where p was higher than 0.05, the differences were statistically significant. For p values lower than 0.05, the null hypothesis of no difference can be rejected.

The values presented in Table 3 showed no significant statistical differences in the melting point of all components, except for Pr-9, but in this case, the largest difference could be attributed to the possible elimination of some volatile compounds from beeswax or fir resin, after which the melting point values tend to be stabilized. This is supported by the fact

that the p -value for Pr-9 was lower than the significance level of 0.05. The values of T_g are significantly affected by the cyclic thermal stressing regime, but this is not unusual, taking into consideration that the glass transition temperature is a kinetic parameter, depending more on the heating/cooling regime than the changes in the material. This is consistent with the theory of glass transition, which states that the glass transition temperature is not a fixed property of a material but rather a function of the thermal history and the molecular mobility of the material. The results indicate that the peak temperatures for the different compositions were not significantly affected by the cyclic thermal stress. Therefore, it could be concluded that the studied composites maintained their chemical stability under thermal cycling conditions. While the literature data for all-organic biocomposites' thermal stressing are missing, there seems to be associated evidence for the thermal stability of plant-based fillers and fibers embedded in synthetic matrices [19,32–35].

Table 3. Cyclic thermal stressing of the natural composite formulations.

Sample Code	DSC Heating Stage Peak	T (°C)					p Value at 95% Confidence	Observations
		1st Cycle	2nd Cycle	3rd Cycle	4th Cycle	5th Cycle		
Pr-1	Wax melting	68.5	69.4	68	68.7	68.6	0.92	No significant changes
Pr-2	Resin softening point (T_g)	30	33.4	38.1	43.8	44.1	0.00049	Significant changes
	Resin melting	58.1	60	58.4	58.5	58.6	0.97	No significant changes
Pr-9	softening point (T_g)	15.8	22.6	21.7	38.4	48.5	0.00015	Significant changes
	Melting	58.4	66.2	65.3	65.2	65.3	0.0064	Significant changes
Pr-4	Melting	70.6	69.6	68.5	68.3	68.3	1	No significant changes
Pr-6	Melting	71.2	70	69.3	68.8	68.7	1	No significant changes
Pr-7	Melting	68.2	71.5	69.5	69.4	69.4	1	No significant changes
Pr-8	Melting	65.6	64	63.2	63.5	63.5	1	No significant changes

Figure 1 shows the optical microscopy images of the composite samples prepared from different natural materials, as listed in Table 1. The samples were composed of a cellulosic pulp base, onto which a mixture of beeswax, fir resin, and various fillers was added. The fillers included horsetail powder, rice flour, and ground fir needles. Sample Hr (Figure 1) consisted of pure cellulosic pulp microfibers, which had a compact and uniform appearance. The microfibers might also contain some traces of binder, lignin, and other components from the original paper source.

Samples Pr-1 to Pr-9 consisted of cellulosic pulp microfibers embedded with beeswax, fir resin, or their blends, along with different fillers. The integration of horsetail powder, rice flour, or ground fir needles with molten wax or resin imparts unique characteristics to each composite. For instance, samples with horsetail powder exhibit a more granular texture due to the incorporation of fine particles. The uniform distribution of these additives within the cellulosic matrix is crucial for enhancing the mechanical and thermal properties of the composites. The microscopy images illustrate this uniformity and hint at an effective bonding between the cellulosic fibers and added materials. This bonding is essential for achieving enhanced structural integrity and durability. Furthermore, it can be observed that there is a variation in color tones across different samples; this could be attributed to the natural pigments present in horsetail powder, rice flour, or fir needles. These variations not only contribute esthetically but may also influence properties like UV resistance.

An analysis revealed that the wetting of cellulose fibers was optimal with beeswax (samples Pr-1, Pr-4, Pr-6, Pr-7) due to its lower melting viscosity. For fir resin, the results showed the formation of resin-rich clusters near the surface (Pr-2) and that mixing with beeswax improved its ability to penetrate the cellulosic matrix (Pr-8 and Pr-9). Based on microscopic analysis, there is no clear distinction between the ground biomass fillers from the cellulosic fibers, likely due to the homogeneous distribution of the fillers within the cellulose pulp.

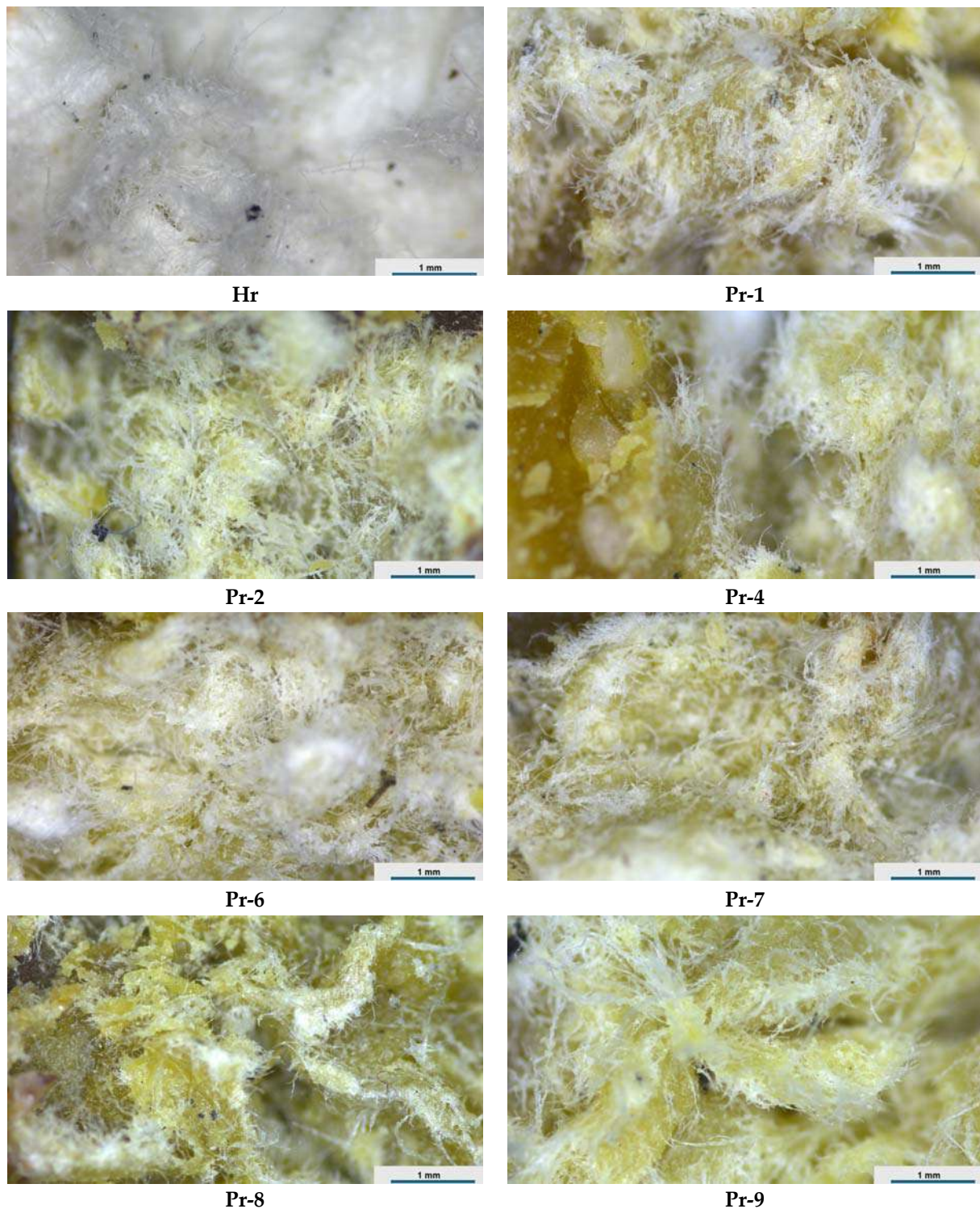


Figure 1. Microscopic images of the obtained composite recipes.

One of the objectives of this study was to determine the feasibility of natural composite formulations as sound insulation materials. One feasible hypothesis was that the natural composite formulations would have comparable or better acoustic properties than the conventional sound insulation materials. To test this hypothesis, the sound absorption coefficient and the sound transmission loss of the natural composite samples were measured and compared with the literature values of the conventional materials. In contrast with “filled” materials, the voids and internal patterns of sound-absorbing materials are important factors that affect their acoustic performance, as they influence the interaction of sound waves with the material’s structure. Different shapes and sizes of voids can create different modes of sound absorption, such as viscous dissipation, thermal conduction, and resonance. Different internal patterns can also affect the sound propagation and reflection within the material [36].

The acoustic impedance spectra results for the different compositions formulated in Table 1, as cast on paper pulp and molded with different patterns, are presented below. Three parameters were analyzed from the acoustic impedance spectra, namely the sound transmission loss (TLn), sound absorption coefficient (α), and reflection (R). These parameters quantify the amount of sound energy that is transmitted, absorbed, and reflected by the material, respectively. Sound transmission loss (TLn) is defined as the difference in sound power level between the incident and transmitted sound waves [37]. The sound absorption coefficient (α) is defined as the ratio of the absorbed sound power to the incident sound power [38]. The reflection (R) is defined as the ratio of the reflected sound pressure to the incident sound pressure [39]. These parameters are important for evaluating the acoustic performance of natural composites, as they indicate the effectiveness of the material in reducing noise and improving sound quality.

The results from Figure 2 illustrate the acoustic impedance envelope for the poured and molded composite formulations.

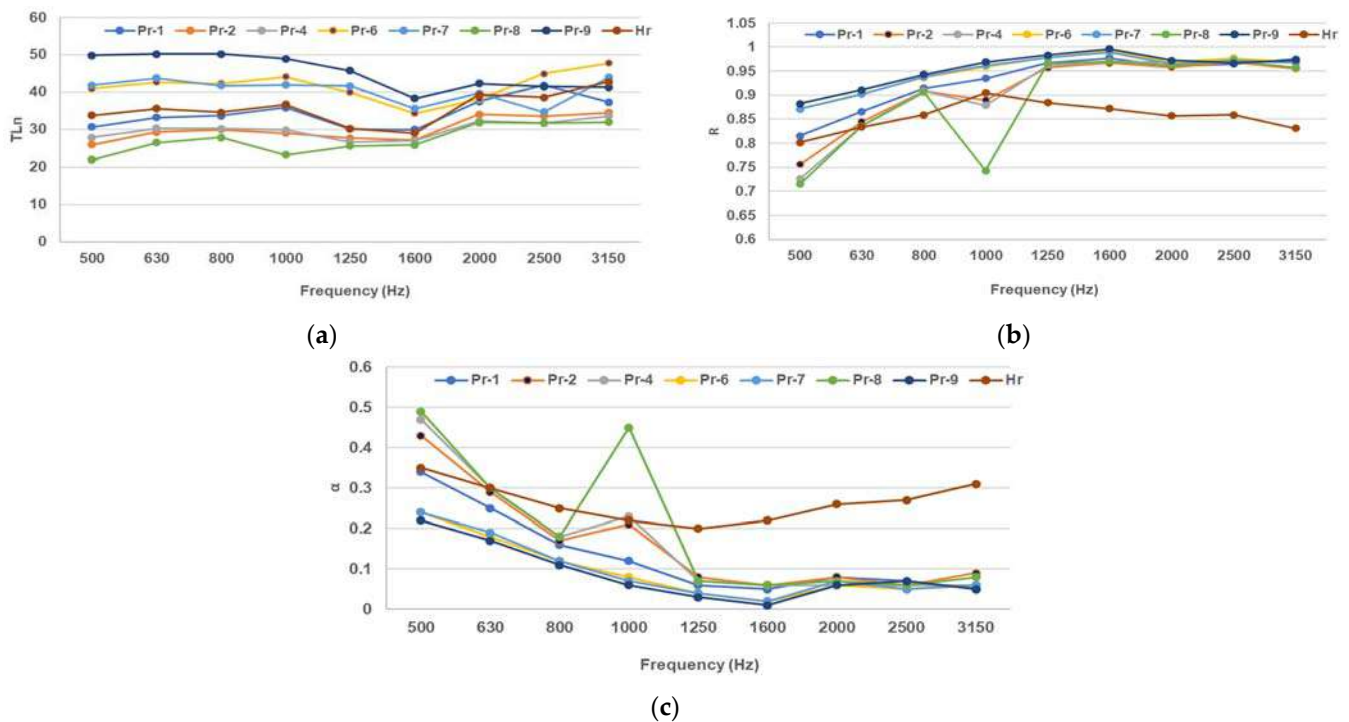


Figure 2. Acoustic measurements for the full molded composites and paper pulp: (a) sound transmission loss (TLn), (b) sound absorption coefficient, (c) sound reflection coefficient.

A higher TLn means a lower sound transmission and better sound insulation. All samples show an increase in TLn with frequency, which means they are more effective in blocking high-frequency sound waves (Figure 2a). All the composite samples have

higher TLn than Hr, which means they have higher density and lower porosity than paper pulp. Among the Pr samples, Pr-7 (with fir needles and beeswax mixture) has the highest TLn, which means it could have the lowest air gap among the natural composites. The literature values of TLn for porous materials range from 10 dB to 40 dB, depending on the frequency, thickness, and density of the material. The Pr samples have similar or higher TLn than the literature values, which means they have comparable or better sound insulation performance than the usual insulation materials [40].

A higher α means a higher sound absorption and a lower sound reflection. The Pr samples show a peak in α around 1000 Hz, which means they have a resonance frequency at this point (Figure 2b). The resonance frequency depends on the thickness, density, and elasticity of the material. The Pr samples have lower α than Hr (paper pulp) at low and high frequencies, which means they have lower surface area and higher flow resistivity than paper pulp. Among the Pr samples, Pr-1 (paper pulp with beeswax) has the highest α , which means it could have the lowest filler content and the highest air gap among the natural composites. The literature values of α for porous materials range from 0.1 to 0.9, depending on the frequency, porosity, and flow resistivity of the material. The Pr samples have relatively similar or comparable α than the literature values, which means they have comparable sound absorption performance to the usual insulation materials [36].

Conversely, a higher sound reflection coefficient R means a lower sound absorption and a higher sound transmission. The composites show a significant peak in R around 1000 Hz, which corresponds to the resonance frequency of the sound absorption coefficient (Figure 2c). This means that the Pr samples reflect most of the sound energy at this frequency, which reduces their sound absorption performance. The Pr samples have higher R than Hr at most frequencies, which means they have a higher impedance mismatch with the surrounding air than paper pulp. Among the Pr samples, Pr-9 (with fir resin and beeswax mixture) has the highest R, which means it could have the highest density and the lowest porosity among the natural composites. The literature values of R for porous materials range from 0.1 to 0.9, depending on the frequency, impedance, and thickness of the material. The Pr samples have similar or higher R than the literature values, which means they have comparable or higher sound reflection performance than the usual porous materials [36].

An improvement in the acoustic parameters of the material can be obtained by the introduction of patterned voids in the material. This is advantageous due to two main reasons: firstly, the material does not need further modifications (amendments in composition), and second, by introducing gaps, the overall cost or cost per weight parameters present significant improvements.

Figure 3 presents the acoustic parameters for the samples obtained with circular patterns.

The composites with circular hole patterns have lower TLn than the filled composites (Figure 3a), which means they have lower density and higher porosity than the filled composites. The composites with circular hole patterns also show more fluctuations in TLn with frequency, which means they have more resonance modes than the filled composites. The composites with circular hole patterns also have higher α than the filled composites at most frequencies, which means they have higher surface areas and lower flow resistivities than the filled composites (Figure 3b). The composites with circular hole patterns have lower R than the filled composites at most frequencies (Figure 3c).

The composites with triangular pattern voids have lower TLn than the plain and circular-void composites (Figure 4a), higher α than the plain and circular-void composites at most frequencies (Figure 4b), and lower R than the plain and circular-void composites at most frequencies (Figure 4c), which means that there is an improvement in the sound insulative properties and there is a lower number of reflected soundwaves compared to the filled composites and those with circular patterns.

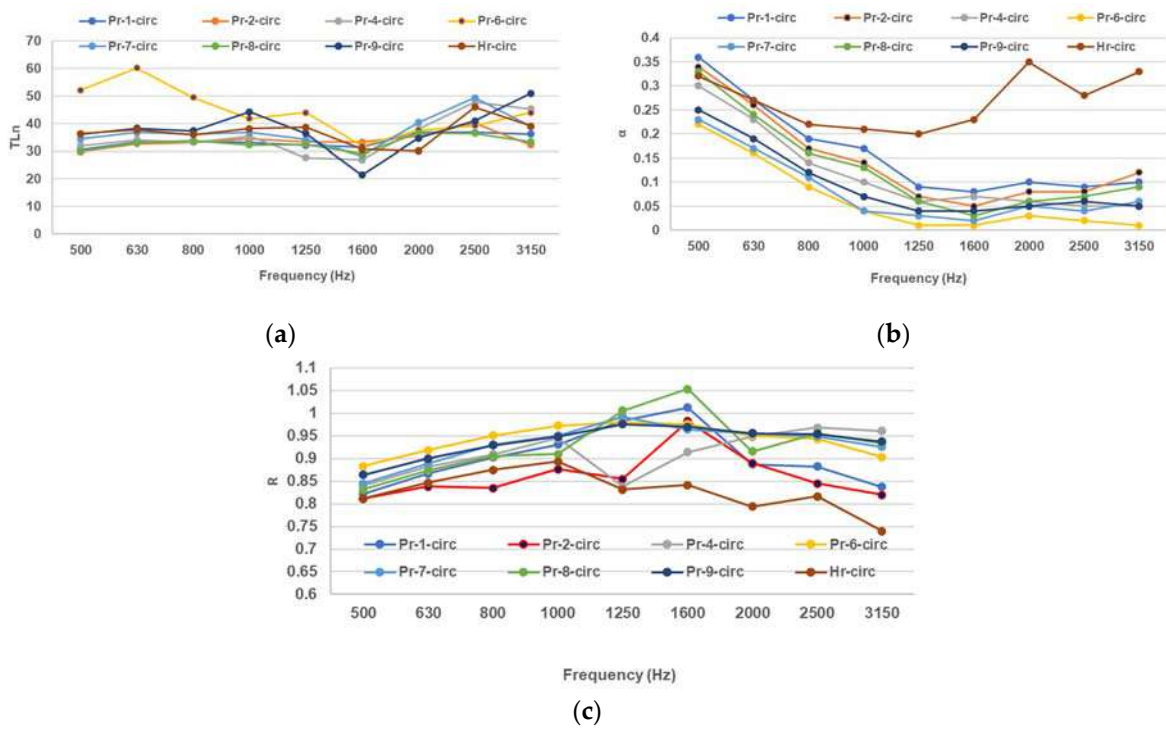


Figure 3. Acoustic measurements for the circular-patterned molded composites and paper pulp: (a) sound transmission loss (TLn), (b) sound absorption coefficient, (c) sound reflection coefficient.

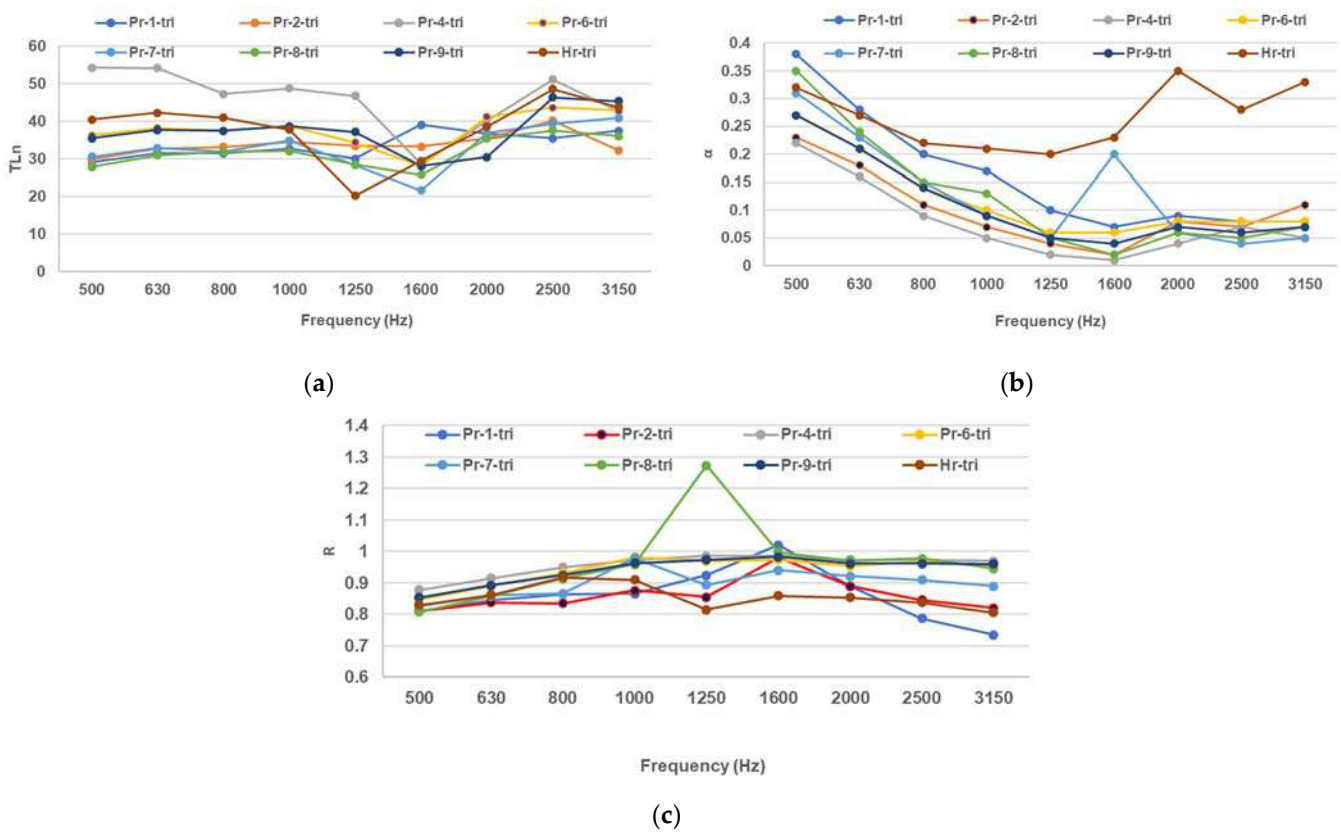


Figure 4. Acoustic measurements for the triangular-patterned molded composites and paper pulp: (a) sound transmission loss (TLn), (b) sound absorption coefficient, (c) sound reflection coefficient.

Among the composites with undulated perforations, the sound transmission loss TLn is, on average, generally lower than the filled composites or the composites with circular or triangular patterns (Figure 5a). Composites with undulated perforations present a higher sound absorption coefficient α than the plain and circular-void composites at most frequencies but lower than the triangular-void ones (Figure 5b).

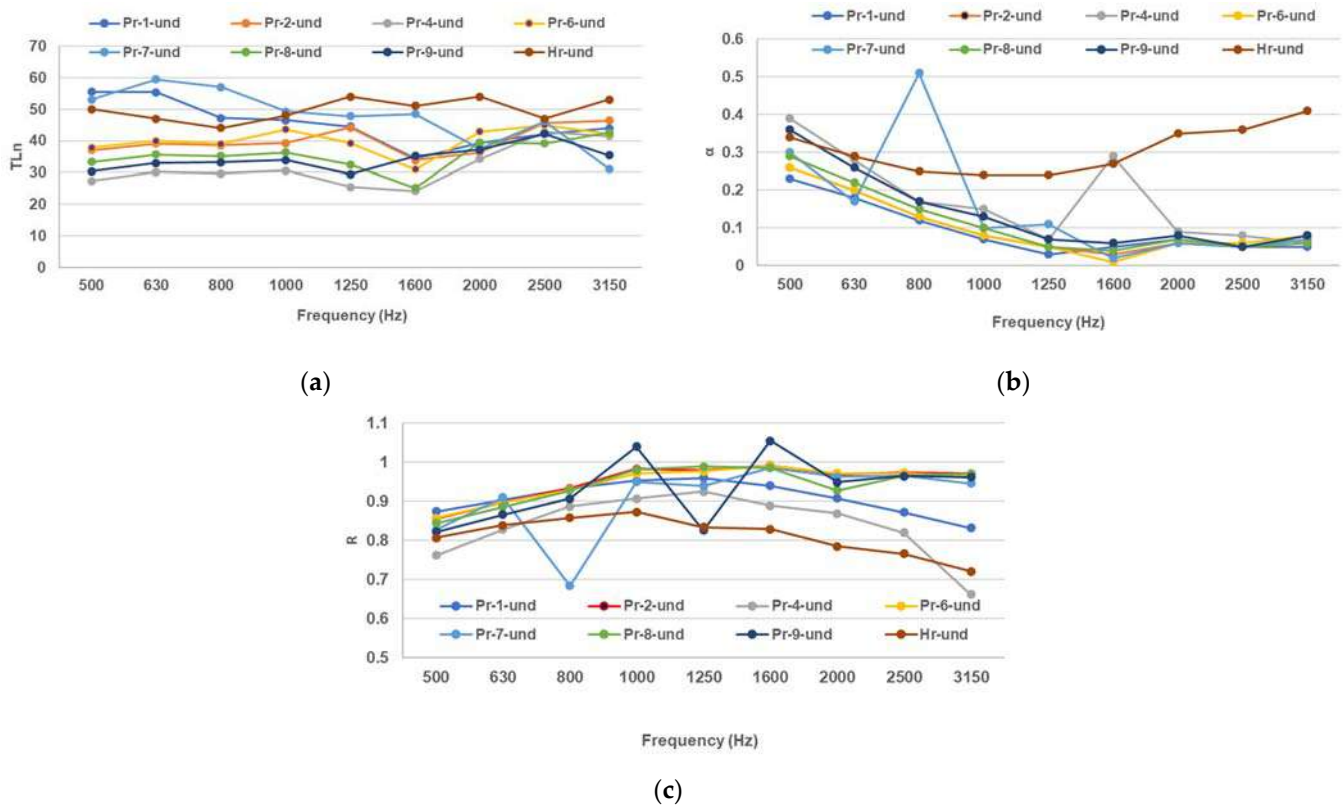


Figure 5. Acoustic measurements for the undulated-patterned molded composites and paper pulp: (a) sound transmission loss (TLn), (b) sound absorption coefficient, (c) sound reflection coefficient.

Complementary to the sound absorption coefficient α , the sound reflection coefficient R presents the lowest values for the undulated pattern composites at most frequencies (Figure 5c).

To summarize the effect of the material type and internal structure on the acoustical parameters, the average values of the acoustic parameters over the whole frequency domain were used, and the top five materials were selected in terms of performance. The average values can reflect the overall acoustic performance of the materials, while the values at a specific frequency may vary depending on the resonance modes and the geometry of the materials. Even if the general trends for the variation in the acoustic parameters were summarized above, compositions from each category of material could present, in some cases, the best performance.

The ranking of the composites in terms of the acoustic parameters is presented in Figure 6.

A high TLn means that the material can block most of the sound energy from passing through, which is desirable for sound insulation applications. It can be seen from Figure 6a that the best sound insulation character is registered for sample Pr-7-und, based on a paper core impregnated with beeswax and ground fir needles. However, a high TLn does not necessarily mean a high sound absorption coefficient (α) or a low sound reflection coefficient (R). These parameters measure the amount of sound energy that is absorbed or reflected by the material, respectively. A high α means that the material can reduce the noise level and improve the sound quality, which is desirable for sound absorption applications.

A low R means that the material can avoid unwanted echo or noise, which is also desirable for sound absorption applications. Therefore, depending on the application, it may be better to have a high TLn, a high α , or a low R. For example, if the noise from outside sources needs to be reduced, a material with a high TLn is desired. For improvement in the acoustics of a room, a material with a high α and a low R might be more suitable.

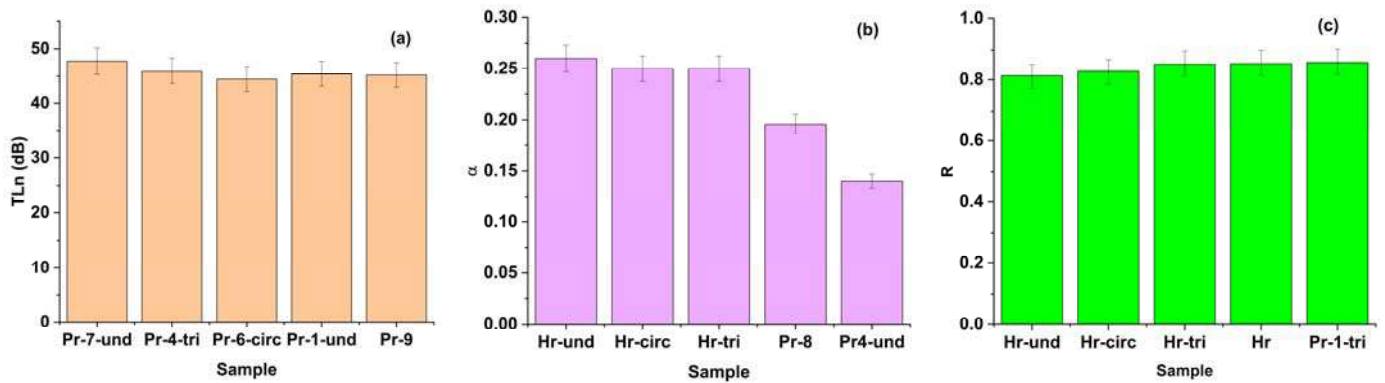


Figure 6. Average values of the selected materials in terms of acoustic performance: (a) sound transmission loss (TLn), (b) sound absorption coefficient, (c) sound reflection coefficient (Hr: paper pulp core; Pr: composites with paper core impregnated with the formulations from Table 1).

The highest sound absorbing properties were registered for the plain paper composites with undulated and circular patterns (Figure 6b), for which the lowest sound reflection coefficient was also registered (Figure 6c). The advantage of using the Pr composites over plain paper is that they have higher density, lower porosity, higher flow resistivity, and higher surface area than plain paper. These factors contribute to the higher sound transmission loss of the Pr composites, which means they have better acoustic performance than plain paper for insulation purposes.

Even if for sound absorption and reflection, the Hr samples (paper pulp) slightly outperformed the composite formulations (Figure 6b,c), the Pr composites still have acceptable acoustic performance for these parameters. The Pr composites have moderate-to-high sound absorption coefficients, ranging from 0.2 to 0.8, depending on the frequency and the pattern. The Pr composites (based on impregnated paper pulp) also have low-to-moderate sound reflection coefficients, ranging from 0.1 to 0.5, depending on the frequency and the pattern. These values are comparable to or slightly lower than the literature values of sound absorption and reflection coefficients for porous materials, such as polyurethane foam, mineral wool, fiberglass, and textile fabrics (Table 4).

Table 4. Acoustical performance of traditional insulators from literature data.

Material	Density (kg/m ³)	Thickness (mm)	Sound Absorption Coefficient (α)	Sound Transmission Loss (dB)	Reflection Coefficient (R)	References
Mineral wool	30–200	25–200	0.8–1.0	40–60	0.2–0.4	[41]
Recycled basalt fibers with bio-binders	10–100	10–50	0.6–0.9	20–40	0.3–0.6	[42]
Polyurethane foams	20–80	10–50	0.6–0.9	20–50	0.3–0.6	[43]
Polystyrene foams	10–40	10–50	0.2–0.4	10–30	0.7–0.9	[44]
Wood particleboard composites	300–800	10–20	0.4–0.7	15–35	0.5–0.8	[45]
Recycled textile materials	10–100	10–50	0.4–0.8	15–30	0.4–0.8	[46]

In terms of sound transmission loss, the composite formulation with beeswax and fir needles impregnated paper pulp core (Pr-7) and the one with beeswax and horsetail powder impregnated paper pulp core (Pr-4) with undulated or triangular pattern bordered

or slightly outperformed the synthetic foams or basalt fiber in terms of their sound transmission loss, which means it can effectively block the sound transmission. Furthermore, as compared to wood-based panels or mineral fibers, paper-core composites have the clear advantage of having higher specific acoustical properties (attributed to their density).

However, the Pr composites also show some drawbacks, such as a significant peak in sound absorption and reflection coefficients around 1000 Hz, which corresponds to the resonance frequency of the materials. This means that the Pr composites absorb and then reflect most of the sound energy at this frequency, which reduces their sound absorption and insulation performance. This peak can be attributed to the thickness, density, and elasticity of the materials, which can be optimized by further modifying the formulation and the pattern of the composites.

The Pr composites, due to their components, could have the advantage of being more durable, stable, and biodegradable than plain paper, which means they have better mechanical, thermal, and environmental properties than plain paper. The Pr composites have higher thermal stability than plain paper, which means they can resist higher temperatures and dissipate heat more efficiently.

Through the simple modification of the obtained technology for the composite panels, namely gravitational pouring (without supplementary pressing of the material in the mold), an improvement in the sound absorption coefficient for the Pr-4 sample (beeswax –62.5% and horsetail powder –37.5%) from 0.15 to 0.58 and the Hr sample from 0.26 to 0.78 can be achieved. The sound absorption behavior is influenced by the micropores, resulting in the composite material when it is not supplementary pressed.

4. Conclusions

The utilization of natural materials in sound insulation panels presents a significant advancement in the realm of acoustic engineering, offering a promising alternative to traditional synthetic counterparts. These panels demonstrate exceptional performance across various acoustic parameters, often surpassing conventional materials in specific scenarios. One key advantage lies in their multifaceted composition, incorporating diverse natural components that synergistically enhance their thermal stability, mechanical strength, and environmental sustainability.

The study elucidates the thermal behavior of natural composite materials derived from recycled paper pulp, beeswax, fir resin, and various fillers like horsetail powder, rice flour, and ground fir needles. As evidenced by our findings, these natural composite panels exhibit superior thermal degradation behavior, the onset of degradation being as high as 290 °C compared to polyurethane foams. Also, promising thermal stability under cyclic heating–cooling regimes has been registered, showcasing the potential for applications requiring resistance to thermal stress.

The incorporation of patterned voids in the composites offers a promising avenue for improving their acoustic parameters. Several architectures of these voids were researched in this study, namely circular-, triangular-, and undulated voids, with the undulated ones showing the highest sound absorption and transmission-blocking. Regarding the acoustical dampening, the composites with beeswax and fir needles showed comparable or marginally higher sound transmission loss coefficients to traditional materials such as foams or wood particleboard.

While the results show promise for the use of these biocomposites as insulation or acoustic panels, their suitability is restricted to indoor or climatically stable outdoor applications. Due to the natural organic composition of the matrix and fillers, these materials would likely be vulnerable to degradation if exposed to prolonged cold and damp conditions. However, when encased in shells (made from polymers, polymers composites, wood, metallic, etc.), frames, or in indoor applications, the components are protected from weather factor variations as well as from biological attack by fungi, molds, insects, and rodents.

Future research could focus on further optimizing the composition and structure of these composites to enhance their acoustic performance while maintaining their thermal stability and environmental benefits. By modifying the internal structure and the pressure of molding, the composites can achieve good sound insulation and absorption properties (sound absorption coefficients as high as 0.78, as determined from our preliminary experiments), making them versatile candidates for diverse acoustic applications. Additionally, exploring novel filler materials and refining the manufacturing processes could unlock new possibilities for improving the overall efficiency and applicability of these natural composite materials.

Supplementary Materials: The following supporting information can be downloaded at: <https://www.mdpi.com/article/10.3390/polym16050672/s1>, Figure S1: (a): DSC and (b): TG/DTA thermograms for beeswax (Pr-1). Figure S2: (a): DSC and (b): TG/DTA thermograms for fir resin (Pr-2). Figure S3: (a): DSC and (b): TG/DTA thermograms for Beeswax (50%) + fir resin (50%) (Pr-9). Figure S4: (a): DSC and (b): TG/DTA thermograms for Beeswax (62.5%) + horsetail powder (37.5%) (Pr-4). Figure S5: (a): DSC and (b): TG/DTA thermograms for Beeswax (45.5%) + rice flour (54.5%) (Pr-6). Figure S6: (a): DSC and (b): TG/DTA thermograms for Beeswax (61.5%) + ground fir needles (38.5%) (Pr-7). Figure S7: (a): DSC and (b): TG/DTA thermograms for Beeswax (31.25%) + fir resin (31.25%) + horsetail powder (37.5%) (Pr-8). Figure S8: (a): DSC and (b): TG/DTA thermograms for the paper pulp sample (Hr).

Author Contributions: Conceptualization, M.A.P., C.C. and S.-M.Z.; methodology, M.A.P. and C.C.; software, M.A.P. and C.C.; validation, M.A.P., M.C. and C.C.; formal analysis, C.C.; investigation, M.A.P., S.M., C.S. and C.C.; resources, M.A.P.; data curation, M.A.P., S.M., C.S. and S.-M.Z.; writing—original draft, M.A.P. and C.C.; writing—review and editing, M.A.P., S.M., S.-M.Z., C.S. and C.C.; visualization, M.A.P. and C.C.; supervision, M.A.P. and C.C.; project administration, M.A.P.; funding acquisition, M.A.P. All authors have read and agreed to the published version of the manuscript.

Funding: This work was supported by a grant from the Ministry of Research, Innovation and Digitization, CNCS–UEFISCDI, project number PN-III-P1-1.1-TE-2021-0294, within PNCDI III.

Institutional Review Board Statement: Not applicable.

Informed Consent Statement: Not applicable.

Data Availability Statement: Data are contained within the article. Supporting information can be made available on request by the corresponding author.

Acknowledgments: This work was supported by a grant from the Ministry of Research, Innovation and Digitization, CNCS–UEFISCDI, project number PN-III-P1-1.1-TE-2021-0294, within PNCDI III. We also acknowledge the structural funds project PRO-DD (POS-CCE O.2.2.1, ID 123, SMIS 2637, ctr. No 11/2009) for partially providing the infrastructure used in this work at the CDI Institute of Transilvania University of Brasov.

Conflicts of Interest: The authors declare no conflicts of interest.

References

1. Alabdulkarem, A.; Ali, M.; Iannace, G.; Sadek, S.; Almuzaiqer, R. Thermal analysis, microstructure and acoustic characteristics of some hybrid natural insulating materials. *Constr. Build. Mater.* **2018**, *187*, 185–196. [CrossRef]
2. Ouhaibi, S.; Gounni, A.; Belouaggadia, N.; Ezzine, M.; Lbibb, R. Thermal performance of new ecological material integrated into residential building in semi-arid and cold climates. *Appl. Therm. Eng.* **2020**, *181*, 115933. [CrossRef]
3. Asdrubali, F.; D’Alessandro, F.; Schiavoni, S. A review of unconventional sustainable building insulation materials. *Sustain. Mater. Technol.* **2015**, *4*, 1–17. [CrossRef]
4. Thyavihalli Girijappa, Y.G.; Mavinkere Rangappa, S.; Parameswaranpillai, J.; Siengchin, S. Natural fibers as sustainable and renewable resource for development of eco-friendly composites: A comprehensive review. *Front. Mater.* **2019**, *6*, 226. [CrossRef]
5. Rusu, R.D.; Abadie, M.J. *New High-Performance Materials: Bio-Based, Eco-Friendly Polyimides*. In *Polyimide for Electronic and Electrical Engineering Applications*; IntechOpen: London, UK, 2020.
6. Maryanto, E.T.; Setyawan, A.; Maria, T.S.B.; Astuti, W. Analysis of the Performance of Natural Composite Materials Reinforced with Sago Sheath Fibers as an Alternative Material in Overcoming the Effect of Urban Heat Islands on Buildings. *Buildings* **2022**, *13*, 18. [CrossRef]

7. Hassan, T.; Jamshaid, H.; Mishra, R.; Khan, M.Q.; Petru, M.; Novak, J.; Choteborsky, R.; Hromasova, M. Acoustic, mechanical and thermal properties of green composites reinforced with natural fibers waste. *Polymers* **2020**, *12*, 654. [[CrossRef](#)] [[PubMed](#)]
8. Sair, S.; Mansouri, S.; Tanane, O.; Abboud, Y.; El Bouari, A. Alfa fiber-polyurethane composite as a thermal and acoustic insulation material for building applications. *SN Appl. Sci.* **2019**, *1*, 667. [[CrossRef](#)]
9. Neto, J.S.; de Queiroz, H.F.; Aguiar, R.A.; Banea, M.D. A review on the thermal characterisation of natural and hybrid fiber composites. *Polymers* **2021**, *13*, 4425. [[CrossRef](#)] [[PubMed](#)]
10. Dobrosielska, M.; Dobrucka, R.; Kozera, P.; Brzakałski, D.; Gabriel, E.; Głowacka, J.; Jałbrzykowski, M.; Kurzydłowski, K.J.; Przekop, R.E. Beeswax as a natural alternative to synthetic waxes for fabrication of PLA/diatomaceous earth composites. *Sci. Rep.* **2023**, *13*, 1161. [[CrossRef](#)]
11. Aldas, M.; Pavon, C.; López-Martínez, J.; Arrieta, M.P. Pine resin derivatives as sustainable additives to improve the mechanical and thermal properties of injected moulded thermoplastic starch. *Appl. Sci.* **2020**, *10*, 2561. [[CrossRef](#)]
12. Mohanty, A.K.; Misra, M.; Drzal, L.T. Sustainable bio-composites from renewable resources: Opportunities and challenges in the green materials world. *J. Polym. Environ.* **2002**, *10*, 19–26. [[CrossRef](#)]
13. Gliścińska, E.; Krucińska, I.; Michalak, M.; Puchalski, M.; Ciechańska, D.; Kazimierczak, J.; Bloda, A. Bio-based composites for sound absorption. In *Composites from Renewable and Sustainable Materials*; IntechOpen: London, UK, 2016; pp. 217–239.
14. Jawaid, M.H.P.S.; Khalil, H.A. Cellulosic/synthetic fibre reinforced polymer hybrid composites: A review. *Carbohydr. Polym.* **2011**, *86*, 1–18. [[CrossRef](#)]
15. García, D.; Bustamante, F.; Alarcón, E.; Donate, J.M.; Canoira, L.; Lapuerta, M. Improvements of thermal and thermochemical properties of rosin by chemical transformation for its use as biofuel. *Waste Biomass Valorization* **2020**, *11*, 6383–6394. [[CrossRef](#)]
16. Chang, R.; Lata, R.; Rohindra, D. Study of mechanical, enzymatic degradation and antimicrobial properties of poly (butylene succinate)/pine-resin blends. *Polym. Bull.* **2002**, *77*, 3621–3635. [[CrossRef](#)]
17. Asim, M.; Paridah, M.T.; Chandrasekar, M.; Shahroze, R.M.; Jawaid, M.; Nasir, M.; Siakeng, R. Thermal stability of natural fibers and their polymer composites. *Iran. Polym. J.* **2020**, *29*, 625–648. [[CrossRef](#)]
18. Khalil, H.A.; Bhat, A.H.; Yusra, A.I. Green composites from sustainable cellulose nanofibrils: A review. *Carbohydr. Polym.* **2012**, *87*, 963–979. [[CrossRef](#)]
19. Gholampour, A.; Ozbakkaloglu, T. A review of natural fiber composites: Properties, modification and processing techniques, characterization, applications. *J. Mater. Sci.* **2020**, *55*, 829–892. [[CrossRef](#)]
20. Jang, E.S. Sound Absorbing Properties of Selected Green Material—A Review. *Forests* **2023**, *14*, 1366. [[CrossRef](#)]
21. Hassan, T.; Jamshaid, H.; Mishra, R.; Khan, M.Q.; Petru, M.; Tichy, M.; Muller, M. Factors affecting acoustic properties of natural-fiber-based materials and composites: A review. *Textiles* **2021**, *1*, 55–85. [[CrossRef](#)]
22. Bhuiyan, M.R.; Ali, A.; Mohebbullah, M.; Hossain, M.F.; Khan, A.N.; Wang, L. Recycling of cotton apparel waste and its utilization as a thermal insulation layer in high performance clothing. *Fash. Text.* **2023**, *10*, 22. [[CrossRef](#)]
23. Chen, J.; Yan, Z.; Li, H.; Zhang, Z.; Gong, J.; Zhang, J. Fabrication, sound absorption simulation and performance optimization of multi-layer gradient fiber-based composites. *Polym. Compos.* **2023**, *44*, 5044–5057. [[CrossRef](#)]
24. Khem, S.; Sutikno, S.; Suwarta, P.; Istana, B. Experimental Study of Sound Absorption Coefficient Characteristics of Oil Palm Frond Reinforced Composite. *Key Eng. Mater.* **2023**, *941*, 257–263. [[CrossRef](#)]
25. Haghghat, M.; Samaei, S.E.; Amininasab, S.; Faridan, M.; Mehrzad, S.; Sheikhmozafari, M.J.; Taban, E. The Impact of Fiber Size on the Sound Absorption Behavior of Composites Made from Sugarcane Bagasse Wastes Fibers. *J. Nat. Fibers* **2023**, *20*, 2175760. [[CrossRef](#)]
26. Tang, X.; Yan, X. Acoustic energy absorption properties of fibrous materials: A review. *Compos. Part A Appl. Sci. Manuf.* **2017**, *101*, 360–380. [[CrossRef](#)]
27. Marinkovic, B.A.; White, M.A.; Chen, J.; Sanson, A. Recent Advances in Low-Positive, Zero, and Negative Thermal Expansion Materials: Fundamentals and Applications. *Front. Mater.* **2022**, *9*, 873553. [[CrossRef](#)]
28. Jaafar, J.; Siregar, J.P.; Mohd Salleh, S.; Mohd Hamdan, M.H.; Cionita, T.; Rihayat, T. Important considerations in manufacturing of natural fiber composites: A review. *Int. J. Precis. Eng. Manuf. Green Technol.* **2019**, *6*, 647–664. [[CrossRef](#)]
29. Abare, A.Y.; Jawaid, M.; Hamid, N.H.; Bakar, B.F.A.; Ismail, A.S.; Sarmin, S.N.; Fouad, H.; Midani, M. Evaluation of physical, mechanical, and thermal properties of woven kenaf/bio-epoxy composites. *J. Ind. Text.* **2023**, *53*, 15280837231163342. [[CrossRef](#)]
30. Bharti, P.; Verma, S.; Kumar, M.; Devnani, G.L. Thermal Stability of Polymer Composites Reinforced with Bast Fibers. In *Bast Fibers and Their Composites: Processing, Properties and Applications*; Springer Nature: Singapore, 2022; pp. 147–166.
31. Katunin, A. Evaluation of criticality of self-heating of polymer composites by estimating the heat dissipation rate. *Mech. Compos. Mater.* **2018**, *54*, 53–60. [[CrossRef](#)]
32. Jubsilp, C.; Mora, P.; Rimdusit, S. Thermal Stability and Flame Retardancy of Epoxy/Natural Fiber Composites. In *Handbook of Epoxy/Fiber Composites*; Springer Nature: Singapore, 2022; pp. 713–743.
33. Poletto, M.; Ornaghi Júnior, H.L.; Zattera, A.J. Native Cellulose: Structure, Characterization and Thermal Properties. *Materials* **2014**, *7*, 6105–6119. [[CrossRef](#)]
34. Salasinska, K.; Barczewski, M.; Borucka, M.; Górny, R.L.; Kozikowski, P.; Celiński, M.; Gajek, A. Thermal stability, fire and smoke behaviour of epoxy composites modified with plant waste fillers. *Polymers* **2019**, *11*, 1234. [[CrossRef](#)]
35. Chang, B.P.; Mohanty, A.K.; Misra, M. Studies on durability of sustainable biobased composites: A review. *RSC Adv.* **2020**, *10*, 17955–17999. [[CrossRef](#)] [[PubMed](#)]

36. Otaru, A.J. Review on the acoustical properties and characterisation methods of sound absorbing porous structures: A focus on microcellular structures made by a replication casting method. *Met. Mater. Int.* **2020**, *26*, 915–932. [[CrossRef](#)]
37. Miles, R.N.; Miles, R.N. Sound Transmission Loss. In *Physical Approach to Engineering Acoustics*; Springer: Cham, Switzerland, 2020; pp. 53–82.
38. Qiu, X. Principles of sound absorbers. In *Acoustic Textiles*; Springer: Singapore, 2016; pp. 43–72.
39. Sharma, S.K.; Shukla, S.R.; Sethy, A.K. Acoustical behaviour of natural fibres-based composite boards as sound-absorbing materials. *J. Indian Acad. Wood Sci.* **2020**, *17*, 66–72. [[CrossRef](#)]
40. Huang, S.; Li, Y.; Zhu, J.; Tsai, D.P. Sound-absorbing materials. *Phys. Rev. Appl.* **2023**, *20*, 010501. [[CrossRef](#)]
41. Arenas, J.P.; Asdrubali, F. Eco-materials with noise reduction properties. In *Handbook of Ecomaterials*; Martinez, L.M.T., Kharissova, O.V., Kharisov, B.I., Eds.; Springer: Cham, Switzerland, 2018; pp. 3031–3056.
42. Available online: <https://www.knaufnorthamerica.com/en-us/sound-control> (accessed on 25 February 2024).
43. Rastegar, N.; Ershad-Langroudi, A.; Parsimehr, H.; Moradi, G. Sound-absorbing porous materials: A review on polyurethane-based foams. *Iran. Polym. J.* **2022**, *31*, 83–105. [[CrossRef](#)]
44. Sabbagh, M.; Elkhateeb, A. Sound absorption characteristics of polyurethane and polystyrene foams as inexpensive acoustic treatments. *Acoust. Aust.* **2019**, *47*, 285–304. [[CrossRef](#)]
45. Mohammed, A.S.; Meincken, M. Thermal and acoustic insulation properties of wood plastic composites (WPCs) for interior housing applications. *Eur. J. Wood Wood Prod.* **2023**, *81*, 421–437. [[CrossRef](#)]
46. Özdil, N.; Kayseri, G.Ö.; Mengüç, G.S. Investigation of sound absorption characteristics of textile materials produced from recycled fibers. In *Waste in Textile and Leather Sectors*; IntechOpen: London, UK, 2020; pp. 1–20.

Disclaimer/Publisher’s Note: The statements, opinions and data contained in all publications are solely those of the individual author(s) and contributor(s) and not of MDPI and/or the editor(s). MDPI and/or the editor(s) disclaim responsibility for any injury to people or property resulting from any ideas, methods, instructions or products referred to in the content.

Article

Investigation into the Acoustic Properties of Polylactic Acid Sound-Absorbing Panels Manufactured by 3D Printing Technology: The Influence of Nozzle Diameters and Internal Configurations

Simona Matei ¹, Mihai Alin Pop ^{1,*}, Sebastian-Marian Zaharia ², Mihaela Coșniță ³, Cătălin Croitoru ⁴,
Cosmin Spîrchez ⁵ and Cristina Cazan ³

- ¹ Department of Materials Science, Transilvania University of Brasov, 500036 Brasov, Romania; simona.matei@unitbv.ro
- ² Department of Manufacturing Engineering, Transilvania University of Brasov, 500036 Brasov, Romania; zaharia_sebastian@unitbv.ro
- ³ Department of Product Design, Mechatronics and Environment, Transilvania University of Brasov, 500036 Brasov, Romania; mihaela.cosnita@unitbv.ro (M.C.); c.vladuta@unitbv.ro (C.C.)
- ⁴ Materials Engineering and Welding Department, Transilvania University of Brasov, 500036 Brasov, Romania; c.croitoru@unitbv.ro
- ⁵ Wood Processing and Design Wooden Product Department, Transilvania University of Brasov, 500036 Brasov, Romania; cosmin.spirchez@unitbv.ro
- * Correspondence: mihai.pop@unitbv.ro



Citation: Matei, S.; Pop, M.A.; Zaharia, S.-M.; Coșniță, M.; Croitoru, C.; Spîrchez, C.; Cazan, C.

Investigation into the Acoustic Properties of Polylactic Acid Sound-Absorbing Panels Manufactured by 3D Printing Technology: The Influence of Nozzle Diameters and Internal Configurations. *Materials* **2024**, *17*, 580. <https://doi.org/10.3390/ma17030580>

Academic Editor: Antonino Recca

Received: 5 January 2024

Revised: 19 January 2024

Accepted: 23 January 2024

Published: 25 January 2024

Correction Statement: This article has been republished with a minor change. The change does not affect the scientific content of the article and further details are available within the backmatter of the website version of this article.



Copyright: © 2024 by the authors. Licensee MDPI, Basel, Switzerland. This article is an open access article distributed under the terms and conditions of the Creative Commons Attribution (CC BY) license (<https://creativecommons.org/licenses/by/4.0/>).

Abstract: Sound-absorbing panels are widely used in the acoustic design of aircraft parts, buildings and vehicles as well as in sound insulation and absorption in areas with heavy traffic. This paper studied the acoustic properties of sound-absorbing panels manufactured with three nozzle diameters (0.4 mm, 0.6 mm and 0.8 mm) by 3D printing from three types of polylactic acid filaments (Grey Tough PLA; Black PLA Pro; Natural PLA) and with six internal configurations with labyrinthine zigzag channels (Z1 and Z2). The absorption coefficient of the sample with the Z2 pattern, a 5.33 mm height, a 0.6 mm nozzle diameter and with Black PLA Pro showed the maximum value ($\alpha = 0.93$) for the nozzle diameter of 0.6 mm. Next in position were the three samples with the Z1 pattern (4 mm height) made from all three materials used and printed with a nozzle diameter of 0.4 mm with a sound absorption coefficient value ($\alpha = 0.91$) at 500 Hz. The highest value of the sound transmission loss (56 dB) was found for the sample printed with a nozzle size of 0.8 mm with the Z2 pattern (8 mm height) and with Black PLA Pro. The extruded material, the nozzle diameter and the internal configuration had a significant impact on the acoustic performance of the 3D-printed samples.

Keywords: acoustic properties; 3D printing process; sound-absorbing panels; polylactic acid

1. Introduction

Noise pollution is the excessive and uncontrolled presence of unwanted and disturbing sounds in a given environment, which can have negative effects on human health, wildlife and ecosystems. The additive manufacturing of sound-absorbing panels with high acoustic performance is a topical and intensively researched subject, mainly due to the low cost, short manufacturing time and diversity of materials used in these types of 3D printing processes.

Noise is defined as a compound of sounds that affect the psychological and biological state of humans and other organisms which are found in nature. It is one of the main types of pollution, and constant exposure to it can cause different types of health problems such as hearing loss, cardiovascular diseases, sleep disorders, discomfort, etc. [1–4]. In this regard, sound-absorbing materials made of environmentally friendly materials [5–7] or synthetic materials [7–9] have been developed. Of these materials, the most important

factor influencing their acoustic performance is the porosity [10–13]. The most common application for porous materials is sound absorption, for example in room acoustics [14,15] or porous linings in aircraft engines or next to porous laminated composite structures for wings or empennage [16]. Porous materials exhibit favorable acoustic properties, especially those with a high absorption coefficient [17].

One method of developing acoustically efficient materials is fused-filament fabrication (FFF), also known as 3D printing. The 3D printing process allows for complex shapes to be manufactured directly from computer-aided design (CAD) templates by successively adding layers of extruded material [18]. For porous materials, 3D printing processes result in samples whose microstructure is known and can therefore be related to the macroscopic homogenized quantities. There are several examples in the literature where the 3D printing process has been used to manufacture sound absorbers. Setaki et al. [19] obtained such sound absorbers on the basis of the destructive interference principle. With this principle, if a peak of a single wave encounters a minimum of another wave, then the amplitude is equal to the difference between the individual amplitudes. Ghaffarivardavagh et al. [20] presented another approach for sound attenuation, namely a structure that reduces sound transmission in pipes while being permeable and can thus be further used in fluid flows using the same principle (destructive interference).

Liu et al. [21] developed multi-layer perforated sound-absorbing panels using 3D printing technology. The acoustic properties of porous media can be estimated using several material designs of different complexity, among which the BIOT model is the most complex [22]. This model estimates the acoustic behavior based on parameters such as the airflow resistivity, sinuosity, porosity, and others. Ring et al. [23] obtained porous and acoustically efficient absorber structures using the material extrusion (MEX) process and demonstrated the potential of these structures.

Boulvert et al. [24] researched the geometrical factors influencing the acoustic properties and reported a numerical optimization procedure of a continuous-gradient porous layer properties to obtain perfect absorption under normal-incidence conditions for 3D-printed samples. Following the study in [24], the best-performing continuous-gradient microstructure, which provides optimal acoustic reflectance and/or transmission, was designed by a nonlinear conjugate-gradient algorithm for 3D-printed cylindrical samples.

In the studies by Gino Iannace [25] and Maria Grazia De Giorgi et al. [26], natural fibers with good sound absorption coefficients were reported that were similar to synthetic porous materials, and upon increasing the sample thickness, the highest values of the sound absorption coefficient moved towards the lowest frequencies with diverse applications, including building restorations for sound isolation.

Carbajo et al. [27] obtained 3D-printed macro-perforated porous polylactic acid filament (PLA) materials using fused deposition modeling (FDM) with a simple filling pattern that provided open porosities ranging from 8% to 39% with pore sizes of at least 0.2 mm. The experimental results showed a high absorption performance for the samples that exhibited macro-perforations. In addition, a comparative study on predictions obtained with the double-porosity theory in conjunction with the Johnson–Champoux–Allard (JCA) approach using macroscopic parameters obtained by an inverse characterization procedure and absorption measurements showed acceptable agreement.

Gliscinska et al. [28] developed sound-absorbing materials from viscose and polylactic-acid-based composites. They found that the presence of the polymer layer on the surface of the composite material improved the sound absorption. In the low-frequency range of sound, the absorption frequency range tended to expand towards lower frequencies as the thickness of the polymer surface layer increased.

The acoustic performances of sound-absorbing panels are characterized by two important properties: the sound absorption coefficient (α) and the sound transmission loss (STL). The sound absorption coefficient (α) is defined as the ratio of the sound energy absorbed by the medium through which the wave passes to the energy of the incident wave. The

sound transmission loss (STL) is defined as the ratio of the sound power that enters the sound attenuator to the transmitted sound power.

In the case of porous materials, in addition to the sound absorption characteristics, many researchers have also studied the sound reflection properties [29]. The study in [29] of the natural behavior of infinite uniform layers of a porous material considered the relationship between pressure and velocity, and the results focused on the evaluation of the intrinsic properties of the material based on the acoustic surface impedance of plane waves using two parameters: the energy deviation index and the real reflection angle. Sound reflection is the phenomenon of a sound returning to the medium from which it originates when it meets the separation surface with another medium, which has a different density [30,31].

Zvonicek et al. [32] analyzed the acoustic properties of 3D-printed sound-absorbing panels made of polylactic acid filament (PLA), polyethylene terephthalate modified with glycol (PET-G) and acrylonitrile styrene acrylate (ASA). These researchers observed that the PLA samples demonstrated the best results for the reflection coefficient. Also, from the data analyzed, in terms of the acoustic performance as well as economic constraints, the ideal combination for 3D printing stringed instruments was PET-G material with either a gyroid or grid infill structure printed with a deposition layer height of 0.3 mm or 0.5 mm.

Monkova et al. [33] found that the reflective properties of PLA samples were influenced not only by the type of structure but also by the porosity and thickness of the samples. In a recent study [34], the influence of arbitrarily varying cross-sectional perforations on the acoustic behavior of 3D-printed PLA parts with a divergent–convergent pattern was studied. The results indicated that the sound absorption of perforated panels with a varying cross section was better than that of perforated panels with a uniform cross section for the given frequency range.

The influence of the spherical perforations and their grading on the acoustic characteristics (sound absorption coefficient and sound transmission loss) of a 3D-printed PLA biodegradable material were experimentally analyzed and simulated. The results demonstrated that the sound absorption coefficient of all the functionally graded perforations was higher at low frequencies [35]. Another study [36] researched the acoustic properties of 3D-printed porous polycarbonate material (PPM). The acoustic tests found that with increasing the perforation angle and with the porosity being constant, the sound absorption decreased. Also, the acoustic results indicated that by adjusting the perforation angle and the airgap behind the sample, a high level of sound absorption at low frequencies could be obtained.

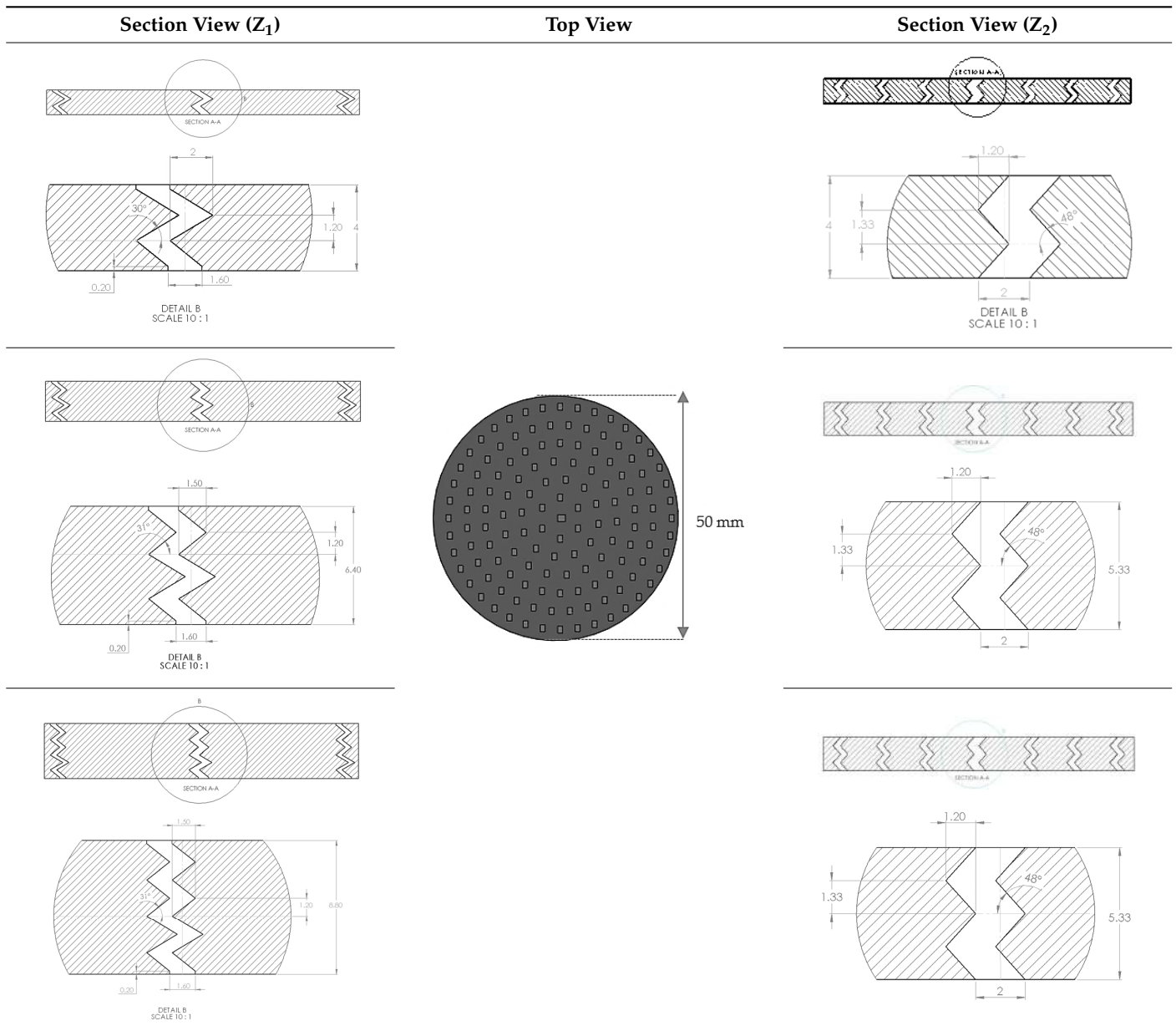
Vasina et al. [37] analyzed the different factors (open–porous material structure, the excitation frequency, the sample thickness and the air gap size) that influenced the sound absorption behavior of ABS samples. From the current state of the literature, it can be stated that additive manufacturing processes, particularly FDM, are increasingly being used in studies that analyze the acoustic performance of sound-absorbing panels [36], but there are unexplored research directions that can bring important results in the acoustic field.

In this paper, sound-absorbing panels with different internal configurations made of different types of PLA filaments were designed and manufactured by 3D printing. The obtained samples were acoustically tested by the transfer function method using an acoustic impedance tube. Within this study, the analyzed acoustic properties were as follows: the sound absorption coefficient (α), the sound transmission loss (STL) and the sound reflection coefficient (β).

2. Materials and Methods

2.1. Design of Acoustic Test Samples

The sample design was carried out using the SolidWorks 2016 software system in accordance with specific acoustic testing standards [38–40]. Two sample designs were used for acoustic testing: Z_1 and Z_2 , as shown in Table 1.

Table 1. Dimensional characteristics of 3D-printed samples.

For each design (Z_1 and Z_2), samples of three different thicknesses were designed. Thus, for model Z_1 , the samples were 4 mm, 6.4 mm and 8.8 mm thick, respectively, and for design Z_2 , they were 4 mm, 5.33 mm and 8 mm thick, respectively. The samples were 3D-printed with three nozzle diameters (0.4 mm, 0.6 mm and 0.8 mm) and from three types of polylactic acid filaments (Grey Tough PLA; Black PLA Pro; Natural PLA). These sample sizes were in accordance with the mentioned standards [39,40] as well as with the technical characteristics of the impedance tube used in the acoustic tests.

2.2. Three-Dimensional Printing of the Samples

Three types of filaments, based on polylactic acid, were used to manufacture the samples for acoustic testing: Grey Tough PLA [41], Black PLA Pro [42] and Natural PLA [43]. The sound-absorbing panels were 3D-printed using a CreatBot DX-3D printer (Henan Suwei Electronic Technology Co., Ltd., Zhengzhou, China). In this study, PLA filament was chosen as the base because it is based on a thermoplastic polyester made from corn starch or sugar cane, which are renewable resources. Admittedly, other advantages of this type

of filament were also considered, such as [44,45] its diverse range of filaments and colors, low cost, ease of 3D printing, low 3D printing temperature (180–220 °C), high printing quality and accuracy and low shrinkage. The manufacturing parameters were selected according to each filament type and were controlled via the 3D printing slicing software CreatBot—CreatWare V6.5.2. The specimens were measured after the 3D printing, and a dimensional precision of approx. 0.1 mm was obtained. The most important manufacturing parameters of the 3D-printed sound-absorbing panels with the 3 types of PLA filaments are presented in Table 2.

Table 2. Filament characteristics and 3D-printed sample parameters [41–43].

Parameter	Value		
	Grey Tough PLA	Black PLA Pro	Natural PLA
Filament diameter (mm)	2.85	2.85	2.85
Filament color	Grey	Black	Natural
Printed Part Density (g/cm ³)	1.22	1.25	1.24
Glass Transition Temperature (°C)	59	63	55–60
Melting Temperature	152	170–180	-
Layer height (mm)	0.2	0.2	0.2
Building plate temperature (°C)	40	40	40
Infill density (%)	60	60	60
Infill pattern	Cubic	Cubic	Cubic
Print speed (mm/s)	40	40	40
Travel speed (mm/s)	120	120	120
Printing temperature (°C)	215	210	210
Top layers	4	4	4
Bottom layers	4	4	4
Nozzle diameter (mm)	0.4/0.6/0.8	0.4/0.6/0.8	0.4/0.6/0.8

The six designs shown in Table 1, with their different thicknesses and internal configurations, were 3D-printed with the three nozzles (0.4 mm; 0.6 mm; 0.8 mm), resulting in 54 samples (Figure 1).

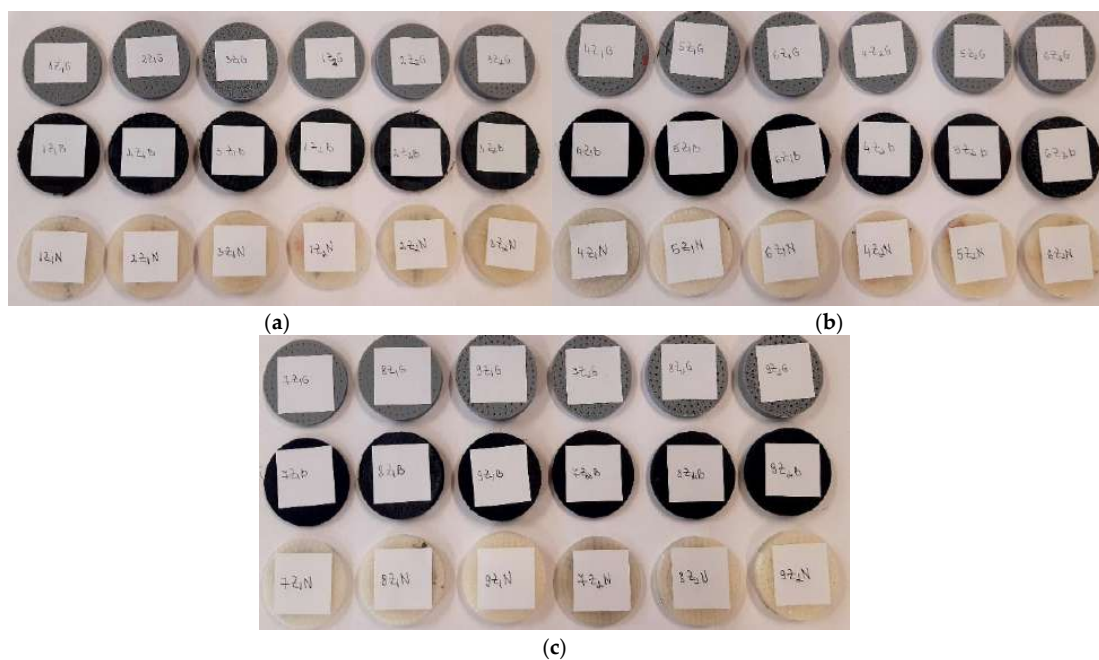


Figure 1. The 3D-printed samples of the three types of materials (Grey Tough PLA; Black PLA Pro; Natural PLA): (a) 3D-printed samples with 0.4 mm nozzle; (b) 3D-printed samples with 0.6 mm nozzle; (c) 3D-printed samples with 0.8 mm nozzle.

Depending on the internal configuration of the sample (Z_1 or Z_2) and the type of filament (Grey Tough PLA—abbreviated G; Black PLA Pro—abbreviated B; Natural PLA—abbreviated N), the 3D-printed samples were labelled as shown in Figure 2.

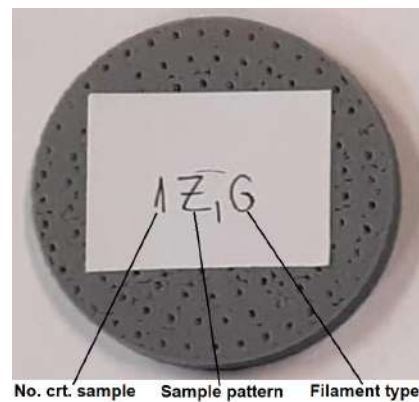
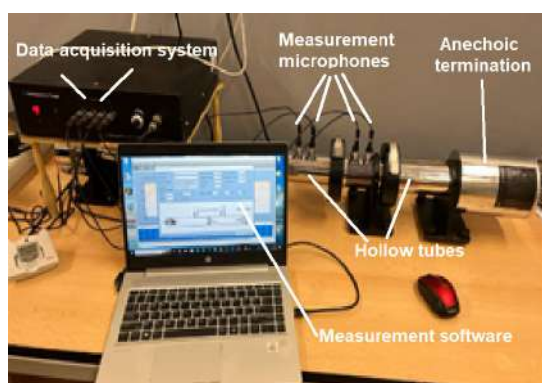


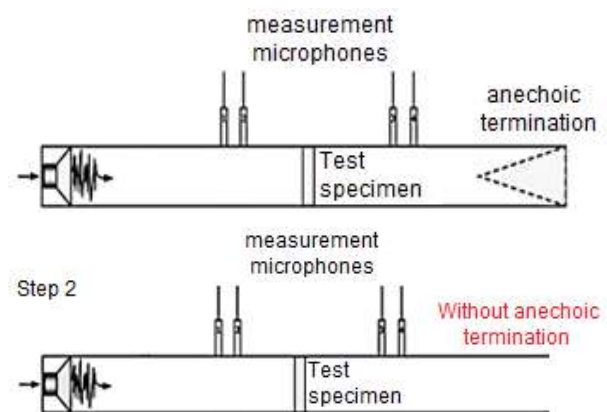
Figure 2. Labelling of the 3D-printed samples.

2.3. Acoustic Analysis of 3D-Printed Samples

The acoustic analysis of 3D-printed samples was carried out using a Holmarc HO-ED-A-03 acoustic impedance tube (Holmarc Opto-Mechatronics Ltd., Kochi, India). The impedance system contained an anodized aluminum tube with an inner diameter of 50 mm that could perform the acoustic analysis in the frequency range of 500 Hz–3150 Hz (Figure 3a). The acoustic properties were investigated by the transfer function method according to the current standards [39,40]. The acoustic impedance tube had the following parts: hollow tubes, two pairs of microphones, sample holders, a data acquisition system and measurement software.



(a)



(b)

Figure 3. The equipment used for acoustic tests [44]: (a) parts of Holmarc HO-ED-A-03 impedance tube; (b) description of impedance tube operation.

In this paper, the frequency dependencies of the sound absorption coefficient (α), the sound transmission loss (STL) and the reflection coefficient (β) of the 3D-printed samples using the transfer function method were investigated. The impedance tube presented two schematic configurations through which the acoustic performance of the 3D-printed sound-absorbing panels could be determined [46]. For the determination of the sound absorption coefficient, the equipment also included an anechoic termination component, and for the sound transmission loss, this anechoic termination part was removed (Figure 3b). When testing each sample, the geometrical parameters of the samples (50 mm), the microphone spacing (30 mm), the temperature and the humidity recorded at each test were entered. For

each sample, the height (thickness) was measured, and the sample was then inserted into the impedance tube between the two sets of microphones in a fixed position provided by the device, according to Figure 3b. The device could determine the sound coefficients with samples up to 80 mm.

3. Results and Discussion

3.1. Influence of Nozzle Diameter on Acoustic Performance of 3D-Printed Samples

A major advantage of 3D printing is that it can produce parts by the changing manufacturing parameters (nozzle diameters, layer height, printing temperature, printing speed, etc.) in a short time. Thus, a total of 54 acoustic tests were carried out for the 3D-printed sound-absorbing panels, with which the following three important parameters were determined: the sound absorption coefficient (α), the sound transmission loss (STL) and the reflection coefficient (β). The values for the 3D-printed samples with nozzle diameters of 0.4 mm, 0.6 mm and 0.8 mm made from the three types of material (Grey Tough PLA; Black PLA Pro; Natural PLA) with the dix configurations (as shown in Table 1) are presented in Tables 3–5.

Table 3. The acoustic test results for the 3D-printed samples (nozzle diameter 0.4 mm).

No.	Filament Type	Acoustic Properties	Nozzle Diameter (0.4 mm)					
			Z ₁ Pattern			Z ₂ Pattern		
			4 mm	6.4 mm	8.8 mm	4 mm	5.33 mm	8 mm
1.	Grey Tough PLA	Sample type	7Z ₁ G	8Z ₁ G	9Z ₁ G	7Z ₂ G	8Z ₂ G	9Z ₂ G
		α	0.91	0.86	0.84	0.84	0.83	0.78
		STL (dB)	30.1	30.7	30.9	28.1	28.5	29.9
		β	0.863	0.877	0.889	0.885	0.847	0.89
2.	Black PLA Pro	Sample type	7Z ₁ B	8Z ₁ B	9Z ₁ B	7Z ₂ B	8Z ₂ B	9Z ₂ B
		α	0.91	0.82	0.76	0.83	0.87	0.83
		STL (dB)	27.9	31.8	31.9	24.1	29.8	30.9
		β	0.879	0.9	0.887	0.793	0.845	0.907
3.	Natural PLA	Sample type	7Z ₁ N	8Z ₁ N	9Z ₁ N	7Z ₂ N	8Z ₂ N	9Z ₂ N
		α	0.91	0.83	0.78	0.87	0.80	0.80
		STL (dB)	29.7	31	31.7	28.7	29.4	30.4
		β	0.868	0.902	0.912	0.81	0.833	0.883

Table 4. The acoustic test results for the 3D-printed samples (nozzle diameter 0.6 mm).

No.	Filament Type	Acoustic Properties	Nozzle Diameter (0.6 mm)					
			Z ₁ Pattern			Z ₂ Pattern		
			4 mm	6.4 mm	8.8 mm	4 mm	5.33 mm	8 mm
1.	Grey Tough PLA	Sample type	4Z ₁ G	5Z ₁ G	6Z ₁ G	4Z ₂ G	5Z ₂ G	6Z ₂ G
		α	0.84	0.77	0.57	0.91	0.89	0.74
		STL (dB)	30	31.7	32.4	29	30.2	31.3
		β	0.937	0.918	0.931	0.89	0.899	0.933
2.	Black PLA Pro	Sample type	4Z ₁ B	5Z ₁ B	6Z ₁ B	4Z ₂ B	5Z ₂ B	6Z ₂ B
		α	0.58	0.82	0.55	0.87	0.93	0.79
		STL (dB)	32.4	32.1	32.9	31.7	31.4	32
		β	0.914	0.905	0.937	0.897	0.889	0.873
3.	Natural PLA	Sample type	4Z ₁ N	5Z ₁ N	6Z ₁ N	4Z ₂ N	5Z ₂ N	6Z ₂ N
		α	0.38	0.34	0.36	0.77	0.65	0.71
		STL (dB)	42.9	38.9	36.1	30.6	34.5	32.4
		β	0.942	0.955	0.944	0.893	0.92	0.93

Table 5. The acoustic test results for the 3D-printed samples (nozzle diameter 0.8 mm).

No.	Filament Type	Acoustic Properties	Nozzle Diameter (0.8 mm)					
			Z ₁ Pattern			Z ₂ Pattern		
			4 mm	6.4 mm	8.8 mm	4 mm	5.33 mm	8 mm
1.	Grey Tough PLA	Sample type	1Z ₁ G	2Z ₁ G	3Z ₁ G	1Z ₂ G	2Z ₂ G	3Z ₂ G
		α	0.65	0.50	0.32	0.84	0.78	0.60
		STL (dB)	33.4	35.2	33.8	31	32.5	36.1
		β	0.911	0.94	0.957	0.923	0.921	0.93
2.	Black PLA Pro	Sample type	1Z ₁ B	2Z ₁ B	3Z ₁ B	1Z ₂ B	2Z ₂ B	3Z ₂ B
		α	0.14	0.15	0.14	0.13	0.15	0.25
		STL (dB)	43.6	42.6	44.8	46.2	38.5	56
		β	0.983	0.983	0.983	0.989	0.981	0.958
3.	Natural PLA	Sample type	1Z ₁ N	2Z ₁ N	3Z ₁ N	1Z ₂ N	2Z ₂ N	3Z ₂ N
		α	0.29	0.23	0.16	0.46	0.25	0.29
		STL (dB)	37.3	42.8	43.3	39.1	38	47.2
		β	0.957	0.955	0.974	0.927	0.959	0.951

Figure 4 plots the influence of the sound absorption coefficient (α) as a function of the type of 3D-printed sample. In the case of the sound-absorbing panels printed with a 0.4 mm diameter nozzle (Figure 4a), an almost constant trajectory of the sound absorption coefficient was observed. From Figure 4a, it can be observed that the highest value for the absorption coefficient was found in three types of samples, namely 7Z₁B, 7Z₁G and 7Z₁N. The absorption coefficient value for the three samples was 0.91, which occurred at a frequency of 500 Hz. All the three samples had the same value for the absorption coefficient and had the same sample thickness (4 mm) with the three types of materials analyzed (Grey Tough PLA; Black PLA Pro; Natural PLA). The average of the 18 absorption coefficient values for the nozzle diameter of 0.4 mm was 0.837. For the 3D-printed panels with a 0.6 mm nozzle diameter (Figure 4b), an increase in the absorption coefficient value to 0.93 was found for sample 5Z₂B, which was recorded at a frequency of 500 Hz. In this case, the average of the 18 absorption coefficient values for the 0.6 mm nozzle diameter was 0.692. In contrast to the panels printed with a 0.4 mm nozzle diameter and a 0.6 mm nozzle diameter, the samples printed with a 0.8 mm nozzle diameter (Figure 4c) showed lower absorption coefficient values. In this case (0.8 mm nozzle diameter), the highest absorption coefficient value was obtained for sample 1Z₂G (0.84) at a frequency of about 1600 Hz. The average of the 18 absorption coefficient values for the 0.8 mm nozzle diameter was 0.351.

Of all the samples, the highest value for the absorption coefficient ($\lambda = 0.93$) was found for sample 5Z₂B, which means that the noise was very well absorbed. Based on the analysis of the average sound absorption coefficient values for the three nozzle diameters, it can be concluded that the average absorption coefficient values for the 3D-printed samples with a nozzle diameter of 0.4 mm were 17% higher than the average absorption coefficient values of the samples manufactured with a nozzle diameter of 0.6 mm and 58% higher than the average absorption coefficient values of the samples manufactured with a nozzle diameter of 0.8 mm, respectively. Thus, it can be stated that the nozzle diameter had a significant influence on the sound absorption coefficient, and the highest values were shown for a nozzle size of 0.4 mm. This was because the nozzle diameter of 0.4 mm printed with more voids compared to the nozzle sizes of 0.6 mm and 0.8 mm [47], and these small defects (voids between layers of extruded material) are beneficial to better sound absorption [11]. Thus, in acoustic testing, the specific defects of the 3D printing process are an advantage because they create a porosity at the structural level of the sample that leads to higher values of the sound absorption coefficient. The defects that occur improve the passage of sound waves entering the sample, and the air inside the voids can thus move easily, which increases the viscous friction, causing a loss of sound wave energy and, thus, sound is absorbed more efficiently [48]. In Figure 4d, the absorption coefficient curves are plotted for the highest values obtained as a function of the nozzle size, and for the nozzle diameter

0.4 mm, there were three samples with the same absorption coefficient value. As illustrated in Figure 4d, the shape of these curves was similar for all the material types with very small variations, peaking at approximately 500 Hz, 1000 Hz and 1600 Hz. On further analysis of the experimental data, when only the nozzle diameters of 0.4 mm, 0.6 mm and 0.8 mm were varied and the other factors were kept constant (same material, same sample thickness and same internal configuration), it was concluded that about 80% of the maximum absorption coefficient values were obtained with the 0.4 mm nozzle diameter and 20% of the maximum values were obtained for the 0.6 mm nozzle diameter. Thus, it can be stated that another important aspect regarding the FFF process was the correct choice of the deposition layer height (0.2 mm), which is recommended to not exceed the print nozzle diameter (0.4 mm) in order to obtain good mechanical and acoustic performance [49–51].

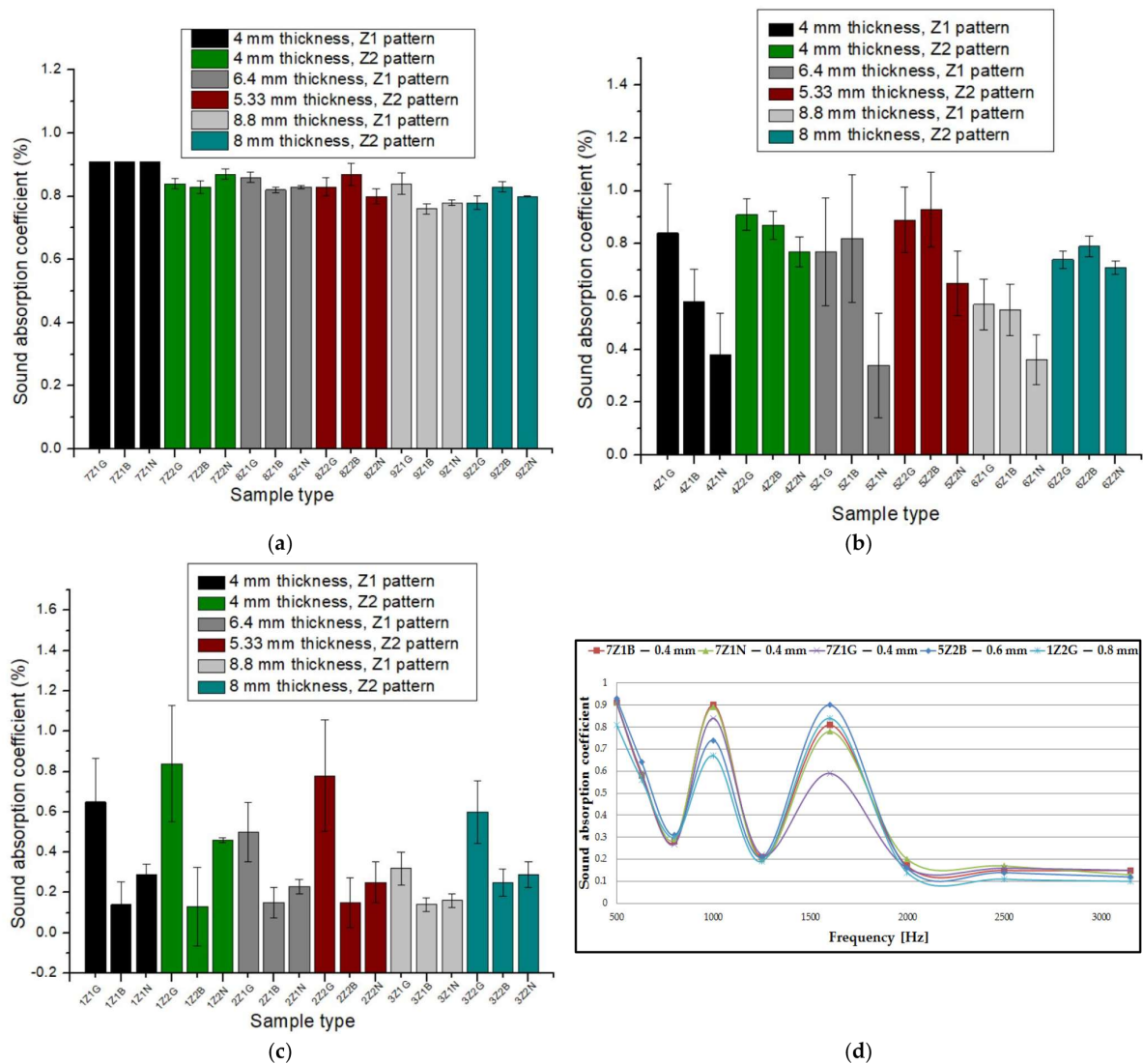


Figure 4. Sound absorption coefficient of 3D-printed sound-absorbing panels: (a) samples printed with 0.4 mm nozzle diameter; (b) samples printed with 0.6 mm nozzle diameter; (c) samples printed with 0.8 mm nozzle diameter; (d) variation in the absorption coefficient as a function of frequency.

Figure 5 plots the influence of the sound transmission loss (STL) as a function of the 3D-printed sample. In the case of the 3D-printed samples with a nozzle size of 0.4 mm, it can be seen that the highest value for the sound transmission loss was 31.9 dB for sample 9Z₁B, which was obtained at a frequency of 3150 Hz (Figure 5a). For the 3D-printed samples with a nozzle diameter of 0.6 mm (Figure 5b), an increase in the sound transmission loss up

to 42.9 dB was observed for sample 4Z₁N at the same frequency (3150 Hz). An increase in the sound transmission loss was also observed for the samples printed with a nozzle size of 0.8 mm (Figure 5c). In this case, the highest value was recorded for sample 3Z₂B (STL = 56 dB). The curves representing the influence of the sound transmission loss as a function of the frequency (Figure 5d) showed similar shapes, with a peak of values for all samples at 3150 Hz.

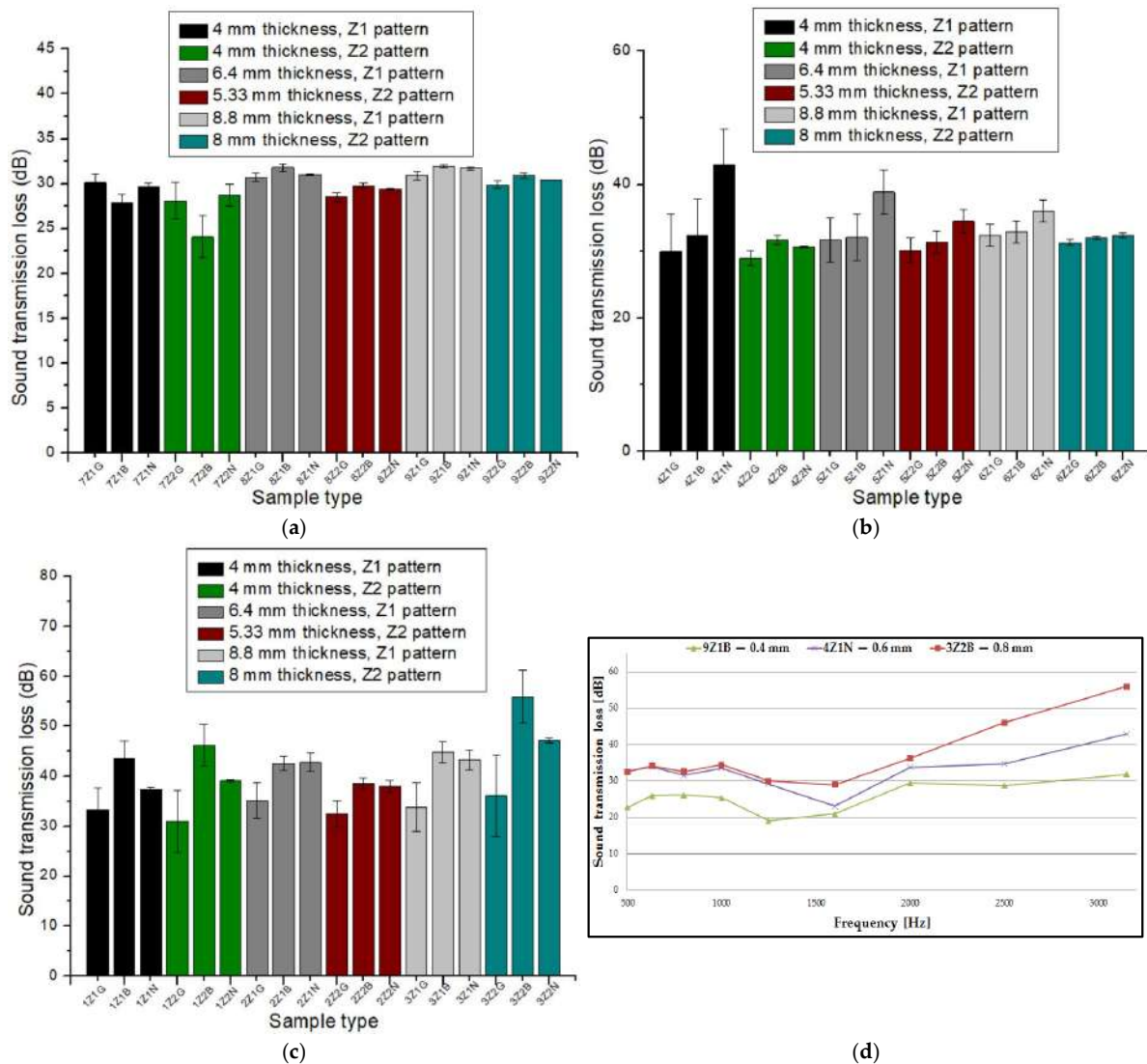


Figure 5. Sound transmission loss of 3D-printed sound-absorbing panels: (a) samples printed with 0.4 mm nozzle diameter; (b) samples printed with 0.6 mm nozzle diameter; (c) samples printed with 0.8 mm nozzle diameter; (d) variation in the transmission loss as a function of frequency.

After analyzing the average sound transmission loss values as a function of the three nozzle diameters, it can be noted that the 3D-printed samples with a nozzle size of 0.6 mm showed a 10% increase in values compared to the average 3D-printed samples with a nozzle size of 0.4 mm, and the 3D-printed samples with a nozzle size of 0.8 mm showed a 34% increase in values compared to the average 3D-printed samples with a nozzle size of 0.4 mm. A conclusion that can be drawn from the analysis of the samples printed with the three nozzle diameters is that the highest value of the sound transmission loss (comparing the same material, the same sample thickness and the same internal configuration) was determined for the nozzle diameter of 0.8 mm (for all cases). This was attributable to the panel, which acts as a barrier preventing sound transmission. This was because the

3D-printed panels with a 0.8 mm diameter nozzle showed fewer defects as compared to the 3D-printed panels with 0.6 mm and 0.4 mm diameter nozzles [47].

Figure 6 plots the influence of the reflection coefficient (β) of sound as a function of the sample type. The highest value for the reflection coefficient, in the case of the sound-absorbing panels printed with a 0.4 mm nozzle (Figure 6a), was 0.912 for sample 9Z₁N. For the samples printed with a nozzle diameter of 0.6 mm (Figure 6b), there was an increase in the reflectivity coefficient, with sample 5Z₁N showing the highest value of 0.955. The reflectance coefficient further showed an increase to a value of 0.989 for sample 1Z₂B, which was printed with nozzle size 0.8 mm (Figure 6c).

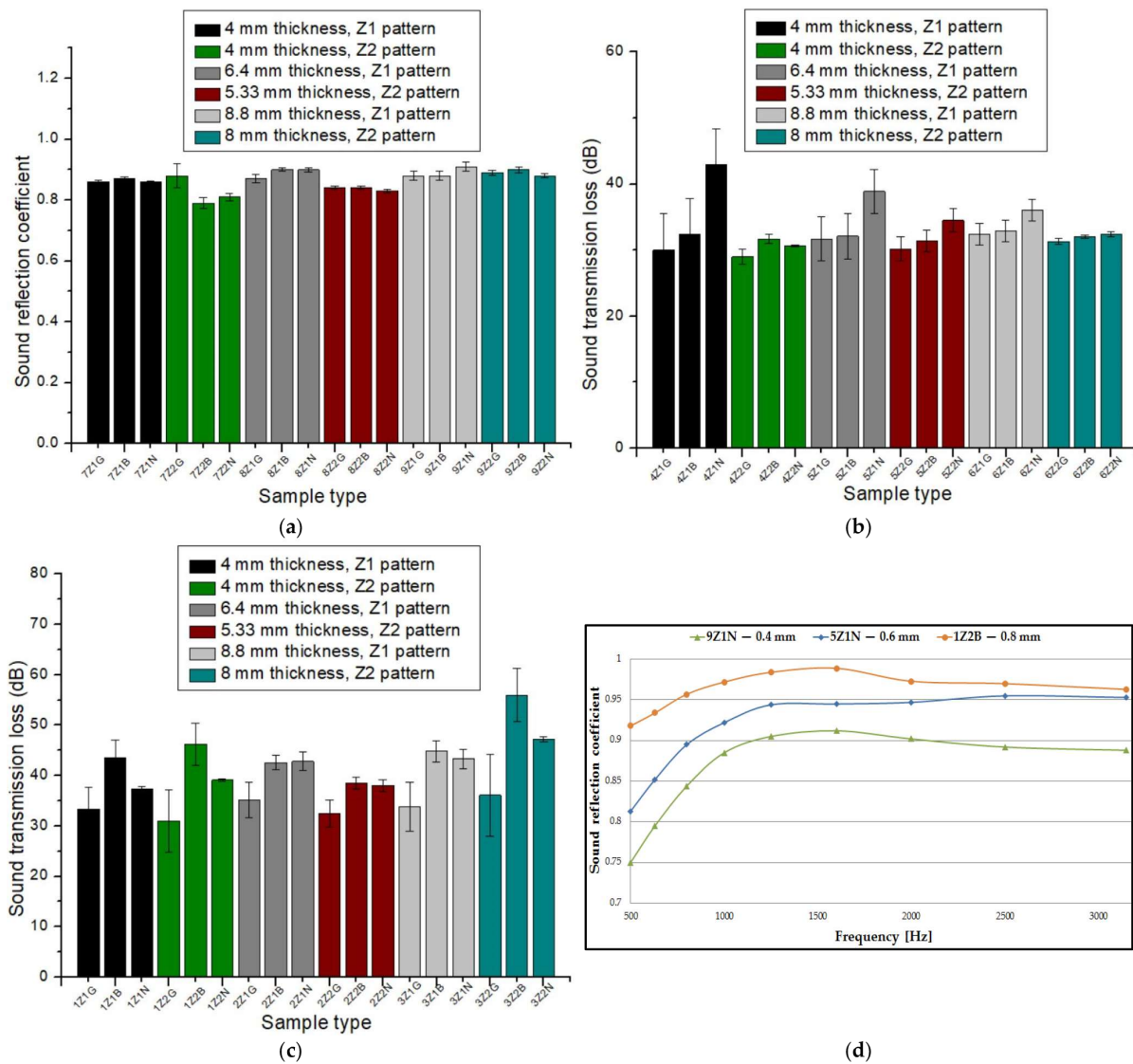


Figure 6. Sound reflection coefficient of 3D-printed sound-absorbing panels: (a) samples printed with 0.4 mm nozzle diameter; (b) samples printed with 0.6 mm nozzle diameter; (c) samples printed with 0.8 mm nozzle diameter; (d) variation in the reflection coefficient as a function of frequency.

As can be found in Figure 6d, the three reflection coefficient curves peaked at around 1600 Hz, with high values for all three types of 3D printing nozzle diameters. It can be concluded that as the nozzle diameter increased, the reflection coefficient showed higher values, which was due to the reduced number of defects in the 3D printing with the 0.8 mm nozzle diameter, resulting in a better acoustic reflection of sound waves propagating through the 3D-printed samples.

3.2. The Influence of Material Type on the Acoustic Performance of 3D-Printed Samples

The choice of the type of extruded material, in the case of 3D-printed acoustic panels, is one of the important factors in obtaining good acoustic performance. In this sub-chapter, the three types of polylactic acid (PLA), from which the samples were manufactured, were analyzed. This analysis was carried out while keeping the other manufacturing parameters constant (same nozzle diameter, same internal configuration and same sample thickness) and by conducting a horizontal analysis of the materials (Grey Tough PLA; Black PLA Pro; Natural PLA) to determine the influence of the extruded material on the acoustic performance (absorption coefficient, transmission loss and sound reflection coefficient).

As a result of the acoustic tests and a thorough analysis of the three types of materials, the following conclusions can be drawn regarding the sound absorption coefficient:

- For the samples printed with a nozzle diameter of 0.8 mm with the same sample thickness and internal configuration, the Grey Tough PLA material showed the highest values for α (with a minimum of 0.32—sample 3Z₁—and a maximum of 0.84—sample 1Z₂G). For the Grey Tough PLA material, these values were 3 times higher as compared to the Black PLA Pro material and double that of the Natural PLA material. An explanation for this high value of α for the Grey Tough PLA printed samples could be attributed to the lower density (1.24 g/cm³) of the printed samples that exhibited a higher sound absorption capacity, as demonstrated in other studies [52–54].
- In contrast, for the 3D-printed samples with a nozzle diameter of 0.6 mm with the same sample thickness and internal configuration, the absorption coefficient values (with a maximum of 0.91 for Grey Tough PLA—sample 4Z₂G—and a maximum of 0.93—sample 5Z₂B for Black PLA Pro) were close for the materials (Grey Tough PLA and Black PLA Pro). For the Natural PLA material, the values were lower compared to the first two and varied for the Z₁ configuration ($\alpha = 0.34$ – 0.38) and were higher for the Z₂ configuration ($\alpha = 0.65$ – 0.77). But on further analysis, it can be stated that the maximum absorption coefficient values (4Z₂G and 5Z₂B) were reached for two (Grey Tough PLA and Black PLA Pro) of the three materials.
- For the samples manufactured with a nozzle diameter of 0.4 mm with the same sample thickness and the same internal configuration, the absorption coefficient was close to the maximum for each material type (Grey Tough PLA with $\alpha = 0.91$ —sample 7Z₁G; Black PLA Pro with $\alpha = 0.91$ —sample 7Z₁B; Natural PLA with $\alpha = 0.91$ —sample 7Z₁N). Therefore, it can be stated that for the different materials (Grey Tough PLA; Black PLA Pro; Natural PLA) and with the following characteristics, the same absorption coefficient results were obtained: nozzle diameter of 0.4 mm, the same sample thickness (4 mm) and the same internal configuration (Z₁). Thus, it can be concluded that the FFF additive manufacturing process showed high stability in 3D printing with a 0.4 mm diameter nozzle for the three materials analyzed. The nozzle diameter of 0.4 mm provided, in the case of the acoustically tested samples, a balance between the details of the printed parts (fine details on X and Y axes) and the 3D printing time.

In terms of sound transmission loss, which was analyzed considering the three types of materials, the following can be outlined:

- For the 0.8 mm nozzle diameter with the same sample thickness and the same internal configuration, the Black PLA Pro material showed the highest results (minimum 38.5 dB and maximum 56 dB);
- For the 0.6 mm nozzle diameter with the same sample thickness and the same internal configuration, the Natural PLA material showed the highest results (minimum 32.4 dB and maximum 42.9 dB);
- For the 0.4 mm nozzle diameter with the same sample thickness and the same internal configuration, the Black PLA Pro material showed the highest results (minimum 24.1 dB and maximum 31.9 dB).

Based on the aforementioned results, the sound transmission loss had a maximum value of 56 dB, but these values are very rare, and most values for the STL are between

30 dB and 40 dB as related to PLA material, with a maximum at high frequency (3150 Hz), as observed in other studies [5,34,35,54].

The sound reflection coefficient (β) measures the vertical propagation of sound waves through 3D-printed samples [33] by using the impedance tube method. A summary of the sound absorption coefficient results is presented as follows: the highest values for the 0.8 mm nozzle diameter were obtained with the Black PLA Pro material; for the 0.6 mm diameter nozzle, the highest values of β were attributed to the Natural PLA material; for the 0.4 mm diameter nozzle, the maximum values were very close (exceeding 0.9), and each material had two maximum values.

3.3. The Influence of Internal Configuration on the Acoustic Performance of 3D-Printed Samples

The internal configuration of the 3D-printed samples had a significant influence on the acoustic performance [23,34,35]. In this case, the analysis was carried out on the internal configurations of the samples (the two zigzag configurations Z_1 and Z_2), and the constant factors were: a sample thickness of 4 mm, the material (Grey Tough PLA; Black PLA Pro; Natural PLA) and the print nozzle diameter (0.4 mm, 0.6 mm and 0.8 mm). The two internal configurations differed in terms of the tilt angle (for Z_1 , it was 31° ; for Z_2 , it was 48°) and the internal configuration width (for Z_1 , it was 1.6 mm; for Z_2 , it was 2 mm).

The two internal configurations were labyrinthine with zigzag channels, as used in various studies [55–59], due to the major advantage they confer; they are the most efficient in terms of broad-band sound absorption, and they offer a light weight and compact size. The analyses of the absorption coefficient and sound transmission loss were carried out for the following sample pairs (1 Z_1 G–1 Z_2 G; 1 Z_1 B–1 Z_2 B; 1 Z_1 N–1 Z_2 N; 4 Z_1 G–4 Z_2 G; 4 Z_1 B–4 Z_2 B; 4 Z_1 N–4 Z_2 N; 7 Z_1 G–7 Z_2 G; 7 Z_1 B–7 Z_2 B; 7 Z_1 N–7 Z_2 N). With regard to the absorption coefficient, among the samples analyzed, an internal configuration (Z_1) was outlined that showed the maximum values, for all types of material, at a nozzle diameter of 0.4 mm. The best absorption coefficient values ($\alpha = 0.91$) were obtained for the Z_1 configuration, for a tilt angle of 31° and for a sample thickness of 4 mm. An important factor that has a strong influence on the sound absorption coefficient is the sample thickness [48,60,61], and this was also validated in this paper, where the best results, for all the types of material studied, were obtained at a sample thickness of 4 mm.

In the case of these types of 3D-printed parts, it was also observed in other specialized studies [5,46,62] that the design of the core and the material itself have good sound-absorbing properties up to a frequency of approximately 2000 Hz, after which the absorption coefficient variation has a downward trend with low-intensity variations. The same type of variation in the absorption coefficient was also encountered in the case of all the analyzed samples made by the authors in this study, which were similarly obtained by 3D printing. It should be noted that the Z_2 configuration also showed high values for the sound absorption coefficient (at a nozzle diameter of 0.4 mm and a sample thickness of 4 mm), with a decrease of between 6–9% as compared to the Z_1 configuration. In the case of 3D-printed samples with nozzle diameters of 0.6 mm and 0.8 mm, the maximum absorption coefficient values were obtained for the Z_2 configuration. From these absorption coefficient values, it can be concluded that the tilt angle of the zigzag channels is another important factor in determining the absorption coefficient of 3D-printed samples.

The sound transmission loss for 3D-printed samples represents their ability to provide sound insulation, and the results were opposed to the absorption confinement. Thus, the highest STL results were obtained for the samples printed with a nozzle diameter of 0.6 mm and 0.8 mm for the Z_1 configuration, whereas for the samples printed with a nozzle diameter of 0.4 mm, the transmission loss had the highest values for the Z_2 configuration as compared to the Z_1 configuration.

4. Conclusions

The influence of three factors (nozzle diameter, material and internal configuration) of sound-absorbing panels on their acoustic performance (sound absorption coefficient, sound

transmission loss and sound reflection coefficient) were determined by the impedance tube method.

The analysis, according to the diameter of the 3D printing nozzle, showed some important aspects regarding the acoustic properties:

- For the nozzle diameter of 0.4 mm, the highest values of the absorption coefficient were obtained ($\alpha = 0.76\text{--}0.91$);
- For the nozzle diameter of 0.6 mm, the highest value of the absorption coefficient ($\alpha = 0.93$) was obtained for sample 5Z₂B (5.33 mm thickness, Black PLA Pro filament and Z₂ internal configuration);
- For the nozzle diameter of 0.8 mm, the lowest values of the absorption coefficient were recorded;
- The average value for α with a nozzle diameter of 0.4 mm was 17% higher than the value of α for the nozzle diameter of 0.6 mm and 58% higher as compared to α for the nozzle diameter of 0.8 mm;
- Based on the analysis of the samples printed with the three nozzle diameters, the highest value of the sound transmission loss (STL = 0.56 dB) was obtained for the nozzle diameter of 0.8 mm;
- The reflection coefficient showed the highest value ($\beta = 0.989$) for sample 1Z₂B, which was printed with a nozzle size of 0.8 mm, and which had the maximum value that corresponded to the lowest absorption coefficient ($\alpha = 0.02$ at a frequency of 1600 Hz).

The extruded material used in 3D-printed samples also has an important influence on the acoustic performance. Thus, for the absorption coefficient, the following conclusions were drawn: for a nozzle size of 0.8 mm, the Grey Tough PLA filament had the highest values; for a nozzle size of 0.6 mm, the Grey Tough PLA and Black PLA Pro filaments had close values and the Natural PLA filament had lower values; for a nozzle size of 0.4 mm, the closest maximum values of α were obtained for the three material types. The transmission loss recorded usual values for the PLA materials, showing a maximum of 56 dB for a nozzle size of 0.8 mm for the Black PLA Pro material. The reflection coefficient had the highest values for the nozzle size of 0.8 mm and using the Black PLA Pro material.

Another important factor that was investigated in this study was the internal labyrinthine configuration of the 3D-printed samples with zigzag channels. Thus, the two configurations (Z₁ and Z₂) had very close values of α for the three materials and for a nozzle size of 0.4 mm. It was noteworthy that the maximum value of the absorption coefficient ($\alpha = 0.91$) was obtained for the Z₁ configuration, a tilt angle of 31° and a sample thickness of 4 mm for the three materials analyzed. The sound transmission loss had the opposite values of the sound absorption coefficient, so the samples printed with a nozzle diameter of 0.6 mm and 0.8 mm, for the Z₁ configuration, had the highest values.

In conclusion, the sound-absorbing panels proposed in this study can be successfully used in various industrial applications (in automotive manufacturing, they can be used in the hood, the spaces next to the engine block, the interior of a car door panel, etc.; they can also be used in aircraft panels, houses and buildings) due to their high acoustic performance, affordable manufacturing method, lightweight internal structure and long lifetime of 3D-printed polylactic acid material.

Author Contributions: Conceptualization, M.A.P., S.M. and S.-M.Z.; methodology, M.A.P., S.M., S.-M.Z. and C.C. (Cătălin Croitoru); software, M.A.P., S.M. and C.S.; validation, M.A.P., M.C. and C.C. (Cristina Cazan); formal analysis, C.C. (Cătălin Croitoru) and C.C. (Cristina Cazan); investigation, M.A.P., S.M. and C.C. (Cătălin Croitoru); resources, M.A.P.; data curation, M.A.P., S.M. and S.-M.Z.; writing—original draft preparation, M.A.P., S.M., S.-M.Z. and C.C. (Cătălin Croitoru); writing—review and editing, M.A.P., S.M., S.-M.Z. and C.C. (Cătălin Croitoru); visualization, M.A.P. and S.M.; supervision, M.A.P., C.C. (Cătălin Croitoru), M.C. and C.C. (Cristina Cazan); project administration, M.A.P.; funding acquisition, M.A.P. All authors have read and agreed to the published version of the manuscript.

Funding: This work was supported by a grant from the Ministry of Research, Innovation and Digitization, CNCS-UEFISCDI, project number PN-III-P1-1.1-TE-2021-0294, within PNCDI III.

Institutional Review Board Statement: Not applicable.

Informed Consent Statement: Not applicable.

Data Availability Statement: Data are contained within the article.

Acknowledgments: This work was supported by a grant from the Ministry of Research, Innovation and Digitization, CNCS-UEFISCDI, project number PN-III-P1-1.1-TE-2021-0294, within PNCDI III. We also acknowledge the structural funds project PRO-DD (POS-CCE O.2.2.1, ID 123, SMIS 2637, ctr. No 11/2009) for partially providing the infrastructure used in this work at the CDI Institute of Transilvania University of Brasov.

Conflicts of Interest: The authors declare no conflicts of interest.

References

1. Ritesh, V.; Chandan, K.; Manoj, K. Assessment of Traffic Noise on Highway Passing from Urban Agglomeration. *Fluct. Noise Lett.* **2014**, *13*, 1450031.
2. Leventhall, G.; Pelmear, P.; Benton, S. *A Review of Published Research on Low Frequency Noise and Its Effects*; Department for Environment, Food Rural Affairs: London, UK, 2003.
3. Alves, J.A.; Silva, L.T.; Remoaldo, P.C.C. The Influence of Low-Frequency Noise Pollution on the Quality of Life and Place in Sustainable Cities: A Case Study from Northern Portugal. *Sustainability* **2015**, *7*, 13920–13946. [[CrossRef](#)]
4. Allen, T.; Chally, A.; Moser, B.; Widenhorn, P. Sound Propagation, Reflection, and Its Relevance to Ultrasound Imaging. *Phys. Teach.* **2019**, *57*, 134–137. [[CrossRef](#)]
5. Pop, M.A.; Cosnita, M.; Croitoru, C.; Zaharia, S.M.; Matei, S.; Spîrchez, C. 3D-Printed PLA Molds for Natural Composites: Mechanical Properties of Green Wax-Based Composites. *Polymers* **2023**, *15*, 2487. [[CrossRef](#)] [[PubMed](#)]
6. Otaru, A.J. Review on the Acoustical Properties and Characterization Methods of Sound Absorbing Porous Structures: A Focus on Microcellular Structures Made by a Replication Casting Method. *Met. Mater. Int.* **2020**, *26*, 915–932. [[CrossRef](#)]
7. Yang, T.; Hu, L.; Xiong, X.; Petru, M.; Noman, M.T.; Mishra, R.; Militký, J. Sound Absorption Properties of Natural Fibers: A Review. *Sustainability* **2020**, *12*, 8477. [[CrossRef](#)]
8. Kino, N.; Ueno, T. Comparison between Characteristic Lengths and Fiber Equivalent Diameter in Glass Fiber and Melamine Foam Materials of Similar Flow Resistivity. *J. Appl. Acoust.* **2008**, *69*, 325–331. [[CrossRef](#)]
9. Zhang, B.; Chen, T.N. Calculation of sound absorption characteristics of porous sintered fiber metal. *Appl. Acoust.* **2009**, *70*, 337–346.
10. Peng, L.; Song, B.; Wang, J.; Wang, D. Mechanic and Acoustic Properties of the Sound-Absorbing Material Made from Natural Fiber and Polyester. *Adv. Mater. Sci. Eng.* **2015**, *2015*, 274913. [[CrossRef](#)]
11. Zielinski, T.G.; Dauchez, N.; Boutin, T.; Leturia, M.; Wilkinson, A.; Chevillotte, F.; Becot, F.-X.; Venegas, R. Taking advantage of a 3D printing imperfection in the development of sound-absorbing materials. *Appl. Acoust.* **2022**, *197*, 108941. [[CrossRef](#)]
12. Johnston, W.; Sharma, B. Additive manufacturing of fibrous sound absorbers. *Addit. Manuf.* **2021**, *41*, 101984. [[CrossRef](#)]
13. Gao, N.; Hou, H. Sound absorption characteristic of micro-helix metamaterial by 3D printing. *Theor. Appl. Mech. Lett.* **2018**, *8*, 63–67. [[CrossRef](#)]
14. Kuschmitz, S.; Ring, T.P.; Watschke, H.; Langer, S.C.; Vietor, T. Design and Additive Manufacturing of Porous Sound Absorbers—A Machine-Learning Approach. *Materials* **2021**, *14*, 1747. [[CrossRef](#)]
15. Antonio, J.; Tadeu, A.; Godinho, L. Analytical evaluation of the acoustic insulation provided by double infinite walls. *J. Sound Vib.* **2003**, *263*, 113–129. [[CrossRef](#)]
16. Nayfeh, A.H.; Kaiser, J.E.; Telionis, D.P. Acoustics of Aircraft Engine-Duct Systems. *AIAA J.* **1975**, *13*, 130–153. [[CrossRef](#)]
17. Yang, M.; Sheng, P. Sound absorption structures: From porous media to acoustic metamaterials. *Annu. Rev. Mater. Res.* **2017**, *47*, 83–114. [[CrossRef](#)]
18. Azlin, M.N.M.; Ilyas, R.A.; Zuhri, M.Y.M.; Sapuan, S.M.; Harussani, M.M.; Sharma, S.; Nordin, A.H.; Nurazzi, N.M.; Afiqah, A.N. 3D Printing and Shaping Polymers, Composites, and Nanocomposites: A Review. *Polymers* **2022**, *14*, 180. [[CrossRef](#)]
19. Setaki, F.; Tenpierik, M.; Turrin, M.; van Timmeren, A. Acoustic absorbers by additive manufacturing. *Build. Environ.* **2014**, *72*, 188–200. [[CrossRef](#)]
20. Ghaffarivardavagh, R.; Nikolajczyk, J.; Anderson, S.; Zhang, X. Ultra-open acoustic metamaterial silencer based on Fano-like interference. *Phys. Rev. B* **2019**, *99*, 024302. [[CrossRef](#)]
21. Liu, Z.; Zhan, J.; Fard, M.; Davy, J. Acoustic properties of multilayer sound absorbers with a 3D printed micro-perforated panel. *Appl. Acoust.* **2017**, *121*, 25–32. [[CrossRef](#)]
22. Dazel, O.; Brouard, B.; Dauchez, N.; Geslain, A. Enhanced Biot's finite element displacement formulation for porous materials and original resolution methods based on normal modes. *Acta Acust. United Acust.* **2009**, *95*, 527–538. [[CrossRef](#)]

23. Ring, T.P.; Langer, S.C. Design, Experimental and Numerical Characterization of 3D-Printed Porous Absorbers. *Materials* **2019**, *12*, 3397. [CrossRef]
24. Boulvert, J.; Costa-Baptista, J.; Cavalieri, T.; Perna, M.; Fotsing, E.R.; Romero-García, V.; Gabard, G.; Ross, A.; Mardjono, J.; Groby, J.-P. Acoustic modeling of micro-lattices obtained by additive manufacturing. *Appl. Acoust.* **2020**, *164*, 107244. [CrossRef]
25. Iannace, G. The acoustic characterization of green materials. *Build. Acoust.* **2017**, *24*, 101–113. [CrossRef]
26. De Giorgi, M.G.; Congedo, P.M.; Baglivo, C.; Bonomolo, M.; Milone, D. Experimental Characterization and Acoustic Correction of a Multipurpose Performance Hall: The Italian Theatre “Cavallino Bianco”. *Buildings* **2022**, *12*, 1344. [CrossRef]
27. Carbajo, J.; Molina-Jordá, J.; Maiorano, L.; Fang, N. Sound absorption of macro-perforated additively manufactured media. *Appl. Acoust.* **2021**, *182*, 108204. [CrossRef]
28. Gliścińska, E.; Michalak, M.; Krucińska, I.; Strakowska, M.; Kopeć, M.; Więcek, B. A new thermographic method for determining the thickness of the polymer surface layer in sound-absorbing fibrous composite materials. *Polym. Test.* **2022**, *115*, 107748. [CrossRef]
29. Dragonetti, R.; Napolitano, M.; Romano, R.A. A study on the energy and the reflection angle of the sound reflected by a porous material. *J. Acoust. Soc. Am.* **2019**, *145*, 489–500. [CrossRef]
30. Szeląg, A.; Lewińska, M.; Kamiński, T.M.; Rubacha, J.; Pilch, A. The characteristic of sound reflections from curved reflective panels. *Arch. Acoust.* **2014**, *39*, 549–558. [CrossRef]
31. Vercammen, M. Sound Reflections from Concave Spherical Surfaces. Part I: Wave Field Approximation. *Acta Acust. United Acust.* **2010**, *96*, 82–91. [CrossRef]
32. Zvoníček, T.; Vašina, M.; Pata, V.; Smolka, P. Three-Dimensional Printing Process for Musical Instruments: Sound Reflection Properties of Polymeric Materials for Enhanced Acoustical Performance. *Polymers* **2023**, *15*, 2025. [CrossRef]
33. Monkova, K.; Vasina, M.; Monka, P.P.; Vanca, J.; Kozak, D. Effect of 3D-Printed PLA Structure on Sound Reflection Properties. *Polymers* **2022**, *14*, 413. [CrossRef] [PubMed]
34. Sailesh, R.; Yuvaraj, L.; Pitchaimani, J.; Doddamani, M.; Mailan Chinnapandi, L.B. Acoustic Behaviour of 3D Printed Bio-Degradable Micro-Perforated Panels with Varying Perforation Cross-Sections. *Appl. Acoust.* **2021**, *174*, 107769. [CrossRef]
35. Sailesh, R.; Yuvaraj, L.; Doddamani, M.; Mailan Chinnapandi, L.B.; Pitchaimani, J. Sound absorption and transmission loss characteristics of 3D printed bio-degradable material with graded spherical perforations. *Appl. Acoust.* **2022**, *186*, 108457. [CrossRef]
36. Liu, Z.; Zhan, J.; Fard, M.; Davy, J.L. Acoustic properties of a porous polycarbonate material produced by additive manufacturing. *Mater. Lett.* **2016**, *181*, 296–299. [CrossRef]
37. Vasina, M.; Monkova, K.; Monka, P.P.; Kozak, D.; Tkac, J. Study of the Sound Absorption Properties of 3D-Printed Open-Porous ABS Material Structures. *Polymers* **2020**, *12*, 1062. [CrossRef]
38. Suarez, L.; Espinosa, M.D. Assessment on the use of additive manufacturing technologies for acoustic applications. *Int. J. Adv. Manuf. Technol.* **2020**, *109*, 2691. [CrossRef]
39. SO 10534-2 (1998-11); Acoustics—Determination of Sound Absorption Coefficient and Impedance in Impedance Tubes—Part 2: Transfer-Function Method. International Organization for Standardization (ISO): Geneva, Switzerland, 1998.
40. E1050; Standard Test Method for Impedance and Absorption of Acoustical Materials Using a Tube, Two Microphone and a Digital Frequency Analysis System. ASTM International: West Conshohocken, PA, USA, 2010.
41. Ultimaker Tough PLA, Technical Data Sheet. Available online: <https://ultimaker.com/materials/s-series-tough-pla/> (accessed on 10 December 2023).
42. Ultrafuse PLA PRO, Technical Data Sheet. Available online: https://move.forward-am.com/hubfs/AES%20Documentation/Engineering%20Filaments/PLA%20PRO1/TDS/Ultrafuse_PLA_PRO1_TDS_EN_v3.3.pdf (accessed on 10 December 2023).
43. SMARTFIL PLA, Technical Data Sheet. Available online: https://c.cdnmp.net/490505258/custom/prod/1_fisa_tehnica_1803.pdf?rv=1702072800 (accessed on 10 December 2023).
44. Joseph, T.M.; Kallingal, A.; Suresh, A.M.; Mahapatra, D.K.; Hasanin1, M.S.; Haponiuk, J.; Thomas, S. 3D printing of polylactic acid: Recent advances and opportunities. *Int. J. Adv. Manuf. Technol.* **2023**, *125*, 1015–1035. [CrossRef]
45. Bergaliyeva, S.; Sales, D.L.; Delgado, F.J.; Bolegenova, S.; Molina, S.I. Manufacture and Characterization of Polylactic Acid Filaments Recycled from Real Waste for 3D Printing. *Polymers* **2023**, *15*, 2165. [CrossRef]
46. Zaharia, S.-M.; Pop, M.A.; Cosnita, M.; Croitoru, C.; Matei, S.; Spîrchez, C. Sound Absorption Performance and Mechanical Properties of the 3D-Printed Bio-Degradable Panels. *Polymers* **2023**, *15*, 3695. [CrossRef]
47. He, F.; Khan, M. Effects of Printing Parameters on the Fatigue Behaviour of 3D-Printed ABS under Dynamic Thermo-Mechanical Loads. *Polymers* **2021**, *13*, 2362. [CrossRef]
48. Sekar, V.; Eh Noum, S.Y.; Sivanesan, S.; Putra, A.; Chin Vui Sheng, D.D.; Kassim, D.H. Effect of Thickness and Infill Density on Acoustic Performance of 3D Printed Panels Made of Natural Fiber Reinforced Composites. *J. Nat. Fibers* **2022**, *19*, 7132–7140. [CrossRef]
49. Mykhailyshyn, R.; Duchoň, F.; Mykhailyshyn, M.; Majewicz Fey, A. Three-Dimensional Printing of Cylindrical Nozzle Elements of Bernoulli Gripping Devices for Industrial Robots. *Robotics* **2022**, *11*, 140. [CrossRef]
50. Yang, Y.; Wang, H.; Li, H.; Ou, Z.; Yang, G. 3D printed tablets with internal scaffold structure using ethyl cellulose to achieve sustained ibuprofen release. *Eur. J. Pharm. Sci.* **2018**, *115*, 11–18. [CrossRef]

51. Grgić, I.; Karakašić, M.; Glavaš, H.; Konjatić, P. Accuracy of FDM PLA Polymer 3D Printing Technology Based on Tolerance Fields. *Processes* **2023**, *11*, 2810. [[CrossRef](#)]
52. Smardzewski, J.; Batko, W.; Kamisiński, T.; Flach, A.; Pilch, A.; Dziurka, D.; Mirski, R.; Edward Roszyk, E.; Majewski, A. Experimental study of wood acoustic absorption characteristics. *Holzforschung* **2013**, *68*, 467–476. [[CrossRef](#)]
53. Nandanwar, A.; Kiran, M.C.; Varadarajulu, K.C. Influence of Density on Sound Absorption Coefficient of Fibre Board. *Open J. Acoust.* **2017**, *7*, 1–9. [[CrossRef](#)]
54. Maroo, T.; Wright, A. Sound transmission loss improvement using additively manufactured multimaterial. *Proc. Meet. Acoust.* **2022**, *46*, 030001.
55. Attenborough, K. Analytical Approximations for Sub Wavelength Sound Absorption by Porous Layers with Labyrinthine Slit Perforations. *Appl. Sci.* **2021**, *11*, 3299. [[CrossRef](#)]
56. Krushynska, A.O.; Bosia, F.; Pugno, N.M. Labyrinthine acoustic metamaterials with space-coiling channels for low-frequency sound control. *Acta Acust. United Acust.* **2018**, *104*, 200–210. [[CrossRef](#)]
57. Chen, J.S.; Chung, Y.T.; Wang, C.Y.; Liu, C.H.; Yu, C.H.; Chang, I.L.; Lin, T.R. Ultrathin arch-like labyrinthine acoustic metasurface for low-frequency sound absorption. *Appl. Acoust.* **2023**, *202*, 109142. [[CrossRef](#)]
58. Almeida, G.D.N.; Vergara, E.F.; Barbosa, L.R.; Lenzi, A.; Cassettari, I.; Mikulski, R.Z. Sound absorption performance of a labyrinthine metamaterial with arbitrary cross-sectional microperforations. *J. Braz. Soc. Mech. Sci. Eng.* **2023**, *45*, 607. [[CrossRef](#)]
59. Kumar, S.; Lee, H.P. Labyrinthine acoustic metastructures enabling broadband sound absorption and ventilation. *Appl. Phys. Lett.* **2020**, *116*, 134103. [[CrossRef](#)]
60. Gómez Escobar, V.; Moreno González, C.; Rey Gozalo, G. Analysis of the Influence of Thickness and Density on Acoustic Absorption of Materials Made from Used Cigarette Butts. *Materials* **2021**, *14*, 4524. [[CrossRef](#)]
61. Jiang, C.; Moreau, D.; Doolan, C. Acoustic Absorption of Porous Materials Produced by Additive Manufacturing with Varying Geometries. In Proceedings of the ACOUSTICS 2017, Perth, Australia, 19–22 November 2017.
62. Goh, G.D.; Neo, S.J.C.; Dikshit, V.; Yeong, W.Y. Quasi-static indentation and sound-absorbing properties of 3D printed sandwich core panels. *J. Sandw. Struct. Mater.* **2022**, *24*, 1206–1225. [[CrossRef](#)]

Disclaimer/Publisher’s Note: The statements, opinions and data contained in all publications are solely those of the individual author(s) and contributor(s) and not of MDPI and/or the editor(s). MDPI and/or the editor(s) disclaim responsibility for any injury to people or property resulting from any ideas, methods, instructions or products referred to in the content.

Article

Tensile Behavior of Parts Manufactured Using a Material Extrusion Process from a Filament with Short Carbon Fibers and PET Matrix

Madalina-Ioana Blaj¹, Sebastian-Marian Zaharia¹ , Cristin Olimpiu Morariu¹, Mihai Alin Pop² , Mihaela Cosnita³  and Gheorghe Oancea^{1,*} 

- ¹ Department of Manufacturing Engineering, Transilvania University of Brasov, 500036 Brasov, Romania; madalina.blaj@unitbv.ro (M.-I.B.); zaharia_sebastian@unitbv.ro (S.-M.Z.); c.morariu@unitbv.ro (C.O.M.)
- ² Department of Materials Science, Transilvania University of Brasov, 500036 Brasov, Romania; mihai.pop@unitbv.ro
- ³ Department of Product Design, Mechatronics and Environment, Transilvania University of Brasov, 500036 Brasov, Romania; mihaela.cosnita@unitbv.ro
- * Correspondence: gh.oancea@unitbv.ro

Abstract: One of the latest tendencies in research related to material extrusion based on additive manufacturing is to determine the mechanical characteristics of parts taking into consideration the most influential manufacturing parameters. The main research objective is to describe how the manufacturing parameters, part orientation, layer thickness and infill density influence the tensile behavior of specimens made from PET with 15% short carbon fibers. The most advantageous result is obtained for a layer thickness of 0.15 mm, with 100% material infill, and material deposition on the longitudinal direction of the part. The obtained mean values are: 65.4 MPa tensile strength, 1.93% strain at rupture, and 9 GPa Young Modulus. For these values, the tensile behavior of specimens manufactured along transverse and thickness directions are presented. The least favorable results are obtained for manufacturing by thickness. The novelty of the discussed research consists in all these aspects together with an original mathematical model that was determined based on design of experiments with a correlation of the regression model of over 90%. By optical and electronic microscopy material gaps are visible in the filament and manufactured parts, and the failure occurs in most cases in form of matrix cracks and delamination.

Keywords: MEX process; PET; short carbon fibers; mechanical properties; microscopy; manufacturing defects



Citation: Blaj, M.-I.; Zaharia, S.-M.; Morariu, C.O.; Pop, M.A.; Cosnita, M.; Oancea, G. Tensile Behavior of Parts Manufactured Using a Material Extrusion Process from a Filament with Short Carbon Fibers and PET Matrix. *Processes* **2024**, *12*, 334. <https://doi.org/10.3390/pr12020334>

Academic Editor: Li Xi

Received: 27 December 2023

Revised: 27 January 2024

Accepted: 1 February 2024

Published: 3 February 2024



Copyright: © 2024 by the authors. Licensee MDPI, Basel, Switzerland. This article is an open access article distributed under the terms and conditions of the Creative Commons Attribution (CC BY) license (<https://creativecommons.org/licenses/by/4.0/>).

1. Introduction

At present, Additive Manufacturing (AM) is one of the most important topics in the industry with various applications, from the automotive and aerospace industries to medicine and food industry. From all processes of AM, Material Extrusion (MEX) occurs in 69% of its applications due to its advantages regarding the variety of materials which can be used for parts manufacturing, the cost-to-quality ratio of the part, the complexity of parts that can be manufactured through this process and their final mechanical and chemical properties [1,2]. MEX is the manufacturing process which uses heated material in filament form that is stacked layer by layer according to a specific desired geometry [3]. Even though the printing process is preferred due to its simplicity, variations of the mechanical characteristics of the obtained parts occur due to its values of the manufacturing parameters. The main parameters are: layer thickness, infill, raster angle, part orientation on the manufacturing platform, temperature (at the nozzle, on the printing platform and in the environment) and work environment [1–4]. A further research challenge is also identifying the optimum combination of these parameter setpoints in order to maximize the mechanical characteristics [4,5].

The filaments used for manufacturing vary from simple thermoplastic materials to thermoplastic materials combined with particles and fibers (short or continuous), called composite filaments. In literature [4,5] also the similarity with conventional composite materials is presented, and theoretical models for tensile strength prediction are developed considering the transverse isotropy hypothesis, classical lamination theory and the Hill-Tsai anisotropic plasticity criterion or the hypothesis of orthotropic materials in plane stress state. Also, from the description of the mechanical properties, the anisotropy of the specimens is highlighted. Other novelties are related to printable materials with shape memory, based on the effect of thermal programming, which are translated into shape recovery and fixity and stress recovery [6].

This study aims to present the behavior of short carbon fibers used as a reinforcement material in a polymer matrix, which have a significant impact on the MEX process when it is. The importance of Short Carbon Fibers (short-CF) in Additive Manufacturing resides in the improvement of the mechanical properties of the manufactured parts and their addition to the matrix which offer higher stiffness, strength, and thermal resilience [1,5,7,8]. As an example, in the research reported in [9] led to obtaining a tensile strength for composite filaments increased by 57%, compared to filaments of pure Poly(Acrylonitrile-co-Butadiene-co-Styrene) (ABS). In [10] the researchers obtained an increased Young Modulus of 8% for an addition of 5% glass fibers into Polylactic Acid filaments. In [11] the researchers obtained an increased tensile strength of 20% for an addition of 10% fibers into the same type of samples as in [10]. Furthermore, Young's Modulus is increased by 28%. In [12], the addition of 10% carbon fibers into the Onyx matrix increased the tensile strength from 28.92 MPa to 418 MPa.

Besides its advantages, the addition of fibers has also a negative effect on the geometrical accuracy [1]. Another study [2] reports a behavior consequently to using short-CF in the matrix; however, anisotropy of the studied materials was observed due to the alignment of the majority of fibers by the direction of printing. In [13] a comparative study is presented involving specimens made from polyamide with carbon fibers through by MEX and by injection-molding, respectively. The worst results are obtained for printed specimens due to their higher porosity of 9 to 12%, these display lower values for yield stress and 17 to 22% lower values for Young's Modulus compared to specimens obtained by injection molding.

Related to layer thickness as a manufacturing parameter in [14] it is asserted that the geometrical stability is affected most by this criterion. Thus, as the value of the layer thickness is increased, the cross section of the deposited material is more rounded, which translates into a smaller contact surface between deposited material layers. Deposited material cross-sections are related to the "stair-effect" presented in [4,5], affecting also the surface quality and mechanical properties. Thus, by decreasing the layer thickness, the mechanical properties are improved due to the reducing of the gaps in the deposited material [5]. In another study [15], researchers identified that yield stress, tensile and flexural strength increased 1.16, 1.27 and 1.28 times, respectively, for a layer thickness of 0.2 mm compared to a layer thickness of 0.3 mm of Poly(vinyl chloride) (PVC).

Regarding the infill type, according to [4,5] the material can be deposited in different patterns: linear, rectangular, honeycomb, zig-zag at a certain density. A higher infill density entails increased part manufacturing time and material; due to their greater stiffness these parts can carry more load.

Other papers [4,7] mentioned that the tensile strength is maximized if the direction of load follows the printing direction. In [5] the authors investigated the impact of several manufacturing parameters on the tensile behavior, the most influential being: the part orientation on the printing platform, layer thickness and infill. In [7] the investigation is concerns tensile testing of short carbon fiber polyamide parts, the most influential manufacturing parameters being layer thickness and raster angle, which confirms the information in [4]. The research presented in [8] provides a review of MEX, confirming the previously presented results. Paper [16] discusses tensile testing of specimens with 100% infill while varying layer thickness for the same material. The best result of 58 MPa is

obtained for the specimens with the thinnest layer of 0.15 mm. The study is performed on BCN3D Sigma, which is a printer without enclosure.

The research reported in [17] carries out comparisons of ABS versus ABS CF, PLA versus PLA CF, Polyethylene terephthalate glycol (PETG) versus PETG CF and Amphora versus Amphora CF, respectively, also considering part orientation from 0° to 90°. In this case, the most advantageous results are obtained in specimens manufactured at a direction of 0°, while the worst results correspond to a direction of 90°. Carbon fiber addition to the matrix brought an improvement of tensile strength for 0° orientation, ranging from 5.1% in Amphora CF to a maximum of 48% in PETG CF for the specimens made from the matrix material. The tensile strength for PETG CF is 68.3 MPa, Young's Modulus is 8.47 GPa and strain at rupture is 2.99%. These results are presented for longitudinal material deposition.

In order to obtain a larger spectrum of results of the proposed study, Table 1 below presents a summary of short carbon fiber utilization in composite filaments. It can be concluded that the used matrix has an increased impact on the mechanical properties, the most used matrix in studies being Poly(lactic Acid) (PLA). Based on this table material defects can be highlighted: weak bonding between layers and material gaps, also revealed as the most important defects by the research presented in [15]. In [18], upon identifying these issues, the authors established that a higher enclosure temperature increases the tensile strength of parts due to improved bond formation. These findings are verified by scanning electron microscopy (SEM) that revealed a porosity reduced to 4.2%. Also, from the studies mentioned in Table 1, the most common manufacturing parameters are thickness layer and infill density.

Table 1. Composite filaments with short carbon fibers studies-summary.

Ref.	Material	Testing Methods	Remarks
[19]	PLA-CF 30%	SEM Tensile	Fiber conglomerate & Weak bonding fiber–matrix/Rm = 49.41 MPa, E = 1.26 GPa, ϵ at rupture = 7.81%
[20]	PLA CF	DOE Tensile	Parameters: printing speed (60,80, 100 mm/min), infill (40%, 60%, 80%), layer thickness (0.1 mm, 0.2 mm, 0.3 mm) \Rightarrow Rp = 26.49 MPa at 100 mm/min, Infill 60% & layer thickness = 0.2 mm.
[21]	ABS/PLA/PC/PETG-CF15% PA-CF25%	Notch in tension Notch in compression	Matrix type has an important impact over mechanical properties–ABS; PLA & PETG–most consistent results
[22]	PLA-CF10% PLA-CF20% PLA-CF30%	Tensile Porosity Roughness	Most advantageous results–PLA-CF10%: Rm \approx 23 MPa, E \approx 1.8 GPa Weak matrix bonding with fibers \Rightarrow mechanical properties are decreasing as the % of CF is increasing
[23]	PLA-CF	Tensile	Infill–highest impact over mechanical properties–Rm = 61.83 MPa with 90% infill density and 0.05 mm layer thickness Highest strength for 100% infill density.
[24]	PLA-CF 10%/ABS-CF 32%	Tensile SEM	From studied materials–most advantageous results for PLA-CF. More materials gaps for specimens with fibers compared to the simple specimens made from matrix.

In the research presented in this paper the considered polymer is Polyethylene Terephthalate, also known as PET, which forms the matrix of the composite filament of PET CF15, namely a matrix with 15% of short and chopped carbon fibers in its composition. Based on the findings reported in paper [25] the 15% fiber content was selected due to the most favorable results that were obtained for this composition, namely 98 MPa tensile strength and 14.4 GPa Young's Modulus, the research included tensile tests for specimens with 5%, 10% and 15% short carbon fibers in polypropylene (PP) matrix.

Other studies related to PET CF composite filaments, such as discussed in [26], assert that a reinforcement with short carbon fibers up to 40.7% determined an increased Young Modulus of up to 390%, but also a weak interface between the fibers and the matrix.

The purpose of this research is to determine the most advantageous behavior regarding tensile strength for PET CF15 specimens, considering several of the most influential manu-

facturing parameters, such as layer thickness, part orientation and infill. Also taken into account are the results obtained by other researchers, namely that mechanical properties improve as the layer thickness decreases and the infill density tends towards 100%.

For a thorough study of the influence of manufacturing parameters on the tensile strength of PET CF15 specimens, investigations included also various methods of experiment design. The test specimens were manufactured from material deposited by the longitudinal direction, taking into consideration the best results obtained by other researchers for this direction. For corroboration purposes a visual inspection is also performed in order to determine manufacturing defects and failure causes in search for other defects besides material gaps, as done in the work of other researchers. A comparison of results by the type of 3D printer can also be performed, based on the results presented in [16].

2. Materials and Methods

The material used in the research discussed in this paper is PET CF15 produced by Ultrafuse BASF (BASF, Ludwigshafen am Rhein, Germany), whose filament has a nominal diameter of 2.85 mm. The material is recommended especially for industrial applications. While it is resistant to up to 100 °C, maximized characteristics can be obtained if the material is kept under proper conditions, such as a dry environment. The producer offers a description of the mechanical properties, as shown in Table 2 below.

Table 2. Material description: PET CF15 [27].

Property	XY Plane	XZ Plane	ZX Plane
Tensile Strength	63.2 MPa	-	12.5 MPa
Strain at Break	3.7%	-	0.5%
Young Modulus	6178 MPa	-	2822 MPa

The digital model of the specimen reproduces the dimensions of the Type I specimen included in ASTM D634-14 standard [28], because the material investigated in the research falls into the category of reinforced composites. This standard is used due to the similarity of additive manufactured parts and composite materials. The nominal thickness of the specimen is 3.2 mm, with a total length of 165 mm. The gage length is 57 mm and its width is 13 mm.

The machine used for manufacturing in this research is BCN3D Epsilon [29]. It has an enclosure and functions based on the MEX method. It covers a volume of 420 mm × 300 mm × 400 mm, with filaments of 2.85 mm diameter. The manufacturing parameters used in the research are defined in the printer's software for slicing, BCN3D Cura 1.5.5, (BCN3D Technologies, Barcelona, Spain) and are presented in Table 3 above.

Table 3. Manufacturing parameters for specimens defined in BCN3D Cura software.

Parameter	Value
Layer Thickness [mm]	0.15/0.2/0.25
Wall Thickness [mm]	1.8
Top Thickness [mm]	0.8
Bottom Thickness [mm]	0.8
Top/ Bottom Pattern	Lines
Infill Pattern	Lines
Infill density %	100/75/25
Nozzle Temperature [°C]	265
Build Plate Temperature [°C]	60
Print Cooling	Off
Nozzle diameter	0.6 mm

Figure 1a presents a set of 5 specimens prepared for manufacturing, represented in the slicing software. The orientation of the parts is 45° in order to have raster angles

of 0° and 90° , respectively, and to have the material deposited in the tensile direction. Figure 1b presents a set of manufactured specimens on the printer platform. The applied method included the manufacturing of a set of five specimens, for each combination of selected manufacturing parameters. Five specimens is the minimum number required by the standard for obtaining conclusive results.

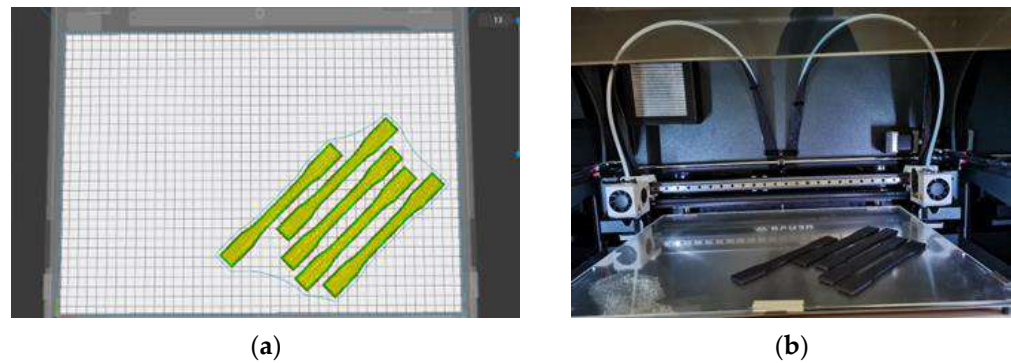


Figure 1. Tensile specimens: (a) Preview of five specimens in BCN3D Cura software; (b) five specimens after manufacturing.

The tests carried out as part of this research take into consideration two variables: layer thickness and infill. For each manufacturing parameter three values are relevant:

- Thickness layer: 0.15 mm, 0.20 mm and 0.25 mm;
- Infill density: 100%, 75%, and 25%.

The tensile tests are conducted for each combination of parameters, using the following codification: C_t_I_no, where "t" is the value for layer thickness, "I" is the infill percentage and "no" is the specimen number from the considered set.

While the studied material is anisotropic, for the purposes of this research it is considered orthotropic with its maximum tensile strength obtained along the direction of machining. The study is performed considering the material being deposited along the longitudinal direction (X) of the specimen, obtaining the tensile values along direction XX or 11. A local coordinate system is considered for each specimen, with the X axis along specimens length. According to [30] for laminate composite materials the tensile values are equivalent for directions X or 11 and for directions Y or 22, respectively—see Figure 2 [30]. In this case, the results obtained for the specimens with longitudinally deposited material, are considered with regard to the manufacturing parameters to be drivers for the next steps of the research. The testing of the specimens and the results are presented separately for each group, according to the orientation of the material deposition process.

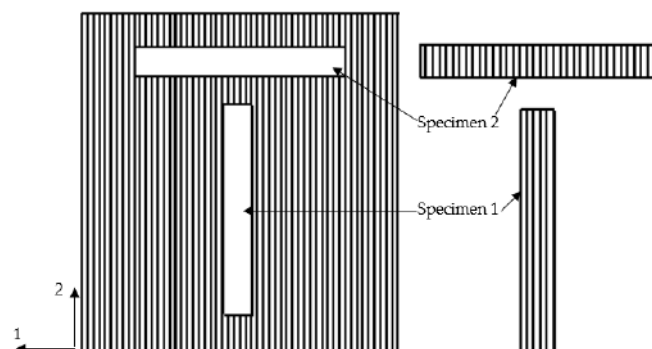


Figure 2. Composite specimen extraction from a composite panel [30].

The values of tensile strength on the transverse and thickness directions are necessary for a complete material description. In order to obtain the best tensile strength, the optimum combination of manufacturing parameter setpoints has to be identified. For this a set of

five specimens was manufactured by the transverse and thickness directions in order to be tested, as presented in Figure 3 below. Due to the reduced contact area of the specimen with the printer plate and the increased risk of printing failure, auxiliary supports are generated for the part during manufacturing. These supports are removed after the manufacturing of the specimen.

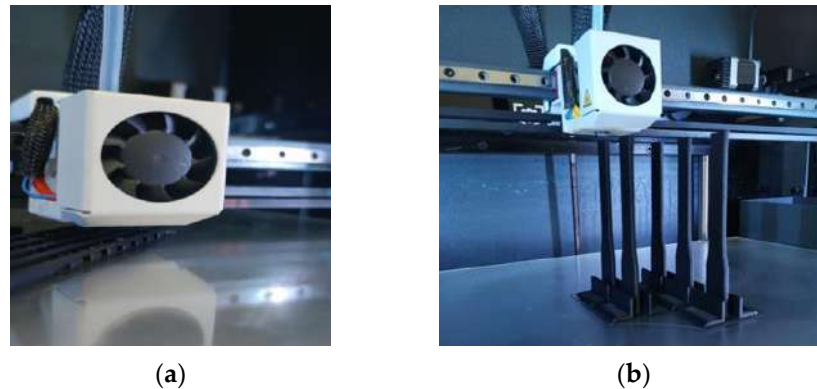


Figure 3. Tensile specimens: (a) In the transverse direction with supports; (b) In the thickness direction with supports.

The generated specimens were tested for tensile strength on the Universal Testing Machine WDW-150S (Jinan Testing Equipment IE Corporation, Jinan, China) equipped with a hydraulic parallel grip. The specimens are placed between the grips of the testing machine, the longitudinal axis of the specimen being aligned with an imaginary axis between grips. The grips are tightened to prevent the slippage of specimens from the machine. By means of the MaxTest V1 machine software data is collected for plotting the stress-strain curve for each specimen. This is then post-processed according to [28], due to machine artifacts.

The post-processed results are presented in Section 3. Manufacturing defects are verified visually as well as by means of the Nikon T1-SM microscope (Nikon, Tokyo, Japan) and the Emspira 3 microscope (Leica Microsystems GmbH, Wetzlar, Germany). SEM analysis is performed using a Hitachi S3400N type II machine, produced in Japan, Tokyo. After tensile testing, failure can also be identified by visual inspection. Dimensional deviations of the specimen width and thickness were checked against the nominal dimensions. Design of experiments (DoE) was conducted in Minitab 21 (Minitab, LLC, State College, PA, USA). The input data used in DoE were the results obtained after post-processing the specimens manufactured by longitudinal material deposition. DoE is performed as an iterative process, starting with a linear regression model, then moving to a polynomial model, and to a second-order polynomial regression. A higher order regression is not recommended as it would yield a complex and difficult to use model. The regression model is selected based on the level of correlation, which is recommended to be over 90%, and on the significance of the constituent terms expressed by their respective p -value. A term is significant if its p -value is below 0.05.

3. Results and Discussions

3.1. Tensile Testing and Results

3.1.1. The Longitudinal Direction

Each specimen is tested according to [20] and presented in Figure 4 and in Appendix A in Figures A1–A8, before and after testing. The behavior of specimens for 100% Infill is almost similar. The rupture of all specimens occurred in almost the same place, showing that specimens are compact and homogenous if the infill is 100%. The thickness layer has a reduced impact on the location of the rupture. As the infill density is reduced, rupture occurs in a random location, the highest impact being on specimens with 25% infill density.

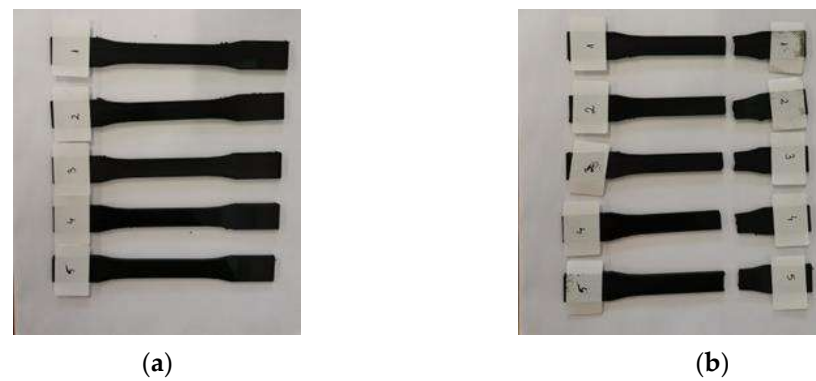


Figure 4. Longitudinal Tensile Specimens C_15_100: (a) Before testing; (b) After testing.

Figure 5, Tables 4 and 5, and Appendix B present the stress-strain curves for each set of specimens and the results for each specimen: F_m (kN)—force at rupture, R_m (MPa)—tensile strength, F_p (kN)—force at yield point, R_p (MPa)—Yield stress, E (GPa)—Young's Modulus and ϵ (%)—total strain percent at rupture of the considered specimen. All the values are calculated by the testing machine software.

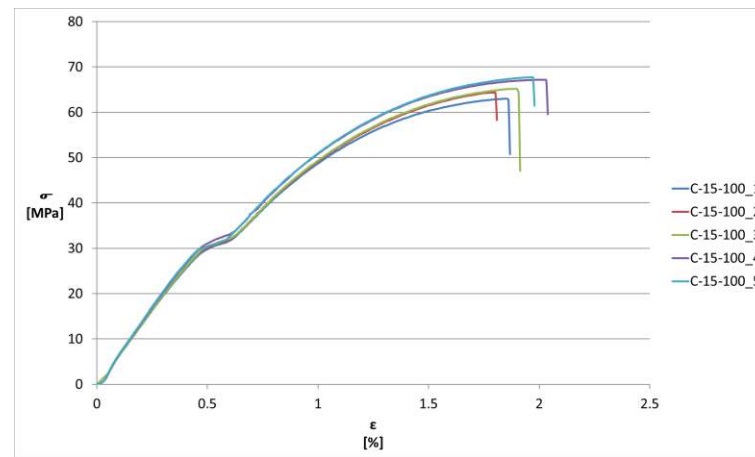


Figure 5. Longitudinal Tensile Specimens results—Stress-Strain curves for C_15_100.

Table 4. Longitudinal Tensile Specimens Result—C_15_100.

Specimen	F_m [kN]	R_m [MPa]	F_p [kN]	R_p [kN]	E [GPa]	ϵ [%]
C_15_100_1	2.661	63	2.066	49	9	1.88
C_15_100_2	2.718	64	2.133	50	9	1.82
C_15_100_3	2.753	65	2.146	51	9	1.91
C_15_100_4	2.837	67	2.228	53	9	2.05
C_15_100_5	2.86	68	2.326	55	9	1.99
Average	2.77	65.40	2.18	51.60	9	1.93

Table 5. Longitudinal Tensile Specimens Result—C_15_100—Deviations from the mean value.

Specimen	F_m [%]	R_m [%]	F_p [%]	R_p [%]	E [%]	ϵ [%]
C_15_100_1	−3.79	−3.67	−5.22	−5.04	0.00	−2.59
C_15_100_2	−1.73	−2.14	−2.15	−3.10	0.00	−5.70
C_15_100_3	−0.46	−0.61	−1.55	−1.16	0.00	−1.04
C_15_100_4	2.57	2.45	2.21	2.71	0.00	6.22
C_15_100_5	3.41	3.98	6.71	6.59	0.00	3.11

An average value is calculated for each set, as well as the deviation for each such value. These are presented in Appendix B. Material behavior is described by the stress-strain curves. In the linear area Hooke's Law is applicable and the material is elastic. The specimen will regain its initial dimensions and shape after removal of the load. Beyond the elastic region the strains increase faster up to the yielding point. Beyond this point the material enters the plastic area with a greater resistance to deformation.

The best results are obtained for the set of specimens with 100% material infill and a thickness layer of 0.15 mm. These have the following average values: $R_m = 65.4$ MPa, $R_p = 51.6$ MPa, $E = 9$ GPa and $\epsilon = 1.93\%$. These values are used for further testing specimens machined transversally and in-depth.

For this set the obtained strength ranged from 68 MPa to 63 MPa. Young's Modulus had a constant value for the entire set. The strain at rupture ranged from 1.82% to 2.05%. The maximum strain values were not recorded on the specimens with maximum strength.

Comparing the results for all sets of specimens by infill reveals the increased impact of the thickness layer: the values have a tendency of decreasing if the infill percentage is lower and the thickness layer increases, as already stated in Introduction.

The least beneficial results are recorded for the set of specimens with a material infill density of 25% and the layer thickness of 0.25 mm, where the average value of strength is 36.3 MPa, yield strength is 29 MPa, Young's Modulus is 7 GPa and the strain at rupture is 1.44%.

According to the stress-strain curves for each set the behavior of each specimen is almost similar. The curves tend to overlap, especially for the specimens with infill of 100% and 75%. The overlap is almost identical especially for the elastic area of the curves, differences being noticed only in the plastic area. These can be explained by the fact the manufacturing problems of the specimens—from the raw material to the deposited material. These results can be corroborated with the results presented in Appendix A, where the specimens with increased infill values display a tendency towards similar behavior.

The deviations of the results for each set are calculated by means of Equation (1):

$$P\% = (P_i - P_m)/P_i\% \quad (1)$$

where:

- $P\%$ —the difference between the specific value of a specimen and the average value of the specimens in the set, expressed as a percentage;
- P_i —the specific value of the considered specimen;
- P_m —the average value of a parameter in a set of specimens.

Table 6 presents the maximum deviations for all the sets:

Table 6. Maximum deviations from the average value for all the studied sets.

	F_m [%]	R_m [%]	F_p [%]	R_p [%]	E [%]	ε [%]
Max deviation	−6.91	−7.32	15.81	14.97	−14.89	19.89

The maximum deviations of the strength are recorded for specimens with 25% infill density. This result supports the inconsistency in the behavior of the material with a decreased infill value.

Having the results for the longitudinal direction, the specimens were machined transversally using the same parameter setpoints, however with unfavorable results—see the specimens in Section 3.1.2 for the transverse direction and in Section 3.1.3 for the thickness direction.

3.1.2. The Transverse Direction

Figure 6 presents the manufactured specimens before and after tensile testing. The best results from the previous tests were used as manufacturing parameters.

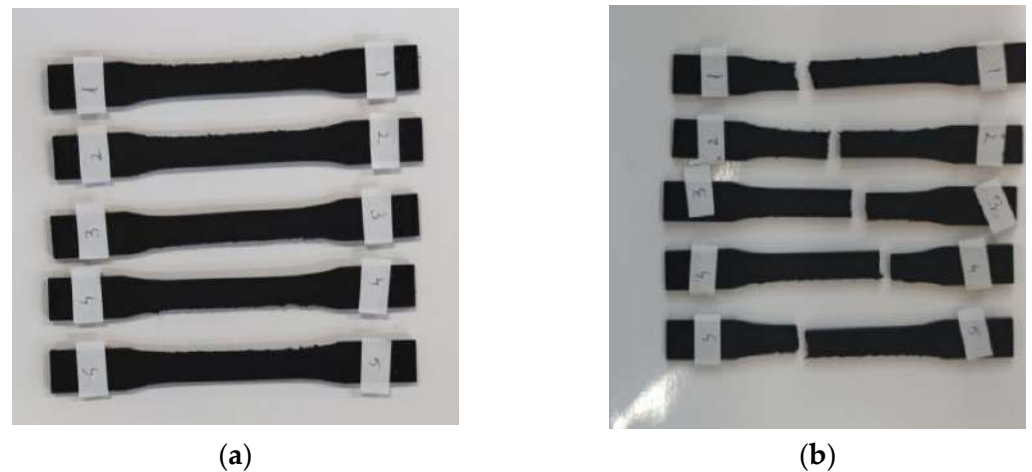


Figure 6. Transverse Direction Tensile Specimens C_15_100: (a) Before testing; (b) After testing.

Figure 7 below shows that the curves are not overlapping completely; the failure is initiated in different points up to different strain values. These discrepancies are explained by the specimens' inconsistencies that are described in Section 3.2.

In this case, as presented in Table 7, for three out of the five specimens the material yielding starts from 9–10 MPa, compared to the other two where the yielding starts from values over 40 MPa. The failure occurs for Rm ranging from 41 MPa to 49 MPa. Strains at rupture recorded lower values compared to the specimens in the longitudinal direction, ranging from 1.00% to 1.80%.

Table 7. Transverse Direction Tensile Specimens Result—C_15_100.

Specimen	Fm [kN]	Rm [MPa]	Fp [kN]	Rp [kN]	E [GPa]	ϵ [%]
C_15_100_1_t	1.769	41	0.384	9	7	1.76
C_15_100_2_t	2.027	44	2.021	44	7	1.20
C_15_100_3_t	2.004	46	0.388	9	7	1.80
C_15_100_4_t	1.741	42	0.419	10	7	1.00
C_15_100_5_t	2.045	49	1.901	45	7	1.60

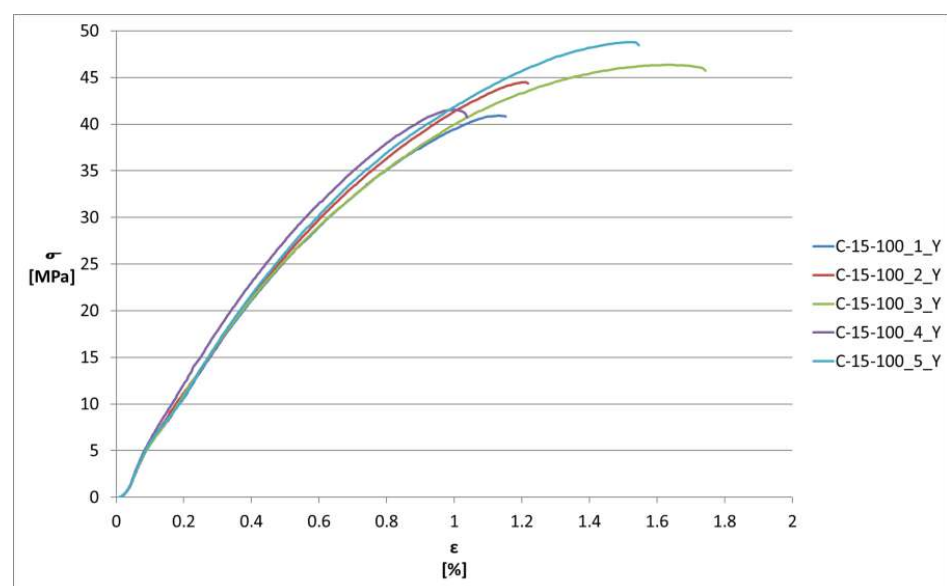


Figure 7. Transverse Direction Tensile Specimens results—Stress-Strain curves for C_15_100.

The discrepancies between these results can be explained by the fact that the specimens where the R_p is closer to the R_m value behave like brittle materials, whereas the others behave like ductile materials. These differences are related to carbon fiber consistency and arrangement in the matrix.

3.1.3. The Thickness Direction

Figure 8 presents the manufactured specimens before and after tensile testing. The best results from the previous tests were used as manufacturing parameters.



Figure 8. Thickness Direction Tensile Specimens C_15_100: (a) Before testing; (b) After testing.

Figure 9 presents the results obtained for tensile specimens oriented by the thickness direction, in this case the inconsistency between specimens is clear: the stress-strain curves differ and failure occurs immediately. A reason for this result is the weak bondage between the layers, also asserted in [31]. Also, this alignment of parts on the printing plate is contrary to the recommendations found in literature based on that fact that increased tensile strength is obtained in the printing direction. In Figure 9 it can be observed that for specimen 3 the bondage of the layers is stronger compared to the rest of the specimens.

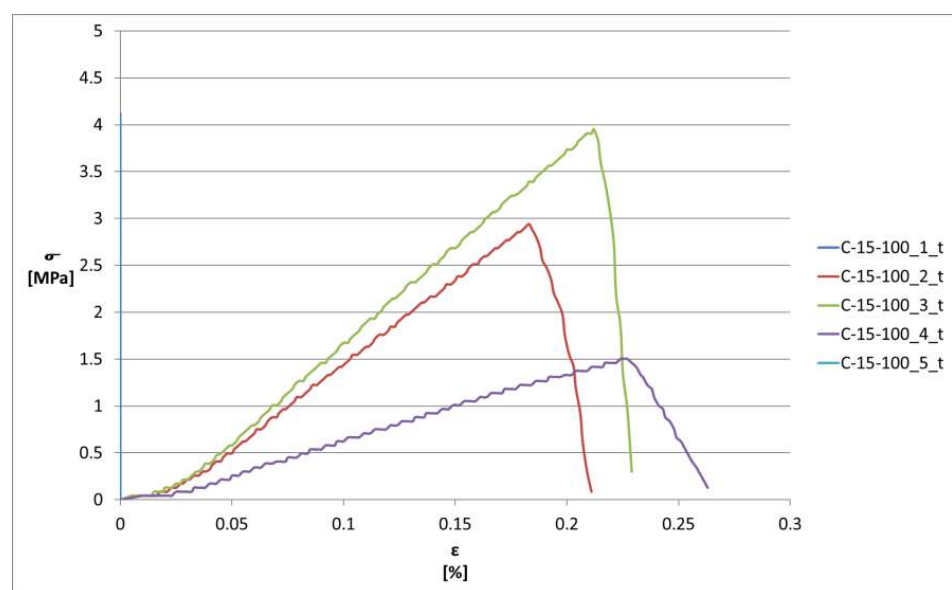


Figure 9. Thickness Direction Tensile Specimens results—Stress-Strain curves for C_15_100.

In Table 8 no values are recorded for specimens number 1 and 5 due to the fact that these specimens could not be fit between the grips for testing. Thus an average value could be calculated. Further on the following average values were used: 3 tensile strength MPa, 1 MPa Yield Strength, 1 GPa Young's Modulus, and 0.23% strain at rupture. The results are necessary to offer a material description in all directions, i.e., to build the stiffness matrix in the hypothesis of an orthotropic material. These values are selected as an average for each type of result.

Table 8. Thickness Direction Tensile Specimens Result—C_15_100.

Specimen	Fm [kN]	Rm [MPa]	Fp [kN]	Rp [kN]	E [GPa]	ϵ [%]
C_15_100_1_t	0.192	4	0.099	2	-	0.30
C_15_100_2_t	0.137	3	-	-	2.94	0.21
C_15_100_3_t	0.184	4	0.045	1	1	0.23
C_15_100_4_t	0.070	2	-	-	1	0.26
C_15_100_5_t	-	-	-	-	-	-

Considering the presented results, achieving an ideal positioning of the part on the machine table represents a challenge. The final utilization of the part should be known, as well as the load path that can appear in the assembly and the weak points in the structure, because the load path during operation is not singular and the risk of failure is increased. If a predominant uniaxial tensile loading appears in the structure, it is recommended to conduct material deposition in the part along the direction of load direction.

Another comparison can be made by the type of machine: with enclosure or without an enclosure, respectively. For a machine without an enclosure, as stated in [16], the best result is obtained for a thickness layer of 0.15 mm with an infill density of 100%. The tensile strength is 58 MPa. When using a printer with an enclosure with the same combination of parameter setpoints the tensile strength increases to 65.4 MPa. This can be explained by the fact that the enclosure preserves better the environmental temperature, the deposited material maintains its temperature for a longer period of time thus improving material bonding.

3.2. Defects—From Raw Material to Final Part

The differences in behavior can be explained by defects that appear from raw material to manufacturing. A “snow-ball effect” is generated because the raw material defects are transferred to the final part as manufacturing defects, affecting the part's functionality.

3.2.1. PET CF15 Raw Material Defects

PET CF15 raw material was studied under the microscope in order to check dimensional deviations, fiber orientation and arrangement in the matrix before utilization. Figure 10 below presents a section through the PET CF15 filament used in the research. The section shows deviations from the circularity, with several grooves at the edges. The darker areas visible in the cross-section indicate randomly scattered material voids and gaps. It can be noticed further that the fibers are oriented perpendicularly on the section, with some exceptions that are marked.

Figure 11 shows the same issues enhanced 100 times.

Figure 12 presents a longitudinal section of the filament, enhanced 100 times on the microscope. Material voids scattered randomly are also visible. This image offers a “map” of the studied section with fiber conglomerates and voids. This explains the unequal material distribution in the fiber and also in the studied specimens. Fibers are orientated mainly longitudinally in the filament. There are also fibers oriented randomly in the matrix, as confirmed by the findings reported in [11]. Visually fiber length varies between 50 and 200 μm , as concluded by analyzing the plots.

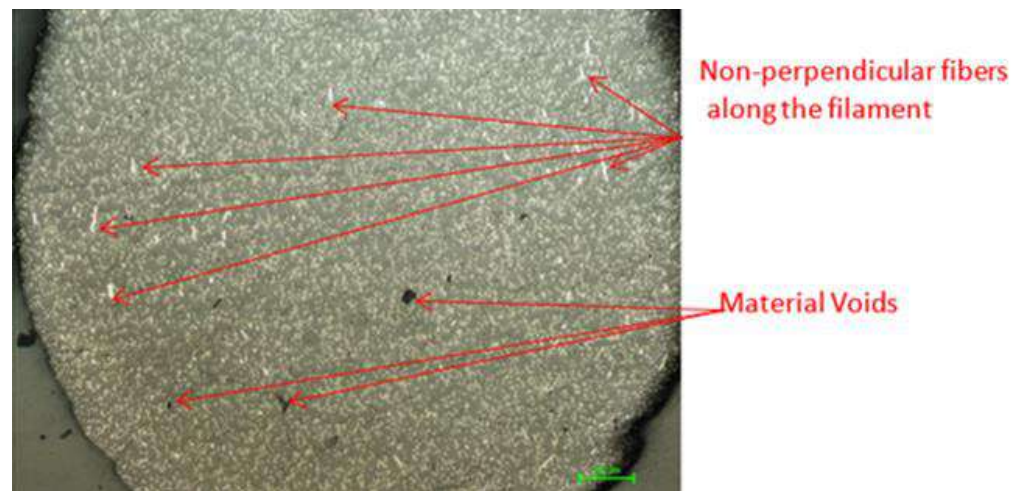


Figure 10. Ultrafuse PET CF15—Transversal view of the filament—Scale 50× (Scale length 200 μm)
—Nikon T1-SM.



Figure 11. Ultrafuse PET CF15—Transversal view of the filament—Scale 100× (Scale length 200 μm)
—Nikon T1-SM.

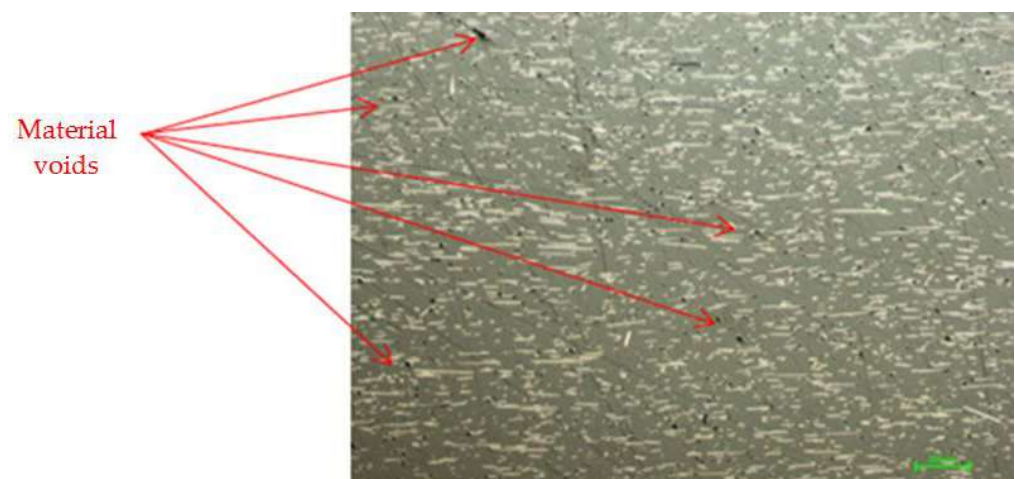


Figure 12. Ultrafuse PET CF15—Longitudinal view of the filament—Scale 100× (Scale length 200 μm)
—Nikon T1-SM.

The results of the SEM analyses conducted on the filament are displayed in Figures 13–16. Figure 13 shows the longitudinal view of the filament at a scale factor of 350 \times and in Figure 14 shows the detailed view enhanced 600 \times of the area marked in Figure 13.

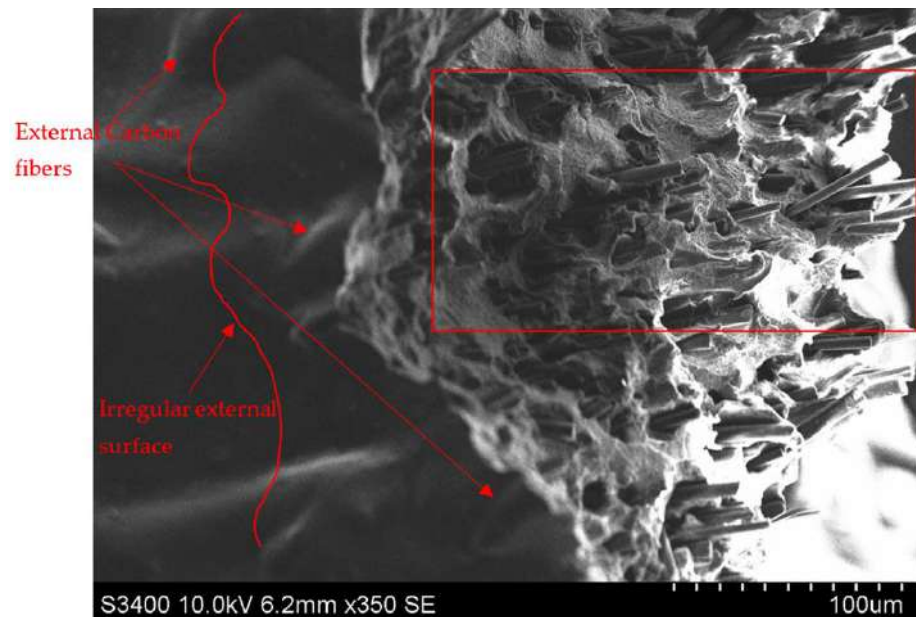


Figure 13. Ultrafuse PET CF15—Longitudinal view of the filament—Scale 350 \times (Scale length 100 μ m)—Hitachi S3400N Type II.

Figure 13 shows the external surface of the filament which is irregular, some randomly oriented carbon fibers can be noticed on the external surface. Based on the orientation of the fibers in the rupture area it can be asserted that the main orientation of fibers is longitudinal. In the detailed view in Figure 14 areas without any carbon fiber are visible, circled red, as well as areas with fiber conglomerates. Both Figures 13 and 14 reveal areas around the fibers with micropores, accounting for the lack of adhesion of the fibers to the matrix. Figure 14 shows also the areas of fiber breakage, In the section through the filament voids are visible that bear the print of the pulled-out fiber.

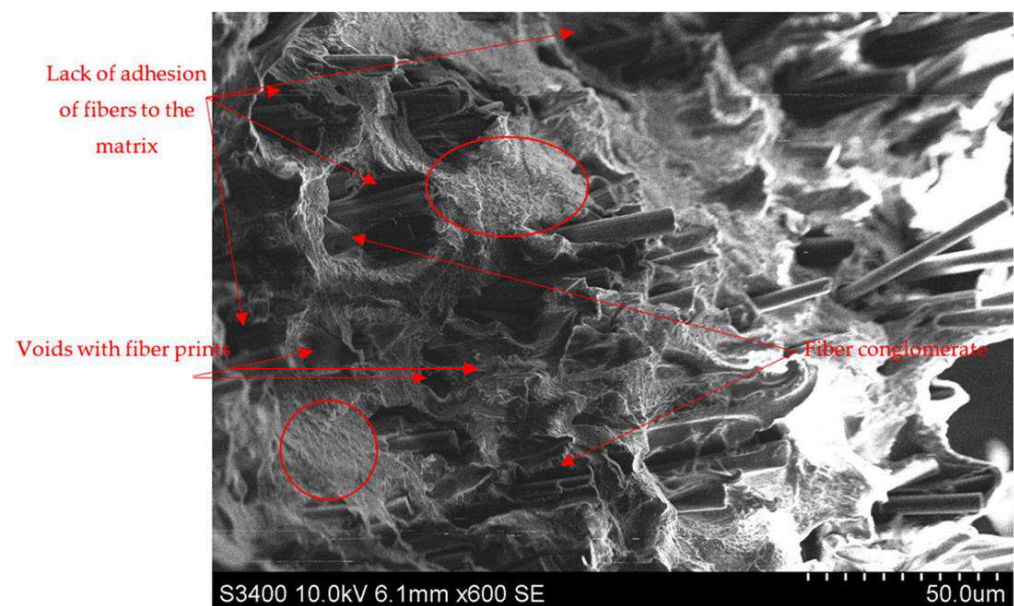


Figure 14. Ultrafuse PET CF15—Longitudinal view of the filament—Scale 600 \times (Scale length 50 μ m)—Hitachi S3400N Type II.

Figure 15 shows a transversal view of the PET CF15 filament after SEM analysis. The 320 \times scaled image shows the increased number of voids of different dimensions. Only some of these are marked in the figure given the large amount of this defect. The same figure reveals several areas where fiber orientation deviates from the required one. In Figure 14 lower fiber density areas are marked with red circles, indicative of a random distribution of fibers.

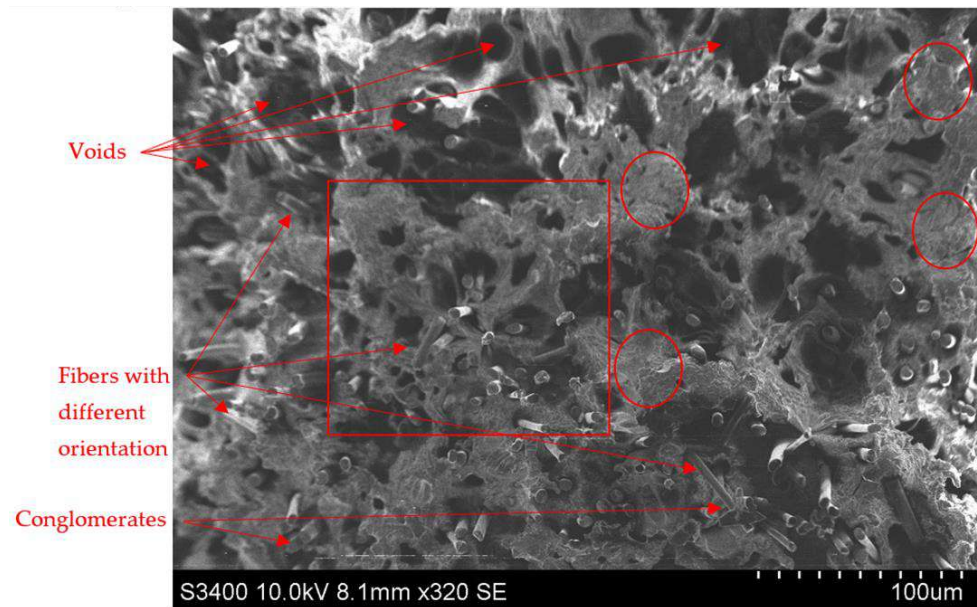


Figure 15. Ultrafuse PET CF15—Transversal view of the filament—Scale 320 \times (Scale length 100 μ m)—Hitachi S3400N Type II.

Figure 16 shows the detail marked by the red box in Figure 15. The defects highlighted in Figure 15 are more visible, resulting from the voids that mark the poor adhesion of the fibers to the PET matrix. Also differently oriented fibers are more visible. In this detail image a complete fiber is visible, as well as an increased area without fibers marked with a red ellipse. Carbon fiber conglomerates are also visible confirming an irregular distribution of fibers in the raw material.

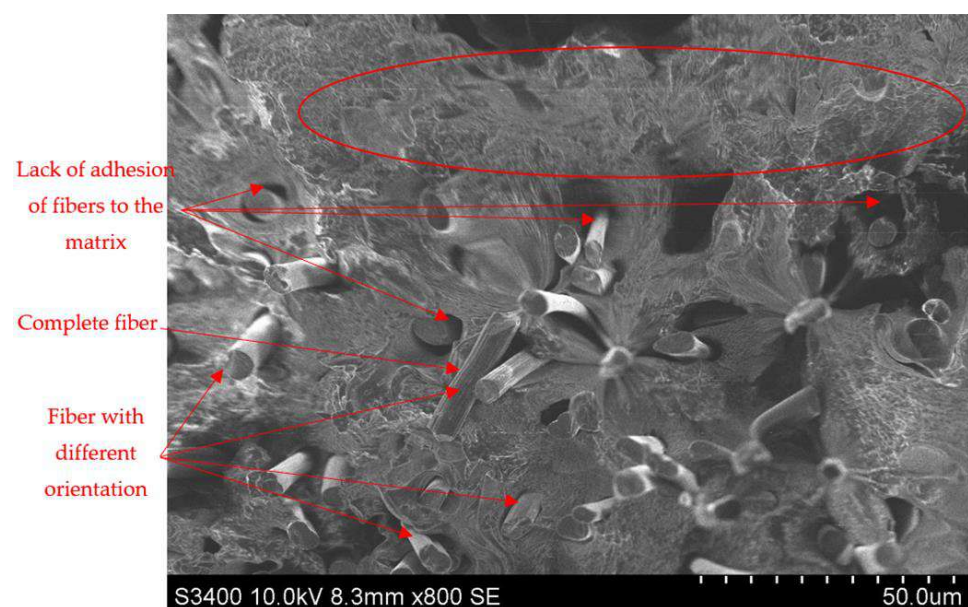


Figure 16. Ultrafuse PET CF15—Transversal view of the filament—Scale 800 \times (Scale length 50 μ m)—Hitachi S3400N Type II.

Raw material issues are presented also in [32], where the studied material is PAHT-CF15 (Polyamide matrix with 15% Carbon Fibers from Innofil/Ultrafuse (BASF, Ludwigshafen, Germany)). In this case the porosity is described during the manufacturing phase because the matrix is not adhering completely to fibers, resulting in material voids.

3.2.2. PET CF15 Tensile Specimen Manufacturing Defects

The defects mentioned in the previous subsection influence the characteristics of the final parts that depend also on the machine functionality, the manufacturing parameters and the state of the environment. All the tested specimens were visually inspected by means of a microscope, in order to identify the manufacturing issues caused by the previously mentioned factors.

Figures 17–35 present the identified manufacturing issues of the tested specimens. Material gaps were identified in all specimens, as presented in [24]. FEM validation of the tests is difficult due to unpredictable manufacturing issues. The volume of manufacturing defects is higher in specimens with a lower infill density of 25%, confirming the geometric instability mentioned in Section 1. It also offers an explanation for the results obtained for tensile testing, namely the increased number of defects in the considered parts. Also, because of material gaps, the differences in failure of parts with 100% infill are explained by their distribution and volume.

In Figure 17 a region is highlighted where the deposited material is not bonded, resulting in an area with material inconsistency. Also, due to the gap, the material deposited in its vicinity tends to be affected by slippage resulting in a cross-section of variable area, highlighted by the red polyline in Figure 17.

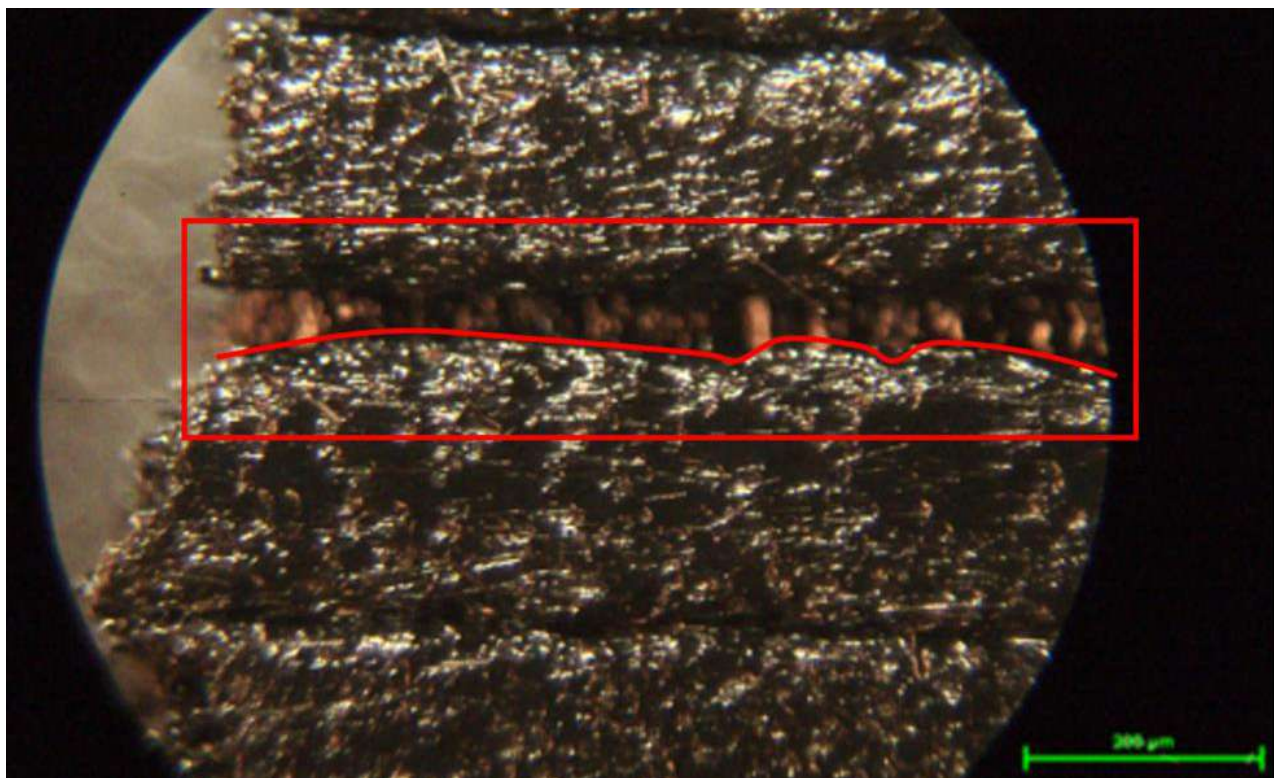


Figure 17. Specimens—Manufacturing defects—Voids between the layers (Scale 100×)—Scale length 200 μm—Nikon T1-SM.

Figure 18 shows another case of not bonded material in a specimen obtained by material deposition in the thickness direction. The deposited material from the infill area is not adhering to the shell causing gaps.

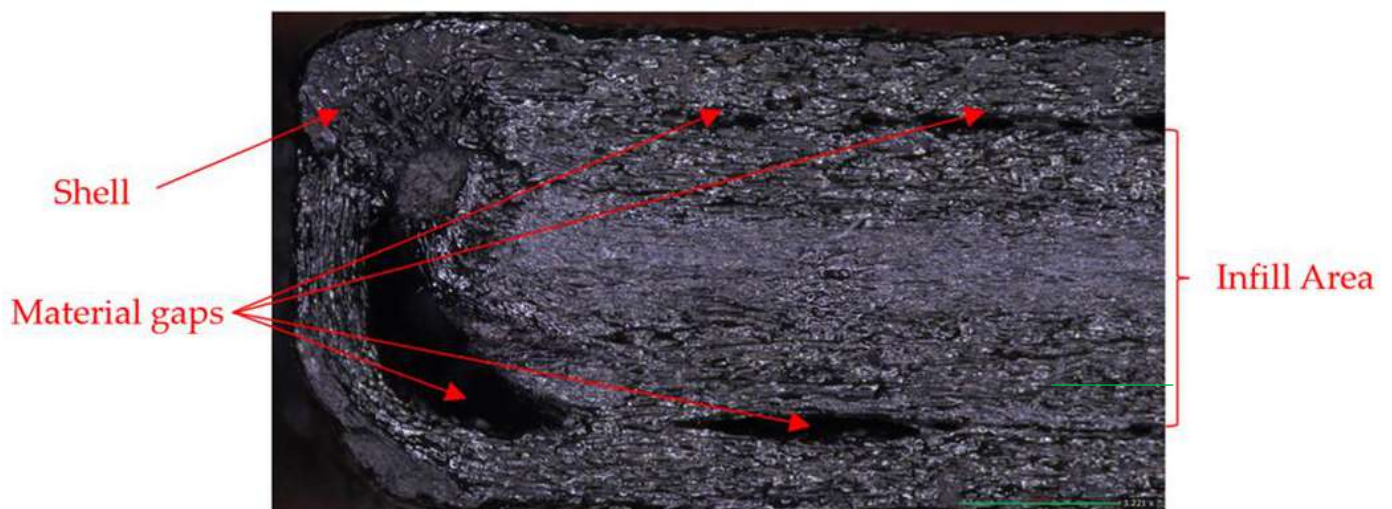


Figure 18. Specimens—Manufacturing defects—Voids between the layers (Scale 50×—Scale length 1 mm)—Emspira 3, Leica.

In Figure 19 an area is highlighted where the material is not deposited equally. The layers in the vicinity of the variable width raster have defined edges. Also, the resulted surface is not smooth due to some carbon fibers. The matrix is visibly darker and the fibers whiter, oriented along the direction of material deposition.

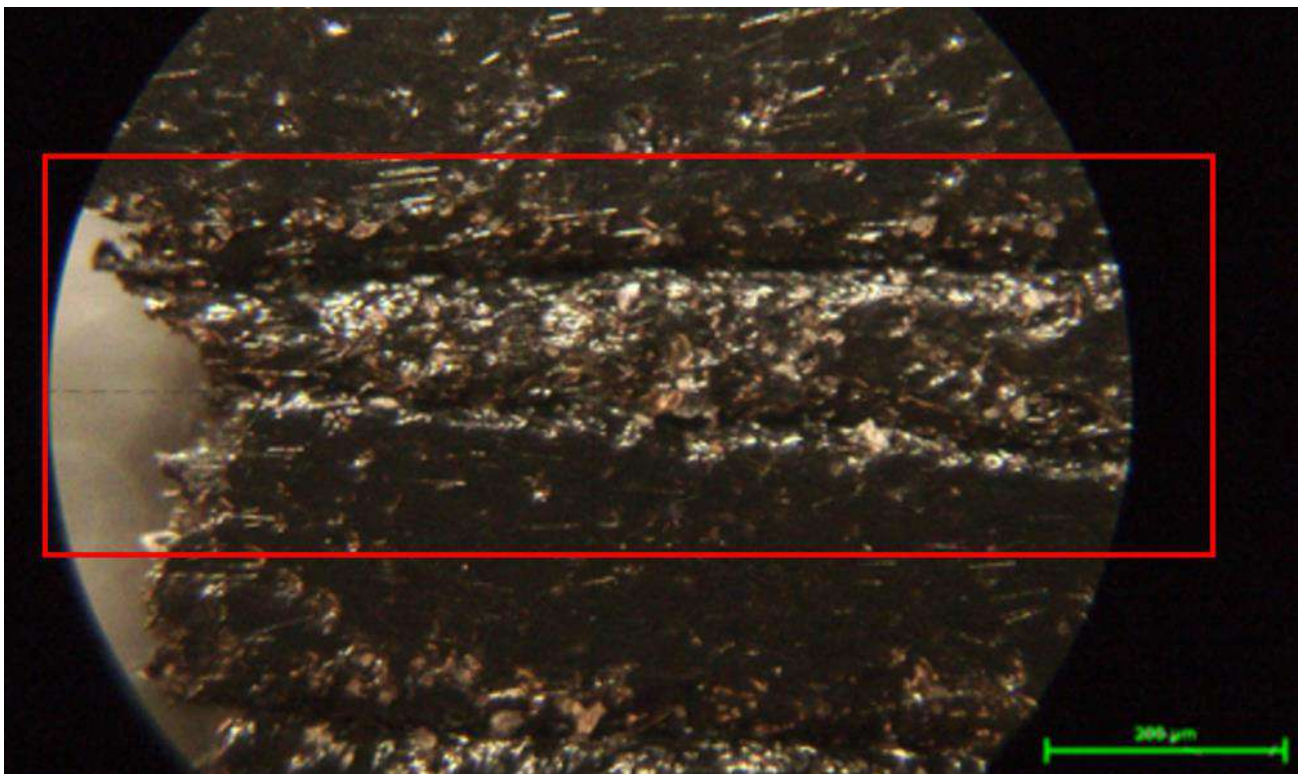


Figure 19. Specimens—Manufacturing defects—Unequal layer thicknesses (Scale 100×)—Scale length 200 μm—Nikon T1-SM.

In Figure 20 the areas are highlighted where the layers lack adhesion., The rupture during tensile tests is initiated in this area. Also, layer 1 is narrower than layer 2.

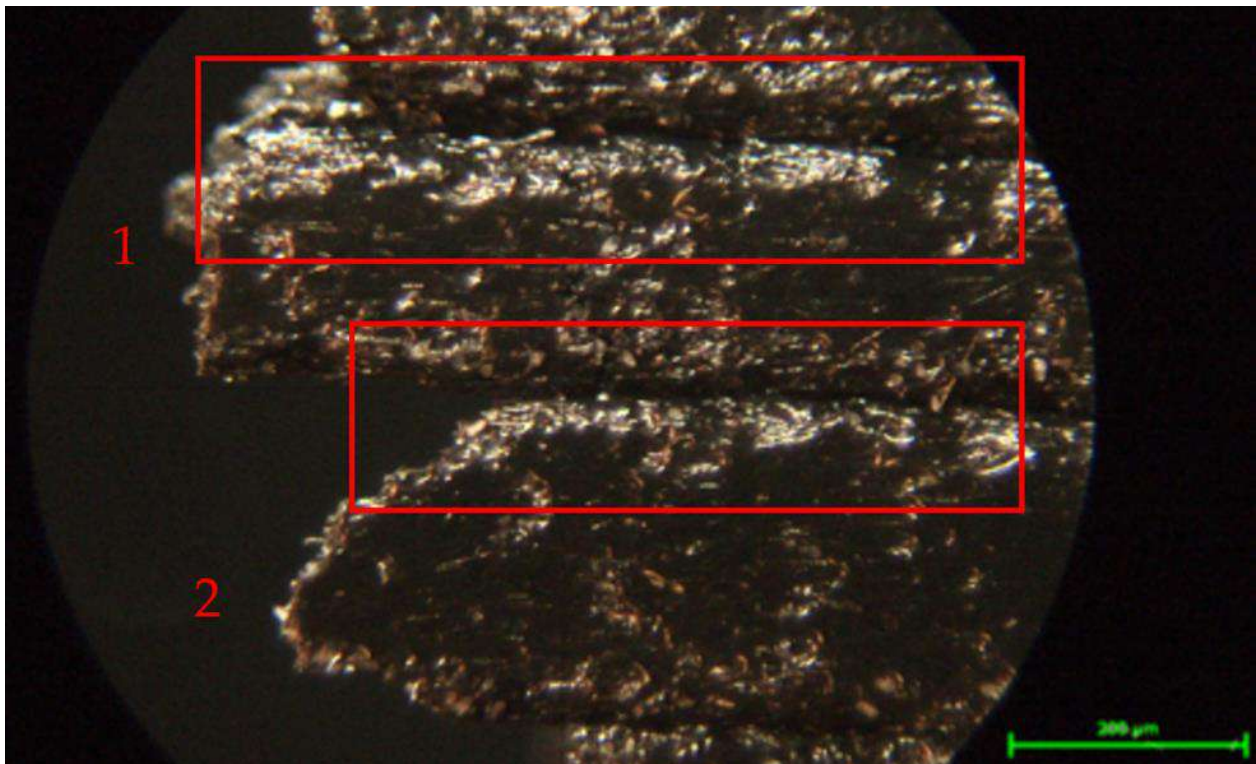


Figure 20. Specimens–Manufacturing defects–Lack of adhesion between the layers (Scale 100×)–Scale length 200 μm–Nikon T1-SM.

In Figure 21 an area of variable layer thickness is highlighted. This type of defect can be due to a variable flow rate that causes a material conglomerate followed by an area of lesser material deposition.

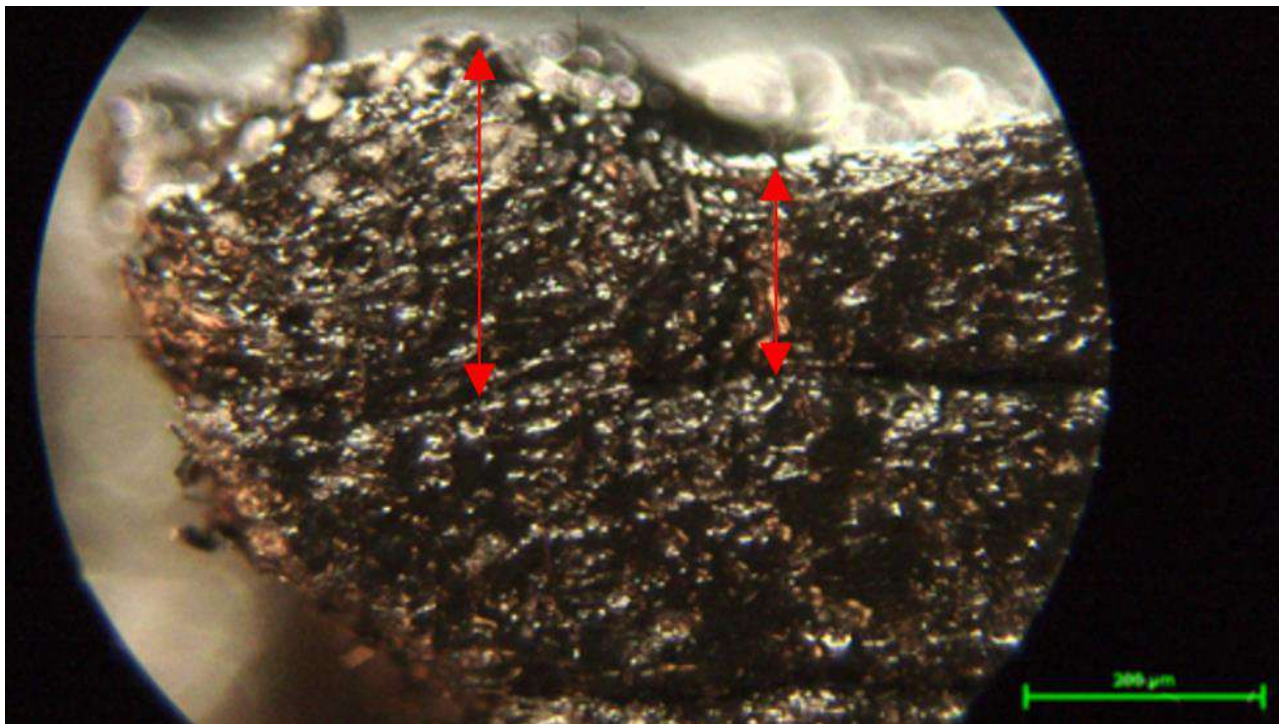


Figure 21. Specimens–Manufacturing defects–Non-constant thickness (Scale 100×)–Scale length 200 μm–Nikon T1-SM.

In Figure 22 an area is highlighted where a material conglomerate is deposited between the layers, causing a smaller width of the upper layer. Here the width of the specimen is different due to the layer on the left side of the highlighted region.

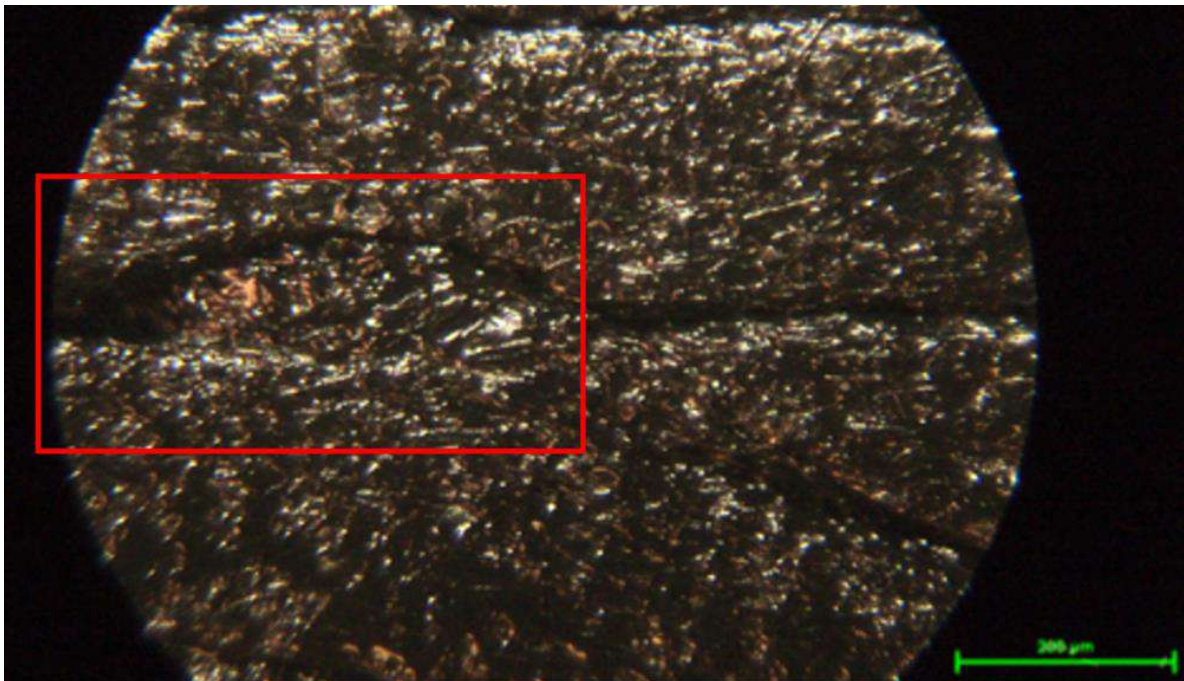


Figure 22. Specimens–Manufacturing defects–Material conglomerate (Scale 100×)–Scale length 200 μm–Nikon T1-SM.

In Figure 23 the highlighted region displays a faulty material deposition that fails to follow the normal direction of manufacturing. Thus the load path is affected leading to a maximum tensile load in the direction of material deposition.



Figure 23. Specimens–Manufacturing defects–Inadequate material deposition (Scale 100×)–Scale length 200 μm–Nikon T1-SM.

Figure 24 shows lack of material in the specimen, causing material inconsistency. This defect occurred near the tensile failure area, leading to breakage in this region.

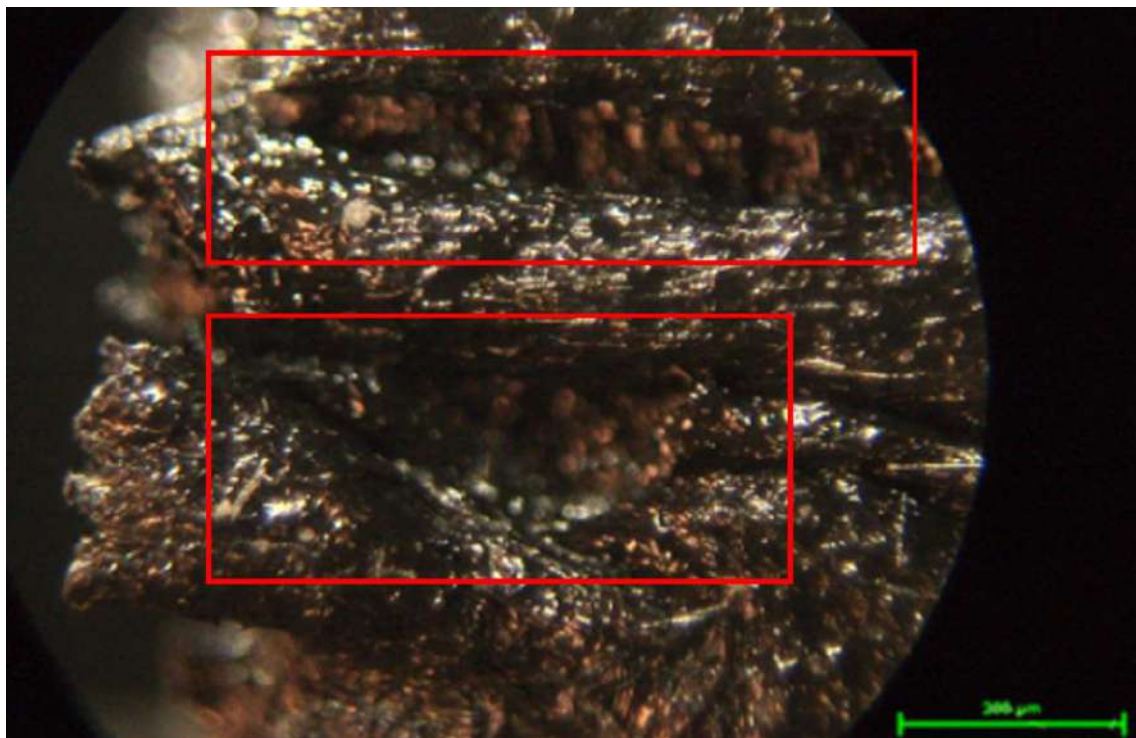


Figure 24. Specimens–Manufacturing defects–Material voids (Scale 100×)–Scale length 200 μm–Nikon T1-SM.

Figures 25 and 26 show cross-sections of the specimens with material void that cause delamination as a failure mode during the tensile testing.

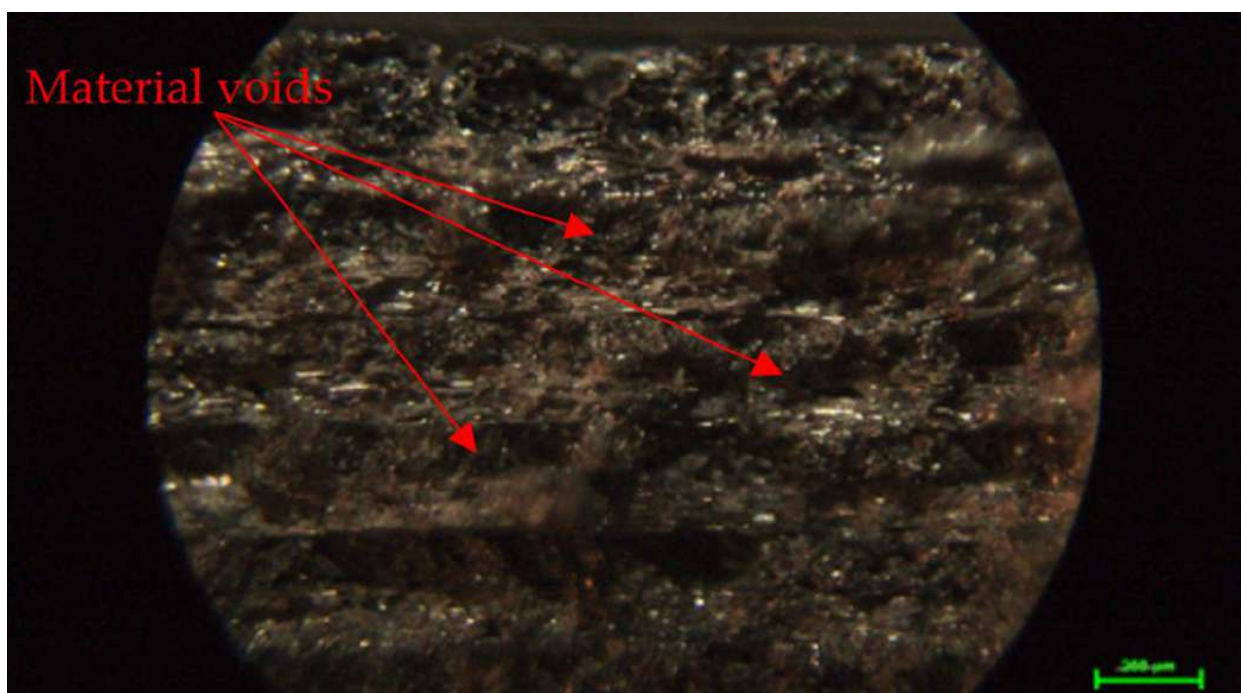


Figure 25. Specimens–Manufacturing defects–Material voids (Scale 50×)–Scale length 200 μm–Nikon T1-SM.

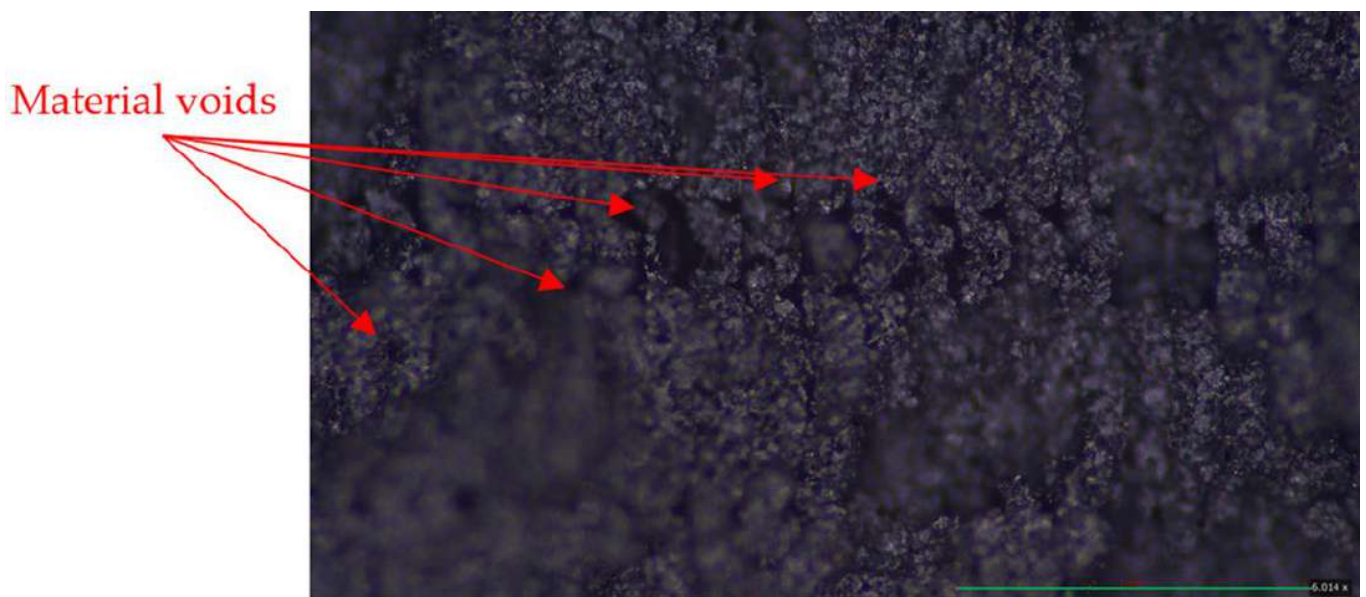


Figure 26. Specimens–Manufacturing defects–Material voids (Scale 100×–Scale length 1 mm)—Emspira 3, Leica.

Figure 27 shows a specimen edge of inadequate geometry.— After manufacturing, the deposited material fails to follow the ideal geometry. The higher material flow rate in this area causes the depositing of a larger amount of material.

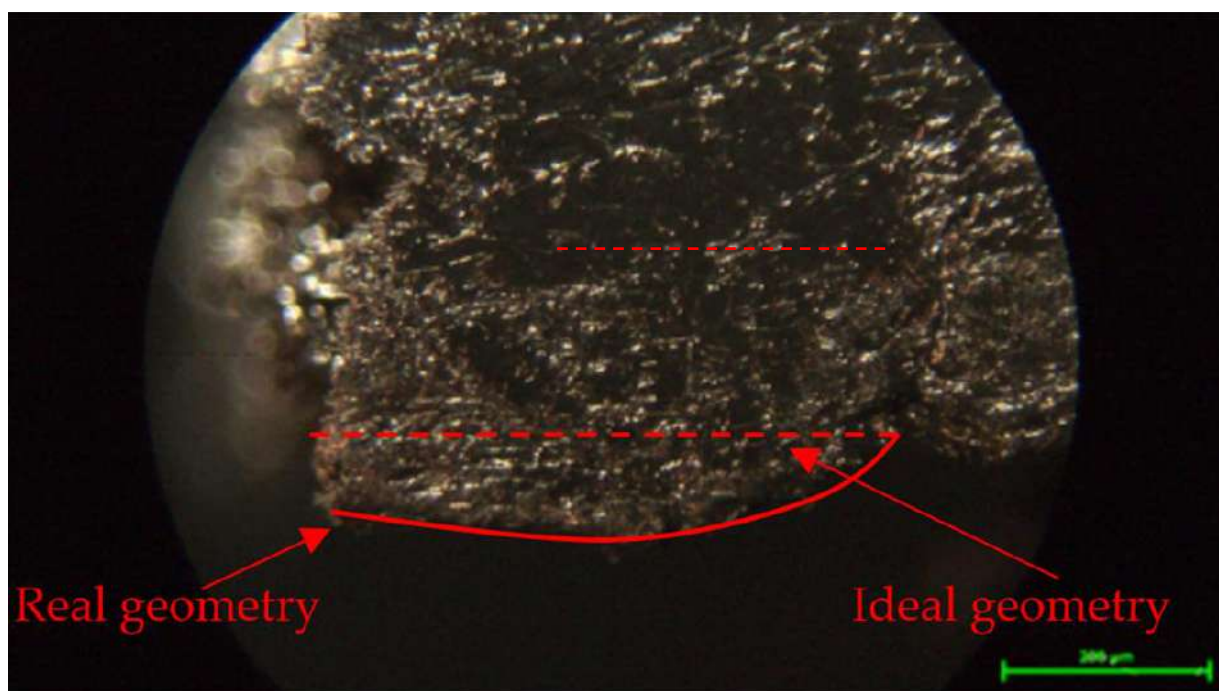


Figure 27. Specimens–Manufacturing defects–Inconsistent geometry (Scale 100×)—Scale length 200 μm —Nikon T1-SM.

Figure 28 shows a specimen with a lower infill density. The weak bonding of the infill layer is highlighted. This defect causes an inadequate load path, and failure is initiated in this area.

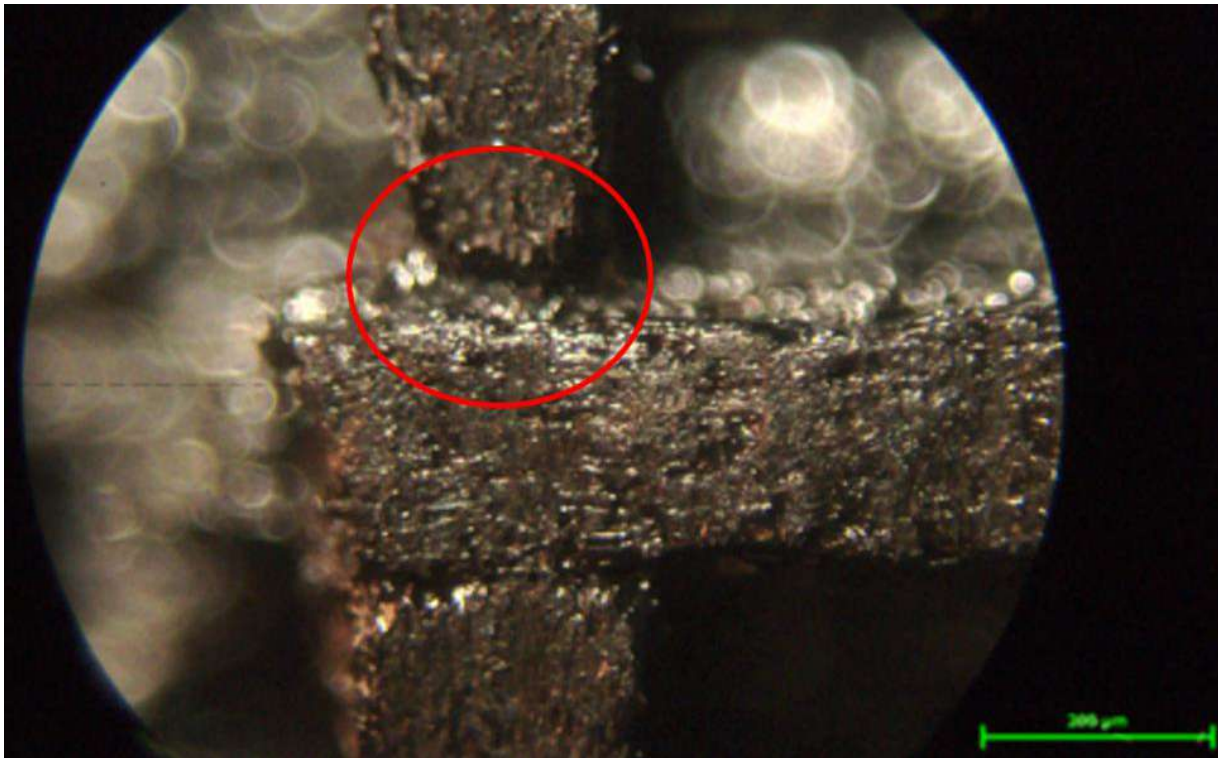


Figure 28. Specimens–Manufacturing defects–Weak bonding at the junction of the infill layer (Scale 100×)–Scale length 200 μm–Nikon T1-SM.

Figure 29 highlights the “stair-effect” that occurs at dimensional variation.. The defect appears in the area of variable width, being limited to the region held by the grips and the region used for tensile analysis. This is more visible in thicker layers.

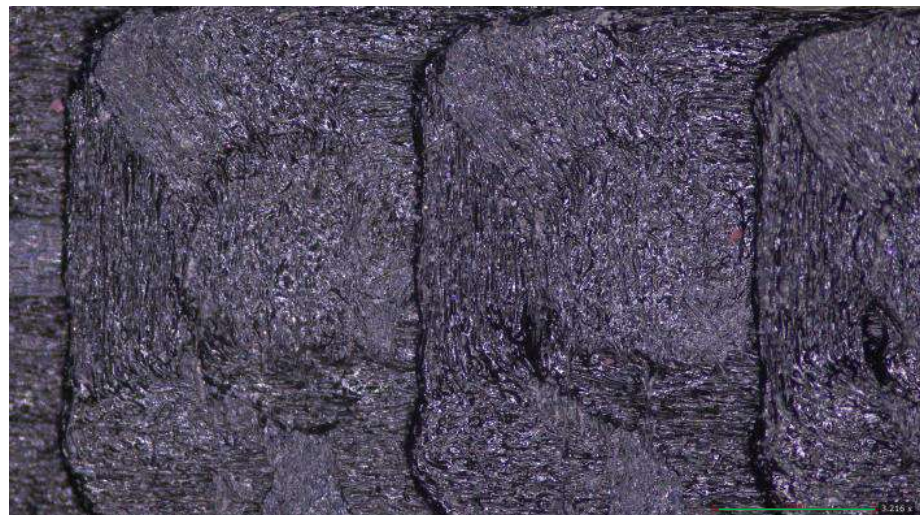


Figure 29. Specimens–Manufacturing defects–“Stair effect” (Scale 50×–Scale length 1 mm)–Emspira 3, Leica.

Figure 30 refers to the same cross-section. The layers do not overlap 100%. The profile of the offset layers follows the red polyline instead of a desired straight line. This defect is more visible in specimens manufactured in the thickness direction.

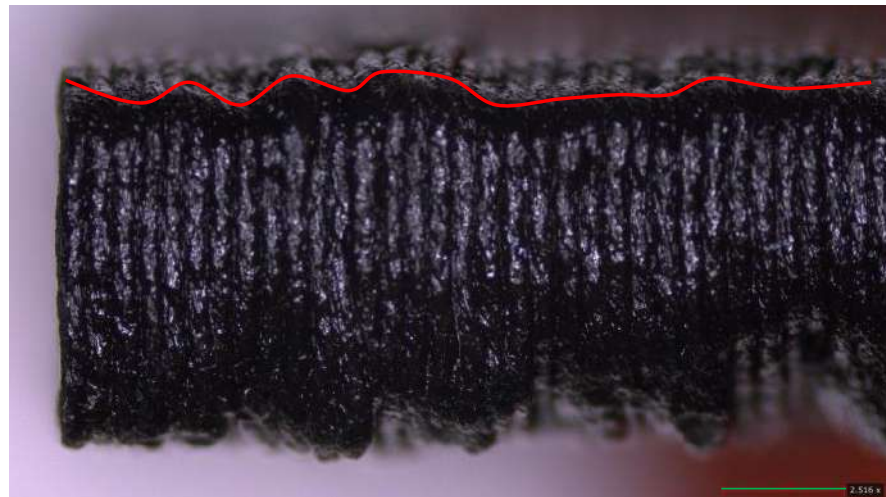


Figure 30. Specimens–Manufacturing defects–Offset layers (Scale 50×–Scale length 1 mm)–Empira 3, Leica.

For specimens with an infill density of 75% or 25% in Figure 31 it can be observed that the unsupported layers tend to flow until the material sets, affecting the internal structure of the specimen. This effect is more visible for specimens with a lower infill density. The straight line in Figure 31 represents the ideal geometry of the specimen. The red rectangle highlights the set material after flowing.

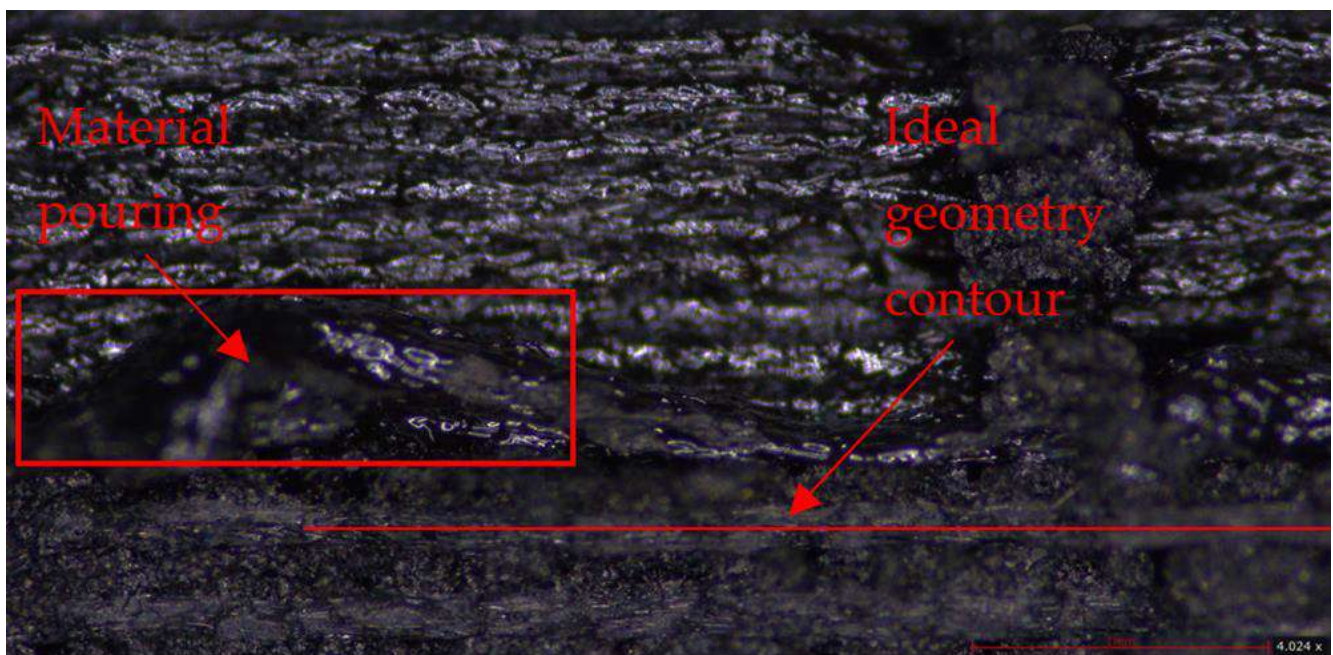


Figure 31. Specimens–Manufacturing defects–Material flowing (Scale 75×–Scale length 1 mm)–Empira 3, Leica.

Figure 32 shows a SEM image of various manufacturing defects, such as deficient inter-layer adhesion and areas with visible carbon fiber dislocation from the PET matrix. The same plot shows the failure area after tensile testing, where the main failure mode is delamination. The red box in Figure 32 marks a detail that is presented in Figure 33. This is an area of inadequate material deposition that does not follow the direction of the nozzle movement.

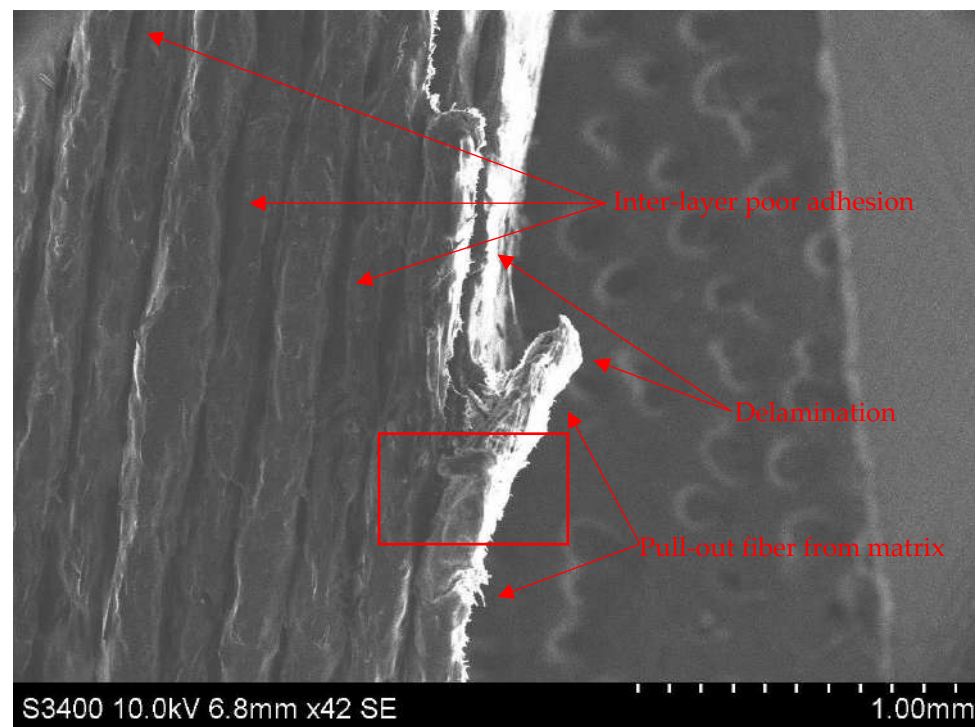


Figure 32. Specimens–Manufacturing defects–Various defects (Scale 42×–Scale length 1 mm)–Hitachi S3400N Type II.

In Figure 33 shows the area of deficient material deposition. An increased distance between the adjacent layers can be observed. Also on each layer material voids and fibers dislocated from the PET matrix are visible.

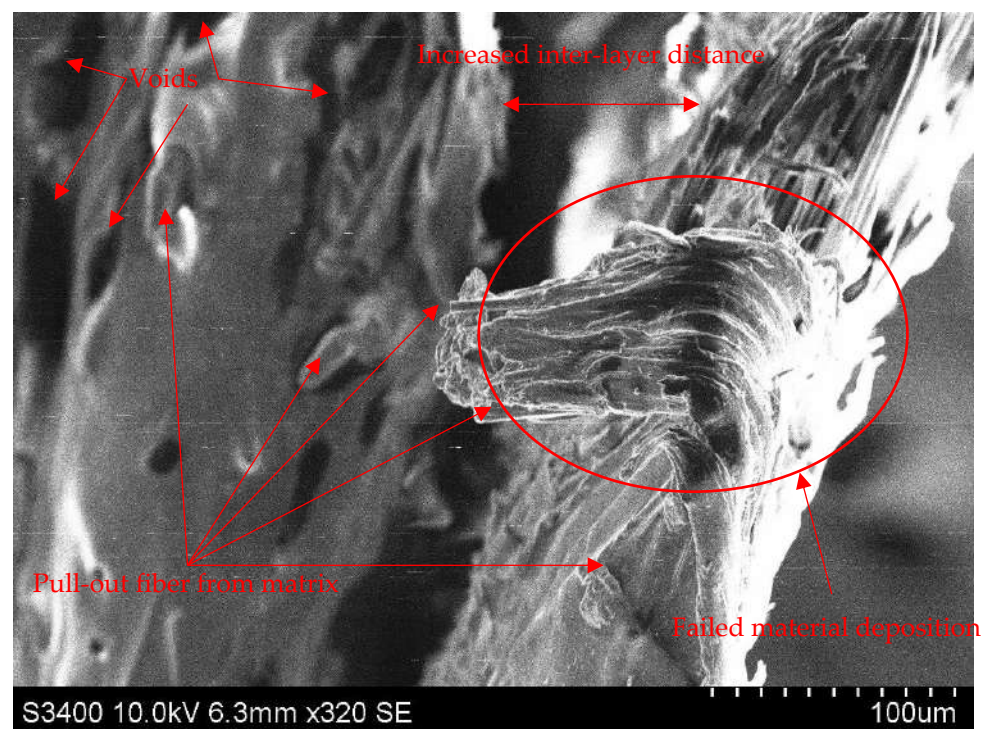


Figure 33. Specimens–Manufacturing defects–Various defects (Scale 320×–Scale length 100 µm)–Hitachi S3400N Type II.

Figure 34 shows a random inter-layer area which is irregular and also has material voids. The randomly oriented carbon fibers are also visible. The red box marks the area detailed in Figure 35.

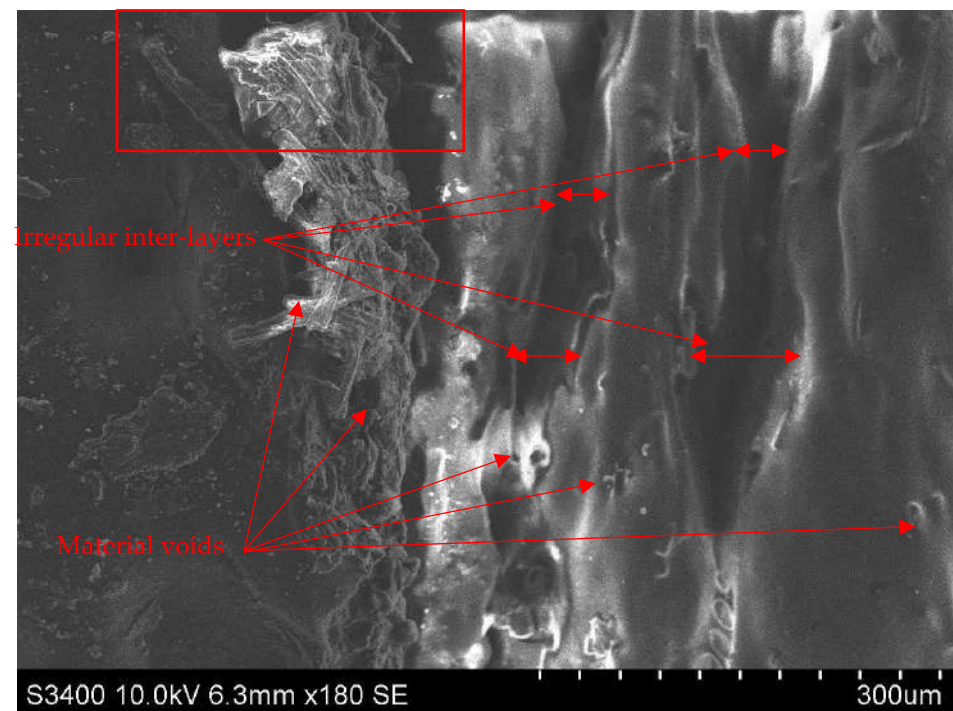


Figure 34. Specimens–Manufacturing defects–Various defects (Scale 180×–Scale length 300 µm)–Hitachi S3400N Type II.

Figure 35 shows an area with voids of different dimensions, with fibers of different orientations dislocated from the matrix. The variable inter-layer distance it is also visible.

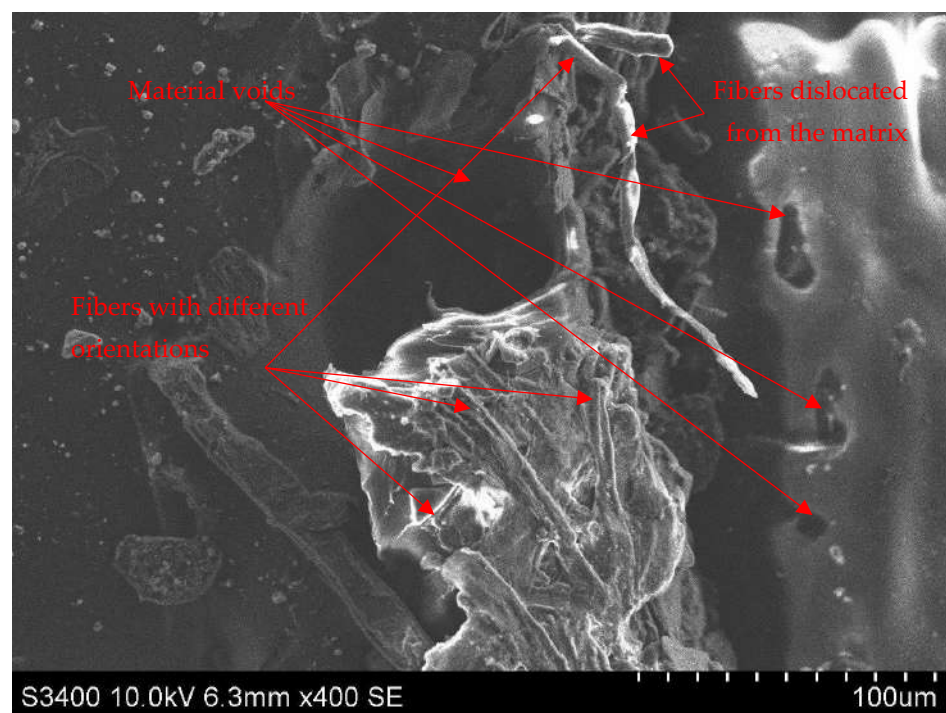


Figure 35. Specimens–Manufacturing defects–Various defects (Scale 400×–Scale length 100 µm)–Hitachi S3400N Type II.

As a conclusion, all manufacturing defects affect the mechanical properties because of material inconsistency that also affects the load path on the parts and, in the end, its performance. All specimens displayed material voids of different dimensions. Other possible defects cannot be predicted: varying fiber orientation, inconsistent inter-layer gaps or fiber dislocation from the matrix. It is recommended to test for certain failure types in order to define the material behavior, to determine a pattern and the optimal values for the main manufacturing parameters. The rest of the manufacturing parameters must be consistent, and the same machine should be used for printing.

3.2.3. PET CF15 Tensile Specimen Failure Modes

During the tensile tests different failure modes were identified that are caused also by the manufacturing defects. The most common failure issues identified during the visual inspection are presented in Figures 36–39.

Figure 36 shows a specimen after tensile testing, with fibers dislocated from the matrix. This type of failure can appear due to a weaker bonding between the matrix and the fibers, which can also cause fiber breakage.

Figure 37 shows a specimen after tensile testing where the failure is a delamination of the layers. This can be caused by manufacturing defects, such as material gaps or material conglomerates or weak bonding between the layers. Further it can be noticed that layer 2 is wider than its adjacent layers.

Figure 38 shows a specimen after tensile testing and its rupture area; further cracks near the failure area are visible.

Figure 39 shows a specimen after tensile testing and its rupture area; delamination is present and also cracks starting from the failure region and affecting almost all the layers in the vicinity of the rupture.

The main identified failure modes are delamination and material cracks, with fiber breakage. Also in many cases the fibers were dislocated from the matrix, confirming the studies that assert that the matrix does not adhere completely to the fibers.

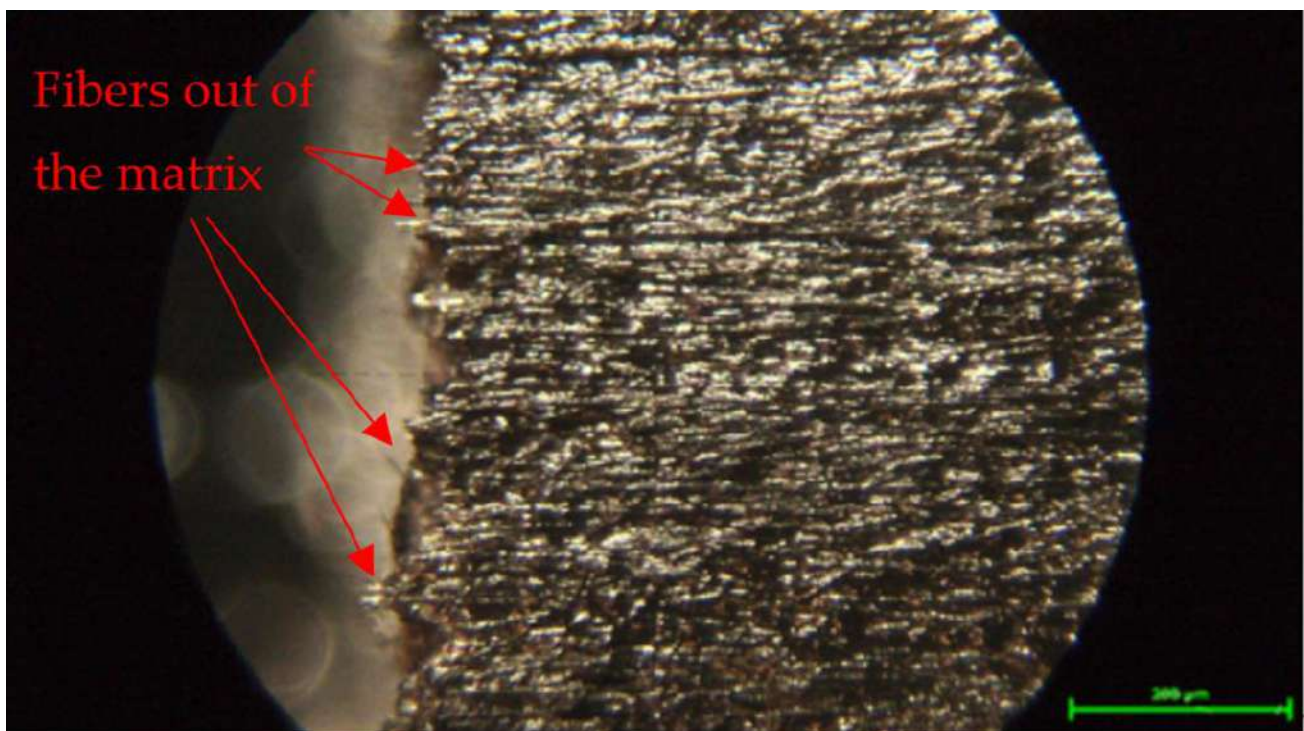


Figure 36. Specimens–Failure Modes–Fibers dislocated from the matrix and fiber breakage (Scale 100×)–Scale length 200 μm–Nikon T1-SM.

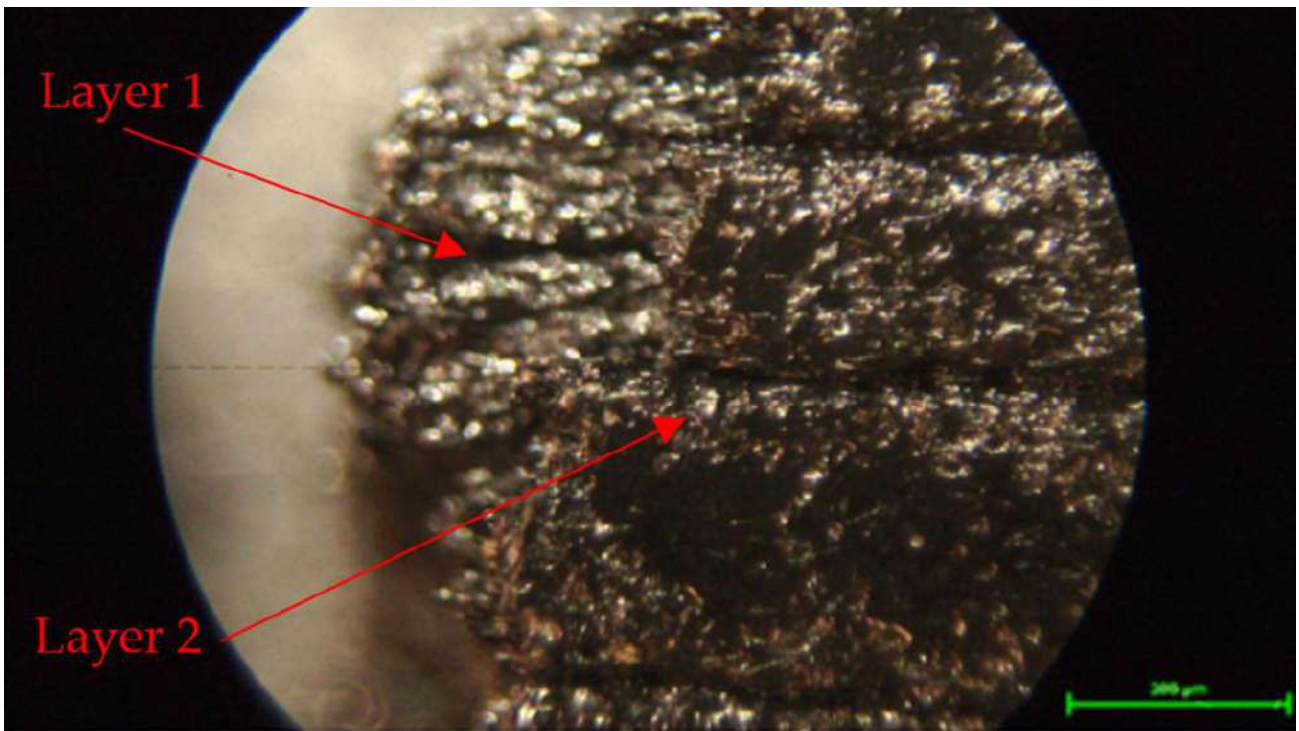


Figure 37. Specimens–Failure Modes–Delamination of the layers (Scale 100×)–Scale length 200 μm–Nikon T1-SM.

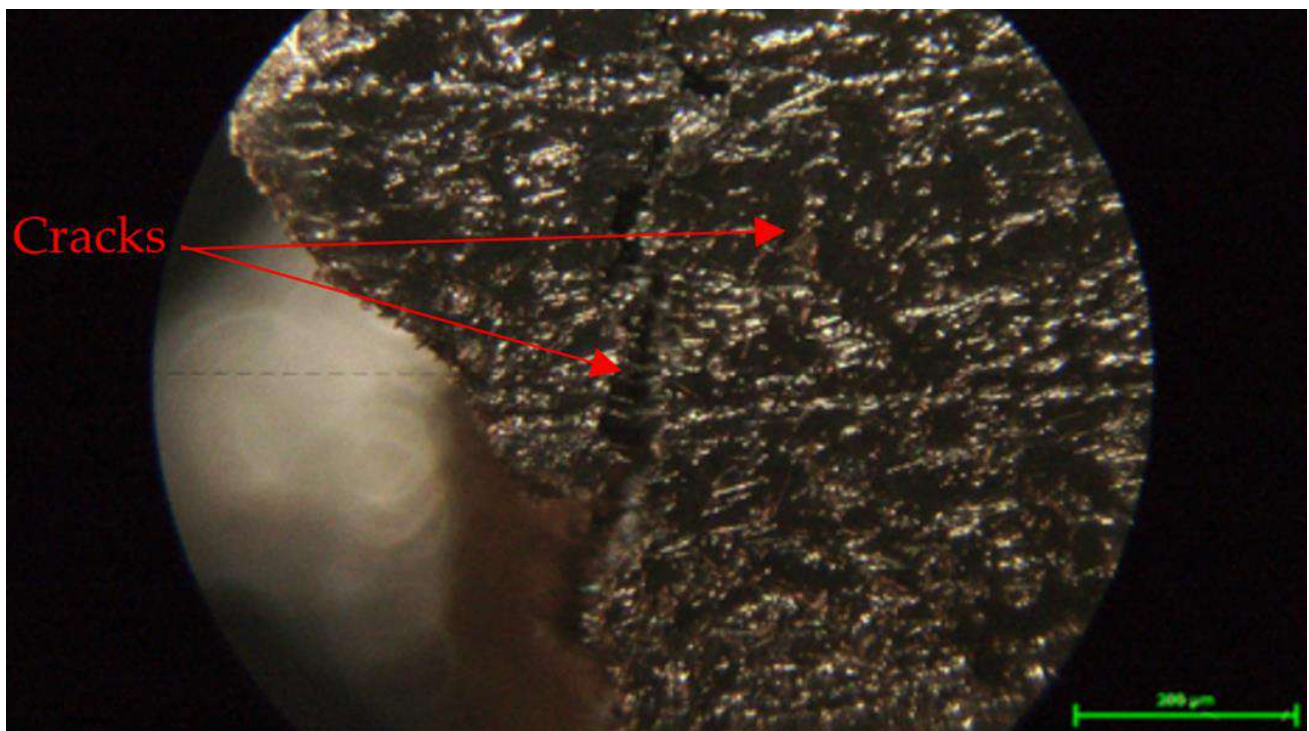


Figure 38. Specimens–Failure Modes–Cracks (Scale 100×)–Scale length 200 μm–Nikon T1-SM.

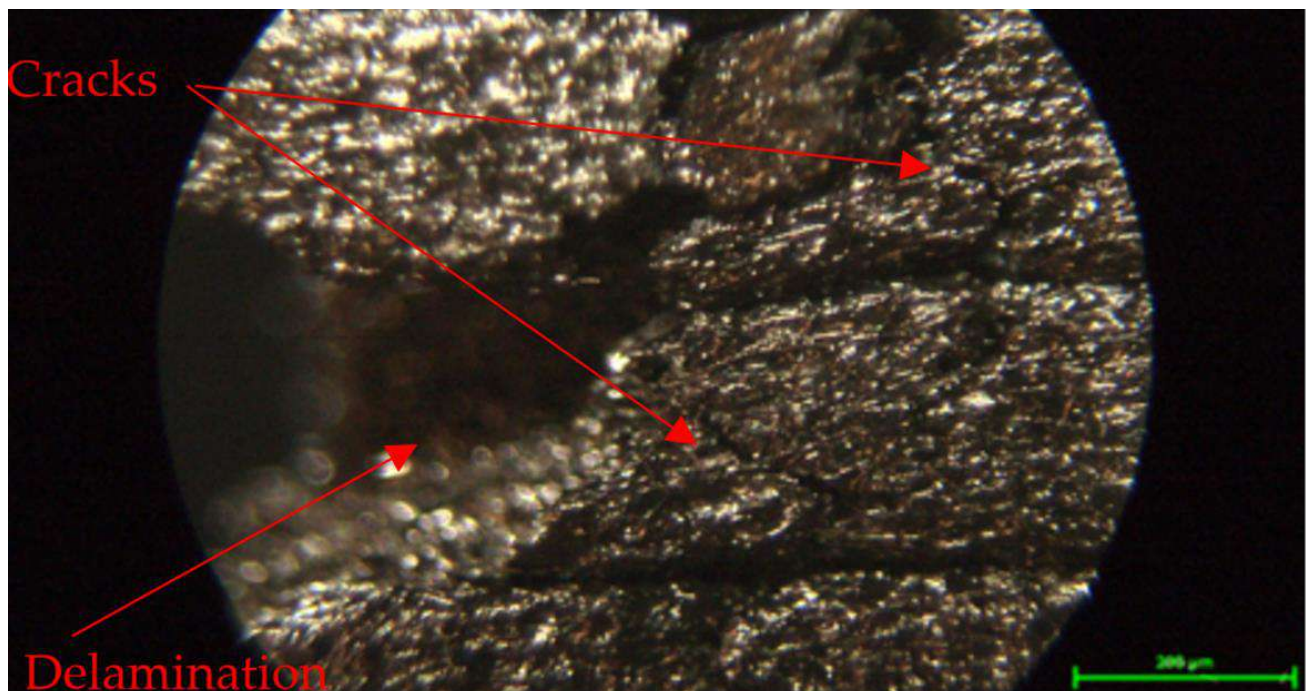


Figure 39. Specimens–Failure Modes–Delamination and cracks (Scale 100×)–Scale length 200 μm –Nikon T1-SM.

3.2.4. PET CF15 Tensile Specimen Dimensional Deviations

On each specimen the thickness and width of the area presumed to be the tensile section was measured. Subsequently the impact of specimen orientation on the geometrical parameters of the parts was determined as follows: for specimens with longitudinal material deposition all width measurements were greater than the nominal dimension of 13 mm; the measured width ranged from 13.21 mm to 13.82 mm. The thickness varied between 3.05 mm and 3.57 mm.

In specimens with transverse material deposition the measured thickness and width were greater than the nominal values. The thickness varied from 3.37 mm to 3.44 mm. The width ranged between 13.21 mm and 13.27 mm.

Material deposition along the transverse direction yielded thickness values ranging from 3.15 mm to 3.66 mm. The width was smaller than the nominal dimension of 13 mm, ranging from 12.82 mm to 12.98 mm.

These different values suggest the idea of a geometrical instability of the parts, even for specimens printed at the same time in sets of five. In [14] it is reported that in specimens with lower layer thickness the geometry varies less than in those with a greater layer thickness. Nevertheless, in this case, in addition to the aspects mentioned before, it can be asserted that part orientation and design also have a significant influence on its geometrical stability.

3.3. Design of Experiments

Statistical data processing and analysis of variance (ANOVA) were applied to the results of the tensile testing of the specimens with longitudinal material deposition. The mathematical model expressed by Equation (2) was obtained using Minitab 21. It can be used without further costs to expand and predict the outputs. Table 9 presents the summary of the model implemented in 45 iterations for the prediction of R_m . It used as input parameters the infill density (I) and the layer thickness (t), defined as independent variables, as well as the results of the tensile testing. Evidently R_m was the predicted dependent variable. The values of the independent variables and the running order are presented in Appendix C.

$$R_m = 67.7 + 0.2739 I - 3.15 t + 0.0653 t^2 \quad (2)$$

Table 9. Summary of the polynomial equation model for the prediction of Rm.

S	R ²	Adjusted R ²	Predicted R ²
2.3268	94.08%	93.65%	92.85%

This model was selected due to the reasonable number of equation terms, it represents a strong relationship defined by the terms R², Adjusted R² and Predicted R² presented above. Their values also describe the correlation of the regression model, which in this case is high, over 90%. This result can be explained by the material inconsistency and the manufacturing defects identified during the tests.

Table 10 presents the ANOVA analysis of the regression model. Equation (2) includes only significant terms, corresponding to the Pareto Chart shown in Figure 32. This result was obtained after iterations where the terms with *p*-values exceeding 0.05 were removed from the mathematical regression model due to their inconsistencies.

Table 10. Analyses of Variance of the regression model.

Source	DF	Adjusted SS	Adjusted MS	F-Value	<i>p</i> -Value
Regression (Rm)	3	3527.67	1175.89	217.19	0
Infill (I)	1	3282.29	3282.29	606.26	0
Layer Thickness (t)	1	38.64	38.64	7.14	0.011
Layer Thickness (t ²)	1	26.68	26.68	4.93	0.032
Error	41	221.97	5.41		
Lack-of-Fit	5	93.57	18.71	5.25	0.001
Pure Error	36	128.40	3.57		
Total	44	3749.64			

Figure 40 describes the impact of each term: A is the layer thickness and B is the infill; in this case, the infill has the most significant level of all the defined terms. The same result was reported in [33]. The significance of each term is expressed by its length in the chart. The vertical red line at 2.02 crosses all the bars representing the terms, which means that all terms impact on the determination of the regression model.

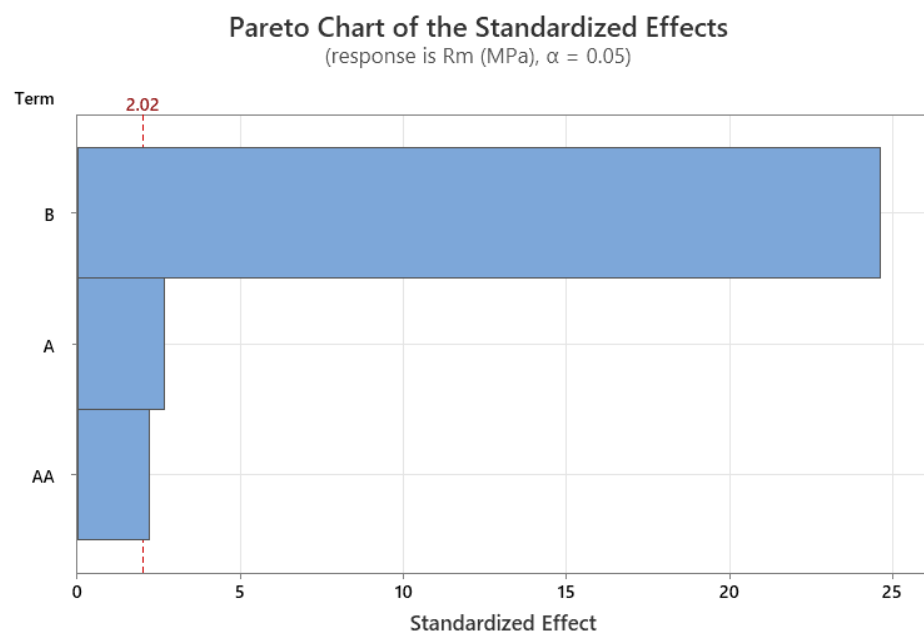


Figure 40. Pareto Chart of the regression model.

Figure 41 shows the graphs that describe the mathematical model: the first plot (a) checks whether the residuals are normally distributed. In this case, the assumption is verified because the residuals follow a straight line. The second plot (b) checks if the points of residuals are randomly distributed and on both sides of the 0-axis. Some patterns of residuals can be explained by the similar behavior of the specimens for the same parameters: infill and layer thickness. In the third plot (c), the chart describes the residual distribution. The last plot (d) verifies whether the residuals are independent from each other; in this case, the points of residuals are randomly distributed on both sides of the center line, indicating that the residuals are not correlated.

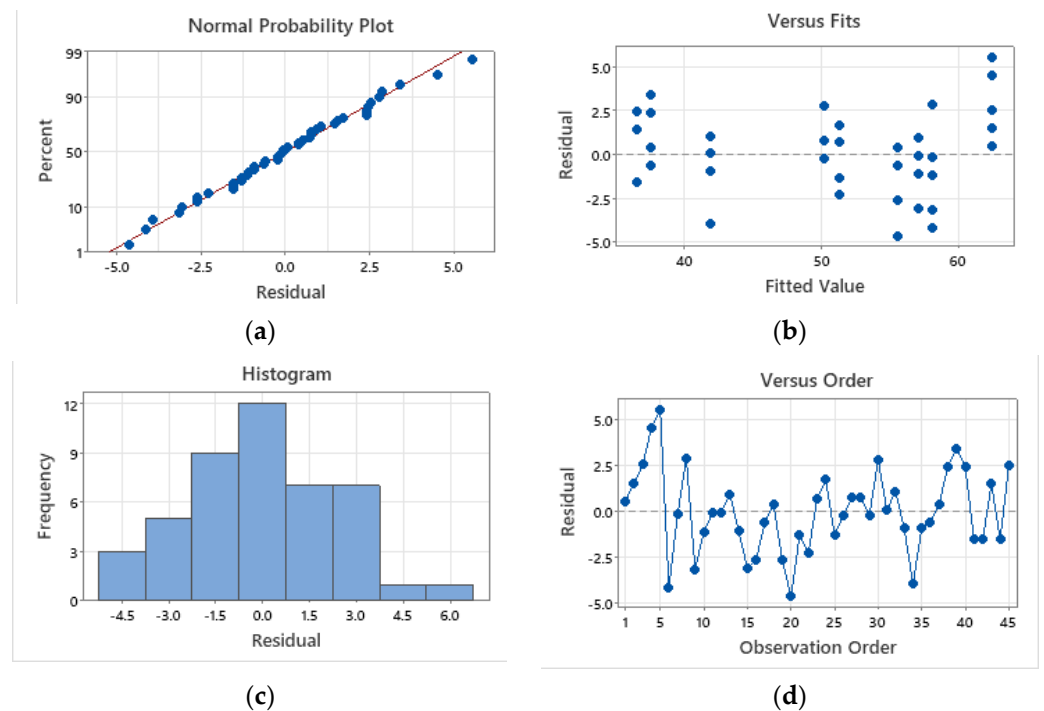


Figure 41. Residual Plots for Rm [MPa]: (a) Normal Probability Plot; (b) Versus Fits; (c) Histogram; (d) Versus Order.

4. Conclusions

The aim of this research is achieved by the performed tensile tests that took into account two of the most important manufacturing parameters, namely layer thickness and infill density. For each parameter three values were considered. For each parameter setpoint combination sets of 5 specimens were manufactured. The material was deposited along the longitudinal axis of the specimens.

The results are validated by a regression model obtained by an analysis of variance, classifying the studied parameters. Having obtained the values of the manufacturing parameters that yield the best results, further tensile tests are conducted to define the tensile values for specimens with material deposited along the transverse and thickness directions. In this manner the material can be described by all main directions, a novelty in the field, as in literature to date only few studies address composite filaments with PET matrices. After testing, specimens are visually checked under a microscope in order to identify manufacturing defects and rupture behavior.

The aspects discussed above yield the following conclusions:

- For the best results obtained for 100% infill and 0.15 mm layer thickness, further tensile tests were performed for specimens manufactured by material deposition in the transverse and thickness directions, because of the anisotropy of the material.

- The results in the longitudinal direction are: $R_m = 65.4$ MPa, $R_p = 51.6$ MPa, $E = 9$ GPa, $\epsilon = 1.93\%$.
- For the transverse direction the results are: $R_m = 41\text{--}49$ MPa, $R_p = 9\text{--}45$ MPa, $E = 7$ GPa, $\epsilon = 1\text{--}1.80\%$.
- For the thickness direction, the results are: $R_m = 3$ MPa, $R_p = 1$ MPa, $E = 1$ GPa and $\epsilon = 0.23\%$.
- If the material is deposited in a different direction than the direction of the load, the results are undesired and the geometrical stability is affected.
- Considering the conducted DOE, between layer thickness and infill density the most influential manufacturing parameter is infill.
- The reliability is influenced by the inconsistent results due to the defects that appear in all stages, from the raw material to the finite parts, these range from filament deviations to material voids and fiber conglomerates in both raw and finite materials.
- The most usual defect identified in each specimen are material voids. Due to material defects different failure modes occur during tensile loading, from layers debonding to material cracks or fibers dislocated from the matrix and brakeage.

The results of this research can be used in other studies concerned with the FEA process of complex products, as well as in manufacturing processes using this type of material and 3D printers. In further research the authors aim to describe the behavior at compression and bending of the same material, working with the most beneficial manufacturing parameter setpoints: layer thickness of 0.15 mm and infill density of 100%. In order to check the influence of carbon fibers on the mechanical properties and geometrical deviations, the same tests will be performed for specimens made from PET filaments.

Author Contributions: Conceptualization, M.-I.B. and G.O.; methodology, M.-I.B., S.-M.Z. and G.O.; software, M.-I.B.; validation, M.-I.B., C.O.M. and G.O.; formal analysis, M.-I.B.; investigation, M.-I.B., C.O.M., S.-M.Z., G.O. and M.C.; resources, M.A.P. and M.C.; writing—original draft preparation, M.-I.B.; writing—review and editing, M.-I.B. and G.O.; visualization, C.O.M., M.A.P. and M.C.; supervision, G.O. and S.-M.Z.; project administration, M.-I.B.; funding acquisition, G.O. All authors have read and agreed to the published version of the manuscript.

Funding: This research received no external funding.

Institutional Review Board Statement: Not applicable.

Data Availability Statement: Data are contained within the article.

Conflicts of Interest: The authors declare no conflict of interest.

Appendix A

The following figures present the tensile specimens before and after testing. The conclusions are discussed in Section 3.

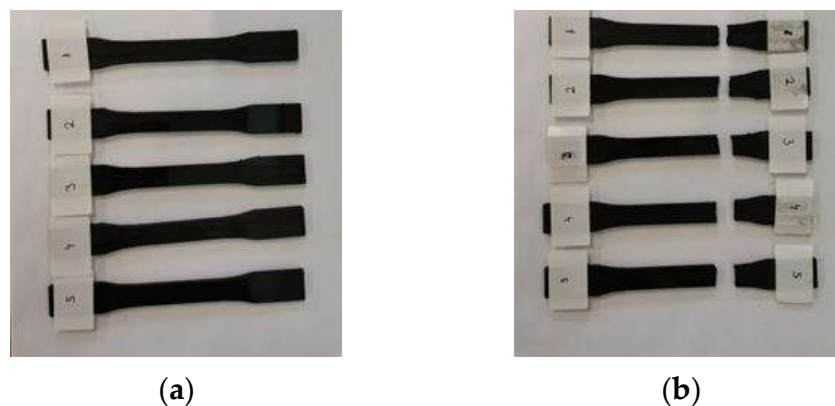
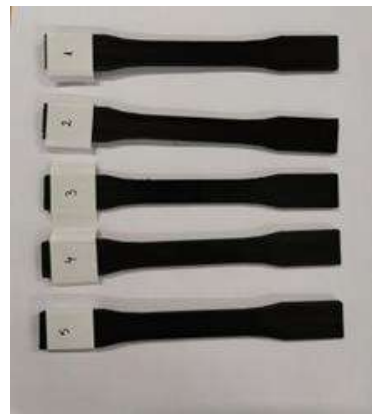
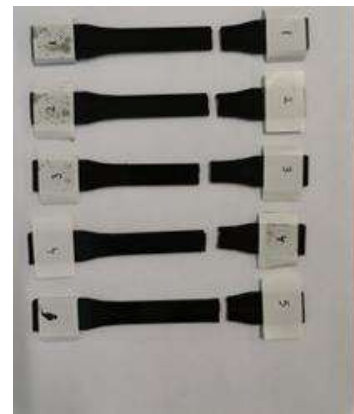


Figure A1. Longitudinal Tensile Specimens C_20_100: (a) Before testing; (b) After testing.



(a)



(b)

Figure A2. Longitudinal Tensile Specimens C_25_100: (a) Before testing; (b) After testing.

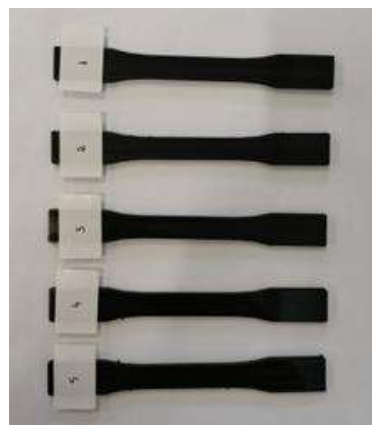


(a)

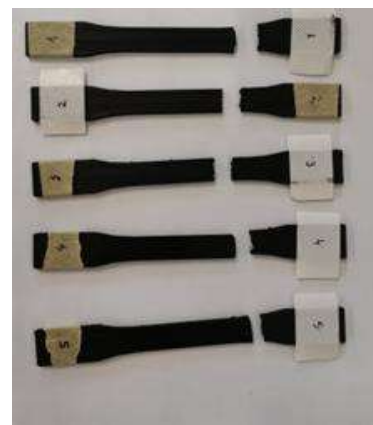


(b)

Figure A3. Longitudinal Tensile Specimens C_15_75: (a) Before testing; (b) After testing.



(a)



(b)

Figure A4. Longitudinal Tensile Specimens C_20_75: (a) Before testing; (b) After testing.

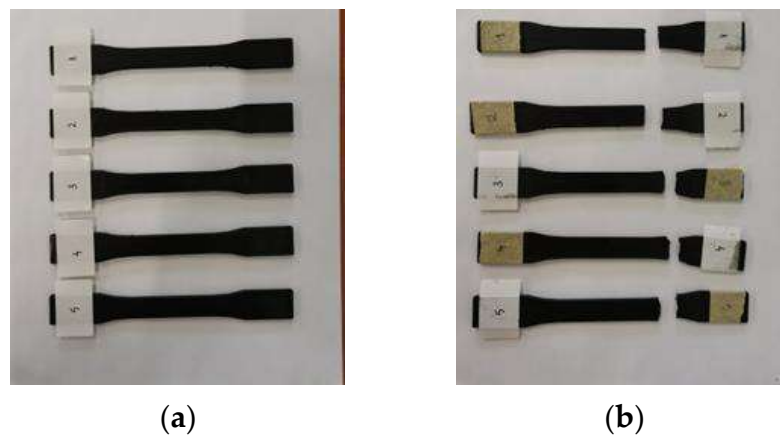


Figure A5. Longitudinal Tensile Specimens C_25_75: (a) Before testing; (b) After testing.



Figure A6. Longitudinal Tensile Specimens C_15_25: (a) Before testing; (b) After testing.

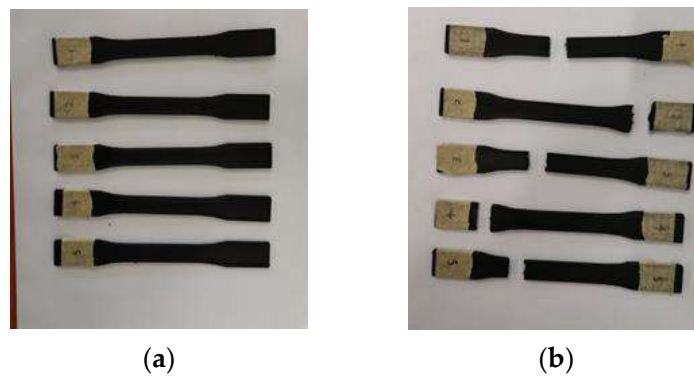
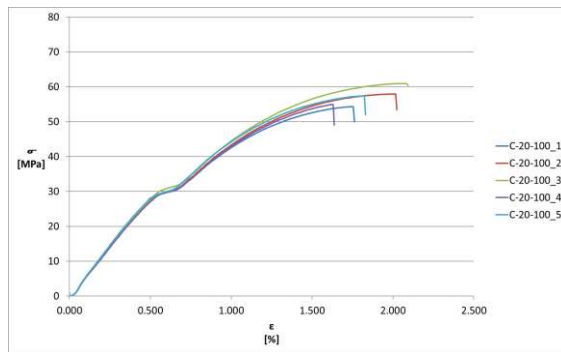


Figure A7. Longitudinal Tensile Specimens C_20_25: (a) Before testing; (b) After testing.

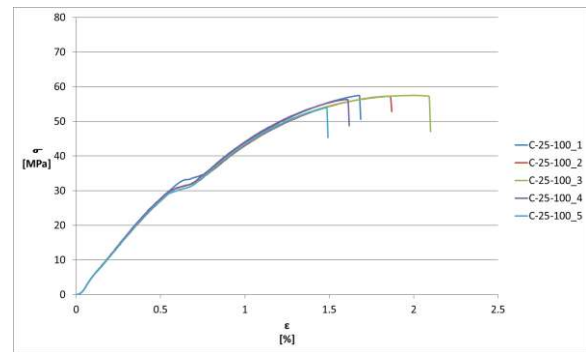


Figure A8. Longitudinal Tensile Specimens C_25_25: (a) Before testing; (b) After testing.

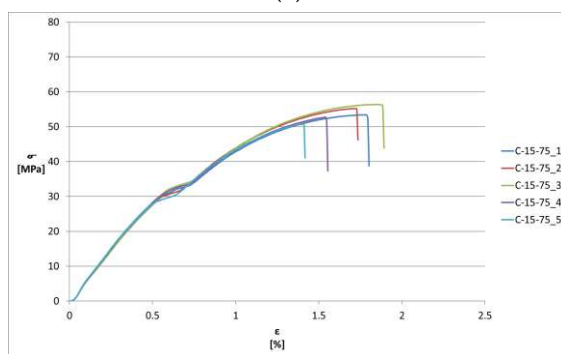
Appendix B



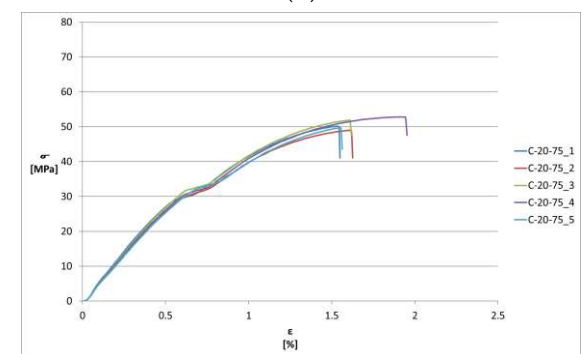
(a)



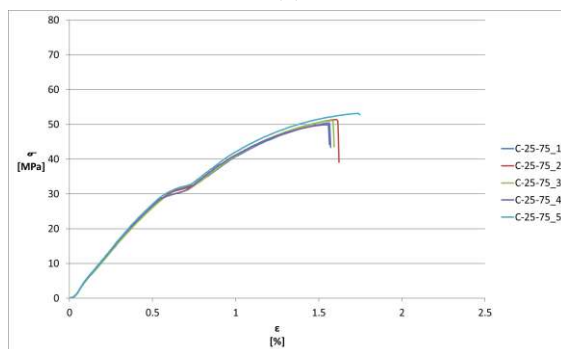
(b)



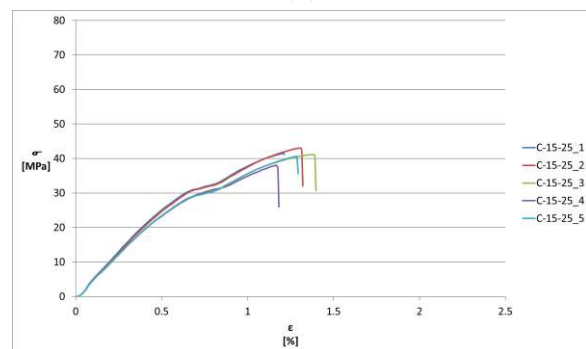
(c)



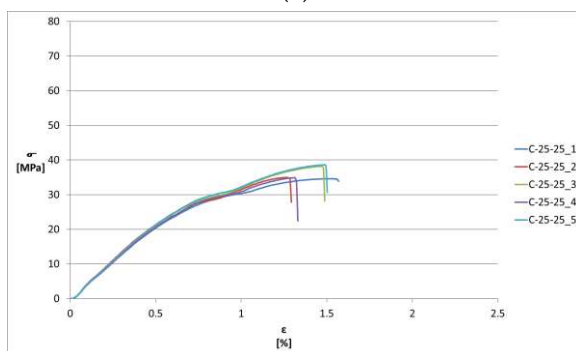
(d)



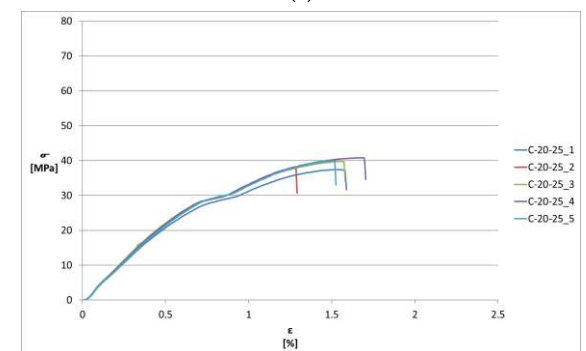
(e)



(f)



(g)



(h)

Figure A9. Longitudinal Tensile Specimens results–Stress-Strain curves: (a) Stress-Strain curves for C_20_100; (b) Stress-Strain curves for C_25_100; (c) Stress-Strain curves for C_15_75; (d) Stress-Strain curves for C_20_75; (e) Stress-Strain curves for C_25_75; (f) Stress-Strain curves for C_15_25; (g) Stress-Strain curves for C_20_25; (h) Stress-Strain curves for C_25_25.

Table A1. Longitudinal Tensile Specimens Result—C_20_100.

Specimen	Fm (kN)	Rm (MPa)	Fp (kN)	Rp(kN)	E (GPa)	ϵ (%)
C_20_100_1	2.402	54	1.573	36	9	1.77
C_20_100_2	2.562	58	1.702	38	9	2.03
C_20_100_3	2.695	61	1.821	41	9	2.11
C_20_100_4	2.429	55	1.621	37	9	1.64
C_20_100_5	2.538	57	1.737	39	9	1.84
Mean	2.53	57.00	1.69	38.20	9	1.88

Table A2. Longitudinal Tensile Specimens Result—C_25_100.

Specimen	Fm (kN)	Rm (MPa)	Fp (kN)	Rp(kN)	E (GPa)	ϵ (%)
C_25_100_1	2.483	57	1.629	38	9	1.69
C_25_100_2	2.474	57	1.614	37	9	1.88
C_25_100_3	2.484	58	1.622	38	9	2.11
C_25_100_4	2.431	56	1.632	38	9	1.62
C_25_100_5	2.328	54	1.589	37	9	1.50
Mean	2.44	56.40	1.62	37.20	9	1.76

Table A3. Longitudinal Tensile Specimens Result—C_15_75.

Specimen	Fm (kN)	Rm (MPa)	Fp (kN)	Rp(kN)	E (GPa)	ϵ (%)
C_15_75_1	2.238	53	1.811	43	8	1.8
C_15_75_2	2.314	55	1.534	37	10	1.74
C_15_75_3	2.363	56	1.555	37	9	1.90
C_15_75_4	2.209	53	1.45	35	10	1.55
C_15_75_5	2.126	51	1.469	35	10	1.42
Mean	2.25	53.60	1.56	37.40	9.40	1.68

Table A4. Longitudinal Tensile Specimens Result—C_20_75.

Specimen	Fm (kN)	Rm (MPa)	Fp (kN)	Rp(kN)	E (GPa)	ϵ (%)
C_20_75_1	2.133	50	1.435	34	9	1.56
C_20_75_2	2.084	49	1.407	33	9	1.63
C_20_75_3	2.207	52	1.468	34	9	1.62
C_20_75_4	2.248	53	1.471	35	9	1.96
C_20_75_5	2.115	50	1.46	34	9	1.57
Mean	2.16	50.80	1.45	34.00	9	1.67

Table A5. Longitudinal Tensile Specimens Result—C_25_75.

Specimen	Fm (kN)	Rm (MPa)	Fp (kN)	Rp(kN)	E (GPa)	ϵ (%)
C_25_75_1	2.139	50	1.435	34	9	1.58
C_25_75_2	2.180	51	1.471	35	9	1.620
C_25_75_3	2.166	51	1.448	34	9	1.60
C_25_75_4	2.117	50	1.429	34	9	1.57
C_25_75_5	2.255	53	1.493	35	9	1.75
Mean	2.17	51.00	1.46	34.40	9	1.62

Table A6. Longitudinal Tensile Specimens Result—C_15_25.

Specimen	Fm (kN)	Rm (MPa)	Fp (kN)	Rp(kN)	E (GPa)	ϵ (%)
C_15_25_1	1.686	42	1.305	32	9	1.21
C_15_25_2	1.748	43	1.303	32	9	1.32
C_15_25_3	1.670	41	1.229	30	8	1.40
C_15_25_4	1.545	38	1.255	31	8	1.18
C_15_25_5	1.649	41	1.224	30	8	1.30
Mean	1.66	41	1.26	31	8.40	1.28

Table A7. Longitudinal Tensile Specimens Result—C_20_25.

Specimen	Fm (kN)	Rm (MPa)	Fp (kN)	Rp(kN)	E (GPa)	ϵ (%)
C_20_25_1	1.616	37	1.235	29	7	1.60
C_20_25_2	1.631	38	1.280	30	8	1.30
C_20_25_3	1.719	40	1.254	29	8	1.59
C_20_25_4	1.762	41	1.269	29	8	1.71
C_20_25_5	1.723	40	1.291	30	7	1.53
Mean	1.69	39.20	1.27	29.40	7.60	1.55

Table A8. Longitudinal Tensile Specimens Result—C_25_25.

Specimen	Fm (kN)	Rm (MPa)	Fp (kN)	Rp(kN)	E (GPa)	ϵ (%)
C_25_25_1	1.472	35	1.224	29	7	1.58
C_25_25_2	1.487	35	1.196	28	7	1.29
C_25_25_3	1.626	38	1.253	29	7	1.49
C_25_25_4	1.484	35	1.237	29	7	1.33
C_25_25_5	1.645	39	1.282	30	7	1.50
Mean	1.54	36.40	1.24	29	7	1.44

Table A9. Longitudinal Tensile Specimens Result—C_20_100—Deviations from the mean value.

Specimen	Fm [%]	Rm [%]	Fp [%]	Rp [%]	E [%]	ϵ [%]
C_20_100_1	−4.88	−5.26	−6.97	−5.76	0.00	−5.75
C_20_100_2	1.46	1.75	0.66	−0.52	0.00	8.09
C_20_100_3	6.72	7.02	7.70	7.33	0.00	12.35
C_20_100_4	−3.81	−3.51	−4.13	−3.14	0.00	−12.67
C_20_100_5	0.51	0.00	2.73	2.09	0.00	−2.02

Table A10. Longitudinal Tensile Specimens Result—C_25_100—Deviations from the mean value.

Specimen	Fm [%]	Rm [%]	Fp [%]	Rp [%]	E [%]	ϵ [%]
C_25_100_1	1.76	1.06	0.73	1.06	0.00	−3.98
C_25_100_2	1.39	1.06	−0.20	−1.60	0.00	6.82
C_25_100_3	1.80	2.84	0.30	1.06	0.00	19.89
C_25_100_4	−0.37	−0.71	0.92	1.06	0.00	−7.95
C_25_100_5	−4.59	−4.26	−1.74	−1.60	0.00	−14.77

Table A11. Longitudinal Tensile Specimens Result—C_15_75—Deviations from the mean value.

Specimen	Fm [%]	Rm [%]	Fp [%]	Rp [%]	E [%]	ϵ [%]
C_15_75_1	−0.53	−1.12	15.81	14.97	−14.89	7.02
C_15_75_2	2.84	2.61	−1.91	−1.07	6.38	3.45
C_15_75_3	5.02	4.48	−0.56	−1.07	−4.26	12.96
C_15_75_4	−1.82	−1.12	−7.28	−6.42	6.38	−7.85
C_15_75_5	−5.51	−4.85	−6.06	−6.42	6.38	−15.58

Table A12. Longitudinal Tensile Specimens Result—C_20_75—Deviations from the mean value.

Specimen	Fm [%]	Rm [%]	Fp [%]	Rp [%]	E [%]	ε [%]
C_20_75_1	−1.13	−1.57	−0.91	0.00	0.00	−6.47
C_20_75_2	−3.40	−3.54	−2.84	−2.94	0.00	−2.28
C_20_75_3	2.30	2.36	1.37	0.00	0.00	−2.88
C_20_75_4	4.20	4.33	1.57	2.94	0.00	17.51
C_20_75_5	−1.97	−1.57	0.81	0.00	0.00	−5.88

Table A13. Longitudinal Tensile Specimens Result—C_25_75—Deviations from the mean value.

Specimen	Fm [%]	Rm [%]	Fp [%]	Rp [%]	E [%]	ε [%]
C_25_75_1	−1.49	−1.96	−1.39	−1.16	0.00	−2.71
C_25_75_2	0.40	0.00	1.09	1.74	0.00	−0.25
C_25_75_3	−0.25	0.00	−0.49	−1.16	0.00	−1.48
C_25_75_4	−2.51	−1.96	−1.80	−1.16	0.00	−3.33
C_25_75_5	3.85	3.92	2.60	1.74	0.00	7.76

Table A14. Longitudinal Tensile Specimens Result—C_15_25—Deviations from the mean value.

Specimen	Fm [%]	Rm [%]	Fp [%]	Rp [%]	E [%]	ε [%]
C_15_25_1	1.59	2.44	3.31	3.23	7.14	−5.62
C_15_25_2	5.33	4.88	3.15	3.23	7.14	2.96
C_15_25_3	0.63	0.00	−2.71	−3.23	−4.76	9.20
C_15_25_4	−6.91	−7.32	−0.65	0.00	−4.76	−7.96
C_15_25_5	−0.64	0.00	−3.10	−3.23	−4.76	1.40

Table A15. Longitudinal Tensile Specimens Result—C_20_25—Deviations from the mean value.

Specimen	Fm [%]	Rm [%]	Fp [%]	Rp [%]	E [%]	ε [%]
C_20_25_1	−4.39	−5.61	−2.43	−1.36	−7.89	3.49
C_20_25_2	−3.50	−3.06	1.12	2.04	5.26	−15.91
C_20_25_3	1.70	2.04	−0.93	−1.36	5.26	2.85
C_20_25_4	4.25	4.59	0.25	−1.36	5.26	10.61
C_20_25_5	1.94	2.04	1.99	2.04	−7.89	−1.03

Table A16. Longitudinal Tensile Specimens Result—C_25_25—Deviations from the mean value.

Specimen	Fm [%]	Rm [%]	Fp [%]	Rp [%]	E [%]	ε [%]
C_25_25_1	−4.59	−3.85	−1.16	0.00	0.00	9.87
C_25_25_2	−3.62	−3.85	−3.42	−3.45	0.00	−10.29
C_25_25_3	5.39	4.40	1.18	0.00	0.00	3.62
C_25_25_4	−3.81	−3.85	−0.11	0.00	0.00	−7.51
C_25_25_5	6.62	7.14	3.52	3.45	0.00	4.31

Appendix C

Table A17. Design of Experiments—Independent variable values.

Run Order	Infill [%]	Layer Thickness [mm]
1	75	0.25
2	100	0.15
3	100	0.15
4	75	0.15
5	100	0.2

Table A17. Cont.

Run Order	Infill [%]	Layer Thickness [mm]
6	100	0.2
7	75	0.15
8	75	0.2
9	25	0.25
10	100	0.2
11	25	0.15
12	75	0.2
13	25	0.15
14	25	0.2
15	75	0.15
16	75	0.2
17	100	0.25
18	100	0.25
19	25	0.15
20	100	0.25
21	75	0.25
22	100	0.15
23	75	0.25
24	25	0.25
25	25	0.25
26	25	0.25
27	75	0.2
28	100	0.25
29	25	0.2
30	25	0.15
31	25	0.2
32	75	0.2
33	100	0.25
34	100	0.15
35	100	0.15
36	75	0.25
37	25	0.15
38	75	0.15
39	100	0.2
40	25	0.25
41	25	0.2
42	100	0.2
43	75	0.25
44	75	0.15
45	75	0.25

References

- García, E.; Núñez, P.; Caminero, M.; Chacón, J.; Kamarthi, S. Effects of carbon fibre reinforcement on the geometric properties of PETG-based filament using FFF additive manufacturing. *Compos. Part B Eng.* **2022**, *235*, 109766. [[CrossRef](#)]
- Spoerk, M.; Savandaiah, C.; Arbeiter, F.; Traxler, G.; Cardon, L.; Holzer, C.; Sapkota, J. Anisotropic properties of oriented short carbon fibre filled polypropylene parts fabricated by extrusion-based additive manufacturing. *Compos. A Appl. Sci. Manuf.* **2018**, *113*, 95–104. [[CrossRef](#)]
- Wang, P.; Zou, B.; Ding, S.; Hunag, C.; Shi, Z.; Ma, Y.; Yao, P. Preparation of short CF/GF reinforced PEEK composite filaments and their comprehensive properties evaluation for FDM-3D printing. *Compos. Part B* **2020**, *198*, 108175. [[CrossRef](#)]
- Blaj, M.; Oancea, G. Fused deposition modelling process: A literature review. *IOP Conf. Ser. Mater. Sci. Eng.* **2021**, *1009*, 012006. [[CrossRef](#)]
- Bembenek, M.; Kowalski, L.; Kosoń-Schab, A. Research on the Influence of Processing Parameters on the Specific Tensile Strength of FDM Additive Manufactured PET-G and PLA Materials. *Polymers* **2022**, *14*, 2446. [[CrossRef](#)]
- Soleyman, E.; Rahmatabadi, D.; Soltan Mohammadi, K.; Aberoumand, M.; Ghasemi, I.; Abrinia, K.; Baniassadi, M.; Wang, K.; Baghani, M. Shape memory performance of PETG 4D printed parts under compression in cold, warm, and hot programming. *Smart Mater. Struct.* **2022**, *31*, 85002. [[CrossRef](#)]

7. Muhamedagic, K.; Berus, L.; Potočnik, D.; Cekic, A.; Begic-Hajdarevic, D.; Cohodar Husic, M.; Ficko, M. Effect of Process Parameters on Tensile Strength of FDM Printed Carbon Fiber Reinforced Polyamide Parts. *Appl. Sci.* **2022**, *12*, 6028. [CrossRef]
8. Krajangsawadi, N.; Blok, L.G.; Hamerton, I.; Longana, M.L.; Woods, B.K.S.; Ivanov, D.S. Fused deposition modelling of fibre reinforced polymer composites: A parametric review. *J. Compos. Sci.* **2021**, *5*, 29. [CrossRef]
9. R, M.K.H.; Benal, M.G.M.; G.S., P.K.; Tambrallimath, V.; H.R., G.; Khan, T.M.Y.; Rajhi, A.A.; Baig, M.A.A. Influence of Short Glass Fibre Reinforcement on Mechanical Properties of 3D Printed ABS-Based Polymer Composites. *Polymers* **2022**, *14*, 1182.
10. Rahimizadeh, A.; Kalman, J.; Fayazbakhsh, K.; Lessard, L. Recycling of fiberglass wind turbine into reinforced filaments for use in Additive Manufacturing. *Compos. Part B Eng.* **2019**, *175*, 107101. [CrossRef]
11. Kalman, J.; Fayazbakhsh, K.; Rahimizadeh, A.; Lessard, L. Mechanical and thermal study of 3D printing composite filaments from wind turbine waste. *Polym. Compos.* **2021**, *42*, 2305–2316.
12. Vedrtnam, A.; Ghabezi, P.; Gunwant, D.; Jiang, Y.; Sam-Daliri, O.; Harrison, N.; Goggins, J.; Finnegan, W. Mechanical performance of 3D-printed continuous fibre Onyx composites for drone applications: An experimental and numerical analysis. *Compos. Part C* **2023**, *12*, 100418. [CrossRef]
13. Hou, Y.; Panesar, A. Effect of Manufacture-Induced Interfaces on the Tensile Properties of 3D Printed Polyamide and Short Carbon Fibre-Reinforced Polyamide Composites. *Polymers* **2023**, *15*, 773. [CrossRef]
14. Mollah, M.T.; Comminal, R.; Serdeczny, M.P.; Šeta, B.; Spangenberg, J. Computational analysis of yield stress buildup and stability of deposited layers in material extrusion additive manufacturing. *Addit. Manuf.* **2023**, *71*, 4–11.
15. Rahmatabadi, D.; Soltanmohammadi, K.; Aberoumand, M.; Soleyman, E.; Ghasemi, I.; Baniassadi, M.; Abrinia, K.; Bodaghi, M.; Baghani, M. Development of Pure Poly Vinyl Chloride (PVC) with Excellent 3D Printability and Macro- and Micro-Structural Properties. *Macromol. Mater. Eng.* **2022**, *308*, 2200568. [CrossRef]
16. Blaj, M.I.; Zaharia, S.M.; Pop, M.A.; Oancea, G. Tensile Properties and Manufacturing Defectives of Short Carbon Fiber Specimens Made with the FDM Process. *Mater. Plast.* **2022**, *59*, 33–43. [CrossRef]
17. Jiang, D.; Smith, D. Anisotropic mechanical properties of oriented carbon fiber filled polymer composites produced with fused filament fabrication. *Addit. Manuf.* **2017**, *18*, 84–94. [CrossRef]
18. Ritter, T.; McNiffe, E.; Higgins, T.; Sam-Daliri, O.; Flanagan, T.; Walls, M.; Ghabezi, P.; Finnegan, W.; Mitchel, S.; Harrison, N.M. Design and Modification of a Material Extrusion 3D Printer to Manufacture Functional Gradient PEEK Components. *Polymers* **2023**, *15*, 3825. [CrossRef]
19. Cao, M.; Cui, T.; Yue, Y.; Li, C.; Guo, X.; Jia, X.; Wang, B. Investigation of Carbon Fiber on the Tensile Property of FDM-Produced PLA Specimen. *Polymers* **2022**, *14*, 5230. [CrossRef]
20. Mishra, D.; Das, A.K. Linear model analysis of fused deposition modeling process parameters for obtaining the maximum tensile strength in acrylonitrile butadiene styrene (ABS) and carbon fiber polylactic acid (PLA) materials. *Multidiscip. Model. Mater. Struct.* **2021**, *17*, 915–930. [CrossRef]
21. Patterson, A.E.; Hasanov, S.; Vajipeyajula, B. Influence of Matrix Material on Impact Properties of Chopped Carbon Fiber-Thermoplastic Composites made using FDM/FFF. In Proceedings of the 2022 International Additive Manufacturing Conference, Lisbon, Portugal, 19–20 October 2022; pp. 1–8. [CrossRef]
22. Omar, N.W.Y.; Shuaib, N.A.; Hadi, M.H.J.A.; Azmi, A.I.; Misbah, M.N. Mechanical and Physical Properties of Recycled-Carbon-Fiber-Reinforced Polylactide Fused Deposition Modelling Filament. *Materials* **2022**, *15*, 190. [CrossRef]
23. Saschit, T.S.; Mukul Ramnirajan Saini, D. Vinaykumar, Effect of Printing Parameters on Tensile Strength of 3D Printed PLA + Carbon Fiber Samples—A Taguchi Approach. In *Recent Developments in Mechanical Design*; Springer: Singapore, 2022; pp. 1–3. [CrossRef]
24. Abeykoon, C.; Abeykoon, C.; Fernando, A. Optimization of fused deposition modeling parameters for improved PLA and ABS 3D printed structures. *Int. J. Light. Mater. Manuf.* **2020**, *3*, 284–297. [CrossRef]
25. Unterweger, C.; Mayrhofer, T.; Piana, F.; Duchoslav, J.; Stifter, D.; Poitzsch, C.; Fürst, C. Impact of fiber length and fiber content on the mechanical properties and electrical conductivity of short carbon fiber reinforced polypropylene composites. *Compos. Sci. Technol.* **2020**, *188*, 107998. [CrossRef]
26. Katalagianakis, A.; Van de Voorde, B.; Pien, N.; Polyzos, E.; Duretek, I.; Holzer, C.; Cardon, L.; Bernaerts, K.V.; Van Hemelrijck, D.; Van Vlierberghe, S.; et al. The Effect of Carbon Fiber Content on Physico-Mechanical Properties of Recycled PolyEthylene Terephthalate) Composites Additively Manufactured with Fused Filament Fabrication. *Addit. Manuf.* **2022**, *60*, 103246.
27. Ultrafuse Filaments. Available online: <https://forward-am.com/material-portfolio/ultrafuse-filaments-for-fused-filaments-fabrication-fff/reinforced-filaments/ultrafuse-pet-cf15/> (accessed on 10 April 2023).
28. ASTM International. Standard Test Method for Tensile Properties of Plastics (Metric). Available online: <https://www.astm.org/d0638-14.html> (accessed on 25 January 2024).
29. BCN3D Technologies. Available online: <https://www.bcn3d.com/bcn3d-epsilon/?model=w50> (accessed on 17 April 2023).
30. Tuttle, M.E. *Structural Analysis of Polymeric Composite Materials*, 2nd ed.; CRC Press: Boca Raton, FL, USA, 2012.
31. Mohan, S.R.; Simhambhatla, S. Fabrication of gradient density componenets through extrusion—Based additive manufacturing. In *Advances in Additive Manufacturing and Joining Proceedings of AIMTDR 2018*; Springer: Singapore, 2019; pp. 181–182.

32. Belei, C.; Joeressen, J.; Amancio-Filho, S.T. Fused-Filament Fabrication of Short Carbon Fiber-Reinforced Polyamide: Parameter Optimization for Improved Performance under Uniaxial Tensile Loading. *Polymers* **2022**, *14*, 1292. [[CrossRef](#)]
33. Algarni, M.; Ghazali, S. Comparative study of the sensitivity of PLA, ABS, PEEK, and PETG's mechanical properties to FDM printing process parameters. *Crystals* **2021**, *11*, 995. [[CrossRef](#)]

Disclaimer/Publisher's Note: The statements, opinions and data contained in all publications are solely those of the individual author(s) and contributor(s) and not of MDPI and/or the editor(s). MDPI and/or the editor(s) disclaim responsibility for any injury to people or property resulting from any ideas, methods, instructions or products referred to in the content.

Article

Material Extrusion Additive Manufacturing of the Composite UAV Used for Search-and-Rescue Missions

Sebastian-Marian Zaharia ^{1,*}, Ionut Stelian Pascariu ¹, Lucia-Antoneta Chicos ¹, George Razvan Buican ¹, Mihai Alin Pop ², Camil Lancea ¹ and Valentin Marian Stamate ¹

¹ Department of Manufacturing Engineering, Transilvania University of Brasov, 500036 Brasov, Romania; ionut.pascariu@student.unitbv.ro (I.S.P.); l.chicos@unitbv.ro (L.-A.C.); buican.george@unitbv.ro (G.R.B.); camil@unitbv.ro (C.L.); valentin_s@unitbv.ro (V.M.S.)

² Department of Materials Science, Transilvania University of Brasov, 500036 Brasov, Romania; mihai.pop@unitbv.ro

* Correspondence: zaharia_sebastian@unitbv.ro

Abstract: The additive processes used in the manufacture of components for unmanned aerial vehicles (UAVs), from composite filaments, have an important advantage compared to classical technologies. This study focused on three-dimensional design, preliminary aerodynamic analysis, fabrication and assembly of thermoplastic extruded composite components, flight testing and search-and-rescue performance of an UAV. The UAV model was designed to have the highest possible structural strength (the fuselage has a structure with stiffening frames and the wing is a tri-spar), but also taking into account the limitations of the thermoplastic extrusion process. From the preliminary aerodynamic analysis of the UAV model, it was found that the maximum lift coefficient of 1.2 and the maximum drag coefficient of 0.06 were obtained at the angle of attack of 12°. After conducting flight tests, it can be stated that the UAV model, with components manufactured by the thermoplastic extrusion process, presented high stability and maneuverability, a wide range of speeds and good aerodynamic characteristics. The lack of this type of aircraft, equipped with electric motors, a traffic management system, and a thermal module designed for search-and-rescue missions, within the additive manufacturing UAV market, validates the uniqueness of the innovation of the UAV model presented in the current paper.

Keywords: UAV; additive manufacturing; composite structures; search-and-rescue missions



Citation: Zaharia, S.-M.; Pascariu, I.S.; Chicos, L.-A.; Buican, G.R.; Pop, M.A.; Lancea, C.; Stamate, V.M. Material Extrusion Additive Manufacturing of the Composite UAV Used for Search-and-Rescue Missions. *Drones* **2023**, *7*, 602. <https://doi.org/10.3390/drones7100602>

Academic Editor: Abdessattar Abdelkefi

Received: 13 July 2023

Revised: 20 September 2023

Accepted: 22 September 2023

Published: 25 September 2023



Copyright: © 2023 by the authors. Licensee MDPI, Basel, Switzerland. This article is an open access article distributed under the terms and conditions of the Creative Commons Attribution (CC BY) license (<https://creativecommons.org/licenses/by/4.0/>).

1. Introduction

Unmanned aerial vehicles (UAVs) or so-called aerial drones have experienced a rapid development in recent years, having applications in various industrial fields. The military domain [1–3] has undergone a significant transformation, particularly through the implementation of UAVs in modern warfare strategies, as they can be operated remotely and used for surveillance, reconnaissance, and precise targeting with high accuracy. Currently, UAVs are employed to provide remote medical assistance, offering a new way to deliver supplies and medical services to those in need in remote areas such as rural villages and isolated islands, where traditional delivery methods are not feasible [4–6]. Agricultural drones [7,8] can be used to monitor the condition of crops and animals on farms, map agricultural lands, as well as gather crucial information (crop health, maturity level, moisture level) and perform agricultural tasks like phytosanitary treatments and fertilizer application. Monitoring wildlife using UAV systems provides the opportunity to explore and observe previously inaccessible areas considered challenging or even impossible to reach. UAVs are successfully utilized to observe and document animal behavior, monitor animal migrations, and control poaching activities [9–11]. UAVs equipped with advanced sensors and thermal cameras can be used for [12,13]: scanning large areas in search and rescue operations, monitoring hazardous terrains, investigating disasters, and locating individuals in need

of assistance. Recent uses of UAVs, using thermal vision systems, include the inspection and maintenance of infrastructure such as bridges, tunnels, and wind turbines [14–16]. The delivery process by means of UAVs is implemented in various industries, including the distribution of medical materials (equipment and medicine) and food delivery [17–20].

UAVs designers and manufacturers, when choosing the components materials, consider several factors aimed at functional, aerodynamic, and structural requirements as well as minimizing production and maintenance costs [21,22]. Today, the aerospace research is focused on expanding the use of composite materials in the manufacture of UAVs. Composite materials provide an ideal balance between aircraft weight and aerodynamic strength, fatigue, and corrosion resistance, while reducing maintenance costs [23–26].

To offer a more comprehensive overview of the current research status in this field, five UAV models were studied that shared similar dimensional characteristics and flight performances with the one developed in this study (Table 1).

As a result of this comparative study, the following conclusions were drawn: positioning the wing on the upper section of the fuselage, with a wingspan of 3.4 m, offers numerous advantages (such as easier maintenance, greater stability, a higher lift-to-drag ratio, and improved capacity for gliding over long distances, as well as shorter landing distances); the use of two brushless electric motors, manufactured through metal additive manufacturing, capable of generating a minimum of 11 kg of thrust; implementing a T-tail configuration, with the horizontal tail positioned at 80% of the height of vertical tail, based on considerations including removing the horizontal tail from the wake of the wing, improving structural integrity by connecting the horizontal tail to the vertical tail and fuselage, achieving high stability, and reducing drag; utilizing a tricycle landing gear, which is the most commonly used landing gear configuration, especially for gliders and motor gliders; incorporating a thermal module, allowing the UAV model to perform multiple missions, including search and rescue, surveillance, reconnaissance, and wildlife monitoring. These conclusions represent an initial step in the design, manufacturing, and testing of the UAV model and will serve as input data for the design phases of this study.

Table 1. Design parameters and flight performances of UAV with fixed-wing.

UAV Type	Design Parameters		Performances Data	
Optimum Solutions Condor 300 [27] 	MTOW [kg]	18	Cruise Speed [km/h]	90
	Span [m]	3.2	Range [km]	Long range
	Wing Area [m ²]	N/A	Endurance [hours]	4
	Type of wing	Low wing	Cruise altitude [m]	3000
	Tail	T-Tail	Payload [kg]	6
	Motor type	Twin electric motor mounted on the wings	Mission	Search and Rescue of Missing Persons
	Power [W]	N/A	Takeoff Requirements	Autonomous take-off and landing
	Battery [mAh]	N/A	Takeoff Distance [m]	40
Albatross UAV [28] 	MTOW [kg]	10	Cruise Speed [km/h]	68
	Span [m]	3	Range [km]	280
	Wing Area [m ²]	0.683	Endurance [hours]	4
	Type of wing	High wing	Cruise altitude [m]	Medium
	Tail	Inverted v-tail	Payload [kg]	4.4
	Motor type	Electric	Mission	Surveillance, search and rescue, reconnaissance
	Power [W]	N/A	Takeoff Requirements	Entirely autonomous from takeoff
	Battery [mAh]	N/A	Takeoff Distance [m]	50–100

Table 1. Cont.

UAV Type	Design Parameters		Performances Data	
Silent Falcon UAS [29] 	MTOW [kg]	14.5	Cruise Speed [km/h]	90
	Span [m]	4.4	Range [km]	15
	Wing Area [m ²]	N/A	Endurance [hours]	5
	Type of wing	High wing	Cruise altitude [m]	6000
	Tail	Conventional cruciform	Payload [kg]	3
	Motor type	1.3-hp electric motor	Mission	Search and rescue, wildlife monitoring, agricultural survey
	Power [W]	N/A	Takeoff Requirements	N/A
	Battery [mAh]	N/A	Takeoff Distance [m]	N/A
Vector VTOL fixed wing UAS [30] 	MTOW [kg]	7.4	Cruise Speed [km/h]	70
	Span [m]	2.8	Range [km]	25
	Wing Area [m ²]	N/A	Endurance [hours]	2
	Type of wing	High wing	Cruise altitude [m]	N/A
	Tail	T tail	Payload [kg]	0.4
	Motor type	N/A	Mission	Search and rescue, convoy protection, border patrol, traffic investigation
	Power [W]	N/A	Takeoff Requirements	Vertical takeoff
	Battery [mAh]	N/A	Takeoff Distance [m]	N/A
Penguin BE UAV [31] 	MTOW [kg]	21.5	Cruise Speed [km/h]	79.2
	Span [m]	3.3	Range [km]	180
	Wing Area [m ²]	0.79	Endurance [hours]	2
	Type of wing	High wing	Cruise altitude [m]	6000
	Tail	V-tail splits in two parts	Payload [kg]	6.6
	Motor type	Gas/Electric engine	Mission	N/A
	Power [W]	2700	Takeoff Requirements	Runway, catapult or car-launched
	Battery [mAh]	N/A	Takeoff Distance [m]	30

A modern process for manufacturing components and prototypes of UAVs is the additive process of thermoplastic material extrusion (filament). The additive manufacturing process by materials extrusion provides the following advantages: low price of equipment and materials used, wide range of materials, high manufacturing speed, freedom and creativity on the design of the part, user-friendly interface [32,33]. The additive thermoplastic material extrusion process has two similar terms in the specialized literature [34–36]: FFF (Fused Filament Fabrication) and FDM™ (Fused Deposition Modeling) which describes the same type of additive 3D printing process in which material (filament, fused material) is selectively extruded through a nozzle or orifice.

However, components manufactured by additive material extrusion processes show lower mechanical properties, compared to classic composite materials. This inconvenience comes from the limited properties of the matrices, but also because of the low adhesion between the layers of extruded material. These defects cause a decrease in the strength and elongation of the 3D-printed parts [37,38]. The evolution of 3D-printing systems, by controlling the temperature of the working area, has led to the use of high-performance thermoplastic materials such as [39–41]: Polyether Ether Ketone (PEEK), Polyetherimide (PEI), and composite materials (reinforced with carbon and glass fiber).

Additive manufacturing processes by material extrusion have begun to be used for the realization of UAV prototypes that are tested in flight [42,43]. Starting from three-dimensional digital models to flying UAV prototypes, this process is completed in a few days with minimal designer intervention. Another direction of study is represented by the additive manufacturing by material extrusion of drones [44], starting from the testing stages

of lightweight cellular structures [45] or by using topological optimization techniques for the resistance structure [46].

For the UAV models, produced by material extrusion, the aerodynamic performances were determined by testing in the wind tunnel [47–49]. The manufacturing of morphing wing models [50–53] lends itself very well to the additive manufacturing process by material extrusion, since the components are manufactured in the shortest time and at low costs. Currently, the use of composite filaments, with short [54–56] or continuous fibers [57,58], employed in the 3D-printing process represents an intensively researched field with applications in aerospace. Recent studies have highlighted that by adding short carbon fibers to a PAHT (High-Temperature Polyamide) matrix [59–61] or short glass fibers to a PLA (Polylactic acid) matrix [62–64], the mechanical performance of manufactured parts exhibited a significant increase in various tests (compression, impact, traction, flexural). While various types of UAVs have been manufactured from standard materials (PLA, ABS, PETG) until now, this study extended research to two types of materials reinforced with short carbon and glass fibers, with the goal of enhancing the mechanical performance of UAV model components. Moreover, through the use of these two types of short fiber-reinforced materials, the UAV model will exhibit strong structural strength, leading to higher flight safety.

In this paper, the ability of the additive material extrusion processes of filament reinforced with short carbon and glass fiber to obtain an unmanned aerial vehicle was demonstrated. After completing the stages of design, preliminary aerodynamic analysis, 3D printing, and assembly of the UAV model, the flight tests were performed and the search-and-rescue mission was accomplished using a thermal camera module.

2. Design of UAV Model

2.1. Preliminary Design

For the preliminary design of the composite UAV, four important parameters must be established [65,66]: maximum takeoff weight (M_{UAV}), minimum wing area (S_{min}), motor thrust (T), and autopilot preliminary calculations. In the design process of the UAV model, special attention was paid both to the parameters that must be minimized (M_{UAV}) and the performances that must be maximized within the constraints (autonomy, flight ceiling, aerodynamic performance). In the first stage of designing the UAV model, the basic configuration for the four important structural components (wing, fuselage, wings, and control surfaces) was established.

Throughout the design and physical realization processes of the UAV model, several steps were followed, as presented in Figure 1 [67]. These stages commence with the requirements stage and mission profile establishment, progressing through conceptual design, preliminary design, and detailed design. The UAV prototype was developed to facilitate additive manufacturing of components, followed by testing and flight mission completion. The design and physical realization of the UAV model is a creative and iterative process that combines technical knowledge, experience, and problem-solving skills to develop the UAV solution to answer real-world problems. The seven stages of UAV model development are detailed below.

1. Following the design process depicted in Figure 1, the starting point for the UAV model is to comprehend its purpose and flight mission to determine the appropriate design requirements for the aircraft. Since this study involved design and physical creation of a fixed-wing, twin-engine aircraft for search-and-rescue missions utilizing a thermal module controlled by a ground control station, both flight mission planning and design requirements had to be individually satisfied and concurrently addressed [67]. The UAV model is intended for use in mountainous areas to locate pilots and passengers after aviation accidents, wildlife tracking, and detecting illegal hunting. The selection of these missions for the UAV model was not arbitrary; it was based on studies that highlight significant deficiencies in finding economically and technically efficient solutions for aviation accident response and anti-poaching efforts in mountainous regions.

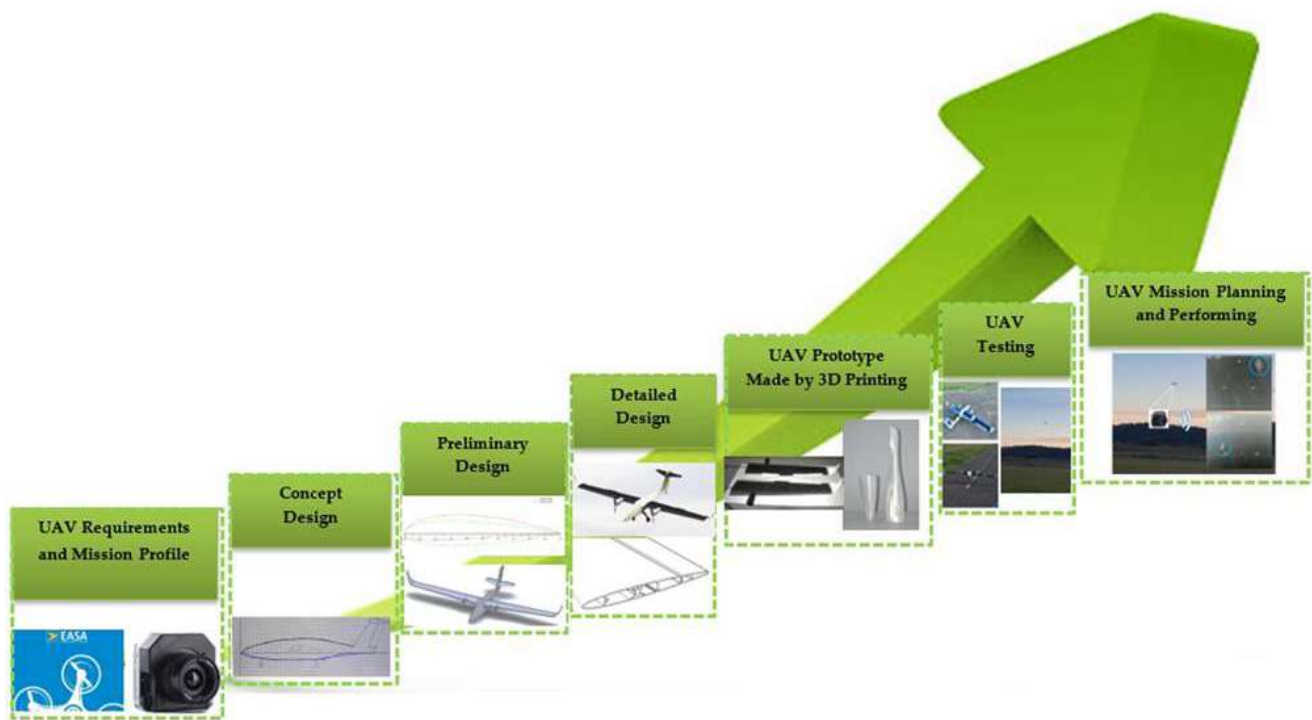


Figure 1. The engineering design process of the UAV model.

2. The conceptual design stage of the UAV model involves analyzing current concepts and designs based on the defined design requirements to visualize the desired UAV configuration. This initial design investigation is crucial, since the entire design phase, up to detailed design, relies on this preliminary analysis [68] and the proposed concept. During this stage, the project team engages in brainstorming sessions that result in a predimensioned sketch of the UAV model. These sessions evaluate the advantages and disadvantages of each proposed idea, taking into consideration specifications, flight mission, manufacturing costs, and the fabrication process [69].
3. In the preliminary design stage, the initial UAV model will be expanded and developed in much greater detail. Optimization compromises within the project will be made to maximize the performances of the aircraft for its intended operational roles and flight mission. In this stage, decisions will be made about which UAV components will be fabricated in-house and which ones will be purchased, involving a cost-benefit analysis. Utilizing specific Computer Aided Design (CAD) software systems, the preliminary UAV model was designed based on the previously established basic dimensions. Additionally, in this stage, estimates of the masses of the main components will be made from the CAD model of the aircraft, along with establishing aerodynamic profiles (for the wing and empennage) and obtaining initial results regarding the aerodynamic performance of the UAV model [70].
4. In the subsequent detailed design stage [71] of the UAV model, computerized methods for design, calculations, simulations (virtual development), and detailed aerodynamic analyses (wing analysis, aircraft analysis) were employed. Furthermore, full characterization (mechanical and thermal) of the two types of materials used in 3D printing the UAV model [72,73] was performed in this stage. The detailed design for the additive manufacturing of the UAV components was also included, considering the 3D printing volume of the equipment used and the method of support structure application and removal for certain parts. In this stage, aspects of performance (autonomy, flight speed, ceiling) of the UAV model were obtained as the components to be used on the aircraft (electric motors, ESC, battery) were determined.
5. During the 3D printing phase of the UAV prototype, detailed CAD models and manufacturing parameters from the previous stage were used to produce segments of

all UAV model components. An important aspect of this phase was testing the mechanical performance of the wing [74], fuselage [73], and landing gear [75]. Following mechanical testing, the wing and fuselage proved capable of withstanding flight loads; however, a solution in the form of CFRP material was chosen for the landing gear to ensure safer takeoff and landing. Also at this stage, detailed tests were carried out on the motors manufactured through the SLS (Selective Laser Sintering) process [76] to determine their performance. This stage concludes with the simultaneous assembly of aircraft components and electronic elements, resulting in the final physical UAV model.

6. Within the testing stage, initial ground tests of the UAV model were conducted, monitoring the correct functioning of controls, motors, and electronic systems (thermal module and ground control station). Ground rolling tests of the UAV model were also conducted during this testing stage. Following these preliminary tests, the final stage involved testing the UAV model in flight using the ground control station and thermal module.
7. The final stage in the development of the UAV model included the flight mission, namely search and rescue using the thermal module. At this stage, the proposed UAV model was validated by successfully completing the specified mission outlined during the flight mission profile establishment phase. The fixed-wing UAV model with a medium altitude is capable of performing search and rescue, surveillance missions, and emergency interventions, serving as a versatile and efficient solution with reduced operating costs. Moreover, the UAV model offers an approximate flight time of 50 min and can cover large search areas rapidly (around 100 km) by thermal imaging capture. Another important aspect of the UAV model is its real-time video transmission capability, providing rescue teams with a clear and detailed view of the operational area, enabling rapid decision-making and a timely response.

2.2. UAV Model Wing Design

The first two design characteristics established for the UAV model were the following: maximum weight of about 11 kg and median positioning of the wings on the fuselage. The minimum wing area (S_{\min}) for the UAV model [42] was calculated using Equation (1) with the following parameters: maximum takeoff weight of the UAV model ($M_{UAV} = 11$ kg), gravitational acceleration ($g = 9.81$ m/s²), air density at sea level ($\rho = 1.225$ kg/m³), maximum lift coefficient ($C_{L\max} = 1.2$), and minimum airspeed of the UAV ($V_{\min} = 13$ m/s).

$$S_{\min} = \frac{2 \cdot M_{UAV} \cdot g}{\delta \cdot C_{L\max} \cdot (V_{\min})^2}, \quad (1)$$

The minimum wing area of the UAV model has been calculated to be 0.868 m². To initiate the wing design process of the UAV model, the minimum wing area required for the aircraft's flight was established. The calculated minimum wing area using Equation (1) was 0.868 m², which is smaller than the wing area of the UAV model (0.897 m²).

Starting from the minimum surface determined with Equation (1), the UAV model will have a wingspan (b) of 3400 mm and the wing will be positioned in the upper part of the fuselage, which determines good stability and reduces the possibility of the wing touching the ground. To determine the dimensions of the UAV wings, a new constraint is necessary. Tapering the wing provides significant aerodynamic advantages (reducing drag force and increasing lift distribution) as well as structural benefits (weight savings for the wing). In the case of UAVs, this taper ratio typically has a value of 0.5 [77,78], a value obtained from data of UAVs with similar configurations and missions. However, for the UAV model analyzed in this paper, a higher value ($\lambda = 0.57$) was chosen because a winglet will be mounted at the tip of wing. This taper ratio is necessary, as the wing-tip chord needs to provide a larger surface area to facilitate the winglet connection and achieve a higher

strength. The root chord of the UAV model was calculated using Equation (2) [77,78], while the tip chord was determined using Equation (3) [77,78].

$$C_r = \frac{2 \cdot S}{b \cdot (\lambda + 1)}, \quad (2)$$

$$C_t = 0.57 \cdot C_r, \quad (3)$$

The mean aerodynamic chord (MAC) of the UAV model was computed using Equation (4) [77,78].

$$MAC = \frac{2}{3} \cdot C_r \cdot \frac{1 + \lambda + \lambda^2}{1 + \lambda}, \quad (4)$$

The aspect ratio [77,78] of the UAV model represents the ratio between the squared wingspan and the wing area (Equation (5)).

$$AR = \frac{b^2}{S}, \quad (5)$$

Another important parameter of the UAV model is the wing loading (WL), which was determined using Equation (6) [77,78].

$$WL = \frac{M_{UAV}}{S}, \quad (6)$$

The wing area ($S = 0.897 \text{ m}^2$) and wing loading ($WL = 120 \text{ N/m}^2$) are currently the most significant constraints for wing sizing and design. The wing used for the aircraft was trapezoidal with a NACA 4415 airfoil. Other basic dimensions of the UAV model were: root chord (C_r) 335 mm and tip chord (C_t) 200 mm (calculated with Equations (2) and (3)). The design of the wings started by using the same airfoil (NACA 4415) at the root and tip of wing. The NACA 4415 airfoil has a relative thickness of 15% and an optimum value for obtaining a maximum lift coefficient. The design of the UAV model was made in the SolidWorks 2021 software system (Dassault Systèmes SolidWorks Corporation, Waltham, MA, USA).

The two electric motors nacelles were also attached to the wing structure. The structural stiffening of the wing has been carried out using a carbon fiber tubular spar (Figure 2a). The internal configuration of the wing shows a three-spar structure (Figure 2b), as follows: a C-shaped spar at the leading edge of the wing, a X truss type spar that is intended to take the stresses from the central part of the wing and offer a mounting platform the carbon fiber tubular spar. The C-shaped spar is required to take the stresses from the wing trailing edge area and has built in cylindrical surfaces, through which the carbon rods needed to facilitate the guidance of the 3D printed wing sections will be inserted. The position of the wing spars is in accordance with aeronautical structure practice: the first C-shaped spar is positioned between 17 and 25% of the chord, the second X truss type spar is placed between 30 and 45% of the chord, and the third C-shaped spar is placed between 60 and 75% of the chord. Other dimensions of the UAV model wing were the following: the thickness of the wing skin was 1 mm; the thickness of the three spars was 0.8 mm; the diameter of the tubular spar was 16 mm.

Also, in order to reduce the mass of the UAV model and facilitate manufacturing, it was chosen to place the resistance ribs on the bonding surfaces between the 3D-printed wing sections, by adding 3 mm borders. The support for the electric motors has been designed on the wing for a higher resistance, because this area is of vital importance in the operation of the UAV model. To control the roll axis, the wing was equipped with ailerons (Figure 3a), which has a resistance structure consisting of a longitudinal spar with I-profile.

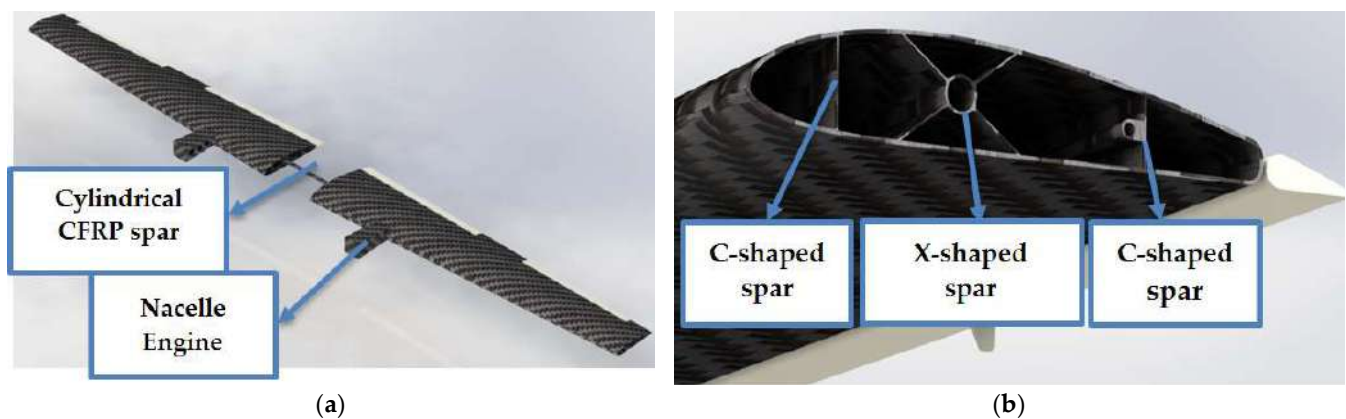


Figure 2. UAV model wing design: (a) wing with tubular spar; (b) the structural components of the wing.

The hyper-sustentation devices used for the UAV model aircraft are the flaps (Figure 3a). The flaps were arranged on the trailing edge of the wing, and by turning them, the lift will be increased during the takeoff and landing stages. The winglet (Figure 3b) reduces the induced drag at the wingtips and increases the lift to drag ratio. By using winglet devices, the power consumption is reduced and the performance of the electric motors used on the UAV model is increased. These engineered components will have a wing-like structure with spars and ribs to facilitate 3D printing without support material and to provide a structure with high stiffness.

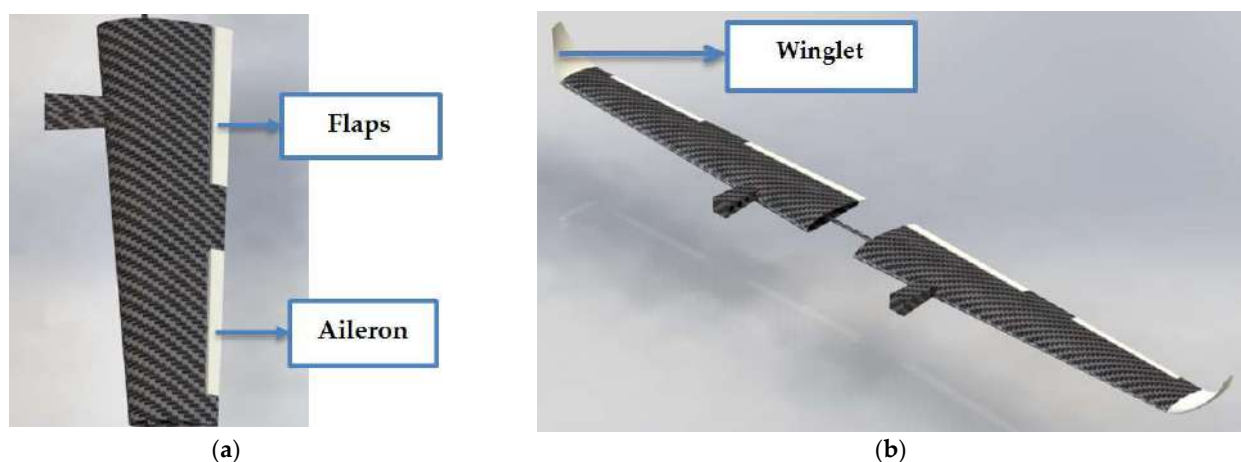


Figure 3. Wing structure: (a) wing equipped with flaps and aileron; (b) wing equipped with winglet.

2.3. UAV Model Fuselage Design

The fuselage of the UAV model (Figure 4a) has an aerodynamic shape and is the component to which the following structures are attached: the wing, the horizontal and vertical empennage, the landing gear, and the thermal vision camera. In order to provide the best resistance to the model, the junction of the wing and the fuselage will be manufactured, as a single part, by thermo-plastic extrusion. The aerodynamic shape of the fuselage ensures the maximum load capacity, at the lowest forward resistance.

To determine the fuselage length of the UAV model, two constraints were employed: it should be between four and six times the mean aerodynamic chord and half of the wingspan. Considering these constraints, the fuselage length (L_f) can be estimated using the UAV wingspan (b), as provided in Equation (7) [78].

$$\frac{L_f}{b} = 0.53, \quad (7)$$

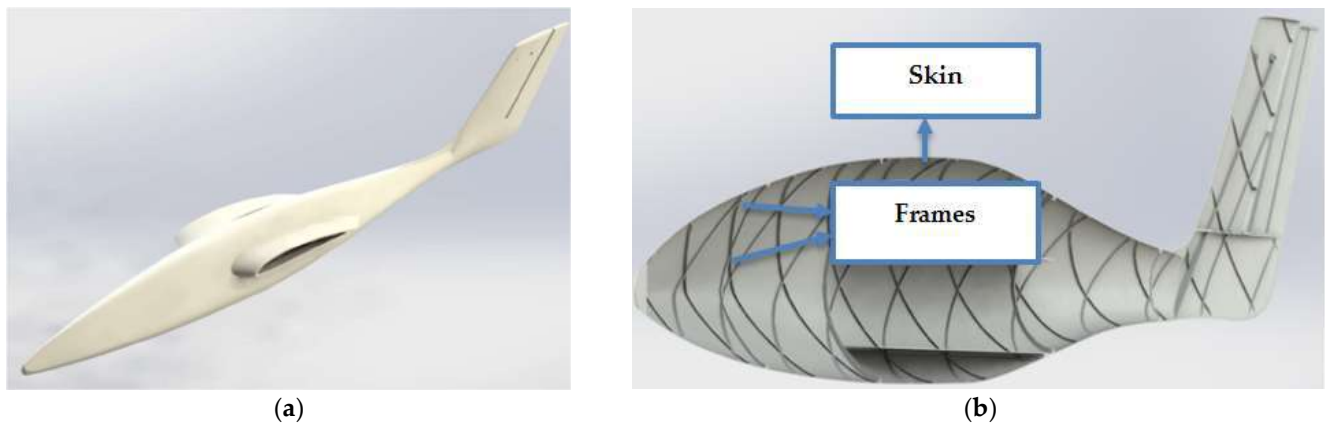


Figure 4. Structure of the fuselage: (a) 3D model of the fuselage and vertical empennage; (b) fuselage strength structure.

In this study, particular value of the fuselage length-to-wingspan ratio was chosen because the vertical tail configuration shares a common area with the fuselage in the tail landing gear section of the UAV model. As a result, the calculated fuselage length using Equation (6) is 1.8 m.

According to statistical data for subsonic aircraft, a practical range for the fineness ratio (Equation (8)) falls between 6 and 8, which is considered optimal [78–80]. However, this can vary based on fuselage design requirements and the placement of electronic equipment and engines. Therefore, in this study, a fineness ratio (λ_f) of 8 was utilized for the design phases. An optimum fineness ratio of the UAV fuselage corresponds to minimal drag force.

$$\lambda_f = \frac{L_f}{D_{mean}}, \quad (8)$$

where L_f is the length of the fuselage (m) and D_{mean} is the mean diameter of the fuselage (m). Consequently, the mean diameter of the UAV model will have a value of 225 mm.

The electronic equipment will be positioned as close as possible to the center of gravity of the UAV model, so that the moments of inertia are as low as possible. The fuselage will have cutouts that will allow access to the electronic components. Also, reinforcement elements will be added to the fuselage structure in the areas where the stresses are more intense (the attachment of the landing gear to the fuselage, the attachment of the thermal chamber to the fuselage).

The fuselage of the UAV model (Figure 4b) is a monocoque type structure, with components of shell and frames type. The frames are positioned in two directions at a 45° angle in order to facilitate a support-free 3D printing. The main dimensions of the fuselage components are the following: thickness skin of fuselage, 1 mm; stringers oriented in two directions at an angle of $\pm 45^\circ$ (X stringers); stringers thickness, 1 mm and stringers height, 4 mm. This constructive solution was chosen to use the interior space of the fuselage as efficiently as possible, and to facilitate its assembly and manufacture.

2.4. Design of Empennages and Landing Gear

In Figure 5a, it can be seen that the fuselage and a part of the vertical empennage were designed together. A classical configuration was selected for both the horizontal and vertical empennage, comprising of a fixed and a movable surface. Thus, the horizontal empennage presents horizontal stabilizer and elevator, and the vertical empennage presents vertical stabilizer and ruder. The horizontal empennage was positioned in the upper section of the rudder, to isolate it from the wing's effects. The airfoil, for both empennages, was NACA 0015. The NACA 0015 profile is a symmetric and thin airfoil used to maintain the

order of magnitude of lift values during elevator or rudder command while also providing minimal drag resistance [70].



Figure 5. Design of the components of the UAV model: (a) horizontal and vertical empennage; (b) fuselage assembly—empennages—tricycle landing gear.

In this stage of the UAV model design process, the tail surfaces (horizontal and vertical) were estimated using empirically found tail volume coefficients [79–81], as presented in Equations (9) and (10) [81,82]. For an aircraft with two engines mounted on the wing, like the UAV model, the horizontal tail moment arm (l_{HT}) was set to 1.25 m, representing the distance between the center of gravity and the aerodynamic center of the horizontal and vertical tail surfaces. Considering a horizontal tail volume ratio (V_{HT}) of 0.5 [81,82] for a UAV-type aircraft, horizontal tail wing area (S_{HT}) can be determined using Equation (9).

$$V_{HT} = \frac{l_{HT} \cdot S_{HT}}{MAC \cdot S'} \quad (9)$$

Therefore, the horizontal tail wing area (S_{HT}), calculated using Equation (9), for the UAV model was 0.098 m². For the UAV model, the vertical tail moment arm (l_{VT}) was 1.1 m, and the vertical tail volume ratio (V_{VT}) was set at 0.2 [82,83].

$$V_{VT} = \frac{l_{VT} \cdot S_{VT}}{b \cdot S}, \quad (10)$$

The vertical tail wing area (S_{VT}), calculated using Equation (10), has a value of 0.055, and the dimensions of the UAV model, computed using Equation (1) to Equation (10), have been presented in Table 2.

Table 2. Characteristics of the UAV model.

Component	Geometric Characteristic	Value
Wing	Wingspan [m]	3.4
	Wing area [m ²]	0.897
	Root chord [m]	0.335
	Tip chord [m]	0.200
	Taper ratio	0.597
	Aspect ratio	12.887
	Mean aerodynamic chord [m]	0.273
Flaps	Chord [m]	0.05
	Span [m]	0.6
Aileron	Chord [m]	0.045
	Span [m]	0.65

Table 2. Cont.

Component	Geometric Characteristic	Value
Winglet	Root chord [m]	0.2
	Tip chord [m]	0.054
	Height [m]	0.18
Fuselage	Length [m]	1.803
	Height [m]	0.228
	Width [m]	0.200
Vertical tail	Span [m]	0.420
	Root chord [m]	0.285
	Tip chord [m]	0.200
Horizontal tail	Span [m]	0.600
	Root chord [m]	0.235
	Tip chord [m]	0.120
Landing gear	Height [m]	0.145
	Wheel Track [m]	0.315

For the manufacture of the empennages, the following strength structures were chosen: the rudder contained ribs positioned at 45° , the rudder included a 60° positioned I-beam spar, the stabilizer featured the wing's structural design (three spars), and the elevator had an I-beam spar. The landing gear of the UAV model aircraft will make it possible to taxi safely on the ground without damaging the aircraft during taxiing, takeoff, and landing. The chosen landing gear configuration for this aircraft is a non-retractable tricycle landing gear, consisting of two side arms and a tail wheel (Figure 5b). The main legs of the landing gear were positioned in the wing's trailing edge area.

2.5. Digital Assembly of the UAV Model

The assembly of the UAV model involved the interconnection of all the essential components (wing, winglet, aileron, flaps, fuselage, landing gear, vertical and horizontal empennage, electric motors, and thermal imaging camera) to showcase the preliminary design. Components assembly was performed using SolidWorks 2021 software system, using the constraints necessary to build the digital model of the UAV. During this stage, the UAV model components were checked for any potential collisions, ensuring a smooth additive manufacturing process without any issues. The assembly process proceeded as follows: it started with the fuselage structure, onto which the left half-wing and right half-wing were subsequently mounted. The left wing and right wing were equipped with ailerons, flaps, winglets, and electric motors. The assembly procedure continued with the positioning of the horizontal and vertical empennages and was finished with the addition of the tricycle landing gear and a thermal imaging camera (Figure 6).

Table 2 summarizes the main characteristics of the UAV model resulting from the preliminary design. It can be seen that the values of the control surfaces (aileron, elevator, and rudder) fall within the range of typical values of airplanes, which are found in various studies in the field [84,85].



Figure 6. Digitally assembled UAV model.

3. Preliminary Aerodynamic Analysis

The XFLR5 software system represents a tool used for the analysis of aerodynamic profiles, wings, and the entire aircraft, aiming to determine the aerodynamic performance in the early stages of the lifecycle of an aeronautical product [86,87]. The modeling of the UAV model was carried out using the geometric characteristics from Table 2. The main stages of the modeling process were as follows: importing the aerodynamic profiles (Figure 7a) NACA 4415 (used for the wing) and NACA 0015 (used for the empennages and winglet), modeling the wing and winglet of the aircraft (Figure 7b), modeling the fuselage and empennages (Figure 7c). The final stage involves the assembly of the UAV model (Figure 7d) by constraining the previously modeled components.

The methodology for calculating the aerodynamic performance of the UAV model, using the XFLR5 software system, is described in Figure 8a. After selecting the aerodynamic profiles, the second step in the aerodynamic analysis of the UAV model was to determine the Reynolds number. The kinematic viscosity (ν) was calculated using the following parameters: altitude of 300 m; temperature of 20 °C, resulting in $\nu = 1.647 \cdot 10^{-5} \text{ m}^2/\text{s}$. Using the kinematic viscosity of $1.647 \cdot 10^{-5} \text{ m}^2/\text{s}$, a velocity of 20 m/s, and an aerodynamic mean chord of 0.273 m, the Reynolds number was calculated to be $Re = 333,966$. The aerodynamic analysis of the UAV model was carried out for a variation of the attack angle within the range of -5° to 12° . Figure 8b shows the variation of the pressure coefficient at an attack angle of 5° .

Figure 8c depicts the variation of the lift coefficient for the entire aircraft as a function of the attack angle. As can be seen, the maximum lift coefficient (C_L) reached a value of 1.2 at an attack angle (Alpha) of 12° . Figure 8d shows that the drag coefficient (C_D) increased with increasing angle of attack (Alpha) and reached a value of 0.06 at an attack angle of 12° .

The variation of aerodynamic coefficients is important for flight tests because the obtained results describe the first aerodynamic performances of the UAV model. To evaluate the aerodynamic performance of the UAV model, the values of the lift coefficient (C_L) and the values of the drag coefficient (C_D) must be known at each angle of attack—in widespread use is the method by which the aerodynamic characteristics are represented in the form of a graph called polar of the airplane.

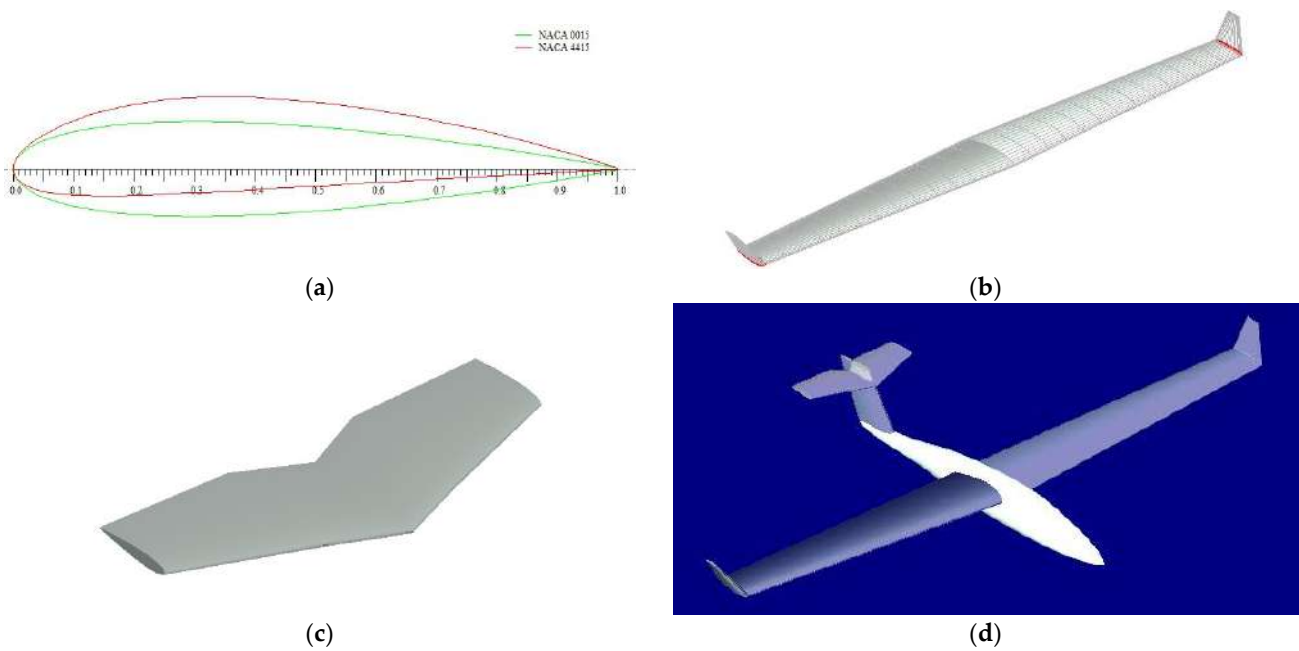


Figure 7. Modeling of the UAV model: (a) aerodynamic profiles used; (b) modeling the wing equipped with a winglet; (c) modeling the horizontal empennage; (d) UAV model made in XFLR5 software system.

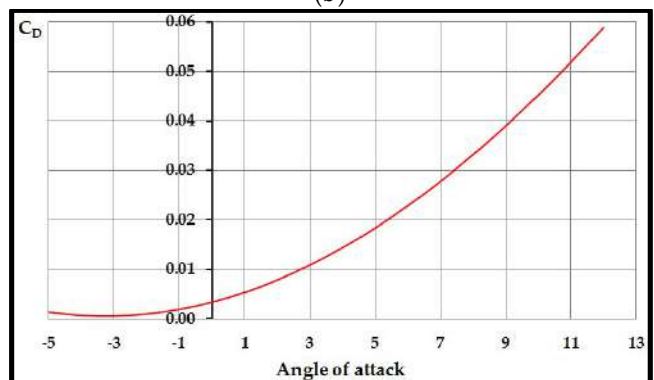
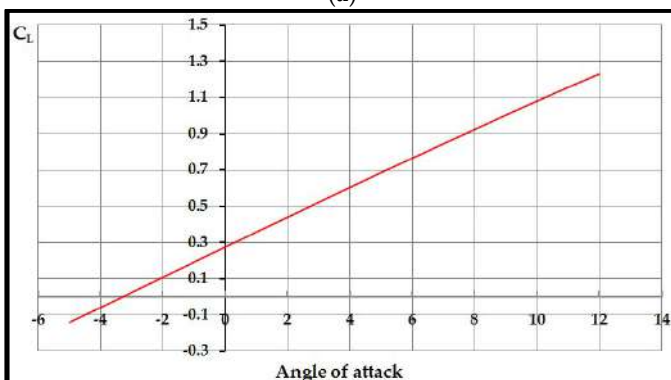
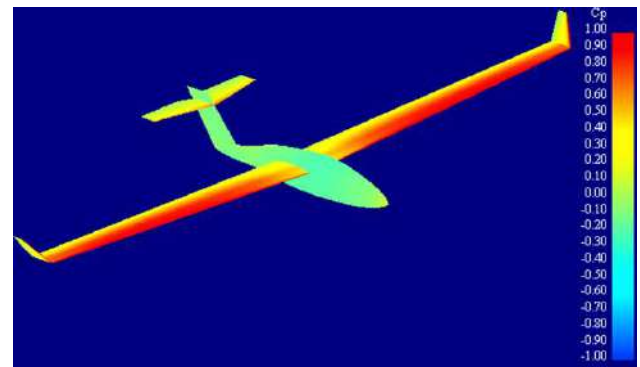
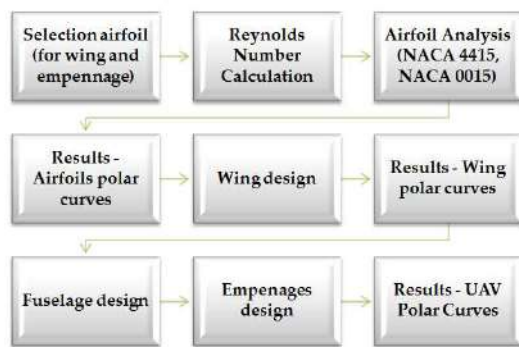


Figure 8. Aerodynamic analysis of the UAV model: (a) calculation methodology in XFLR5; (b) pressure coefficient distribution on the UAV model (angle of attack 5°); (c) dependence of lift coefficient (C_L) and angle of attack; (d) dependence of drag coefficient (C_D) on angle of attack.

4. Manufacturing of the UAV Model Components Using FFF Process

4.1. Fabrication of the Wing Structure Using the FFF Process

This activity began with the testing and manufacturing of specimens and components of the aircraft using various carbon fiber filaments to determine the mechanical performance and optimal manufacturing parameters of the FFF process. In this regard, several studies have been published regarding the FFF manufacturing of specimens/components of the UAV model [73,74]. The first phase in aircraft manufacturing involved dividing the UAV model (Figure 9a) into simpler components suitable for FFF manufacturing using the Ultimaker S5 printer (Ultimaker, Utrecht, The Netherlands).

To manufacture the wings, they were segmented because of their dimensions exceeded the print volume of the printer. Thus, each half-plane of the UAV wing structure was divided into 12 segments (Figure 9b) manufactured as follows: wing segments made from filament reinforced with short carbon fibers—PAHT CF15 [88]; aileron, flap, and winglet segments made from filament reinforced with short glass fibers—Filament PLA Glass Reinforced [89].

The PAHT-CF 15 filament is a high-temperature polyamide reinforced with 15% carbon fiber, exhibiting the following characteristics: high chemical resistance, resistance to high temperatures up to 150 °C, capability to manufacture strong and rigid components, high dimensional stability, ease of processing. The PAHT-CF 15 filament can be successfully used in aerospace and automotive applications [88], increasing the lifespan of components manufactured from this material.

The PAHT-CF15 filament was characterized by [72] in terms of mechanical properties (tensile tests and three-point bending) by varying the infill density (25%, 50%, 75%, and 100%), as well as infill patterns [90]. Once again, it was demonstrated that the specimens with 100% infill density exhibited the highest values for both tensile strength (90.8 MPa) and bending strength (114 MPa). Following the tests [90], for the same type of material (PAHT-CF15), the triangles pattern showed the highest values in three-point bending (108.2 MPa).

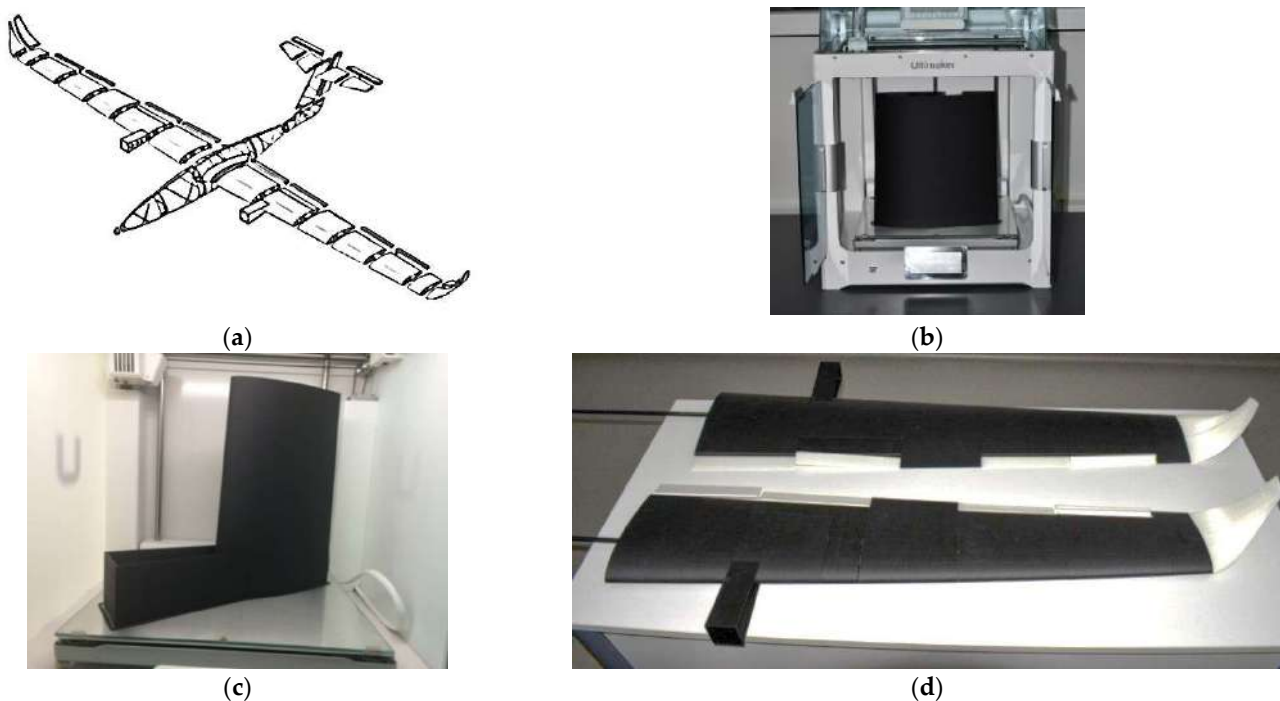


Figure 9. Manufacturing the UAV using the FFF process: (a) the UAV model prepared for FFF manufacturing; (b) manufacturing of wing segment 4; (c) manufacturing of segment 2, including the engine mount; (d) left half-plane and right half-plane of the UAV wing.

The PLA glass-reinforced filament is a biopolymer that offers superior strength and hardness compared to standard PLA filament, making it suitable for FFF-based manufacturing of lightweight components in the aviation and automotive sectors, with reduced warping [89].

For enhanced flight safety, the selection and testing of materials used in the construction of the aircraft components represented a crucial stage in the design and physical realization of the UAV model. Consequently, the testing of PLA glass material was carried out under tensile, flexural, and compressive loading conditions, with the following results: a tensile strength of 49.6 MPa, a flexural strength of 89 MPa, and a compressive strength of 68.2 MPa were obtained for specimens with 100% infill density [73]. Among the three types of tests conducted, it was evident that specimens with a 100% infill density exhibited the highest mechanical characteristics, despite the longer 3D printing time and higher material consumption compared to lower infill density cases of 75% or 50% [73].

After manufacturing the wing segments (Figure 9b,c) for the right half-plane, the next step involved fabricating the segments for the left half-plane (Figure 9d). For manufacturing preparation of the wing segments, the Ultimaker Cura 4.10 software system (Ultimaker, Utrecht, The Netherlands) was used.

The manufacturing parameters for the carbon fiber filament (BASF Ultrafuse PAHT CF15) and glass fiber filament (Filament PLA Glass Reinforced) using the thermoplastic extrusion process for the UAV model components in Table 3 are presented.

The wing segments made from PAHT-CF15 filament were subjected to three-point bending tests and analyzed using finite element analysis (FEA). The maximum bending stress resulting from FEA was 66 MPa, and it was observed that both the tested structure and the finite element simulation exhibited the same mode of deformation, namely, local buckling of the skin in the region of applied load [74]. Additionally, within this study [74], when comparing experimental and simulated results of the wing segments and analyzing reaction forces, it can be stated that there was an error within a maximum range of 3%. The maximum three-point bending force for the wing segments, 3D-printed from PAHT-CF15 filament, reached a maximum value of 300 N with a maximum displacement of 19 mm.

Table 3. Manufacturing parameters for the UAV model components using the FFF process.

FFF Parameter	Value	Value
Filament	BASF Ultrafuse PAHT CF15	Filament PLA Glass Reinforced
Filament diameter [mm]	2.85	2.85
Layer height [mm]	0.2	0.2
Infill density [%]	100	100
Print speed [mm/s]	45	50
Travel speed [mm/s]	100	80
Printing temperature [°C]	260	250
Building plate temperature [°C]	95	60
Nozzle diameter [mm]	0.6	0.6

4.2. Additive Manufacturing of the UAV Fuselage

For the additive manufacturing process of the UAV fuselage, it was divided into six sections during the design stage (Figure 9a) to accommodate the maximum 3D-printing volume of the Creat Bot DX-3D printer (Henan Creatbot Technology Limited, Zhengzhou City, China), which has dimensions of 300 mm × 250 mm × 520 mm. Before manufacturing the fuselage sections, specimens and components of the aircraft were tested and fabricated using different glass fiber filaments to evaluate their mechanical performance and determine the optimal manufacturing parameters for the FFF process [73]. To determine the mechanical performance (compression tests) of the fuselage sections, 3D-printed from PLA glass filament, two variants were tested: a fuselage section with longitudinal stringers and a fuselage section with X-shaped stringers oriented at $\pm 45^\circ$. The 3D-printed fuselage sections with X-shaped stringers began to yield under a compressive force of 8.45 kN, while

those with straight stringers yielded at a load of 6.68 kN. It is evident that 3D printing the fuselage sections with stringers arranged at $\pm 45^\circ$ (with 100% infill density) results in structures with high rigidity compared to those with longitudinal stringers, which is why they are used in the fabrication of the UAV fuselage [73]. After the fuselage was segmented, each segment was exported from the SolidWorks software as an STL file to be loaded into the manufacturing preparation software, CreatBot 6.5.2 (Henan Creatbot Technology Limited, Zhengzhou City, Henan Province, China). The manufacturing procedure was the same for all fuselage segments: importing the STL model, generating the corresponding manufacturing program code, fabrication of the fuselage components (Figure 10a), removing the segments from the print bed, and removing the support material. During this stage, the most complex fuselage component, namely the central segment, was fabricated (Figure 10b), with a 3D-printing time of 74 h. The six fuselage segments manufactured using the FFF additive manufacturing process, with glass fiber filament, in Figure 10c are shown.

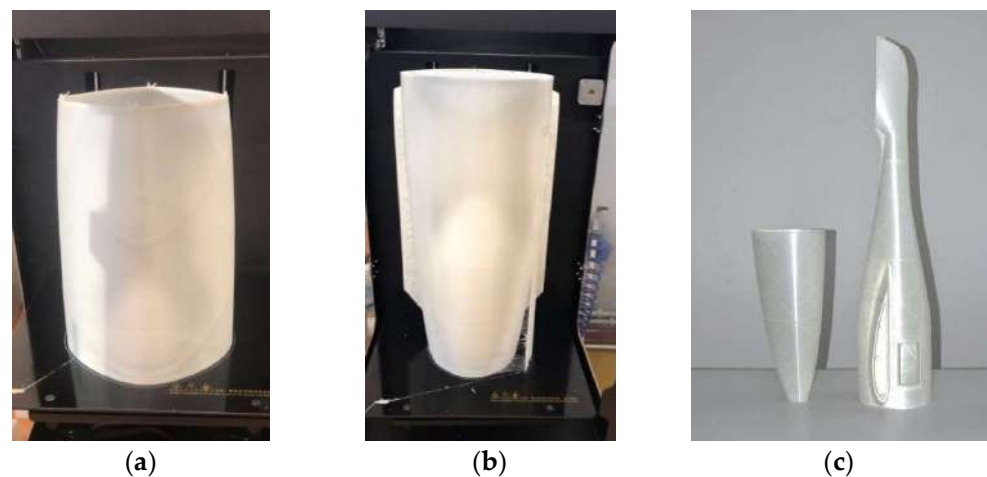


Figure 10. Additive manufacturing of the fuselage: (a) 3D printing of segment 3 of the fuselage; (b) 3D printing of segment 4 of the fuselage; (c) fuselage of the 3D-printed UAV model.

4.3. Additive Manufacturing of the UAV Empennage

Because of its dimensions, the stabilizer was divided in two components (Figure 11a) to fit within the maximum 3D-printing height of the printer. The UAV stabilizer was fabricated from carbon fiber filament (Figure 11a), while the elevator was made from glass fiber filament (Figure 11b). Significant difficulties in 3D printing were encountered during the printing process (frequent nozzle clogging, detachment of parts from the printing bed) for the composite filaments (glass fiber and carbon fiber), which are characteristic of the FFF process [91,92].

The additive manufacturing of the vertical empennage, consisting of the rudder and the vertical stabilizer, was carried out based on the 3D digital model, using glass fiber filament. The two main components of the vertical empennage (rudder and vertical stabilizer) were manufactured without being divided into sections, since they fit within the working volume of the Creat Bot DX-3D printer (Figure 11c). The two components (Figure 11d) were 3D-printed using support structures in the control lever area, where the control rods for the movable surface of the vertical empennage (rudder) will be attached.

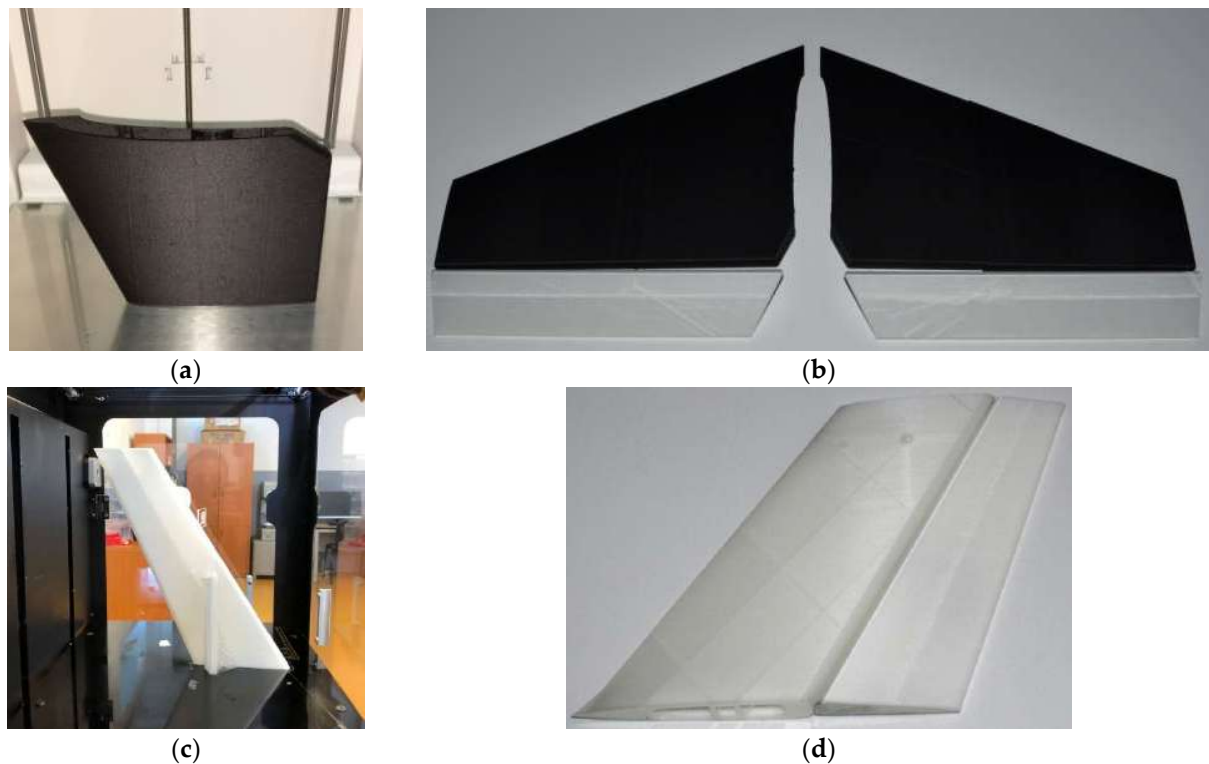


Figure 11. Additive manufacturing of the fuselage: (a) 3D printing of the stabilizer; (b) stabilizer—elevator assembly; (c) 3D printing of ruder; (d) vertical stabilizer—rudder assembly.

4.4. Additive Manufacturing of the UAV Landing Gear

Since the main landing gear is a vital element of the UAV model, its additive manufacturing and testing were carefully studied activities. Takeoff and landing are the most critical stages of flight, which requires a structural analysis of the landing gear. In this regard, the strength of the main landing gear was analyzed using four types of filaments (two with glass fiber and two with carbon fiber) as well as a landing gear manufactured using the vacuum-bagging process from high-quality carbon-fiber-reinforced polymer (CFRP), pressed into a polished mold. The four types of filaments used in the additive manufacturing of the landing gear were: polylactic acid matrix reinforced with short glass fibers (PLA GF), polypropylene matrix reinforced with short glass fibers (PP GF30), polyethylene terephthalate matrix reinforced with short carbon fibers (PET CF15), and polyamide matrix reinforced with short carbon fibers (PAHT CF15). For all four landing gear models, which were 3D-printed using the Ultimaker S5 3D printer, a 100% infill density was used [75]. Based on experimental tests (three-point bending) and finite element simulations, the following conclusion was drawn [75]: the use of landing gear manufactured by the FFF process is not suitable because this technology compromises the structural integrity of the entire UAV model during the most critical stages (takeoff and landing). Therefore, the main landing gear used for the UAV model is the one made of composite materials (CFRP), which exhibit significantly superior performance compared to models manufactured through additive technologies [75].

The finite element method can be employed from the early stages of UAV model development, as it provides rapid and cost-effective insights into the mechanical behavior of both the tested materials and the UAV model components [93,94]. Further studies on enhancing and optimizing the UAV model components and the materials used may be part of future research of the authors, potentially leading to the production of a second version of the UAV model.

5. Assembly of the UAV Model

5.1. Assembly of the UAV Model Components

The assembly of the UAV was performed on sub-assemblies: empennage, fuselage, and wing and landing gear. The main electronic components used in the assembly of the UAV model in Figure 12 are described.

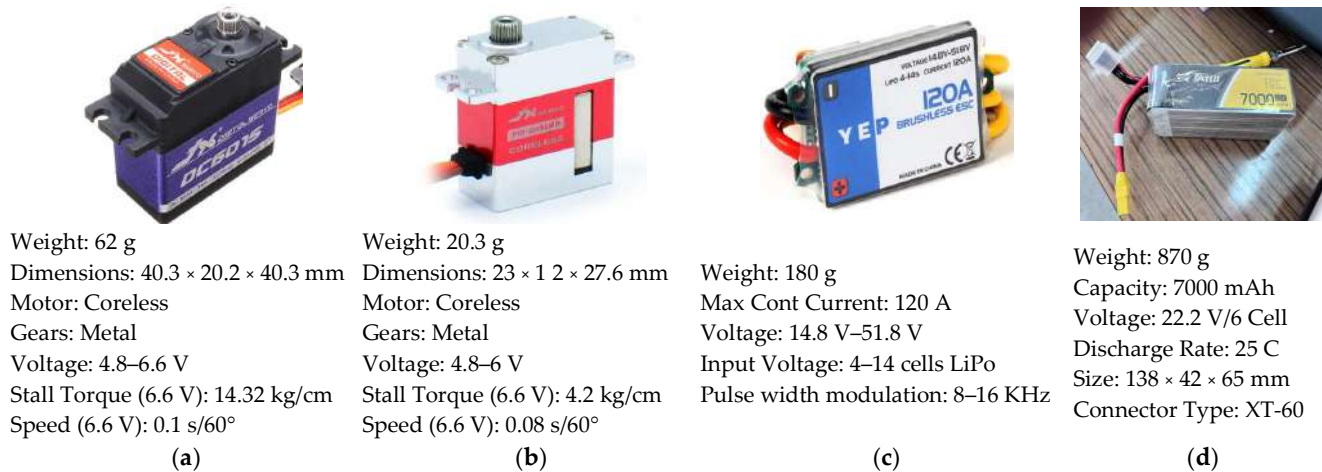


Figure 12. Electronic components used to assemble the UAV: (a) the servomechanism used to control the flaps and ailerons; (b) the servomechanism used to control the elevator and rudder; (c) brushless speed controller (ESC); (d) LiPo battery.

The assembly of the 3D-printed UAV components was carried out using medium density cyanoacrylate adhesive commonly used for bonding plastic/composite materials. The first stage involved the assembly of the empennages (vertical and horizontal). The assembly of the horizontal empennage began with positioning the carbon fiber rods in the central and leading-edge spars, followed by bonding the four segments of the stabilizer. For the elevator control, two servomechanisms were used (Figure 13a), placed between the two segments. Each servomechanism connection involved cable connections and checking the correct linkage of the elevator. A single servomechanism was used for the vertical empennage, positioned on the side surface of the rudder (Figure 13b), in the middle position. In this case, as well, the necessary cables were connected, and proper operation of the rudder was tested. The transmission of motion from the servomechanisms to the elevator and rudder was achieved through the coupling formed by forks connected using threaded rods.

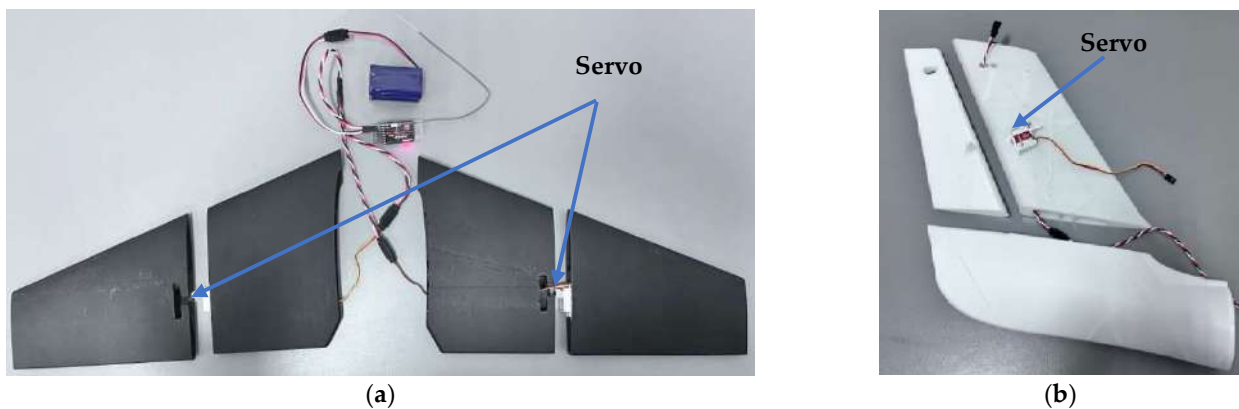


Figure 13. Assembly of electronic components: (a) assembly and testing of the servomechanisms related to the horizontal empennage; (b) assembly and testing of servomechanisms related to vertical empennage.

The final step of empennage assembly was to assemble, through adhesive bonding, segment 6 of the fuselage (Figure 14a,b) to the fixed part of the vertical empennage (rudder). The assembly of the six sections of the fuselage started from the rear, by gluing the stabilizer to the rudder (Figure 14a).

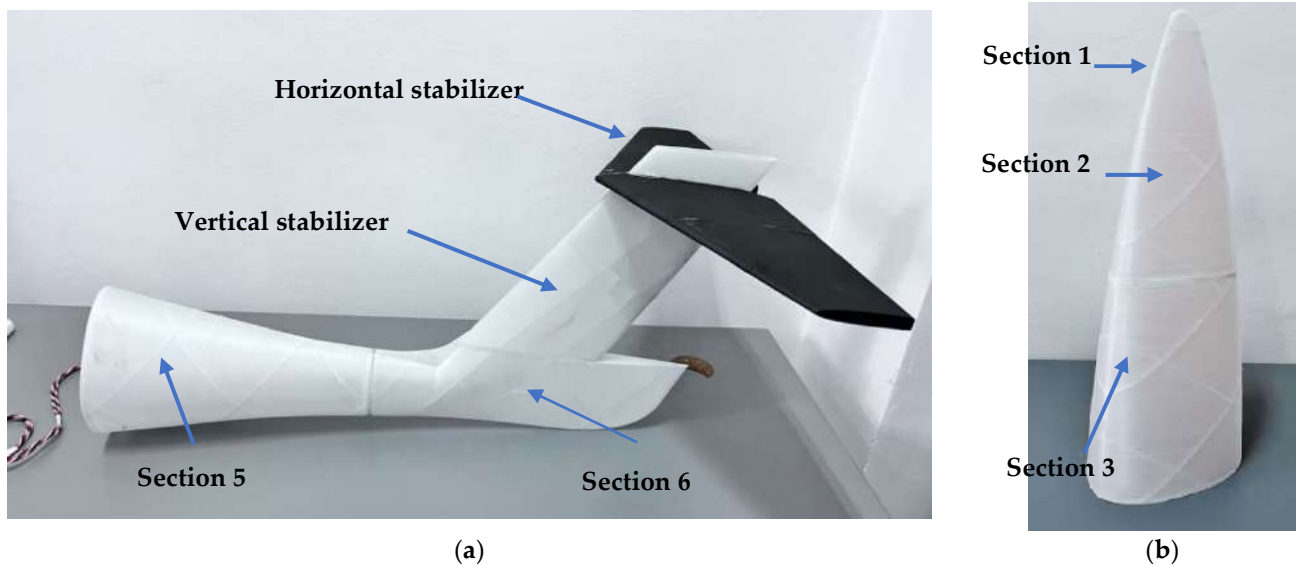


Figure 14. Assembling the fuselage sections: (a) initial assembly of the fuselage—rudder—stabilizer; (b) assembling the front sections.

For wing assembly, the gluing of the wing segments was carefully planned so that the last bonded segments (Figure 15a) would allow for the positioning of the control surfaces (flaps and ailerons) on the 3 mm diameter carbon rods. To achieve optimal alignment of the wing structure, the wing segment gluing was carried out with the carbon rod positioned in the cylindrical surface of the X-spar (Figure 15b). After the bonding stage of the main components (empennage, fuselage, wing), the next steps involved sanding the glued areas and painting the assembled components.



Figure 15. Assembling the UAV wing: (a) the first 3 sections; (b) fully assembled wing.

In the wing assembly, four servomechanisms were mounted inside the wing segments, with two servomechanisms operating the ailerons and two servomechanisms operating the flaps. After positioning the flaps and ailerons on the carbon rods, on which they rotate, the wing segments were glued together. The connection of the aileron and flap servomechanisms was carried out using control rods that link the servo arm and the component arm. After positioning the four control arms, the threaded rods were cut to ensure an appropriate turn, based on the specific functions they perform. The electric motors, manufactured through the SLS process [76], were assembled using four screws secured with nuts at the front side of the motor mount, with the help of two 2.5 mm carbon plates (Figure 16a).

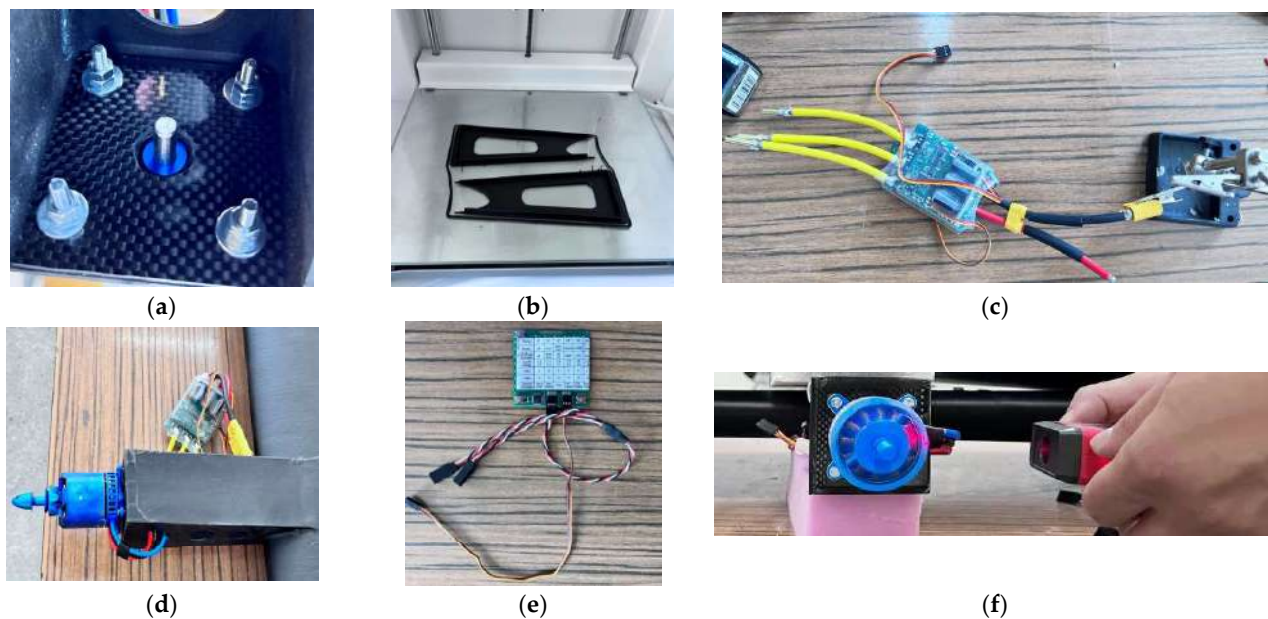


Figure 16. Assembly of electric motors: (a) assembly of the carbon plates for the motor support; (b) 3D printing of the motor support side covers; (c) bonding the speed controller connectors; (d) connecting the speed controller to the electric motor; (e) programming board for the speed controller; (f) verification of the rotation speed of the electric motors.

These carbon plates were designed to reinforce the front surface of the motor mount, which is one of the most stressed areas of the UAV. For the final assembly of the motor mount, the side covers with access cutouts for the motor-speed controller connection were 3D-printed using carbon fiber filament (Figure 16b). The next step involved soldering the speed controller connectors using solder (Figure 16c), which will, in turn, be connected to the electric motor connectors (Figure 16d). An important and complex stage was the configuration of the speed controller settings using the ESC programming card (Figure 16e). The main parameters set for the speed controller were the battery cell count and airplane mode, as well as motor-specific parameters and flight commands. After configuring the speed controller parameters, the last stage was to measure the rotational speed of the two electric motors, manufactured through the SLS process, using a tachometer (Figure 16f), resulting in equal values at various operating regimes.

5.2. Testing the Electronic Systems of the UAV Model

The GCSD4RSV2 ground control station (Digital Micro Devices, Valencia, Spain) serves as a central ground control system that allows human control over the unmanned aerial vehicle model. This professional portable ground control station is equipped with an intelligent antenna (with a control range of 150 km), radio control, telemetry (Mavlink and transparent data link), AES 128 encryption, a 10" Full HD high-brightness IPS LED visible sunlight-readable display, 5.8 GHz video receiver, built-in PC with Windows 10, and a touchscreen. Regarding the transmission of telemetry data from the UAV model to the ground control station (GCS), it is achieved through a radio modem mounted on the UAV model. Using the Mavlink protocol, an open-source protocol, data are sent to the ground station through this modem. On the ground, the information is received by the PC through the USB or Bluetooth interface of the GCSD4RSV2 control station. This technology is compatible with most entry-level controllers such as the RXLRS system, Pixhawk flight controller, or APM. At the software level, everything is implemented on the Mission Planner software system, where takeoff and landing parameters, as well as flight routes, are set for the UAV model [95]. The UAV flight management system consists of three main subsystems: the ground control station, the communication link, and the

UAV model itself equipped with receivers and an autopilot [96]. The Pixhawk Orange cube allows the flight of various types of remote-controlled aircraft (helicopters, multirotor, airplanes), which turns it into a professional UAV platform.

The Pixhawk Orange cube features three accelerometers (one for each axis of the UAV aircraft), which require calibration. The combination of the transmitter assembly and antenna (SMBTS + BQ89) is called the intelligent antenna. Additionally, after verifying the operation of the ground control station, tests were conducted to assess the functionality of the FLIR Tau thermal module (FLIR Systems Inc., Boston, MA, USA) connected to the ground control station (Figure 17a,b).



Figure 17. Testing the thermal module: (a) connecting the thermal module—smart antenna—battery—ground control station receiver; (b) image transmitted by the thermal module.

5.3. Final Assembly of the UAV Model

The final assembly of the UAV model began with the 3D printing, using fiberglass, of the two fairings that protect the motors and ESC system, while also ensuring efficient aerodynamic shapes. Prior to gluing the fairings, the propellers (16 × 8 inches) equipped with carbon fiber reinforcement were mounted. These propellers have a thin profile, low weight, and high efficiency. Since the initial setup of the electric motors and ESC programming, a contra-rotating mode has been utilized, which also applies to the propellers. During the assembly stage of the UAV model, the tail surfaces (horizontal and vertical empennages) were fabricated using thermoplastic extrusion. After assembling the tail surfaces' components (Figure 18a), the control surface positions (elevator and rudder) were determined and tested. For the assembly of the tail wheel landing gear (skid), a 3D-printed part was used to connect the UAV model's tail to the rear wheel assembly (Figure 18b). The rear wheel system consists of a metal rod, two springs, and an 8 cm diameter rubber wheel (Figure 18b). The two metal springs were installed to attenuate shocks during takeoff and landing phases of the UAV model. The main landing gear was attached to the fuselage of the UAV model using screw-nuts, with four screws in the central area (Figure 18c). To further dampen shocks, especially during takeoff and landing, the main landing gear was equipped with a hydraulic shock absorber and a 13 cm diameter rubber wheel. This hydraulic shock absorber was connected to the landing gear using a metal piece secured with four M4 screws (Figure 18d).

To secure the thermal module to the UAV model, a support was designed and manufactured using the thermoplastic extrusion process, which was then fastened to the fuselage using two screws (Figure 18e). After verifying the positioning of the servomotors for the control surfaces (ailerons and flaps), on the wing, the assembly of the left and right wing was checked. Their assembly was carried out through the upper part of the fuselage, using a mating system and a fixing screw (Figure 18f,g). Additionally, the carbon rods inside the wing were connected using aluminum alloy junctions with threaded surfaces (Figure 18g). Winglets were mounted on the carbon rod and then glued to the wingtip. An important

task was to establish, connect, and test all electronic connections (servomotors, electric motors, batteries, thermal module) to the receiver of the ground control station and the Pixhawk cube. Once all connections were verified, the fuselage was connected to the left wing and then to the right wing. Figure 18h illustrates the final structure of the UAV model equipped with the FLIR Tau thermal module.

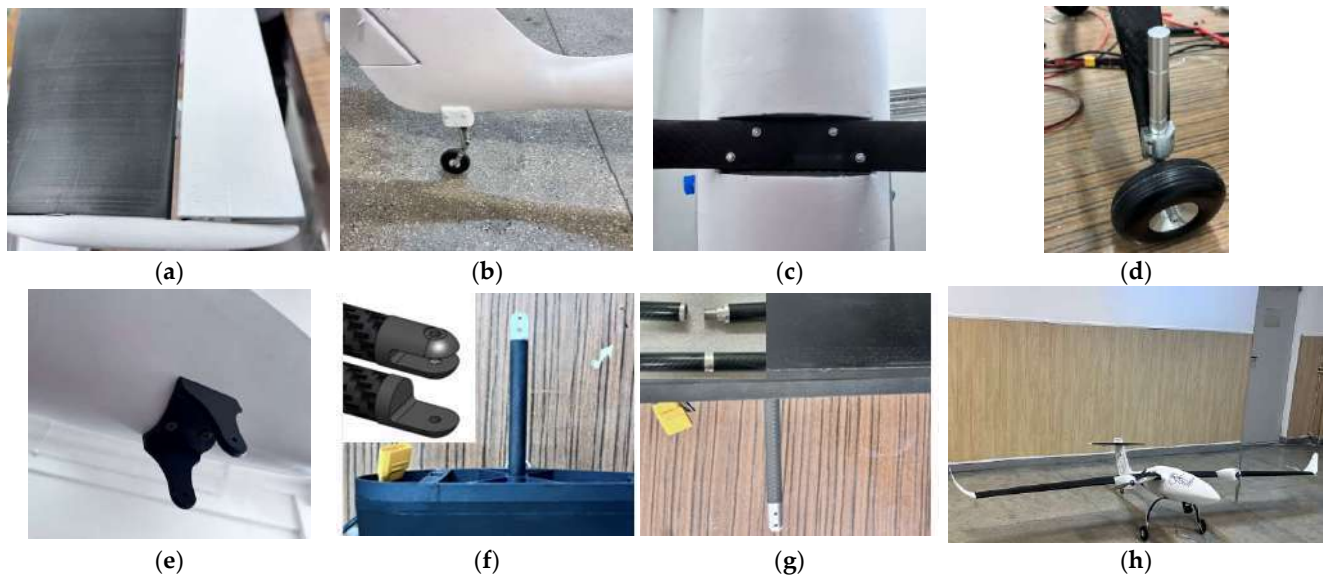


Figure 18. Assembly of the UAV model: (a) assembly of the stabilizer—elevator—carbon rod assembly and gluing of the horizontal empennage tips; (b) assembly of the rear landing gear; (c) attachment of the main landing gear; (d) assembly of the hydraulic shock absorber for the main landing gear and rubber wheel; (e) mounting of the support for the thermal module; (f) left wing half; (g) right wing half; (h) UAV model equipped with the thermal module.

Table 4 describes the weights and manufacturing time for the components of the UAV model made from composite materials.

Table 4. Weight of 3D-printed components of UAV composite model.

Component	Weight [g]	Manufacturing Time [h]
Fuselage	1330	155
Wings	2680	310
Ailerons	170	28
Flaps	232	38
Winglets	240	36
Horizontal tail	248	52
Vertical tail	190	34
Nacelle	240	46
Total	5330	736

6. Testing and Verifying the Mission of the UAV Model

The testing of the model was carried out in two stages: the first stage involved ground testing of the UAV model in the workshop, and the second stage took place on a runway. The first stage began with a crucial activity, namely, the static balance of the model. As an experimental model, the balance was achieved by adding the two batteries (connected in parallel) in the nose area of the aircraft. This resulted in a balance point at 25% of the mean aerodynamic chord, ensuring a maneuverable aircraft with a quick response time.

After balancing the UAV aircraft, ground testing of the motors (Figure 19a) was conducted at maximum throttle. Within this stage, tests were also performed to ensure the connection between the UAV model, ground control station, Pixhawk Orange cube,

and the thermal module (Figure 19b). The runway testing of the UAV model consisted of the following (Figure 19c): verification of servo-mechanism operation, motor functionality, ground taxiing position, examination of the ground station connection with the aircraft, and verification of the thermal module's connection with the ground control station.

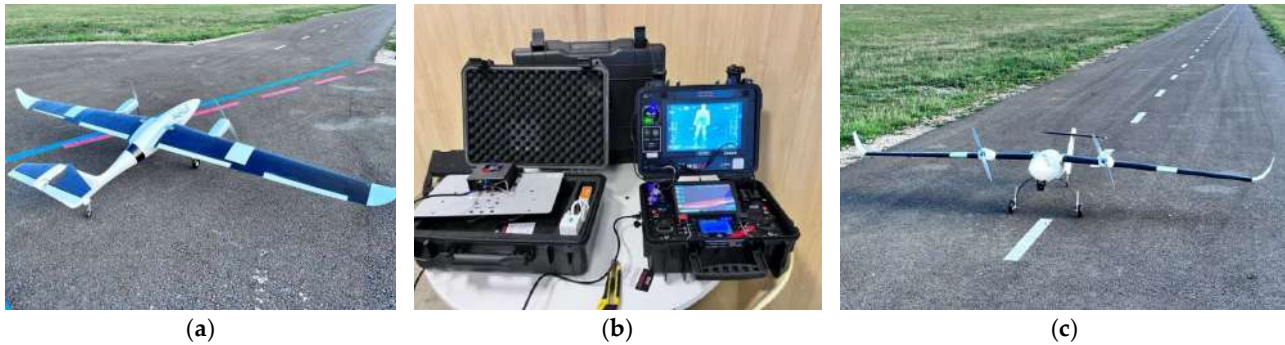


Figure 19. Ground testing of flight controls on the takeoff-landing runway: (a) motors testing; (b) thermal module testing; (c) preparation and verification of ground taxiing for the UAV model.

Following the flight testing, it was found that the UAV model, manufactured through the thermoplastic extrusion process, is stable and capable of achieving a wide range of speeds, with good aerodynamic characteristics and high maneuverability. For the flight tests, an asphalt location was chosen to allow for a rapid takeoff of the UAV model. The stages of the flight testing of the model were as follows: ground taxiing stage covering approximately 30–35 m, followed by the takeoff stage of the UAV model (Figure 20a), the third stage involved climbing to the flight ceiling (approximately 70 m), the horizontal flight stage (Figure 20b), mission execution (search and rescue), turning maneuvers, returning to the area of interest, and the final stage of landing the model on the ground.

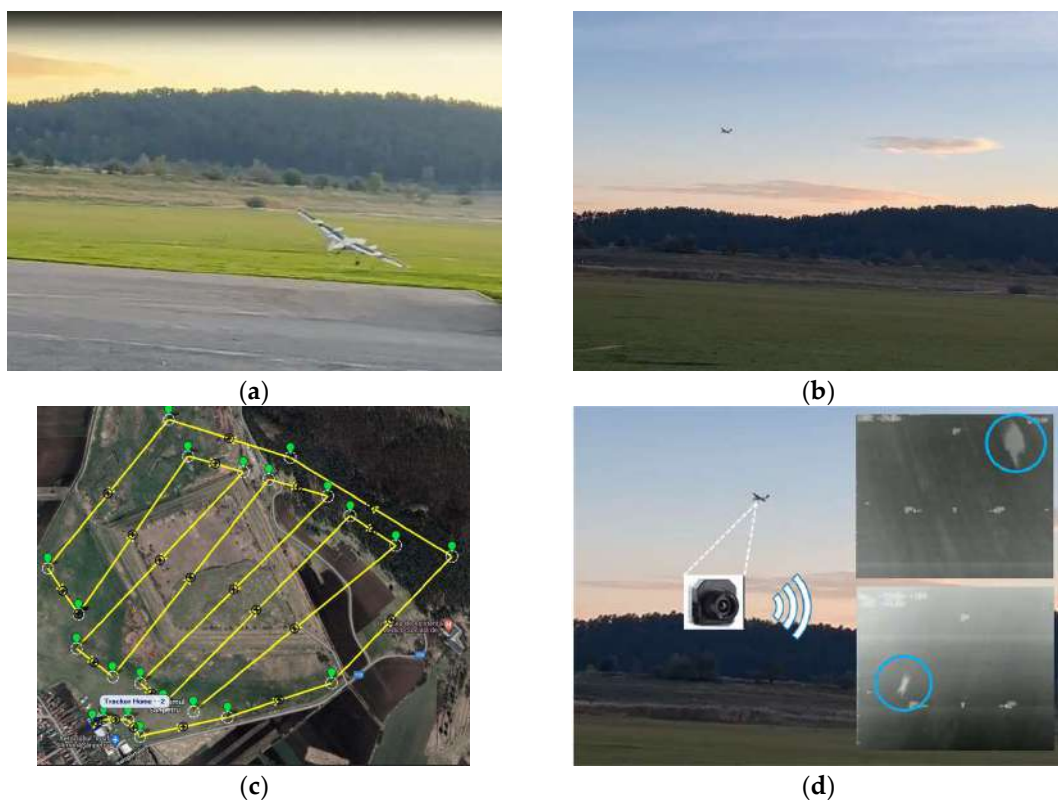


Figure 20. Flight of the UAV model: (a) takeoff; (b) cruising flight; (c) flight path establishment; (d) execution of the UAV model's flight mission using the thermal module.

Manual takeoff and landing were chosen for flight control, using the ground control station. Once the aircraft reached the predetermined flight ceiling, it was switched to semi-automatic mode by the control station, so that the aircraft can follow the predefined waypoints from the flight management program. The flight testing was successfully completed with safety measures in place and maximum maneuverability. The UAV model had a takeoff weight of 11 kg and autonomy of approximately 50 min. Using the map interface of the mission control software (Mission Planner, Q Ground Control), takeoff and landing profiles, as well as the flight path for the UAV model, were defined (Figure 20c) and then were loaded into the flash memory of the Pixhawk Cube Orange autopilot.

To fulfill the flight missions (search and rescue) of the UAV model using the thermal module and ground control station, images were captured during the horizontal flight phase. As a result, temperature variations were detected through the thermal module. In Figure 20d, a human (blue circle) being lying on the ground and another one moving were detected using body-temperature detection.

7. Conclusions

The paper presented a complete cycle of UAV model development, covering all necessary stages, such as: design, preliminary aerodynamic analysis, additive manufacturing, assembly, and flight testing. In the design phase, the dimensions of the UAV model were established, and then all structural components were described, starting from the wing to the landing gear. The final UAV model featured a configuration with the wing positioned on top of the fuselage, twin-engine, T-tail, and tricycle landing gear. The preliminary aerodynamic analysis highlighted that the unmanned aircraft exhibited a high maximum lift coefficient (approximately 1.2), classifying it as a powered glider UAV, with a large wing area and span. The FFF manufacturing of the UAV model's components was completed in approximately 736 h, using filament with short carbon fibers and short glass fibers. By utilizing the FFF process, complex components were manufactured at reduced costs and in a short timeframe for creating a UAV model. An advantage of FFF manufacturing for the aircraft components is the ability to intervene in the model's design at any time without adding additional costs, compared to traditional methods involving molds. The flight testing of UAV model was successfully completed with safety and maximum maneuverability. The UAV model had a takeoff mass of 11 kg, a wingspan of 3.4 m, an autonomy of approximately 50 min, and a control distance of about 100 km. By using the two brushless electric motors, manufactured through the SLS process, the UAV model had a wide range of speeds and was capable of performing search-and-rescue missions using the thermal module and ground control station. The missions that the UAV model can perform are to locate pilots and passengers after aviation accidents that may occur in hard-to-reach areas (such as mountains) and to estimate wild animal populations and detect illegal hunting. These missions can be successfully conducted using the real-time video transmission of the UAV model via the thermal module, which provides rescue teams with a clear and detailed view of the operational area, facilitating rapid and efficient responses.

In conclusion, this study has demonstrated the feasibility of creating the first unmanned aircraft, made from additive manufacturing composite materials, equipped with electric motors (manufactured through the SLS process), a traffic management system (ground control station and autopilot), and a thermal module for search-and-rescue missions. Therefore, the designed, analyzed, and manufactured UAV model serves as clear evidence that a nearly complete UAV model can be fabricated using the FFF process, capable of flying and operating with good aerodynamic characteristics and high maneuverability.

Author Contributions: Conceptualization, S.-M.Z., G.R.B., L.-A.C. and I.S.P.; methodology, S.-M.Z., M.A.P., L.-A.C. and V.M.S.; software, G.R.B. and C.L.; validation, S.-M.Z., G.R.B. and V.M.S.; investigation, S.-M.Z., M.A.P., G.R.B., V.M.S. and I.S.P.; writing—original draft preparation, S.-M.Z., G.R.B. and L.-A.C.; project administration, S.-M.Z. All authors have read and agreed to the published version of the manuscript.

Funding: This work was supported by a grant of the Ministry of Research, Innovation and Digitization, CNCS/CCCDI—UEFISCDI, project number PN-III-P2-2.1-PED-2019-0739, within PNCDI III.

Data Availability Statement: Not applicable.

Acknowledgments: We also acknowledge PRO-DD Structural Funds Project (POS-CCE, O.2.2.1., ID 123, SMIS 2637, ctr. No. 11/2009) for providing the infrastructure used in this work.

Conflicts of Interest: The authors declare no conflict of interest.

References

1. Chamola, V.; Kotesch, P.; Agarwal, A.; Naren; Gupta, N.; Guizani, M. A Comprehensive Review of Unmanned Aerial Vehicle Attacks and Neutralization Techniques. *Ad Hoc Netw.* **2021**, *111*, 102324. [[CrossRef](#)] [[PubMed](#)]
2. Konert, A.; Balcerzak, T. Military autonomous drones (UAVs)—From fantasy to reality. Legal and Ethical implications. *Transp. Res. Procedia* **2021**, *59*, 292–299. [[CrossRef](#)]
3. Schneiderman, R. Unmanned drones are flying high in the military/aerospace sector. *IEEE Signal Process. Mag.* **2012**, *29*, 8–11. [[CrossRef](#)]
4. Nyaaba, A.A.; Ayamga, M. Intricacies of medical drones in healthcare delivery: Implications for Africa. *Technol. Soc.* **2021**, *66*, 101624. [[CrossRef](#)]
5. Nedelea, P.L.; Popa, T.O.; Manolescu, E.; Bouros, C.; Grigorasi, G.; Andritoi, D.; Pascale, C.; Andrei, A.; Cimpoesu, D.C. Telemedicine System Applicability Using Drones in Pandemic Emergency Medical Situations. *Electronics* **2022**, *11*, 2160. [[CrossRef](#)]
6. Poljak, M.; Šterbenc, A.J.C.M. Infection, Use of drones in clinical microbiology and infectious diseases: Current status, challenges and barriers. *Clin. Microbiol. Infect.* **2020**, *26*, 425–430. [[CrossRef](#)] [[PubMed](#)]
7. Rejeb, A.; Abdollahi, A.; Rejeb, K.; Treiblmaier, H. Drones in Agriculture: A Review and Bibliometric Analysis. *Comput. Electron. Agric.* **2022**, *198*, 107017. [[CrossRef](#)]
8. Rahman, M.F.F.; Fan, S.; Zhang, Y.; Chen, L. A Comparative Study on Application of Unmanned Aerial Vehicle Systems in Agriculture. *Agriculture* **2021**, *11*, 22. [[CrossRef](#)]
9. Hodgson, J.C.; Baylis, S.M.; Mott, R.; Herrod, A.; Clarke, R.H. Precision wildlife monitoring using unmanned aerial vehicles. *Sci. Rep.* **2016**, *6*, 22574. [[CrossRef](#)]
10. Kabir, R.H.; Lee, K. Wildlife Monitoring Using a Multi-UAV System with Optimal Transport Theory. *Appl. Sci.* **2021**, *11*, 4070. [[CrossRef](#)]
11. Ivanova, S.; Prosekov, A.; Kaledin, A. A Survey on Monitoring of Wild Animals during Fires Using Drones. *Fire* **2022**, *5*, 60. [[CrossRef](#)]
12. Martinez-Alpiste, I.; Golcarenenji, G.; Wang, Q.; Alcaraz-Calero, J.M. Search and rescue operation using UAVs: A case study. *Expert Syst. Appl.* **2021**, *178*, 114937. [[CrossRef](#)]
13. Półka, M.; Ptak, S.; Kuziora, Ł. The use of UAV's for search and rescue operations. *Procedia Eng.* **2017**, *192*, 748–752. [[CrossRef](#)]
14. Greenwood, W.W.; Lynch, J.P.; Zekkos, D. Applications of UAVs in civil infrastructure. *J. Infrastruct. Syst.* **2019**, *25*, 04019002. [[CrossRef](#)]
15. Ham, Y.; Han, K.K.; Lin, J.J.; Golparvar-Fard, M. Visual monitoring of civil infrastructure systems via camera-equipped Unmanned Aerial Vehicles (UAVs): A review of related works. *Vis. Eng.* **2016**, *4*, 1. [[CrossRef](#)]
16. Lei, B.; Wang, N.; Xu, P.; Song, G. New crack detection method for bridge inspection using UAV incorporating image processing. *J. Aerosp. Eng.* **2018**, *31*, 04018058. [[CrossRef](#)]
17. She, R.; Ouyang, Y. Efficiency of UAV-based last-mile delivery under congestion in low-altitude air. *Transp. Res. Part C Emerg. Technol.* **2021**, *122*, 102878. [[CrossRef](#)]
18. Gu, Q.; Fan, T.; Pan, F.; Zhang, C. A vehicle-UAV operation scheme for instant delivery. *Comput. Ind. Eng.* **2020**, *149*, 106809. [[CrossRef](#)]
19. Miranda, V.R.; Rezende, A.; Rocha, T.L.; Azpúrua, H.; Pimenta, L.C.; Freitas, G.M. Autonomous navigation system for a delivery drone. *J. Control Autom. Electr. Syst.* **2022**, *33*, 141–155. [[CrossRef](#)]
20. Li, Y.; Liu, M.; Jiang, D. Application of Unmanned Aerial Vehicles in Logistics: A Literature Review. *Sustainability* **2022**, *14*, 14473. [[CrossRef](#)]
21. Ahmed, F.; Mohanta, J.C.; Keshari, A.; Yadav, P.S. Recent Advances in Unmanned Aerial Vehicles: A Review. *Arab. J. Sci. Eng.* **2022**, *47*, 7963–7984. [[CrossRef](#)] [[PubMed](#)]
22. Valoriani, F.; Esposito, M.; Gherlone, M. Shape Sensing for an UAV Composite Half-Wing: Numerical Comparison between Modal Method and Ko's Displacement Theory. *Aerospace* **2022**, *9*, 509. [[CrossRef](#)]
23. ElFaham, M.M.; Mostafa, A.M.; Nasr, G. Unmanned aerial vehicle (UAV) manufacturing materials: Synthesis, spectroscopic characterization and dynamic mechanical analysis (DMA). *J. Mol. Struct.* **2020**, *1201*, 127211. [[CrossRef](#)]
24. Liang, Y.-C.; Chin, P.-C.; Sun, Y.-P.; Wang, M.-R. Design and Manufacture of Composite Landing Gear for a Light Unmanned Aerial Vehicle. *Appl. Sci.* **2021**, *11*, 509. [[CrossRef](#)]
25. Boyer, R.R.; Cotton, J.D.; Mohaghegh, M.; Schafrik, R.E. Materials considerations for aerospace applications. *MRS Bull.* **2015**, *40*, 1055–1066. [[CrossRef](#)]

26. Hoa, S.V. *Principles of the Manufacturing of Composite Materials*; DEStech Publications Inc.: Lancaster, PA, USA, 2009.
27. Autonomous Unmanned Aerial Vehicles Condor 300. Available online: <https://www.optimumsolution.com/item14.html> (accessed on 31 August 2023).
28. Applied Aeronautics, Albatross UAV. Available online: <https://www.appliedaeronautics.com/albatross-uav> (accessed on 31 August 2023).
29. Silent Falcon™ Small Unmanned Aircraft System. Available online: <https://www.homelandsecurity-technology.com/projects/silent-falcon-small-unmanned-aircraft-system/> (accessed on 31 August 2023).
30. Vector VTOL Fixed Wing UAS. Available online: <https://bssholland.com/product/vector-vtol-fixed-wing-uas/> (accessed on 31 August 2023).
31. Aiactive Technologies, Penguin BE UAV. Available online: <https://www.aiactive.com/pages/homeland-security-public-safety/uav-home-land-security/penguin-be-uav.html> (accessed on 31 August 2023).
32. Klippstein, H.; Diaz De Cerio Sanchez, A.; Hassanin, H.; Zweiri, Y.; Seneviratne, L. Fused deposition modeling for unmanned aerial vehicles (UAVs): A review. *Adv. Eng. Mater.* **2018**, *20*, 1700552. [[CrossRef](#)]
33. Brischetto, S.; Ferro, C.G.; Maggiore, P.; Torre, R. Compression Tests of ABS Specimens for UAV Components Produced via the FDM Technique. *Technologies* **2017**, *5*, 20. [[CrossRef](#)]
34. Rubies, E.; Palacín, J. Design and FDM/FFF Implementation of a Compact Omnidirectional Wheel for a Mobile Robot and Assessment of ABS and PLA Printing Materials. *Robotics* **2020**, *9*, 43. [[CrossRef](#)]
35. Przekop, R.E.; Kujawa, M.; Pawlak, W.; Dobrosielska, M.; Sztorch, B.; Wieleba, W. Graphite Modified Polylactide (PLA) for 3D Printed (FDM/FFF) Sliding Elements. *Polymers* **2020**, *12*, 1250. [[CrossRef](#)]
36. Tao, Y.; Kong, F.; Li, Z.; Zhang, J.; Zhao, X.; Yin, Q.; Xing, D.; Li, P. A review on voids of 3D printed parts by fused filament fabrication. *J. Mater. Res. Technol.* **2021**, *15*, 4860–4879. [[CrossRef](#)]
37. Baechle-Clayton, M.; Loos, E.; Taheri, M.; Taheri, H. Failures and Flaws in Fused Deposition Modeling (FDM) Additively Manufactured Polymers and Composites. *J. Compos. Sci.* **2022**, *6*, 202. [[CrossRef](#)]
38. Bochnia, J.; Blasiak, M.; Koziar, T. A Comparative Study of the Mechanical Properties of FDM 3D Prints Made of PLA and Carbon Fiber-Reinforced PLA for Thin-Walled Applications. *Materials* **2021**, *14*, 7062. [[CrossRef](#)] [[PubMed](#)]
39. Comelli, C.A.; Davies, R.; van der Pol, H.; Ghita, O. PEEK filament characteristics before and after extrusion within fused filament fabrication process. *J. Mater. Sci.* **2022**, *57*, 766–788. [[CrossRef](#)]
40. El Magri, A.; Vanaei, S.; Vaudreuil, S. An overview on the influence of process parameters through the characteristic of 3D-printed PEEK and PEI parts. *High Perform. Polym.* **2021**, *33*, 862–880. [[CrossRef](#)]
41. Rodzeń, K.; Sharma, P.K.; McIlhagger, A.; Mokhtari, M.; Dave, F.; Tormey, D.; Sherlock, R.; Meenan, B.J.; Boyd, A. The Direct 3D Printing of Functional PEEK/Hydroxyapatite Composites via a Fused Filament Fabrication Approach. *Polymers* **2021**, *13*, 545. [[CrossRef](#)]
42. Pascariu, I.S.; Zaharia, S.M. Design and testing of an unmanned aerial vehicle manufactured by fused deposition modeling. *J. Aerosp. Eng.* **2020**, *33*, 06020002. [[CrossRef](#)]
43. Skawiński, I.; Goetzendorf-Grabowski, T. FDM 3D printing method utility assessment in small RC aircraft design. *Aircr. Eng. Aerosp. Technol.* **2019**, *91*, 865–872. [[CrossRef](#)]
44. de Oliveira, T.L.; de Carvalho, J. Design and numerical evaluation of quadrotor drone frame suitable for fabrication using fused filament fabrication with consumer-grade ABS. *J. Braz. Soc. Mech. Sci. Eng.* **2021**, *43*, 436. [[CrossRef](#)]
45. Palomba, G.; Crupi, V.; Epasto, G. Additively manufactured lightweight monitoring drones: Design and experimental investigation. *Polymer* **2022**, *241*, 124557. [[CrossRef](#)]
46. Yap, Y.L.; Toh, W.; Giam, A.; Yong, F.R.; Chan, K.I.; Tay, J.W.S.; Teong, S.S.; Lin, R.; Ng, T.Y. Topology optimization and 3D printing of micro-drone: Numerical design with experimental testing. *Int. J. Mech. Sci.* **2023**, *237*, 107771. [[CrossRef](#)]
47. Zhu, W. Models for wind tunnel tests based on additive manufacturing technology. *Prog. Aerosp. Sci.* **2019**, *110*, 100541. [[CrossRef](#)]
48. Junka, S.; Schröder, W.; Schrock, S. Design of additively manufactured wind tunnel models for use with UAVs. *Procedia CIRP* **2017**, *60*, 241–246. [[CrossRef](#)]
49. Szwedziak, K.; Łusiak, T.; Bąbel, R.; Winiarski, P.; Podśedek, S.; Doleżał, P.; Niedbała, G. Wind Tunnel Experiments on an Aircraft Model Fabricated Using a 3D Printing Technique. *JMMP* **2022**, *6*, 12. [[CrossRef](#)]
50. Fasel, U.; Keidel, D.; Baumann, L.; Cavolina, G.; Eichenhofer, M.; Ermanni, P. Composite additive manufacturing of morphing aerospace structures. *Manuf. Lett.* **2020**, *23*, 85–88. [[CrossRef](#)]
51. Bishay, P.L.; Burg, E.; Akinwunmi, A.; Phan, R.; Sepulveda, K. Development of a new span-morphing wing core design. *Designs* **2019**, *3*, 12. [[CrossRef](#)]
52. Parancheerivilakkathil, M.S.; Haider, Z.; Ajaj, R.M.; Amoozgar, M. A Polymorphing Wing Capable of Span Extension and Variable Pitch. *Aerospace* **2022**, *9*, 205. [[CrossRef](#)]
53. Parancheerivilakkathil, M.S.; Ajaj, R.M.; Khan, K.A. A compliant polymorphing wing for small UAVs. *Chin. J. Aeronaut.* **2015**, *33*, 2575–2588. [[CrossRef](#)]
54. Belei, C.; Joeressen, J.; Amancio-Filho, S.T. Fused-Filament Fabrication of Short Carbon Fiber-Reinforced Polyamide: Parameter Optimization for Improved Performance under Uniaxial Tensile Loading. *Polymers* **2022**, *14*, 1292. [[CrossRef](#)]
55. Yang, D.; Zhang, H.; Wu, J.; McCarthy, E. Fibre flow and void formation in 3D printing of short-fibre reinforced thermoplastic composites: An experimental benchmark exercise. *Addit. Manuf.* **2021**, *37*, 101686. [[CrossRef](#)]

56. Valvez, S.; Silva, A.P.; Reis, P.N.B. Compressive Behaviour of 3D-Printed PETG Composites. *Aerospace* **2022**, *9*, 124. [[CrossRef](#)]
57. Goh, G.D.; Agarwala, S.; Goh, G.L.; Dikshit, V.; Sing, S.L.; Yeong, W.Y. Additive manufacturing in unmanned aerial vehicles (UAVs): Challenges and potential. *Aerosp. Sci. Technol.* **2017**, *63*, 140–151. [[CrossRef](#)]
58. Zeng, C.; Liu, L.; Bian, W.; Leng, J.; Liu, Y. Compression Behavior and Energy Absorption of 3D Printed Continuous Fiber Reinforced Composite Honeycomb Structures with Shape Memory Effects. *Addit. Manuf.* **2021**, *38*, 101842. [[CrossRef](#)]
59. Kepenekci, M.; Gharehpapagh, B.; Yaman, U.; Özerinç, S. Mechanical performance of carbon fiber-reinforced polymer cellular structures manufactured via fused filament fabrication. *Polym. Compos.* **2023**, *44*, 4654–4668. [[CrossRef](#)]
60. Condruz, M.-R.; Paraschiv, A.; Badea, T.-A.; Useriu, D.; Frigioescu, T.-F.; Badea, G.; Cican, G. A Study on Mechanical Properties of Low-Cost Thermoplastic-Based Materials for Material Extrusion Additive Manufacturing. *Polymers* **2023**, *15*, 2981. [[CrossRef](#)] [[PubMed](#)]
61. Tutar, M. A Comparative Evaluation of the Effects of Manufacturing Parameters on Mechanical Properties of Additively Manufactured PA and CF-Reinforced PA Materials. *Polymers* **2023**, *15*, 38. [[CrossRef](#)] [[PubMed](#)]
62. Wang, G.; Zhang, D.; Li, B.; Wan, G.; Zhao, G.; Zhang, A. Strong and thermal-resistance glass fiber-reinforced polylactic acid (PLA) composites enabled by heat treatment. *Int. J. Biol. Macromol.* **2019**, *129*, 448–459. [[CrossRef](#)] [[PubMed](#)]
63. Shulga, E.; Karamov, R.; Sergeichev, I.S.; Konev, S.D.; Shurygina, L.I.; Akhatov, I.S.; Shandakov, S.D.; Nasibulin, A.G. Fused Filament Fabricated Polypropylene Composite Reinforced by Aligned Glass Fibers. *Materials* **2020**, *13*, 3442. [[CrossRef](#)]
64. Li, X.; Ni, Z.; Bai, S.; Lou, B. Preparation and Mechanical Properties of Fiber Reinforced PLA for 3D Printing Materials. *IOP Conf. Ser. Mater. Sci. Eng.* **2018**, *322*, 022012. [[CrossRef](#)]
65. Sadraey, M. Unmanned aircraft design: A review of fundamentals. *Synth. Lect. Mech. Eng.* **2017**, *1*, 1–193.
66. Roskam, J. *Airplane Design Part I: Preliminary Sizing of Airplanes*, 1st ed.; DARcorporation: Lawrence, KS, USA, 1986; ISBN 978-1-884885-42-6.
67. Dantsker, O.D.; Theile, M.; Caccamo, M. A Cyber-Physical Prototyping and Testing Framework to Enable the Rapid Development of UAVs. *Aerospace* **2022**, *9*, 270. [[CrossRef](#)]
68. Ong, W.; Srigrarom, S.; Hesse, H. Design methodology for heavy-lift unmanned aerial vehicles with coaxial rotors. In Proceedings of the AIAA SciTech Forum, San Diego, CA, USA, 7–11 January 2019.
69. Elmeseiry, N.; Alshaer, N.; Ismail, T. A Detailed Survey and Future Directions of Unmanned Aerial Vehicles (UAVs) with Potential Applications. *Aerospace* **2021**, *8*, 363. [[CrossRef](#)]
70. Sekimoto, S.; Fujii, K.; Anyoji, M.; Miyakawa, Y.; Ito, S.; Shimomura, S.; Nishida, H.; Nonomura, T.; Matsuno, T. Flow Control around NACA 0015 Airfoil Using a Dielectric Barrier Discharge Plasma Actuator over a Wide Range of the Reynolds Number. *Actuators* **2023**, *12*, 43. [[CrossRef](#)]
71. Austin, R. *Unmanned Aircraft Systems: UAVs Design, Development and Deployment*; American Institute of Aeronautics and Astronautics: Reston, VA, USA; Chichester, UK, 2010.
72. Chicos, L.-A.; Pop, M.A.; Zaharia, S.-M.; Lancea, C.; Buican, G.R.; Pascariu, I.S.; Stamate, V.-M. Infill Density Influence on Mechanical and Thermal Properties of Short Carbon Fiber-Reinforced Polyamide Composites Manufactured by FFF Process. *Materials* **2022**, *15*, 3706. [[CrossRef](#)]
73. Chicos, L.-A.; Pop, M.A.; Zaharia, S.-M.; Lancea, C.; Buican, G.R.; Pascariu, I.S.; Stamate, V.-M. Fused Filament Fabrication of Short Glass Fiber-Reinforced Polylactic Acid Composites: Infill Density Influence on Mechanical and Thermal Properties. *Polymers* **2022**, *14*, 4988. [[CrossRef](#)] [[PubMed](#)]
74. Zaharia, S.M.; Pop, M.A.; Chicos, L.-A.; Buican, G.R.; Lancea, C.; Pascariu, I.S.; Stamate, V.-M. Compression and Bending Properties of Short Carbon Fiber Reinforced Polymers Sandwich Structures Produced via Fused Filament Fabrication Process. *Polymers* **2022**, *14*, 2923. [[CrossRef](#)] [[PubMed](#)]
75. Lancea, C.; Chicos, L.-A.; Zaharia, S.-M.; Pop, M.-A.; Pascariu, I.S.; Buican, G.-R.; Stamate, V.-M. Simulation, Fabrication and Testing of UAV Composite Landing Gear. *Appl. Sci.* **2022**, *12*, 8598. [[CrossRef](#)]
76. Zaharia, S.-M.; Pop, M.A.; Buican, G.R.; Chicos, L.-A.; Stamate, V.M.; Pascariu, I.S.; Lancea, C. Design and Testing of Brushless DC Motor Components of A6 Steel Additively Manufactured by Selective Laser Sintering. *Aerospace* **2023**, *10*, 60. [[CrossRef](#)]
77. Dündar, Ö.; Bilici, M.; Ünler, T. Design and performance analyses of a fixed wing battery VTOL UAV. *Eng. Sci. Technol. Int. J.* **2020**, *23*, 1182–1193. [[CrossRef](#)]
78. Reid, W.A.; Albayati, I.M. Design of an unmanned aircraft system for high-altitude 1 kW fuel cell power system. *Aerosp. Syst.* **2021**, *4*, 353–363. [[CrossRef](#)]
79. Götten, F.; Finger, D.; Braun, C.; Havermann, M.; Bil, C.; Gómez, F. Empirical correlations for geometry build-up of fixed wing unmanned air vehicles. In Proceedings of the Asia-Pacific International Symposium on Aerospace Technology, Chengdu, China, 16–18 October 2018; Springer: Singapore, 2018; pp. 1365–1381.
80. Raymer, D. *Aircraft Design: A Conceptual Approach*, 6th ed.; American Institute of Aeronautics and Astronautics: Washington, DC, USA, 2018.
81. Barnhart, R.K.; Marshall, D.M.; Shappee, E. *Introduction to Unmanned Aircraft Systems*; CRC Press: Boca Raton, FL, USA, 2021.
82. Anderson, J.D. *Aircraft Performance and Design*; McGraw-Hill: New York, NY, USA, 1999.
83. Sholz, D. Empennage sizing with the tail volume complemented with a method for dorsal fin layout. *INCAS Bull.* **2021**, *13*, 149–164. [[CrossRef](#)]

84. Keane, A.J.; Sóbester, A.; Scanlan, J.P. *Small Unmanned Fixed-Wing Aircraft Design: A Practical Approach*; John Wiley & Sons: Hoboken, NJ, USA, 2017.
85. Sadraey, M.H. *Aircraft Design: A Systems Engineering Approach*; Aerospace Series; Wiley: Chichester, UK, 2013; ISBN 978-1-119-95340-1.
86. Ahmad, M.; Hussain, Z.L.; Shah, S.I.A.; Shams, T.A. Estimation of Stability Parameters for Wide Body Aircraft Using Computational Techniques. *Appl. Sci.* **2021**, *11*, 2087. [[CrossRef](#)]
87. Humphreys-Jennings, C.; Lappas, I.; Sovar, D.M. Conceptual Design, Flying, and Handling Qualities Assessment of a Blended Wing Body (BWB) Aircraft by Using an Engineering Flight Simulator. *Aerospace* **2020**, *7*, 51. [[CrossRef](#)]
88. Ultrafuse PAHT CF15, Technical Data Sheet. Available online: https://www.ultrafuseeff.com/wp-content/uploads/2019/06/Innofil3D_PAHT_PET_CF15_Factsheet-online.pdf (accessed on 26 March 2023).
89. Filaticum Glass Reinforced. Available online: <https://filaticum.com/en/product/philament-glass-reinforced/> (accessed on 26 March 2023).
90. Pop, M.A.; Zaharia, S.M.; Chicos, L.A.; Lancea, C.; Stamate, V.M.; Buican, G.R.; Pascariu, I.S. Effect of the infill patterns on the mechanical properties of the carbon fiber 3D printed parts. In Proceedings of the 25th Edition of Innovative Manufacturing Engineering & Energy International Conference—IMANEE, Iasi, Romania, 21–23 October 2021.
91. Ismail, K.I.; Yap, T.C.; Ahmed, R. 3D-Printed Fiber-Reinforced Polymer Composites by Fused Deposition Modelling (FDM): Fiber Length and Fiber Implementation Techniques. *Polymers* **2022**, *14*, 4659. [[CrossRef](#)] [[PubMed](#)]
92. Wickramasinghe, S.; Do, T.; Tran, P. FDM-Based 3D Printing of Polymer and Associated Composite: A Review on Mechanical Properties, Defects and Treatments. *Polymers* **2020**, *12*, 1529. [[CrossRef](#)] [[PubMed](#)]
93. Ammarullah, M.I.; Hartono, R.; Supriyono, T.; Santoso, G.; Sugiharto, S.; Permana, M.S. Polycrystalline Diamond as a Potential Material for the Hard-on-Hard Bearing of Total Hip Prosthesis: Von Mises Stress Analysis. *Biomedicines* **2023**, *11*, 951. [[CrossRef](#)] [[PubMed](#)]
94. Grodzki, W.; Łukaszewicz, A. Design and manufacture of unmanned aerial vehicles (UAV) wing structure using composite materials. *Mater. Werkst.* **2015**, *46*, 269–278. [[CrossRef](#)]
95. Zakaria, M.; Abdallah, M.M.; Elshafie, M.A. Design and production of small tailless unmanned aerial vehicle (SAKR 2). In Proceedings of the 15-th International Conference on Applied Mechanics and Mechanical Engineering—AMME, Cairo, Egypt, 29–31 May 2012.
96. Betancourth, N.J.P.; Villamarin, J.E.P.; Rios, J.J.V.; Bravo-Mosquera, P.D.; Cerón-Muñoz, H.D. Design and manufacture of a solar-powered unmanned aerial vehicle for civilian surveillance missions. *J. Aerosp. Technol. Manag.* **2016**, *8*, 385–396. [[CrossRef](#)]

Disclaimer/Publisher’s Note: The statements, opinions and data contained in all publications are solely those of the individual author(s) and contributor(s) and not of MDPI and/or the editor(s). MDPI and/or the editor(s) disclaim responsibility for any injury to people or property resulting from any ideas, methods, instructions or products referred to in the content.

Article

Sound Absorption Performance and Mechanical Properties of the 3D-Printed Bio-Degradable Panels

Sebastian-Marian Zaharia ¹, Mihai Alin Pop ^{2,*}, Mihaela Cosnita ³, Cătălin Croitoru ⁴, Simona Matei ²
and Cosmin Spîrchez ⁵

- ¹ Department of Manufacturing Engineering, Transilvania University of Brasov, 500036 Brasov, Romania; zaharia_sebastian@unitbv.ro
- ² Department of Materials Science, Transilvania University of Brasov, 500036 Brasov, Romania; simona.matei@unitbv.ro
- ³ Department of Product Design, Mechatronics and Environment, Transilvania University of Brasov, 500036 Brasov, Romania; mihaela.cosnita@unitbv.ro
- ⁴ Materials Engineering and Welding Department, Transilvania University of Brasov, 500036 Brasov, Romania; c.croitoru@unitbv.ro
- ⁵ Wood Processing and Design Wooden Product Department, Transilvania University of Brasov, 500036 Brasov, Romania; cosmin.spirchez@unitbv.ro
- * Correspondence: mihai.pop@unitbv.ro

Abstract: The 3D printing process allows complex structures to be obtained with low environmental impact using biodegradable materials. This work aims to develop and acoustically characterize 3D-printed panels using three types of materials, each manufactured at five infill densities (20%, 40%, 60%, 80% and 100%) with three internal configurations based on circular, triangular, and corrugated profiles. The highest absorption coefficient values ($\alpha = 0.93$) were obtained from the acoustic tests for the polylactic acid material with ground birch wood particles in the triangular configuration with an infill density of 40%. The triangular profile showed the best acoustic performance for the three types of materials analysed and, from the point of view of the mechanical tests, it was highlighted that the same triangular configuration presented the highest resistance both to compression (40 MPa) and to three-point bending (50 MPa). The 40% and 60% infill density gave the highest absorption coefficient values regardless of the material analyzed. The mechanical tests for compression and three-point bending showed higher strength values for samples manufactured from simple polylactic acid filament compared to samples manufactured from ground wood particles. The standard defects of 3D printing and the failure modes of the interior configurations of the 3D-printed samples could be observed from the microscopic analysis of the panels. Based on the acoustic results and the determined mechanical properties, one application area for these types of 3D-printed panels could be the automotive and aerospace industries.

Keywords: 3D printing; acoustic properties; mechanical properties; bio-degradable panels



Citation: Zaharia, S.-M.; Pop, M.A.; Cosnita, M.; Croitoru, C.; Matei, S.; Spîrchez, C. Sound Absorption Performance and Mechanical Properties of the 3D-Printed Bio-Degradable Panels. *Polymers* **2023**, *15*, 3695. <https://doi.org/10.3390/polym15183695>

Academic Editors: Santiago Ferrandiz and Dana Luca Motoc

Received: 24 July 2023

Revised: 2 September 2023

Accepted: 4 September 2023

Published: 7 September 2023



Copyright: © 2023 by the authors. Licensee MDPI, Basel, Switzerland. This article is an open access article distributed under the terms and conditions of the Creative Commons Attribution (CC BY) license (<https://creativecommons.org/licenses/by/4.0/>).

1. Introduction

In recent times, with the development of modern industry and air and road traffic, noise has become one of the countless factors affecting human health and the environment worldwide. Noise has become a major problem that causes harmful effects on human health, and combating it requires urgently finding the best solutions through increasingly restrictive regulations and legislation [1,2]. Lately, the improvement of living conditions by regulating noise in the fields of aviation (by reducing the interior noise of passenger aircraft), railways, automobiles and buildings is a requirement forced on industrial companies [3].

In modern industry, noise is one of the most urgent issues to be addressed, researched, and reduced using sound-absorbing materials. For sound reduction, structural design and testing of sound absorption and sound transmission loss of industrial products is

challenging and of great interest [4–6]. Nowadays, various types of natural materials [7–9], composite materials [10–13] and composite sandwich structures [14–17] are acoustically researched because of their low production cost and often environmentally friendly compositions. The application of 3D-printed materials in the aerospace and automotive industry involves higher expenses that are especially justified for prototypes and customized components. In general, the materials used with the FFF process have much lower costs compared to classic technologies (plastic mass injection of components) or additive technologies such as SLS. When sound reaches a barrier, depending on the sound absorption performance of the material, six phenomena can occur: absorption, transmission, reflection, refraction, scattering and diffraction [18].

The main coefficients that evaluate the acoustic performance of materials are the sound absorption coefficient and sound transmission loss [19]. The sound absorption coefficient reflects the ratio between reflected and incident sound intensity (W/m^2). The proper physical quantity is sound intensity, and it varies as a function of the frequency [20,21] and angle [22] at which a sound or sound wave reaches the material under test. Sound transmission loss is the ratio of the transmitted sound energy to the amount of sound energy remaining on the incident side of the material under test. For the design and manufacture of industrial products requiring high acoustic performance, material selection and acoustic testing of selected materials are two very important activities. From the reviewed studies [23–27], the most important factor influencing the acoustic performance of materials is the porosity value.

Currently, additive manufacturing processes using plastics, composites and metallics are considered the most developed and researched processes, which, in the near future, could play a role in traditional manufacturing processes in many industries (aerospace, automotive, marine engineering, medical and many others). Thus, the most used manufacturing process for the development of porous structures subject to acoustic performance studies is fused filament fabrication (FFF) or 3D printing. In a recent study [28] the acoustic performance of a 3D-printed biodegradable material with bubble holes of different sizes was analysed. The results showed improved performance for different sizes of spherical bubbles and different types of hole patterns in the low-frequency range up to 1000 Hz.

Sailesh et al. [29] used polylactic acid (PLA) granules to manufacture perforated samples with different cross-sections via the FFF process for the purpose of determining acoustic indicators. It was found that the maximum values of the sound absorption coefficient are obtained in the range 500–1000 Hz. Other studies [30,31] have shown a significant influence of pore shape, volume ratio, material thickness, and air gap size of 3D-printed acrylonitrile butadiene styrene filament (ABS) structures on acoustic performance. Zielinski et al. [32] proposed and acoustically analyzed a sound-absorbing material, whose acoustic performance resulted not only from the designed pore network but also from the microporosity of the material used during the additive manufacturing process. In this way, a dual porosity material was successfully designed, modelled, and manufactured based on the imperfections of the materials in the manufacturing process to obtain high acoustic performance. Errico et al. [33] studied the vibro-acoustic behaviour of 3D-printed panels using periodic structure theory over a wide frequency range (1000–10,000 Hz). Boulvert et al. [34] 3D printed micro-lattices to study the manufacturing accuracy and prediction of its absorption characteristics using the Johnson–Champoux–Allard–Lafarge (JCAL) model in order to draw conclusions about the defects of the 3D printing process. Thus, the accuracy was affected by the nozzle cross-section shape, which was about 8%, but there were also deviations attributed to thermal shrinkage and micro-grooves of the nozzle. Reentrant auxetic structures are used in various noise reduction applications (in the automotive and aerospace fields). Hence, such cellular structures were modelled and fabricated [35] using keratin-reinforced polylactic acid, which were 3D printed and were able to reduce noise as they reduce the voids and airflow.

With the development of additive manufacturing processes, there is a trend towards the development of acoustically absorbent metamaterials capable of controlling, guid-

ing, and manipulating low- and medium-frequency acoustic waves. Gao and Hou [36] researched the sound absorption coefficient of a 3D-printed polylactic acid microhelix metamaterial. Their research found that the sound absorption coefficient values improve as the gap between the micro-helices increases.

Other studies [37,38] have researched the acoustic properties of multi-layer perforated panels manufactured by additive manufacturing processes (selective laser sintering and stereolithography). The SLA additive process was used to manufacture porous polycarbonate samples to study the effects of hole angle and air gap on sound absorption [39]. The results revealed that increasing the angle of inclination of the pores reduced the value of the sound absorption coefficient when the porosity was kept constant. Jiang et al. [40] researched the feasibility of manufacturing materials by the MultiJet 3D printing process and determined the sound absorption capability of materials with different geometrical parameters (porosity, hole diameter, sample thickness and effect of aspect ratio). The results indicated that the maximum absorption coefficients ranged from 0.24 to 0.99, and for the samples to have good sound absorption performance, they were tested at high frequencies from 4800 Hz to 6400 Hz.

In the research [41], the sound absorption of a micro-perforated panel (MPP) manufactured by the 3D printing process was investigated, and the sound absorption coefficient of a 3D-printed MPP layer supported with a porous material was measured and theoretically predicted using the transfer matrix method (TMM). Moreover, another study available in the literature argued for the use of microstructures with relatively simple pores, such as parallel, identical, and inclined apertures, for the analysis of broadband sound absorption through analytical and additively manufactured models [42]. Sekar et al. [43] focused on the study of micro-perforated panels (MPP) made of polylactic acid (PLA) reinforced with wood fibres fabricated using the FFF process. Acoustic test results indicated that changing the perforation volume affects the acoustic absorption of the MPP. MPP with a thickness of 2 mm and a perforation diameter of 0.2 mm presents a maximum sound absorption coefficient value of 0.93 at a frequency of 2173 Hz.

Currently, numerous studies are aimed at developing sustainable and high-performance materials for manufacturing perforated panels from natural resources. However, obtaining complex holes with different geometries from different materials is an issue that requires detailed acoustic studies and analysis. Therefore, in this study, the acoustic behaviour of perforated panels consisting of three types of materials (PLA with a mixture of 40% ground coconut wood particles, PLA with a mixture of 40% ground birch wood particles and plain PLA) manufactured via the FFF process and were tested using plane rolling waves with an incident perpendicular to the tested surface (tube method). Acoustic analysis of the panels was carried out for five values of infill density (20%, 40%, 60%, 80% and 100%), with three internal configurations (circular profile, triangular profile and corrugated profile). The panel configurations with the best acoustic performance were manufactured via the FFF process and were mechanically tested (compression and bending). Figure 1 briefly describes the organisation of this study.

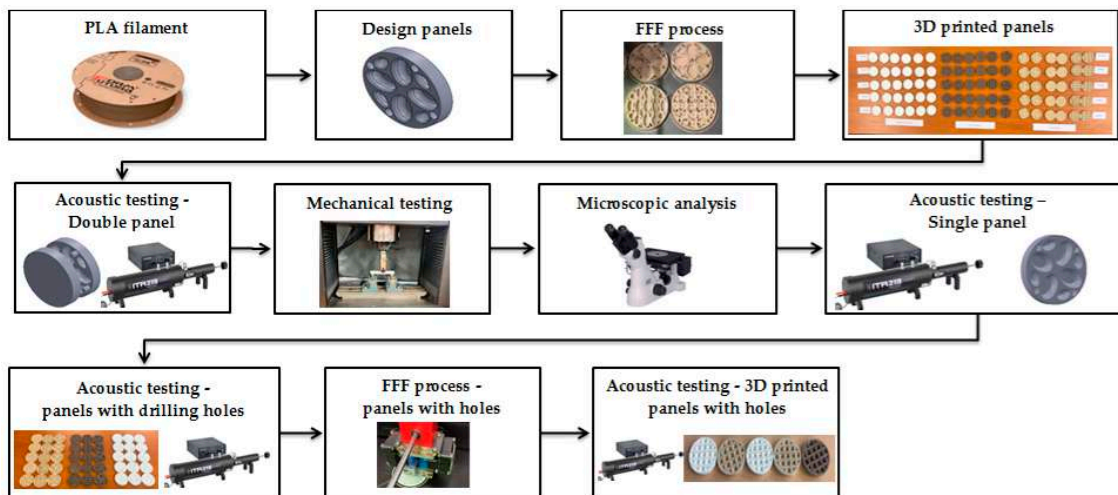


Figure 1. Flow chart of the present study.

2. Materials and Methods

2.1. Design of the Panels

The sample design was carried out in the SolidWorks 2016 software system considering the standards specific to acoustic testing [44,45] and compression and bending testing of sandwich panels [46,47]. The 3D-printed samples for acoustic testing have the following dimensions (Table 1): the upper and lower parts have diameters of 50 mm, thicknesses of 8 mm and holes of 4.2 mm required for the assembly of the two parts. These dimensions are in accordance with the standard as well as with the technical characteristics of the impedance tube. The stages of the acoustic tests and the three-dimensional models of the samples are presented in Table 1 as follows: in the first stage the double panels were tested; the second stage consisted of testing the single panels; the third stage was dedicated to testing the single panels on which holes were drilled by means of a 3D-printed template; and in the last stage, the panels were 3D printed with a triangular internal configuration and a rhombic profile. A side of 1.8 mm was chosen for the holes.

Table 1. The 3D-printed samples used for acoustic testing.

	Acoustic Test Specimens			
	Double panel	Single panel	Panels with drilling holes (Drill gage)	3D-printed panels with holes
Circular profile				
Triangular profile				

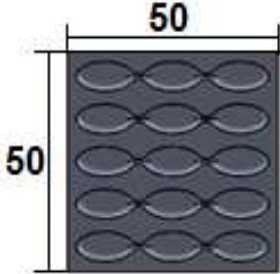
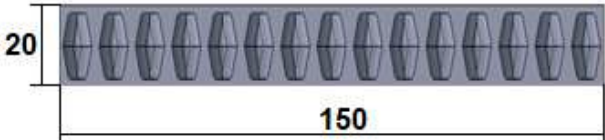
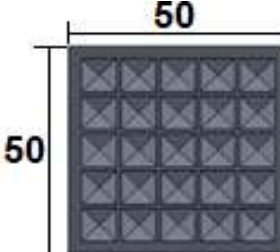
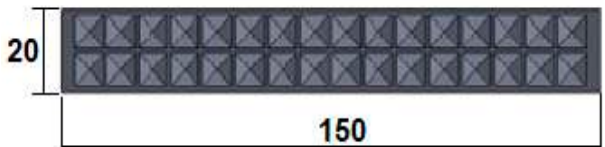
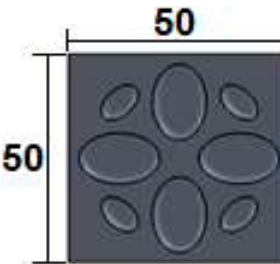
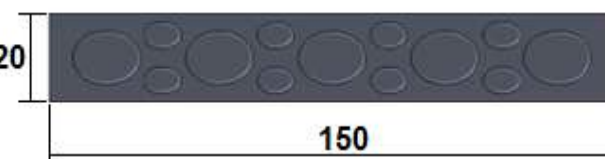
Table 1. Cont.

		Acoustic Test Specimens			
		Double panel	Single panel	Panels with drilling holes (Drill gage)	3D-printed panels with holes
Corrugated profile					

The aim was to compare the way the shape of the gaps influences the sound-absorbing properties. The modes of reflection and absorption of sound waves were a circular profile (gaps that are not interconnected), an interconnected corrugated one (interconnected ovate gaps) and a triangular one (walls with right angles). Those three cases, in our opinion, can cover a large area of cases encountered in practice.

The dimensions of the samples tested at compression were a width of 50 mm and a thickness of 15 mm (Table 2). The samples for the three-point bending tests were manufactured via the FFF process with the following dimensions: length 150 mm, width 20 mm, and thickness 15 mm (Table 2). For the acoustic testing of the 3D-printed specimens, the (ASTM) E1050 [44] and ISO 10534-2 [45] standards were followed.

Table 2. The 3D-printed samples used for mechanical testing.

		Compression Test Specimens		Three-Point Bending Test Specimens	
Circular profile	Section view		Section view		
Triangular profile	Section view		Section view		
Corrugated profile	Section view		Section view		

2.2. Materials Properties

The samples for the experimental tests (acoustic and mechanical) were manufactured from three types of materials: standard PLA [45], PLA with a mixture of 40% ground coconut wood particles [48] and PLA with a mixture of 40% ground birch wood particles. According to the information provided by the filament manufacturer, the particle size of birch and coconut is between 70 and 140 μm [48].

PLA material is one of the most used thermoplastic polymeric materials suitable for the FFF process. PLA has the following advantages [49–51]: it is a low-cost biodegradable polymer; it is very easy to manufacture via the FFF process; it is the best material in terms of dimensional accuracy (it does not undergo deformation during the FFF process nor after cooling); it has good adhesion to the bed plate but also between the extruded layers of material and during the manufacturing process, unpleasant smells are not emitted. PLA reinforced with 40% ground wood particles as a filament very easy to manufacture via the FFF process as it uses the PLA as base (matrix) material and has several important advantages [48,52]: it is a biodegradable material that is easy to manufacture; it has a wood-like smell and appearance; it has good adhesion in the first layer of manufacturing.

2.3. Manufacturing Process of the 3D-Printed Panels

The three types of filaments (PLA coconut, PLA birch and PLA) with different mechanical properties were used for the FFF manufacture of 3D-printed bio-degradable perforated panels. The 3D-printed panels were manufactured via the FFF process with the CreatBot DX-3D double-nozzle printer (Henan Suwei Electronic Technology Co., Ltd., Zhengzhou, China). The manufacturing parameters settings were selected according to the filament type and were controlled via the 3D printing slicing software CreatBot V6.5.2. The main 3D printing parameters of printed panels with the 3 types of filaments are presented in Table 3.

Table 3. FFF parameters of the 3D-printed panels.

Parameter	Value		
	PLA Coconut	PLA Birch	PLA
Filament diameter	2.85 [mm]	2.85 [mm]	2.85 [mm]
Layer height	0.2 [mm]	0.2 [mm]	0.2 [mm]
Infill density	20; 40; 60; 80; 100 [%]	20; 40; 60; 80; 100 [%]	20; 40; 60; 80; 100 [%]
Print speed	50 [mm/s]	50 [mm/s]	40 [mm/s]
Travel speed	120 [mm/s]	120 [mm/s]	120 [mm/s]
Printing temperature	240 [°C]	240 [°C]	240 [°C]
Building plate temperature	50 [°C]	50 [°C]	60 [°C]
Infill pattern	cubic	cubic	cubic
Hotend	0.4 [mm]	0.4 [mm]	0.4 [mm]

2.4. Acoustic Testing

The sound absorption behaviour of samples manufactured via the FFF process was researched using a Holmarc HO-ED-A-03 acoustic impedance tube (Holmarc Opto-Mechatronics Ltd. Kochi, India), which was equipped with the following: hollow tubes, two pairs of microphones, sample holders, a data acquisition system and measurement software. The impedance system contains an anodised aluminium tube with an internal diameter of 50 mm, which can measure in the frequency range 500–3150 Hz.

In this study, the frequency dependencies of the sound absorption coefficient (α) and the sound transmission loss (STL) of 3D-printed samples were investigated by the transfer function method according to the current standards [44,45]. Figure 2a shows the components of the impedance tube system used for acoustic testing. Figure 2b shows the two schematic configurations of the impedance tube system by means of which the acoustic performance of 3D-printed samples can be determined: for the determination of the sound absorption coefficient, the system also contains the anechoic termination component, and

for the sound transmission loss, this anechoic termination component has been removed. For each tested sample, the geometric parameters of the samples (50 mm), microphone spacing (30 mm), temperature and humidity recorded at each current test were entered.

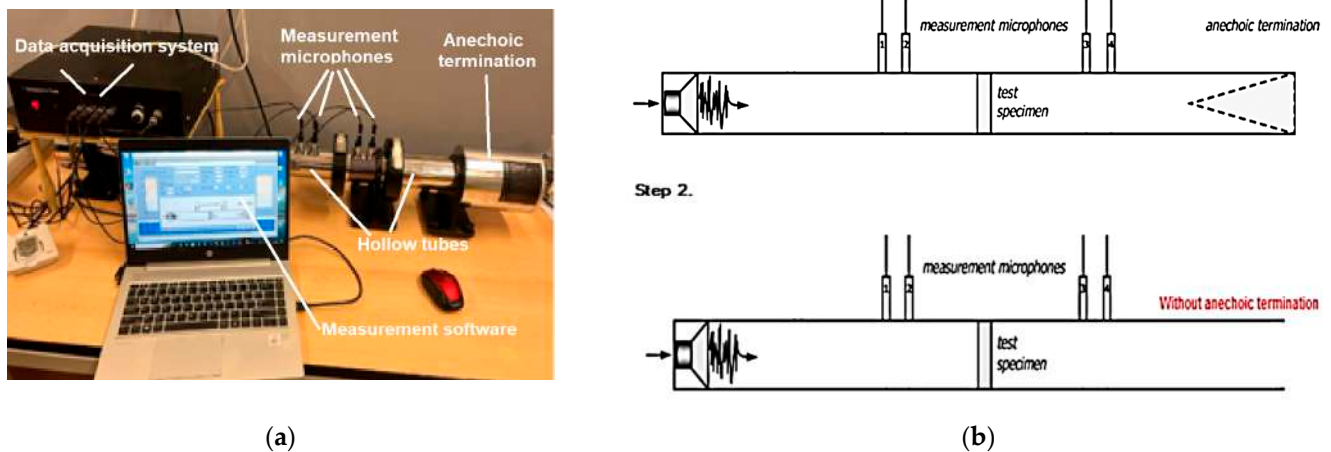


Figure 2. Experimental setup of the acoustic testing: (a) Equipment used for acoustic testing of samples manufactured via the FFF process; (b) Method of measurement of the sound absorption coefficient and of the sound transmission loss.

2.5. Mechanical Testing

Mechanical tests were carried out using the W-150 S universal testing machine (Jinan Testing Equipment IE Corporation, Jinan, China). Compression testing (Figure 3a) was carried out at a loading speed of 5 mm/min according to the current standards [46,47] and highlights the behaviour and response of the 3D-printed bio-degradable panels under a compressive load by measuring the fundamental characteristics (compressive strength and load–displacement curves). The 3D-printed samples were tested in three-point bending according to the requirements of the standards [46,47] in order to determine the key characteristics (bending strength and load–displacement curves). Five samples were tested according to the standards for testing sandwich structures for both types of tests (compression and three-point bending).

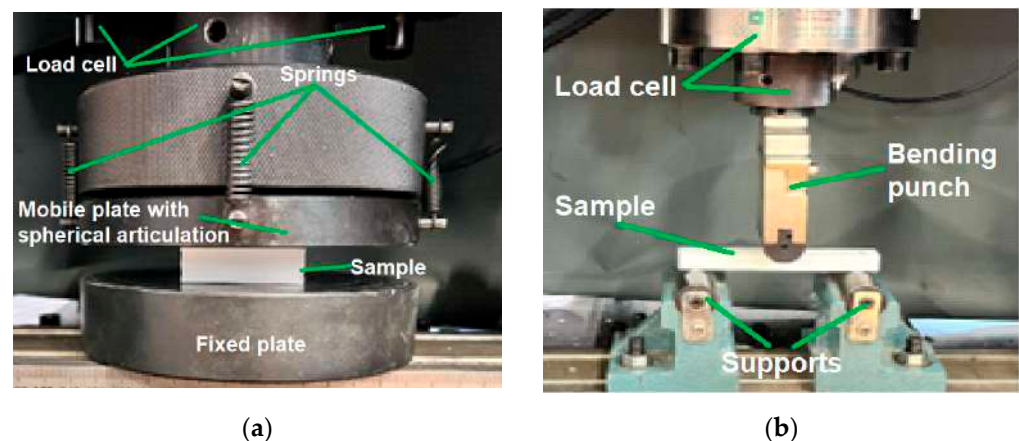


Figure 3. Mechanical testing: (a) Compression testing of the 3D-printed panels; (b) Three-point bending testing of the 3D-printed panels.

2.6. Microscopic Analysis

Electronic Nikon Eclipse MA 100 microscopes (Nikon Corp., Tokyo, Japan) were used to examine the condition of the 3D-printed structures after compression testing in order to detect typical defects and specific failure modes.

3. Results and Discussion

3.1. The Effect of Filling Density on the Acoustic Performance of 3D-Printed Double Panels

Double panels have been designed as consisting of two half-panels (demountable assembly), dedicated to repairs when necessary (damage of only one surface) thus achieving a reduction in manufacturing time and costs associated with their manufacture by replacing only the damaged half-panel. Ultimately, the panels are designed and manufactured in mirror image to each other, thus obtaining as large internal voids as possible, which causes a decrease in the mass of the panel and implies an economy of material and reduced costs.

Analysing all the experimental data obtained for the 3D-printed panels, graphs are drawn for all the samples to observe the differences and variations of the sound absorption coefficient and loss transmission as a function of frequency.

In the first stage of the study, a design was made of the three types of filaments (PLA coconut, PLA birch, and PLA) and with the five types of infill density (20%, 40%, 60%, 80% and 100%) in order to characterize the acoustic performance of those three types of materials. Since the sound absorption coefficient is a ratio of reflected to incident sound energy, a value of 0 indicates complete reflection with no absorption [53]. On the other hand, the value of 1 of the absorption coefficients shows that all the sound energy is absorbed without reflection [53].

For the first acoustic tests (Figure 4), double panel assemblies were used, where the fill density varied as follows: 20%, 40%, 60%, 80% and 100%. These fill density variations were analysed on three types of filaments (PLA–birch, PLA–coconut and PLA) using the three profiles (circular, triangular, and corrugated/undulated). Thus, a total of 45 acoustic tests were carried out for the 3D-printed double panels, where the two most important parameters were determined: sound absorption coefficient (SAC, α) and the sound transmission loss (STL).

For each type of material, the curves for the highest values of sound absorption coefficient (α) were plotted. The markings on the figures are as follows: 20%, 40%, 60%, 80% and 100%. These represent the infill densities for circular, triangular, and corrugated; they are the internal configurations used and PLA–birch, PLA–coconut and PLA represent the materials from which the samples are made. In the case of the double panels, manufactured via the FFF process, the following can be noticed: for the PLA–birch filament, the highest value of sound absorption coefficient ($\alpha = 0.4$) was for the 100% corrugated sample at low frequencies (500 Hz), and the highest value for sound transmission loss (STL = 63 dB) was for 60% corrugated; for the PLA–coconut filament, the highest value of sound absorption coefficient ($\alpha = 0.33$) was for the 40% triangular sample at low frequencies (500 Hz), and the highest value for sound transmission loss (STL = 64 dB) was for 80% triangular; for the PLA filament, the highest value for sound absorption coefficient ($\alpha = 0.36$) was for the 80% triangular sample at low frequencies (500 Hz), and the highest value for sound transmission loss (STL = 62 dB) was for 20% circular.

It can therefore be concluded that the variation of the filling density influences the acoustic performance, and samples with lower filling density result in a higher absorption coefficient. Decreasing the filling density improves the passage of acoustic waves entering the panel, and the air inside the voids can now move easily, which increases the viscous friction, causing a loss of acoustic wave energy and, thus, the sound is absorbed more efficiently [54].

Also, acoustic analyses cannot clearly establish a filling density that shows superior performance compared to the others for all filament types analysed. This finding is based on the typical defects (voids, inter-track voids between the layers) that occur in the parts manufactured via the FFF process [55,56]. In contrast, at this stage, when analysing double panels, it can be concluded that the PLA–birch filament showed the highest sound absorption coefficient ($\alpha = 0.4$). At the same time, the sound transmission loss presented the highest value (STL = 64 dB) in the PLA–birch–triangular configuration at 80% filling density. On the other hand, when analysed in terms of internal configurations, it can be deduced that the triangular configuration type shows the highest values of absorption

coefficient and sound transmission loss in two of the three configurations. The triangular configuration shows higher absorption due to the cell walls interacting with the ultrasonic wave along the in-plane direction [57].

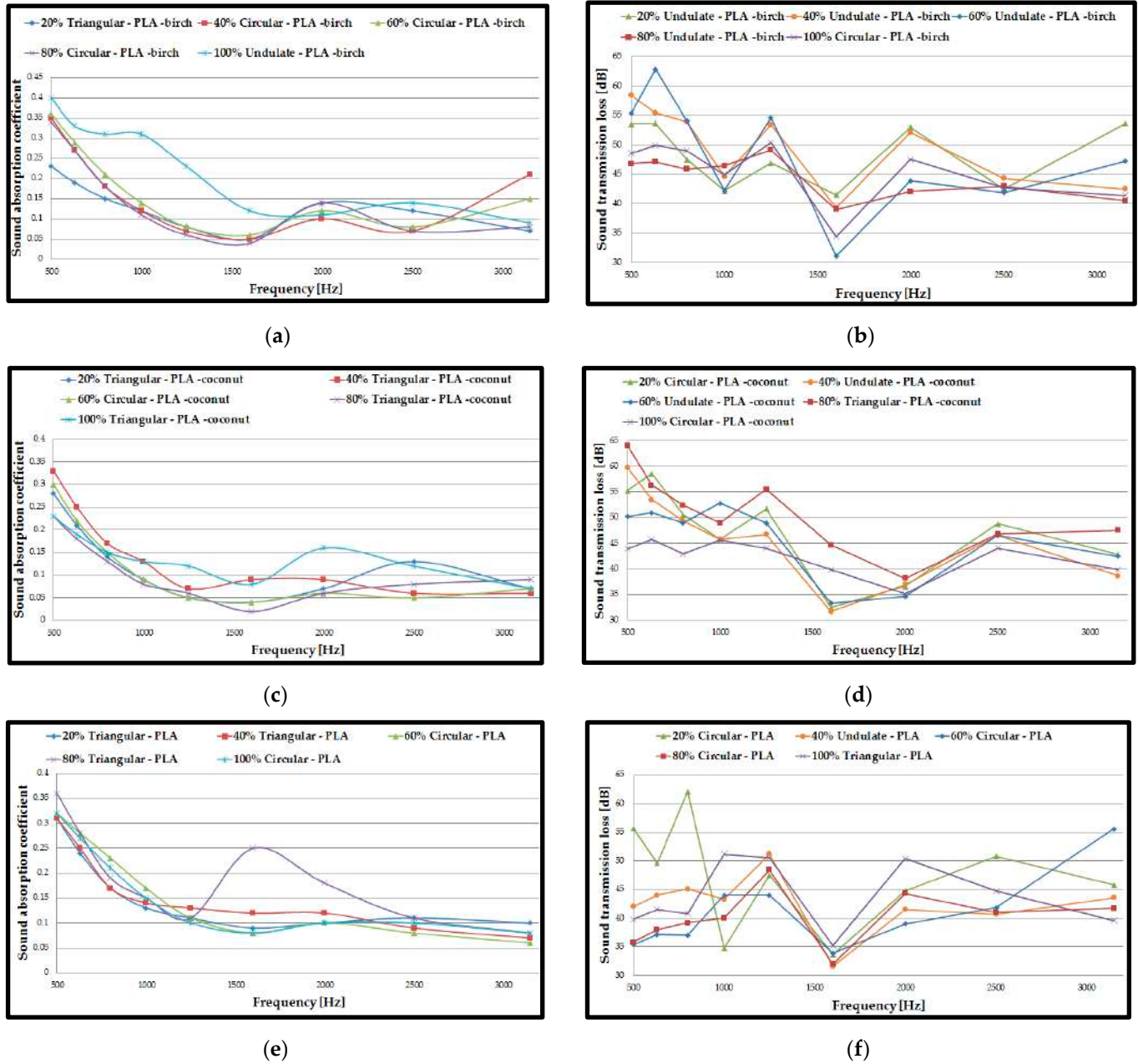


Figure 4. Acoustic test results of assembled double panels: (a) Sound absorption coefficient of PLA–birch samples; (b) Sound transmission loss of PLA–birch samples; (c) Sound absorption coefficient of PLA–coconut samples; (d) Sound transmission loss of PLA–coconut samples; (e) Sound absorption coefficient of PLA samples; (f) Sound transmission loss of PLA samples.

The highest sound absorption coefficient was at the frequency of 500 Hz, namely 0.4 for the PLA–birch–triangular configuration at 80% infill density. The results obtained indicate that approximately 60% of the sound energy is reflected without penetrating the surface of the test specimen. From the results of the acoustic tests, the highest sound absorption coefficient is found at low frequencies (500 Hz), which indicates that the specimen acts as a deflector that transfers the vibro-acoustic energy, providing some damping [53].

Also, the difference between the highest and lowest values of the absorption coefficient was 0.07, which indicates a low absorption of the three types of materials manufactured via the FFF process. The sound absorption coefficient represents an important result in the acoustic tests of the materials (PLA–coconut, PLA–birch, and PLA), but it is not the only significant result. Increased importance is also given to the sound transmission loss parameter for 3D-printed specimens, through which a characterization of a specimen's ability to block sound can be performed.

In the case of these double panels, the alpha coefficient decreases with increasing frequency and the LTR increases very slightly with increasing test frequency.

3.2. Mechanical Performance of 3D-Printed Double Panels

From the results of the acoustic tests, two basic criteria were set for determining the samples to be subjected to mechanical tests: the samples with the highest absorption coefficient depending on the material and the samples with the highest absorption coefficient depending on the profile configuration. Thus, for the three-point compression and bending mechanical testing, four sample configurations were manufactured and tested: 60% circular PLA–birch, 100% corrugated PLA–birch, 40% triangular–PLA–coconut, 80% triangular–PLA. Two configurations (80% triangular–PLA and 100% corrugated PLA–birch) showed the best acoustic performance on both criteria analysed. Five samples were tested for each type of test (compression and three-point bending).

The results of the compression tests were presented below as load–displacement characteristic curves (Figure 5a) for each type of 3D-printed structure. Analysing Figure 5a and considering the numerical results provided by the testing machine in the test report, the maximum breaking force of the 80% triangular–PLA sample reached the maximum value of 90 kN at a displacement of 2.75 mm during the compression process. On the other hand, the 40% triangular–PLA–coconut sample showed the lowest maximum compression force of about 23 kN. For the five samples tested, in each configuration, the average values of compressive strength and compressive modulus of elasticity were calculated and plotted (Figure 5b). The average compressive strength value of the 80% triangular–PLA samples showed the highest value of about 40 MPa. From the analysis of the tested samples, it can be deduced that the parts with a mixture of 40% ground birch and coconut wood particles show close values of compressive strength, but not exceeding 13 MPa.

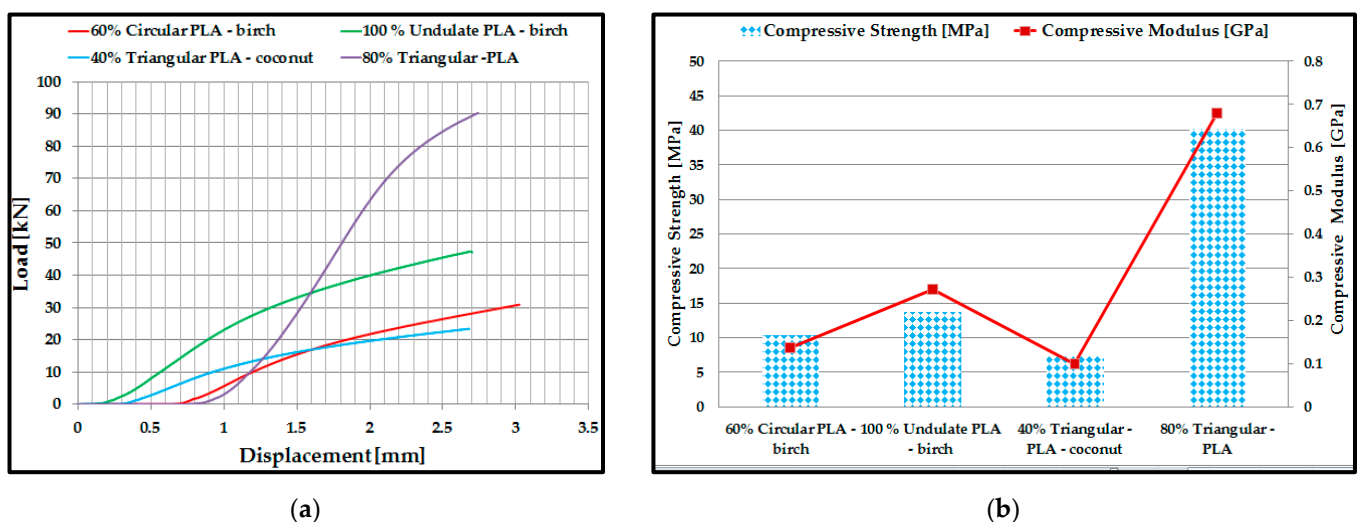


Figure 5. Compression test results: (a) Load–displacement characteristic curves; (b) Compressive strength and modulus of elasticity for 3D-printed samples.

This was due to the lower mechanical performance of the ground wood introduced in this type of filament, i.e., the weaker adhesion between the matrix (PLA) and the ground

wood. Another important aspect is the choice of the configuration type for the 3D-printed samples. It is observed that the triangular profile absorbs the compressive stress much better compared to the other two profiles (circular and corrugated) due to the high-stiffness inner walls.

Following the three-point bending tests of the 3D-printed samples, the characteristic curves of the four types of samples and the bending performance (bending strength and modulus of elasticity) were determined. In this case, the 80% triangular-PLA samples also showed the best three-point bending performance. This is due to the specific bending behaviour: during loading, both tensile (on the lower shell) and compressive (on the upper shell) stresses occur simultaneously in the 3D-printed sample, and the core, in this case, is shear stressed. Core shear occurs quite late because the triangular configuration has very strong walls that maintain the structure during loading. The tests showed that the maximum breaking force of the 80% triangular-PLA sample reached a maximum value of 1.58 kN at a displacement of 6.3 mm during the stretching process (Figure 6a). The maximum value of the bending strength was obtained for the 80% triangular-PLA samples. Analysing the other types of samples made of ground wood, it can be observed that the highest bending strength (Figure 6b) is shown by the 100% corrugated PLA-birch samples due to the 100% filling density, which was confirmed in other recent studies [58,59].

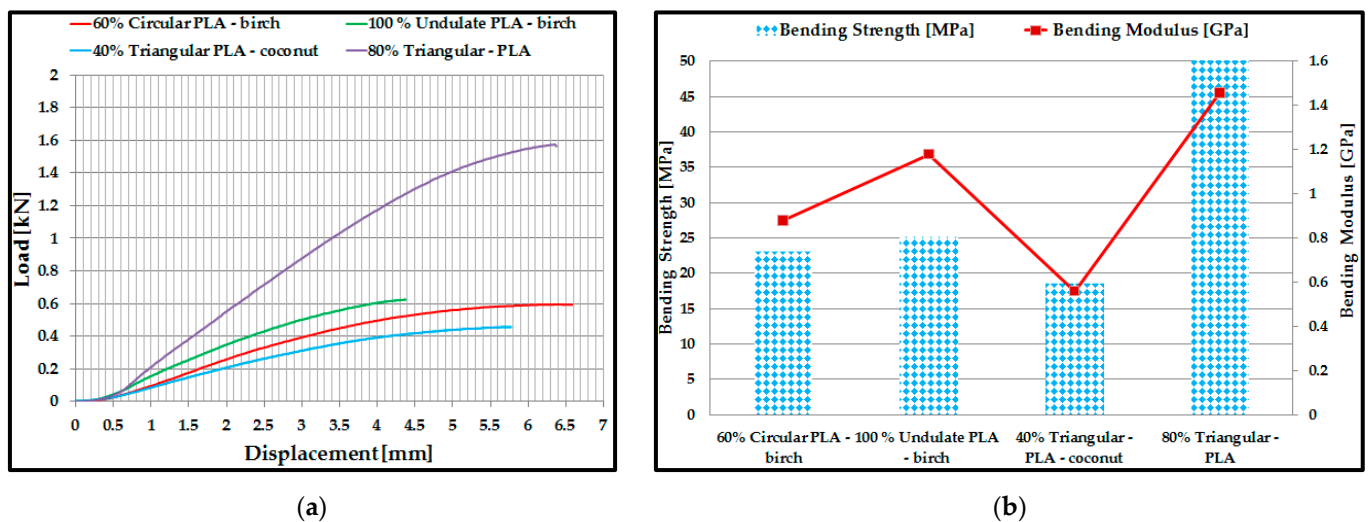


Figure 6. Three-point bending test results: (a) Load–displacement characteristic curves; (b) Bending strength and modulus of elasticity for 3D-printed samples.

3.3. Microscopic Analysis of 3D-Printed Double Panels

For the microscopic analysis of the samples, the 3D-printed double panels (Figure 7) were cross-sectioned, embedded into resin, and polished using a 1 μm grit and 0.5 μm Al_2O_3 suspension.

The microscopic analysis of 3D-printed double panels was carried out to exemplify the deformations of the internal configurations and at the same time to verify the deposition behaviour of the extruded material at different filling densities. The samples that were microscopically analysed were subjected to plane compression tests. In Figure 7a, the sample underwent a deformation in the middle of the part, followed by a crack with propagation in the middle of the part. Interlayer voids are also observed on the left and right sides. In Figure 7b, the following can be observed: uniform distribution of birch ground wood particles, interlayer crack defects, and a reduced number of defects when adding layers of extruded material.

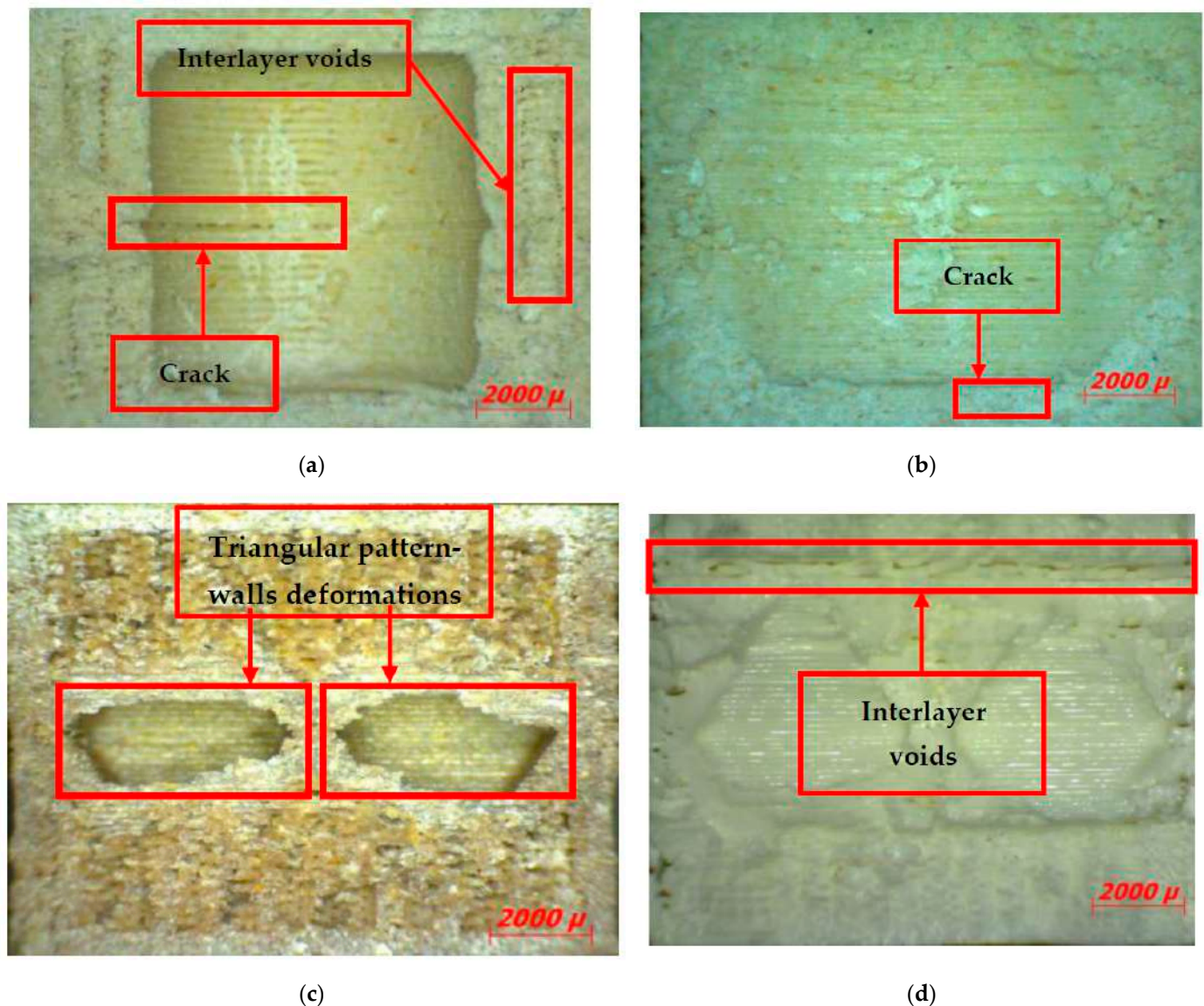


Figure 7. Microscopic analysis of the samples: (a) 60% circular PLA–birch; (b) 100% corrugated PLA–birch; (c) 40% triangular–PLA–coconut; (d) 80% triangular–PLA.

Following the compression tests (Figure 7c), the walls of the 40% triangular–PLA–coconut samples were deformed by lateral buckling. At the same time, a closer analysis of these samples (Figure 7c) reveals end layer voids, defects with different configurations (triangular and parallelepipedal) and porosity defects (voids) between the successive beads, also found in other studies and specific to the FFF process [60–62].

Analysing the 80% triangular–PLA sample (Figure 7d), inter-layer voids and porosity defects were identified, which led to higher performance of acoustically tested samples [32].

3.4. Acoustic Analysis of 3D-Printed Single Panels

For the next acoustic analysis, only half of the previously tested 3D-printed double panel samples (8 mm thick) were used to determine whether the thickness of the tested sample influenced the acoustic performance. Regarding the sound absorption coefficient (Figure 8a,c,e), the acoustic tests showed the same types of configurations, as with the double panels with the highest values (40% triangular–PLA–coconut, corrugated PLA–birch and 80% triangular–PLA). The increase in the absorption coefficient for the three types of samples, compared to the results obtained for the double panels, was as follows: 39% for

the single 40% triangular-PLA-coconut samples; 20% for the single 100% corrugated PLA-birch samples and 33% for the single 80% triangular-PLA samples. Therefore, it can be stated that sample thickness is very important in acoustic tests, as previously found in other studies [40,54,63].

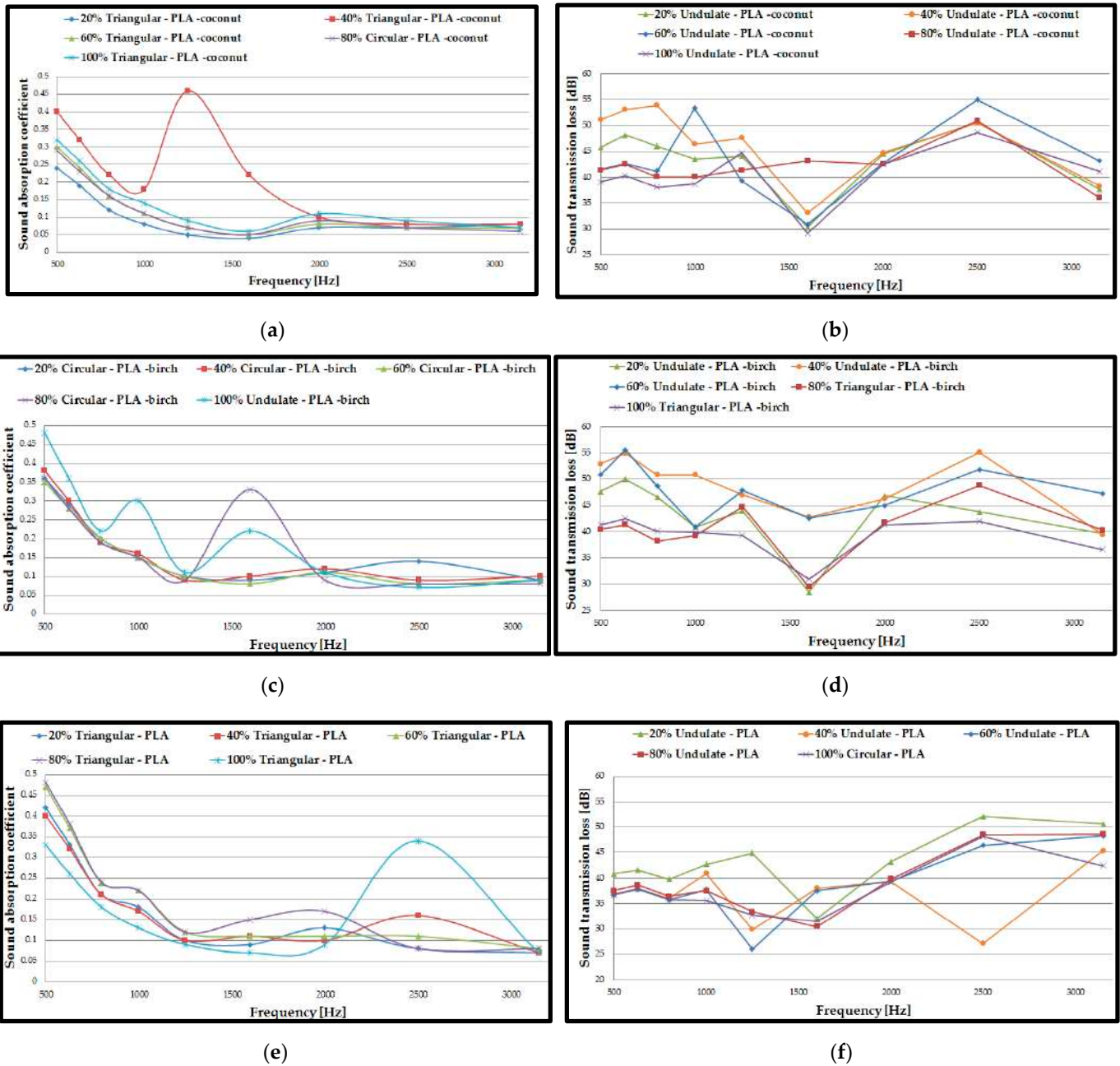


Figure 8. Acoustic test results of 3D-printed single panels: (a) Sound absorption coefficient of PLA-birch specimens; (b) Sound transmission loss of PLA-birch specimens; (c) Sound absorption coefficient of PLA-coconut specimens; (d) Sound transmission loss of PLA-coconut specimens; (e) Sound absorption coefficient of PLA specimens; (f) Sound transmission loss of PLA specimens.

Regarding the sound transmission loss (Figure 8b,d,f), as found in other studies [53,64], the STL value decreases as the thickness of the tested samples decreases, and the maximum value is obtained at a higher frequency (in the case of these samples, at about 2500 Hz). Thus, the values of sound transmission loss for 3D-printed single panels decreased by about

13% compared to 3D-printed double panels. It can also be observed that the corrugated configuration shows the highest STL values for all three material types.

Figure 8 shows that the decrease in the thickness of the specimen, from 16 mm to 8 mm increased the ability to absorb sound at frequencies between 1000 Hz and 2500 Hz. As the thickness of the 3D-printed specimens increases, the acoustic absorption decreases due to the low and mid frequency because the waves have a harder time penetrating the thicker panels. If the thickness of the specimens is too large, the air inside the voids becomes harder to move, and there will effectively be no friction. It can be concluded that the sound absorption coefficient improved at lower frequencies (500 Hz) and, at the same time, an increase was observed when the frequencies were increased (3150 Hz). The decrease in the filling density in most of the tested specimens improves the passage of the acoustic waves to enter the analysed structure, and the air inside the voids can move easily, which provides an increase in the viscous friction, ultimately causing the loss of the energy of the acoustic waves, causing higher sound absorption [51]. By decreasing the thickness of the specimen (from 16 mm to 8 mm), the values of the sound transmission loss parameter decreased, but the specimens still offer good acoustic insulation with values between 30 dB and 55 dB.

3.5. Acoustic Analysis of 3D-Printed Single Panels with Drilled Holes

In these tests, the 3D-printed single panels were perforated to determine the influence of holes on acoustic performance. A template (Table 1) was used to make the holes, and the 3D-printed single panels were then perforated. The holes were round, made with a drill, and the diameter was 1.8 mm. They were made at right angles, as they have a higher absorption coefficient compared to the holes made at inclined angles [39]. After acoustic testing, 3D-printed single panels with holes showed superior performance compared to 3D-printed single panels. From the analysis of the acoustic test results, in comparison with the results obtained on 3D-printed single panels and according to the highest absorption coefficient values, the following was found: 40% triangular-PLA-coconut samples showed a 73% increase in absorption coefficient; 40% triangular-PLA-birch samples showed a 122% increase in absorption coefficient; 60% triangular-PLA samples showed an 82% increase in absorption coefficient. The triangular configuration also had the highest absorption coefficient values for all three material types. The filling densities which indicated the highest absorption coefficient (Figure 9a,c,e) were 40% and 60%. Another important aspect of the tests on 3D-printed single panels with holes was that with the use of the holes, the peak sound absorption coefficients shifted to the value of 1000 Hz [65]. Concerning the material, it can be concluded that PLA had the highest absorption coefficient of 0.86, while for the birch material, a maximum absorption coefficient value of 0.78 was obtained. Thus, it can be implied that the holes of the samples brought a significant increase in the sound absorption coefficient, as observed in another research conducted [29,39,40,66]. The absorption coefficient curves (Figure 9a,c,e) have stabilized, and their shape is similar for all material types, with very small variations between them.

Regarding the sound transmission loss of 3D-printed single panels with holes, it can be observed that the maximum value is found at 3150 Hz, so the sound wave energy dissipation is directly proportional to the frequency [29]. As can be seen from the curves of sound transmission loss (Figure 9b,d,f), they have a similar shape, with a maximum of about 29 dB. Thus, a decrease in sound transmission loss of up to half is observed compared to 3D-printed single panels, and the maximum value in this case was 29 dB for the 60% triangular-PLA-coconut sample.

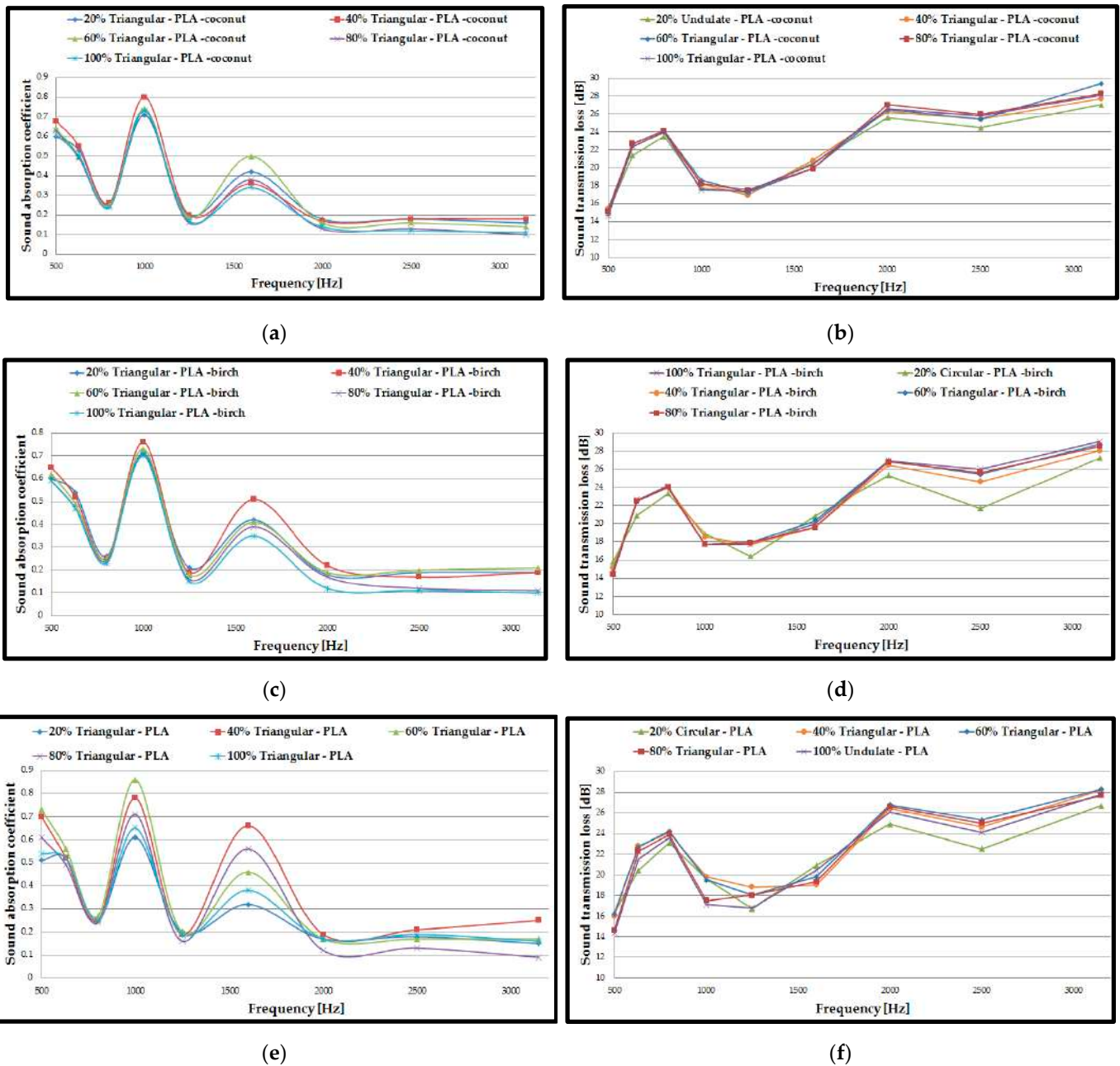


Figure 9. Acoustic tests results of 3D-printed single panels with drilled holes: (a) Sound absorption coefficient of PLA–birch specimens; (b) Sound transmission loss of PLA–birch specimens; (c) Sound absorption coefficient of PLA–coconut specimens; (d) Sound transmission loss of PLA–coconut specimens; (e) Sound absorption coefficient of PLA specimens; (f) Sound transmission loss of PLA specimens.

3.6. Acoustic Analysis of 3D-Printed Single Panels with Holes

In the acoustic testing of 3D-printed single panels with drilled holes, the best performance (in terms of absorption coefficient) was recorded for the following samples: 40% triangular–PLA–coconut; 40% triangular–PLA–birch; 60% triangular–PLA. For these configurations, filling densities and material samples were manufactured via the FFF process, and the results obtained were similar.

Therefore, to optimise the structures, the three configurations (40% triangular–PLA–coconut; 40% triangular–PLA–birch and 60% triangular–PLA) were kept and samples with rhombic holes of 1.8 mm side size were manufactured via the FFF process (Table 1). From the absorption coefficient curves (Figure 10a) the maximum value is found for the

40% triangular-PLA-birch sample of 0.93 at a frequency of 1000 Hz. In contrast, for the 60% triangular-PLA sample, the maximum value of the absorption coefficient is 0.84 at 1600 Hz.



Figure 10. Acoustic test results of 3D-printed single panels with holes: (a) Sound absorption coefficient of 40% triangular-PLA-coconut; 40% triangular-PLA-birch and 60% triangular-PLA; (b) Sound transmission loss of 40% triangular-PLA-coconut; 40% triangular-PLA-birch and 60% triangular-PLA.

From this, it can be concluded that PLA with a mixture of 40% ground birch wood particles can be used at high performance at frequencies up to 1000 Hz and PLA material up to 1600 Hz for the configurations proposed in this study. The 40% triangular-PLA-birch sample with 3D-printed rhombic holes showed a 16% increase compared to the 40% triangular-PLA-birch with drilled holes sample in terms of absorption coefficient value. From the tests, it can be concluded that the triangular structure, at a filling density of 40% and with rhombic holes showed the highest absorption coefficient (0.93).

As for the sound transmission loss (Figure 10b), using rhombic shaped holes increased it by 10% compared to 3D-printed single panels with drilled holes. The maximum STL value is 31 dB and is attributed to the 60% triangular-PLA sample at a frequency of 3150 Hz. The shape of the curves for sound absorption coefficient and for sound transmission loss for 3D-printed single panels with holes shows the same shape as 3D-printed single panels with drilled holes.

Even though perforations of 3D-printed specimens can be seen to improve sound absorption, this is due to the inherent disadvantage demonstrated by micro-perforation in suppressing low-frequency (i.e., <1000 Hz) noise, as observed in other studies [53,67]. This aspect was also validated in the study in this work, namely that in the case of perforated panels, the peak values of the sound absorption coefficient were near the frequency of 1000 Hz (Figures 9 and 10). On the other hand, open porous structures could dampen sound; this aspect is related to the airflow resistivity of these panels [31]. In general, increasing airflow resistivity improves sound absorption properties [31] over the entire frequency range, but only up to an intermediate value.

Because the research started from the analysis of demountable double panels and the optimal one turned out to be a half-panel, this study has comparable results with those obtained in other studies by other researchers.

4. Conclusions

Acoustic analysis and noise absorption are some important and research-intensive aspects of health and the environment that affect people's psychological and biological states.

In this work, the sound absorption performance of samples manufactured from three types of materials (PLA with a mixture of 40% ground coconut wood particles, PLA with a mixture of 40% ground birch wood particles and plain PLA), with three internal configurations (circular, triangular, and corrugated) and at five filling densities (20%, 40%, 60%, 80% and 100%), manufactured via the FFF process, was evaluated.

The acoustic performance was measured for the double panels (designed as consisting of two half-panels in a demountable assembly) and obtained a maximum value of $\alpha = 0.4$ and $STL = 64$ dB. The acoustic results for the double panels (16 mm thickness) indicate excellent sound transmission resistance for all types of materials used, which determines good acoustic insulation, and these types of materials can be successfully used in the aviation, automotive and construction fields for sandwich panels with the aim of sound attenuation.

After several tests, a compromise solution was reached that involved form iterations, panel perforations, and porosity optimization to increase the acoustic performance of the samples considerably, with values ranging from 72% to 122%.

For a complete characterization of the samples, mechanical tests were also carried out, and the PLA material was clearly superior to the other two types of materials (PLA with a mixture of 40% ground coconut wood particles, PLA with a mixture of 40% ground birch wood particles) in both compression and three-point bending tests.

At the mechanical tests, the rhombic holes that presented the best sound absorption results with $\alpha = 0.93$ and $STL = 31$ dB also presented the maximum resistance to compression (40 MPa) and to three-point bending (50 MPa).

Microscopic analysis of the samples tested in compression showed normal defects (voids, interlayer voids) of the FFF process and lateral buckling as the main mode of failure of the internal walls of the samples.

The analysis of the microstructure of the panels confirms that it has been possible to produce samples with controlled morphology and oriented regular cell patterns that could be attained and with high sound-absorbing properties.

In the 3D-printed samples with rhombic holes, an increase of 16% in the absorption coefficient of the PLA material with a mixture of 40% ground birch wood particles ($\alpha = 0.93$) was obtained compared to the samples with round holes.

Predominant factors that influenced sound-absorbing properties in this study were the triangular configuration model, which exhibited the highest performance for all three material types, and filling density, which also played an important role in the acoustic tests of the samples manufactured via the FFF process; thus, it was determined that the highest acoustic performance was obtained at 40% and 60%. The effects of cell orientation impact the acoustic properties as the un-oriented cell morphology leads to enhanced sound absorption capacity compared to the samples with more regular and oriented morphology.

Depending on the field of application, the following are recommended:

- For very good sound absorption properties, the configuration with 40% infill, triangular-PLA with coconut ground particles and 8 mm thickness is recommended.
- The physical-mechanical properties of the material (PLA with ground coconut particles) ensure their use for obtaining protective sound-absorbing panels (near highways or heavily trafficked roads, various casings or covers of engines).
- Transmission loss coefficient (STL) decreases with panel thickness.

As a general observation, the initial idea to obtain highway sound protection panels with the highest possible mechanical resistance and very good sound absorption properties was achieved.

Even if the results obtained are very good from the point of view of the sound absorption coefficient ($\alpha = 0.93$) and the mechanical resistances (40 MPa and 50 MPa), additional scientific research is considered to increase the transmission loss coefficient and at the same time to maintain the α coefficient.

Author Contributions: Conceptualization, M.A.P. and S.-M.Z.; methodology, C.C., S.M., S.-M.Z., M.A.P. and M.C.; software, M.A.P., S.-M.Z. and C.S.; validation, M.A.P., S.M., S.-M.Z. and C.C.; investigation, M.A.P., C.C., S.-M.Z. and M.C.; writing—original draft preparation, S.-M.Z. and M.A.P.; project administration, M.A.P. All authors have read and agreed to the published version of the manuscript.

Funding: This work was supported by a grant from the Ministry of Research, Innovation and Digitization, CNCS-UEFISCDI, project number PN-III-P1-1.1-TE-2021-0294, within PNCDI III.

Institutional Review Board Statement: Not applicable.

Data Availability Statement: The data presented in this study are available on request from the corresponding author.

Acknowledgments: This work was supported by a grant from the Ministry of Research, Innovation and Digitization, CNCS–UEFISCDI, project number PN-III-P1-1.1-TE-2021-0294, within PNCDI III. We also acknowledge the structural funds project PRO-DD (POS-CCE O.2.2.1, ID 123, SMIS 2637, ctr. No 11/2009) for partially providing the infrastructure used in this work at the CDI Institute of Transilvania University of Brasov.

Conflicts of Interest: The authors declare no conflict of interest.

References

1. Sleinus, D.; Sinka, M.; Korjakins, A.; Obuka, V.; Nikolajeva, V.; Brenčis, R.; Savicka, E. Properties of Sound Absorption Composite Materials Developed Using Flax Fiber, Sphagnum Moss, Vermiculite, and Sapropel. *Materials* **2023**, *16*, 1060. [[CrossRef](#)] [[PubMed](#)]
2. Gliscinska, E.; Perez de Amezaga, J.; Michalak, M.; Krucinska, I. Green Sound-Absorbing Composite Materials of Various Structure and Profiling. *Coatings* **2021**, *11*, 407. [[CrossRef](#)]
3. Zhang, J.; Shen, Y.; Jiang, B.; Li, Y. Sound Absorption Characterization of Natural Materials and Sandwich Structure Composites. *Aerospace* **2018**, *5*, 75. [[CrossRef](#)]
4. Bratu, M.; Dumitrescu, O.; Vasile, O.; Constantin, A.; Muntean, M. Research on the sound-absorbing properties of new composite materials with some wastes. *Rom. J. Mater.* **2014**, *44*, 160–168.
5. Tiuc, A.E.; Nemes, O.; Vermeșan, H.; Gavrea, D.R.T.; Vasile, O. New sound absorbing materials obtained from waste rigid polyurethane foam. *Mater. Plast.* **2019**, *56*, 1021–1027. [[CrossRef](#)]
6. Tiuc, A.-E.; Borlea (Mureșan), S.I.; Nemeș, O.; Vermeșan, H.; Vasile, O.; Popa, F.; Pîntoi, R. New Composite Materials Made from Rigid/Flexible Polyurethane Foams with Fir Sawdust: Acoustic and Thermal Behavior. *Polymers* **2022**, *14*, 3643. [[CrossRef](#)] [[PubMed](#)]
7. Yang, T.; Hu, L.; Xiong, X.; Petru, M.; Noman, M.T.; Mishra, R.; Militký, J. Sound Absorption Properties of Natural Fibers: A Review. *Sustainability* **2020**, *12*, 8477. [[CrossRef](#)]
8. Mamtaz, H.; Fouladi, M.H.; Al-Atabi, M.; Namasivayam, S.N. Acoustic absorption of natural fiber composites. *J. Eng.* **2016**, *2016*, 5836107. [[CrossRef](#)]
9. Taban, E.; Tajpoor, A.; Faridan, M.; Samaei, S.E.; Beheshti, M.H. Acoustic Absorption Characterization and Prediction of Natural Coir Fibers. *Acoust. Aust.* **2019**, *47*, 67–77. [[CrossRef](#)]
10. Sujon, A.S.; Islam, A.; Nadimpalli, V.K. Damping and sound absorption properties of polymer matrix composites: A review. *Polym. Test.* **2021**, *104*, 107388. [[CrossRef](#)]
11. Rubino, C.; Bonet Aracil, M.; Gisbert-Payá, J.; Liuzzi, S.; Stefanizzi, P.; Zamorano Cantó, M.; Martellotta, F. Composite Eco-Friendly Sound Absorbing Materials Made of Recycled Textile Waste and Biopolymers. *Materials* **2019**, *12*, 4020. [[CrossRef](#)] [[PubMed](#)]
12. Pakdel, E.; Kashi, S.; Baum, T.; Usman, K.A.S.; Razal, J.M.; Varley, R.; Wang, X.G. Carbon fibre waste recycling into hybrid nonwovens for electromagnetic interference shielding and sound absorption. *J. Clean. Prod.* **2021**, *315*, 128196. [[CrossRef](#)]
13. Kim, B.S.; Cho, S.J.; Min, D.K.; Park, J. Experimental study for improving sound absorption of a composite helical-shaped porous structure using carbon fiber. *Compos. Struct.* **2016**, *145*, 242–247. [[CrossRef](#)]
14. Wang, D.-W.; Wen, Z.-H.; Glorieux, C.; Ma, L. Sound Absorption of Face-Centered Cubic Sandwich Structure with Micro-Perforations. *Mater. Des.* **2020**, *186*, 108344. [[CrossRef](#)]
15. Sui, N.; Yan, X.; Huang, T.Y.; Xu, J.; Yuan, F.G.; Jing, Y. A lightweight yet sound-proof honeycomb acoustic metamaterial. *Appl. Phys. Lett.* **2015**, *106*, 171905. [[CrossRef](#)]
16. Arunkumar, M.P.; Jagadeesh, M.; Pitchaimani, J.; Gangadharan, K.V.; Babu, M.L. Sound radiation and transmission loss characteristics of a honeycomb sandwich panel with composite facings: Effect of inherent material damping. *J. Sound Vib.* **2016**, *383*, 221–232. [[CrossRef](#)]
17. Isaac, C.W.; Pawelczyk, M.; Wrona, S. Comparative Study of Sound Transmission Losses of Sandwich Composite Double Panel Walls. *Appl. Sci.* **2020**, *10*, 1543. [[CrossRef](#)]
18. Li, X.; Peng, Y.; He, Y.; Zhang, C.; Zhang, D.; Liu, Y. Research Progress on Sound Absorption of Electrospun Fibrous Composite Materials. *Nanomaterials* **2022**, *12*, 1123. [[CrossRef](#)]
19. Lee, H.M.; Luo, W.; Xie, J.; Wen, G.; Lee, H.P. Studies on the sound absorption and transmission loss performances of wood-based natural and waste materials. *Acta Mech. Sin.* **2021**, *37*, 861–873. [[CrossRef](#)]
20. Shen, X.; Bai, P.; Yang, X.; Zhang, X.; To, S. Low Frequency Sound Absorption by Optimal Combination Structure of Porous Metal and Microperforated Panel. *Appl. Sci.* **2019**, *9*, 1507. [[CrossRef](#)]
21. Durbaca, I.; Sporea, N.; Vasile, O. Assessment of the Acoustic Absorption Characteristics of Layered Composite Structures Obtained from Plates with Lignocellulosic Coatings (I). *Mater. Plast.* **2020**, *57*, 8–14. [[CrossRef](#)]
22. Zhang, Z.; Denayer, H.; Claeys, C.; Desmet, W.; Deckers, E. Angle-dependent reflection, transmission and absorption coefficients measurement using a 2D waveguide. *Appl. Acoust.* **2021**, *177*, 107946. [[CrossRef](#)]

23. Yang, G.; Huang, Q.; Yang, M.; Huang, Y. Sound Transmission Loss of Metamaterial Honeycomb Core Sandwich Plate Elastically Connected with Periodic Subwavelength Arrays of Shunted Piezoelectric Patches. *Materials* **2022**, *15*, 3923. [CrossRef] [PubMed]
24. Cao, L.; Fu, Q.; Si, Y.; Ding, B.; Yu, J. Porous materials for sound absorption. *Compos. Commun.* **2018**, *10*, 25–35. [CrossRef]
25. Soltani, P.; Taban, E.; Faridan, M.; Samaei, S.E.; Amininasab, S. Experimental and computational investigation of sound absorption performance of sustainable porous material: Yucca Gloriosa fiber. *Appl. Acoust.* **2020**, *157*, 106999. [CrossRef]
26. Rastegar, N.; Ershad-Langroudi, A.; Parsimehr, H.; Moradi, G. Sound-absorbing porous materials: A review on polyurethane-based foams. *Iran. Polym. J.* **2022**, *31*, 83–105. [CrossRef]
27. Miki, Y. Acoustical properties of porous materials. Modifications of Delany-Bazley models. *J. Acoust. Soc. Jpn.* **1990**, *11*, 19–24. [CrossRef]
28. Sailesh, R.; Yuvaraj, L.; Doddamani, M.; Mailan Chinnapandi, L.B.; Pitchaimani, J. Sound absorption and transmission loss characteristics of 3D printed bio-degradable material with graded spherical perforations. *Appl. Acoust.* **2022**, *186*, 108457. [CrossRef]
29. Sailesh, R.; Yuvaraj, L.; Pitchaimani, J.; Doddamani, M.; Mailan Chinnapandi, L.B. Acoustic Behaviour of 3D Printed Bio-Degradable Micro-Perforated Panels with Varying Perforation Cross-Sections. *Appl. Acoust.* **2021**, *174*, 107769. [CrossRef]
30. Monkova, K.; Vasina, M.; Monka, P.P.; Kozak, D.; Vanca, J. Effect of the Pore Shape and Size of 3D-Printed Open-Porous ABS Materials on Sound Absorption Performance. *Materials* **2020**, *13*, 4474. [CrossRef]
31. Vasina, M.; Monkova, K.; Monka, P.P.; Kozak, D.; Tkac, J. Study of the Sound Absorption Properties of 3D-Printed Open-Porous ABS Material Structures. *Polymers* **2020**, *12*, 1062. [CrossRef]
32. Zielinski, T.G.; Dauchez, N.; Boutin, T.; Leturia, M.; Wilkinson, A.; Chevillotte, F.; Becot, F.-X.; Venegas, R. Taking advantage of a 3D printing imperfection in the development of sound-absorbing materials. *Appl. Acoust.* **2022**, *197*, 108941. [CrossRef]
33. Errico, F.; Ichchou, M.; de Rosa, S.; Franco, F.; Bareille, O. Investigations about periodic design for broadband increased sound transmission loss of sandwich panels using 3D-printed models. *Mech. Syst. Signal Process.* **2020**, *136*, 106432. [CrossRef]
34. Boulvert, J.; Costa-Baptista, J.; Cavalieri, T.; Perna, M.; Fotsing, E.R.; Romero-García, V.; Gabard, G.; Ross, A.; Mardjono, J.; Groby, J.-P. Acoustic modeling of micro-lattices obtained by additive manufacturing. *Appl. Acoust.* **2020**, *164*, 107244. [CrossRef]
35. Amaya-Amaya, V.; de Icaza-Herrera, M.; Martínez-Hernández, A.L.; Martínez-Barrera, G.; Velasco-Santos, C. Experimental approximation of the sound absorption coefficient (α) for 3D printed reentrant auxetic structures of poly lactic acid reinforced with chicken keratin materials. *Mater. Lett.* **2021**, *283*, 128757. [CrossRef]
36. Gao, N.; Hou, H. Sound absorption characteristic of micro-helix metamaterial by 3D printing. *Theor. Appl. Mech. Lett.* **2018**, *8*, 63–67. [CrossRef]
37. Yang, W.; Bai, X.; Zhu, W.; Kiran, R.; An, J.; Chua, C.K.; Zhou, K. 3D Printing of Polymeric Multi-Layer Micro-Perforated Panels for Tunable Wideband Sound Absorption. *Polymers* **2020**, *12*, 360. [CrossRef] [PubMed]
38. Liu, Z.; Zhan, J.; Fard, M.; Davy, J. Acoustic properties of multilayer sound absorbers with a 3D printed micro-perforated panel. *Appl. Acoust.* **2017**, *121*, 25–32. [CrossRef]
39. Liu, Z.Q.; Zhan, J.X.; Fard, M.; Davy, J.L. Acoustic properties of a porous polycarbonate material produced by additive manufacturing. *Mater. Lett.* **2016**, *181*, 296–299. [CrossRef]
40. Jiang, C.; Moreau, D.; Doolan, C. Acoustic Absorption of Porous Materials Produced by Additive Manufacturing with Varying Geometries. In Proceedings of the ACOUSTICS 2017, Perth, Australia, 19–22 November 2017.
41. Liu, Z.Q.; Zhan, J.X.; Fard, M.; Davy, J.L. Acoustic measurement of a 3D printed micro-perforated panel combined with a porous material. *Measurement* **2017**, *104*, 233–236. [CrossRef]
42. Opiela, K.C.; Zieliński, T.G.; Attenborough, K. Limitations on validating slitted sound absorber designs through budget additive manufacturing. *Mater. Des.* **2022**, *218*, 110703. [CrossRef]
43. Sekar, V.; Eh Noum, S.Y.; Sivanesan, S.; Putra, A.; Kassim, D.H.; Wong, Y.S.; Chin, K.C. Effect of Perforation Volume on Acoustic Absorption of the 3D Printed Micro-Perforated Panels Made of Polylactic Acid Reinforced with Wood Fibers. *J. Phys. Conf. Ser.* **2021**, *2120*, 012039. [CrossRef]
44. ISO 10534-2 (1998-11); Acoustics—Determination of Sound Absorption Coefficient and Impedance in Impedance Tubes—Part 2: Transfer-Function Method. International Organization for Standardization (ISO): Geneva, Switzerland, 1998.
45. E1050; Standard Test Method for Impedance and Absorption of Acoustical Materials Using a Tube, Two Microphone and a Digital Frequency Analysis System. ASTM International: West Conshohocken, PA, USA, 2010.
46. MIL-STD-401B; Military Standard: Sandwich Constructions and Core Materials, General Test Methods. U.S. Department of Defense: Washington, VA, USA, 1967.
47. ASTM C393/C393M-2011; Standard Test Method for Core Shear Properties of Sandwich Constructions by Beam Flexure. American Society for Testing and Materials: West Conshohocken, PA, USA, 2011.
48. EasyWood PLA Material, Formfutura. Available online: <https://formfutura.com/shop/product/easywood-2804?category=465> (accessed on 26 May 2023).
49. Premium PLA. Available online: <https://formfutura.com/product/premium-pla/> (accessed on 26 May 2023).
50. Ilyas, R.A.; Sapuan, S.M.; Harussani, M.M.; Hakimi, M.Y.A.Y.; Haziq, M.Z.M.; Atikah, M.S.N.; Asyraf, M.R.M.; Ishak, M.R.; Razman, M.R.; Nurazzi, N.M.; et al. Polylactic Acid (PLA) Biocomposite: Processing, Additive Manufacturing and Advanced Applications. *Polymers* **2021**, *13*, 1326. [CrossRef] [PubMed]

51. Bergaliyeva, S.; Sales, D.L.; Delgado, F.J.; Bolegenova, S.; Molina, S.I. Manufacture and Characterization of Polylactic Acid Filaments Recycled from Real Waste for 3D Printing. *Polymers* **2023**, *15*, 2165. [[CrossRef](#)] [[PubMed](#)]
52. Krapež Tomec, D.; Kariž, M. Use of Wood in Additive Manufacturing: Review and Future Prospects. *Polymers* **2022**, *14*, 1174. [[CrossRef](#)] [[PubMed](#)]
53. Koruk, H.; Ozcan, A.C.; Genc, G.; Sanliturk, K.Y. Jute and Luffa Fiber-Reinforced Biocomposites: Effects of Sample Thickness and Fiber/Resin Ratio on Sound Absorption and Transmission Loss Performance. *J. Nat. Fibers* **2021**, *19*, 6239–6254. [[CrossRef](#)]
54. Sekar, V.; Eh Noum, S.Y.; Sivanesan, S.; Putra, A.; Chin Vui Sheng, D.D.; Kassim, D.H. Effect of Thickness and Infill Density on Acoustic Performance of 3D Printed Panels Made of Natural Fiber Reinforced Composites. *J. Nat. Fibers* **2021**, *13*, 7132–7140. [[CrossRef](#)]
55. Bakhtiari, H.; Aamir, M.; Tolouei-Rad, M. Effect of 3D Printing Parameters on the Fatigue Properties of Parts Manufactured by Fused Filament Fabrication: A Review. *Appl. Sci.* **2023**, *13*, 904. [[CrossRef](#)]
56. Gonabadi, H.; Yadav, A.; Bull, S.J. The effect of processing parameters on the mechanical characteristics of PLA produced by a 3D FFF printer. *Int. J. Adv. Manuf. Technol.* **2020**, *111*, 695–709. [[CrossRef](#)]
57. Gao, W.; Hou, Y.; Shang, F.; Zhang, J. 3D Printed Structures for Ultrasound Attenuation in Underwater Environment. *3D Print. Addit. Manuf.* **2022**. *ahead of print*. [[CrossRef](#)]
58. Müller, M.; Jirků, P.; Šleger, V.; Mishra, R.K.; Hromasová, M.; Novotný, J. Effect of Infill Density in FDM 3D Printing on Low-Cycle Stress of Bamboo-Filled PLA-Based Material. *Polymers* **2022**, *14*, 4930. [[CrossRef](#)] [[PubMed](#)]
59. Zhu, Y.; Gao, Y.; Jiang, J.; Gu, H.; Lv, S.; Ni, H.; Wang, X.; Jia, C. Study on effects of FFF 3D printing parameters on mechanical properties of polylactic acid. *IOP Conf. Ser. Mater. Sci. Eng.* **2019**, *688*, 2019.
60. Lupone, F.; Padovano, E.; Venezia, C.; Badini, C. Experimental Characterization and Modeling of 3D Printed Continuous Carbon Fibers Composites with Different Fiber Orientation Produced by FFF Process. *Polymers* **2022**, *14*, 426. [[CrossRef](#)]
61. Naveed, N. Investigating the Material Properties and Microstructural Changes of Fused Filament Fabricated PLA and Tough-PLA Parts. *Polymers* **2021**, *13*, 1487. [[CrossRef](#)] [[PubMed](#)]
62. Tao, Y.; Kong, F.; Li, Z.; Zhang, J.; Zhao, X.; Yin, Q.; Xing, D.; Li, P. A Review on Voids of 3D Printed Parts by Fused Filament Fabrication. *J. Mater. Res. Technol.* **2021**, *15*, 4860–4879. [[CrossRef](#)]
63. Gómez Escobar, V.; Moreno González, C.; Rey Gozalo, G. Analysis of the Influence of Thickness and Density on Acoustic Absorption of Materials Made from Used Cigarette Butts. *Materials* **2021**, *14*, 4524. [[CrossRef](#)] [[PubMed](#)]
64. Hassan, T.; Jamshaid, H.; Mishra, R.; Khan, M.Q.; Petru, M.; Tichy, M.; Muller, M. Factors Affecting Acoustic Properties of Natural-Fiber-Based Materials and Composites: A Review. *Textiles* **2021**, *1*, 55–85. [[CrossRef](#)]
65. Yuvaraj, L.; Jeyanthi, S. Acoustic performance of countersunk micro-perforated panel in multilayer porous material. *Build. Acoust.* **2020**, *27*, 3–20. [[CrossRef](#)]
66. Arjunan, A.; Baroutaji, A.; Latif, A. Acoustic behaviour of 3D printed titanium perforated panels. *Results Eng.* **2021**, *11*, 100252. [[CrossRef](#)]
67. Park, S.H. Acoustic properties of micro-perforated panel absorbers backed by Helmholtz resonators for the improvement of low-frequency sound absorption. *J. Sound Vib.* **2013**, *332*, 4895–4911. [[CrossRef](#)]

Disclaimer/Publisher's Note: The statements, opinions and data contained in all publications are solely those of the individual author(s) and contributor(s) and not of MDPI and/or the editor(s). MDPI and/or the editor(s) disclaim responsibility for any injury to people or property resulting from any ideas, methods, instructions or products referred to in the content.

Article

3D-Printed PLA Molds for Natural Composites: Mechanical Properties of Green Wax-Based Composites

Mihai Alin Pop ¹, Mihaela Cosnita ^{2,*}, Cătălin Croitoru ³, Sebastian Marian Zaharia ⁴, Simona Matei ¹
and Cosmin Spîrchez ⁵

¹ Materials Science Department, Transilvania University of Brasov, 29 Eroilor Ave., 500484 Brasov, Romania; mihai.pop@unitbv.ro (M.A.P.); simona.matei@unitbv.ro (S.M.)

² Department of Product Design, Mechatronics and Environment, Transilvania University of Brasov, 29 Eroilor Ave., 500484 Brasov, Romania

³ Materials Engineering and Welding Department, Transilvania University of Brasov, 29 Eroilor Ave., 500484 Brasov, Romania; c.croitoru@unitbv.ro

⁴ Manufacturing Engineering Department, Faculty of Technological Engineering and Industrial Management, Transilvania University of Brasov, 29 Eroilor Ave., 500484 Brasov, Romania; zaharia_sebastian@unitbv.ro

⁵ Wood Processing and Furniture Design of Wood, Transilvania University of Brasov, 29 Eroilor Ave., 500484 Brasov, Romania; cosmin.spirchez@unitbv.ro

* Correspondence: mihaela.cosnita@unitbv.ro

Abstract: The first part of this paper is dedicated to obtaining 3D-printed molds using poly lactic acid (PLA) incorporating specific patterns, which have the potential to serve as the foundation for sound-absorbing panels for various industries and aviation. The molding production process was utilized to create all-natural environmentally friendly composites. These composites mainly comprise paper, beeswax, and fir resin, including automotive function as the matrices and binders. In addition, fillers, such as fir needles, rice flour, and *Equisetum arvense* (horsetail) powder, were added in varying amounts to achieve the desired properties. The mechanical properties of the resulting green composites, including impact and compressive strength, as well as maximum bending force value, were evaluated. The morphology and internal structure of the fractured samples were analyzed using scanning electron microscopy (SEM) and an optical microscopy. The highest impact strength was measured for the composites with beeswax, fir needles, recyclable paper, and beeswax fir resin and recyclable paper, 19.42 and 19.32 kJ/m², respectively, while the highest compressive strength was 4 MPa for the beeswax and horsetail-based green composite. Natural-material-based composites exhibited 60% higher mechanical performance compared to similar commercial products used in the automotive industry.

Keywords: green composites; beeswax; fir needles; recyclable paper; *Equisetum arvense*; mechanical properties



Citation: Pop, M.A.; Cosnita, M.; Croitoru, C.; Zaharia, S.M.; Matei, S.; Spîrchez, C. 3D-Printed PLA Molds for Natural Composites: Mechanical Properties of Green Wax-Based Composites. *Polymers* **2023**, *15*, 2487. <https://doi.org/10.3390/polym15112487>

Academic Editor: Paul Joseph

Received: 25 April 2023

Revised: 19 May 2023

Accepted: 22 May 2023

Published: 28 May 2023



Copyright: © 2023 by the authors. Licensee MDPI, Basel, Switzerland. This article is an open access article distributed under the terms and conditions of the Creative Commons Attribution (CC BY) license (<https://creativecommons.org/licenses/by/4.0/>).

1. Introduction

The circular (bioresources) economy is considered one of the most sustainable potential solutions to the global challenges of energy crises and environmental pollution. The research community has approached this issue from two main paths: recycling waste to develop novel materials and using natural resources to create new materials. One area of significant attention for researchers is the development of fiber-reinforced composite materials, which have the potential to be used in (semi) structural applications [1]. In the last decade, great attention has been paid by the research community to the developments of fiber (carbon, graphite, graphene, aramid, kevlar, natural, and wood fibers)—polymer (thermoplastic or thermosetting matrices) composites. Fiber-reinforced composite materials (FRPs) are widely used in modern products due to their exceptional combination of properties, including high specific strength and stiffness, low weight, durability, and resistance to creep and fatigue. Due to the special properties in relation to weight, composite

materials have found a safe place in top industries, such as aerospace and aeronautics (applications for propellers of torpedoes, submarines, etc.) [2], in the automotive industry (components of transmission, brake discs, engine components) [2–7], in electronics and electrotechnics (manufacture of packages and layers of integrated circuit-plate supports on which electronic circuits are mounted to capacitors, electronic transducers or electronic filters) [8], and so on. However, achieving adequate interfacial strength between the filler and matrix often requires the use of toxic or expensive compatibility agents. Additionally, when synthetic fibers are used, the manufacturing process can become energy intensive due to the high-temperature curing required for the fiber–polymer blend [9,10].

Extensive studies in the specialized literature indicate that many composite materials with natural reinforcements use polymeric matrices that exhibit good or even very good physical–mechanical properties [11,12]. However, the advantage of these materials is diminished by the polluting factor over their lifetime, as well as the high costs and complex technological/chemical processes required for their manufacturing and the limited recycling options available at the end of their product lifecycle [13–15]. The environmental sustainability and cost effectiveness has pushed researchers' focus to be moved from synthetic FRP composites to more environmentally friendly fillers. Natural plant fibers have emerged as a suitable alternative to synthetic fibers due to their lightweight nature, renewability, sustainability, eco-friendliness, carbon neutrality, low cost, biodegradability, and availability. Moreover, these fibers provide good insulation, toughness, vibration damping, flexibility, and high specific strength and modulus [16,17]. Moreover, legislative pressures on the industrial sector have led to an increased demand for environmentally friendly materials. As a result, natural fibers have gained traction as a commonly used alternative to synthetic fibers in composite materials. Flax, hemp, jute, kenaf, banana, pineapple, and sisal are amongst the most commonly used natural plant fibers as reinforcements in composite materials [1,9,11,17–20]. Compared to synthetic carbon and glass fibers, natural plant fibers are less expensive, lighter, biodegradable, easy to produce, and environmentally friendly. Researchers are now exploring the use of natural fibers for higher-load applications by incorporating ceramic fillers and synthetic fibers as reinforcements. This shift towards biologically sourced and recyclable materials is driven by the growing demand for sustainable and environmentally friendly materials in order to diminish the burden on the environment [21,22]. A study on ramie-reinforced PLA composites was reported, with a positive impact on the mechanical properties (tensile strength) of ramie/PLA composites [17,19]. Farid et al. [23] investigated the use of natural fibers, including kenaf, jute, waste cotton, and flax, in blends with PP and polyester binders for sound-absorbing floor coverings. They found that the sound absorption coefficient increased with the frequency of sound [24]. This research highlights the potential of natural fibers in creating sustainable products. In this context, the assimilation of pine needles (PNs) through biotechnology can offer a valuable opportunity to enhance the circular bio-economy. Converting PNs into biomaterials and bio-energy can help reduce the reliance on petroleum products and promote a healthier environment by maintaining the energy–environment network [22–37].

Composite material development by using natural fibers promotes reductions in greenhouse gas emission, biodegradability, job availability increase, energy saving, easy decomposition, lightweight, high specific mechanical properties, less tool wear during processing, and less density, lowering the product cost. However, there are some shortcomings when using natural fiber composites due to their hydrophilic nature and the potential of moisture absorption, debonding the fillers from the matrix [30–34,38]. The CO₂ release during when obtaining natural fiber composites is negligible as compared to synthetic fiber [35]. The composite structure comprises biodegradable natural fibers, which have found significant applications as sound-proofing material for automobile components. Composite laminates with bamboo, cotton, and flax fibers with PLA fibers showed bending stiffness of 2.5 GPa, but the impact strength, another mechanical property required in such applications, was been reported [36,37].

Beeswax is derived from honey combs and is shown as a complex mixture of several chemical compounds mostly used in the food industry (glazing, carrier of additives in food, and texturizing agent in chewing gum production) [38]. Praveen B. et al. [38] blended cellulose triacetate (CTA) microspheres and beeswax in order to evaluate the controlled release of antidiabetic nateglinide [39]. Pine needles and natural materials were used to obtain valuable products, metabolites, and bio-energy [23,24,28]. Converting natural materials into valuable products not only promotes a sustainable energy–environment network but also reduces the use of conventional petroleum products, resulting in a positive impact on the environment and human health [32,34]. While technology has advanced significantly, virtual information storage cannot completely replace readable paper supports, leading to the continued generation of paper waste.

To the best of our knowledge, there are no previous studies on the fabrication of green composites by pouring natural material blends based on beeswax, fir resin, fir needles, and *Equisetum arvense* onto recyclable paper.

This work presents a novel approach for the development of eco-friendly composites, consisting of two stages. Firstly, specific molds were 3D-printed using PLA to mold the natural composite receipts based on recyclable paper, beeswax, fir resin, fir needles, rice, and *Equisetum arvense*. In the second stage, eco-composites were prepared through mold casting (pouring) several natural blends of beeswax, fir resin, with or without fir needle, rice, or *Equisetum* onto recyclable paper. This study aims to contribute to the development of sustainable materials and to reduce waste generation from paper consumption, while also exploring the potential of natural resources for composite material production.

The major advantage of these composite materials is that both the matrix and reinforcement are natural, biodegradable, and recyclable.

This study is part of a larger research program aimed at assessing the feasibility of using the obtained composites for various industrial applications, such as sound insulation, thermal-insulating panels, or shock absorbers. In this particular study, we will focus specifically on the mechanical properties of the composites. By examining the mechanical properties, we can better understand how these materials can be optimized to provide the necessary insulation and damping and to gain a more specific insight into their potential application domains.

2. Experimental Section

2.1. 3D-Printing Molds for Green Composite Development

The research employs a variety of natural materials, such as polymers, resins, waxes, and biomass waste, to produce composite materials with good sound-absorbing properties. These materials, which include beeswax, fir resin, ground fir needles, horsetail (*Equiseti herba*), rice flour, and paper pulp, offer a high degree of recyclability, low cost, and minimal environmental impact.

Natural wax is an excellent candidate for use as an organic matrix in sound-absorbing materials, due to its high content of saturated fatty acids, n-alkanes, and long-chain alcohols. Similarly, fir resin, with its abundance of resin acids, provides an ideal matrix material for these composites. Not only do these materials possess excellent sound-dissipating properties due to their amorphous nature but they are also easy to process, have low softening points, and act as effective binders for filler materials. This combination of properties makes them an attractive option for creating effective sound-absorbing materials at a low cost.

In the pre-testing phase, it was determined that the most suitable filler material for the composite was in ground form. This decision was based on the groundings' relatively large specific surface area, which enables them to bond more effectively with the matrix material and also helps to create a structure that is as loose as possible. This loose structure is particularly beneficial for sound absorption, as it allows sound waves to be effectively dissipated within the material.

Equisetum and fir needles are not only rich in lignocellulosic material but also in phenolic compounds, resin acids, and silicon dioxide (in the case of horsetail), which contribute to the strengthening and thermal stabilizing effect of wax and/or resin. Rice flour, on the other hand, contains starch, waxes, and proteins that are compatible with the chosen matrices, while milled paper (recycled cellulose) has a high specific surface area and absorbency compared to wax and resin. These unique properties of the natural materials make them excellent candidates for the development of eco-friendly composites with enhanced mechanical and thermal properties.

Thus, the following eco-composites were preliminarily analyzed from the point of view of SHORE D hardness:

- (a) Beeswax (Ca) and ground horsetail (Cc)—a total of 14 composite materials were obtained. Percent of ground horsetail between 0 and 39.4%.
- (b) Beeswax (Ca) and recycled paper (Hr)—a total of 18 composite materials were obtained. Percent of recycled paper was between 0 and 46%.
- (c) Beeswax (Ca) and ground rice (Or)—a total of 10 composite materials were obtained. Percent of ground rice was between 0 and 86.5%.
- (d) Beeswax (Ca) and ground fir needles (Abr)—a total of 10 composite materials were obtained. Percent of ground fir was between 0 and 86.5%.

A common/household grinding machine was used for grinding and bringing it to the desired size, and to determine the granulation size, a system equipped with mesh sieves between 0.036 mm and 0.5 mm diameter was used.

For each material in powder form, the amount was gradually increased step by step with 0.25 g and then calculated as a percentage of the entire composite.

First of all, all the elements (recycled cellulose, *Equiseti herba*, rice flour, and paper pulp) were chopped to the desired granulation, weighed, and prepared according to the preset recipes for the next step, namely mixing with beeswax.

The second step was to create the composites: beeswax was melted (up to a temperature of 100 °C) and mixed with various reinforcements (presented above) in different proportions until the reinforcer/hardener was maximally moistened.

Last step was to pour the composite while it was still in a pasty state in the mold.

The combinations that produced the best results were identified, and we decided to use these combinations as a basis for developing new composite materials, as follows:

1. Recyclable paper 100% denoted as S1 (as base for comparison with new composites)
2. Beeswax (50%) + fir resin (50%) denoted as S2
3. Beeswax (62.5%) + horsetail (37.5%) denoted as S3
4. Beeswax (55.56%) + recycled paper (44.44%) denoted as S4
5. Beeswax (45.5%) + milled rice (54.5%) denoted as S5
6. Beeswax (61.5%) + milled fir needles (38.5%) denoted as S6
7. Beeswax (31.25%) + fir resin (31.25%) + horsetail (37.5%) denoted as S7
8. Beeswax (27.78%) + fir resin (27.78%) + recycled paper (44.44%) denoted as S8

To assess the mechanical properties of the natural composite materials, including their flexural strength, impact resistance, and compression resistance, specific molds were designed using SolidWorks 2016 software. These molds were specifically tailored to the unique characteristics of the natural composite materials under study. The molds were then created using 3D-printing technology, utilizing the Fused Filament Fabrication (FFF) technique to produce positive molds.

Silicone rubber was subsequently cast into the positive molds, creating negative molds that were then used to shape the natural blends into their final form. These natural blends were poured into the negative molds, which were designed to be made from recyclable paper, enabling a sustainable and environmentally friendly production process. By utilizing this process, precise and accurate measurements of the natural composite materials' mechanical properties were obtained, providing valuable insights into their potential applications.

International Standard ISO 14125—Plastics, Subcommittee SC 13, Composites and reinforcement fibers—was the basis for testing the samples but not the only one; ISO 178 or ASTM D 790 was consulted, for example.

The photo images taken from the 3D-printed molds are presented in Figure 1.

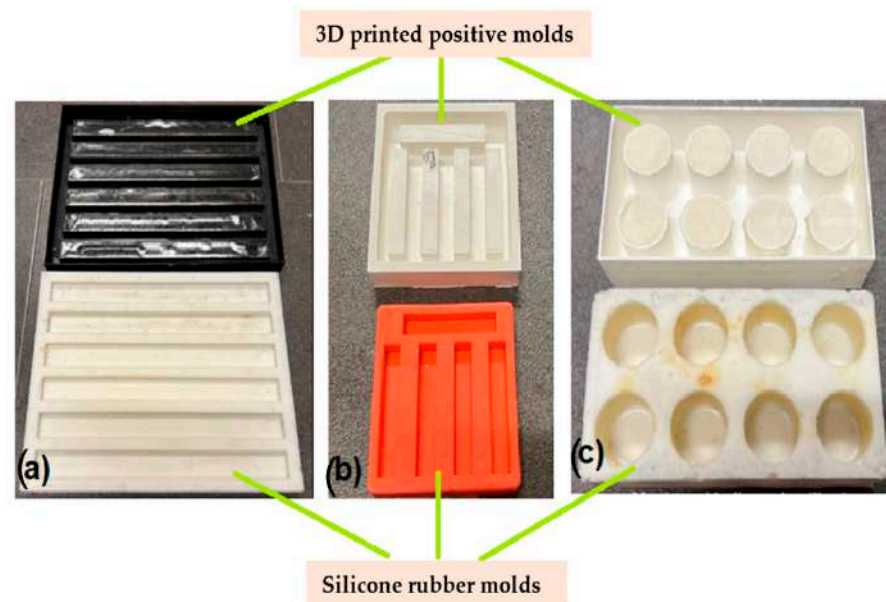


Figure 1. 3D-printed positive and negative molds for mechanical testing of the green composites: (a) for bending; (b) for impact; (c) for compression.

This method of obtaining the molds for testing the mechanical properties of the samples was chosen due to the particularities of these eco-composites: precise, simple, and efficient.

2.2. Materials and Green Composite Preparation

2.2.1. Materials

The green composite materials were developed using natural materials, with beeswax and fir resin serving as the matrix and fir needles, rice, and *Equisetum arvense* as the reinforcing materials. These materials were selected for their biodegradability, recyclability, and sustainable sourcing. Specifically, the fir resin and fir needles were collected during trips to coniferous forests in Brasov, Romania, from fallen branches on the ground. The natural beeswax was purchased from Apsirrom SRL Vaslui, Romania, while the alimentary (grocery-grade) rice and *Equisetum arvense* were obtained from a local shop in Brasov, Romania.

The raw materials used for developing green composite materials are presented in Figure 2.

All these natural materials used for green composite preparation were dried and ground before their blending. After grinding the fir needles, the rice and *Equisetum arvense* grain diameter was under 0.5 mm.

2.2.2. Obtaining Composites

The following steps were taken to prepare the green composite materials:

- (1) The base natural materials (beeswax and/or fir resin) were melted at a temperature of approximately 80–100 °C.
- (2) The reinforcing natural filler powders (fir needles, rice, *Equisetum arvense*) were added in the proportions specified above.

- (3) The natural material blend was mixed thoroughly.
- (4) The blend was poured into silicone rubber molds, as shown in Figure 1, over the recyclable paper.



Figure 2. Raw natural materials used for the green composites.

The recyclable paper was prepared according to the process outlined in Figure 3.

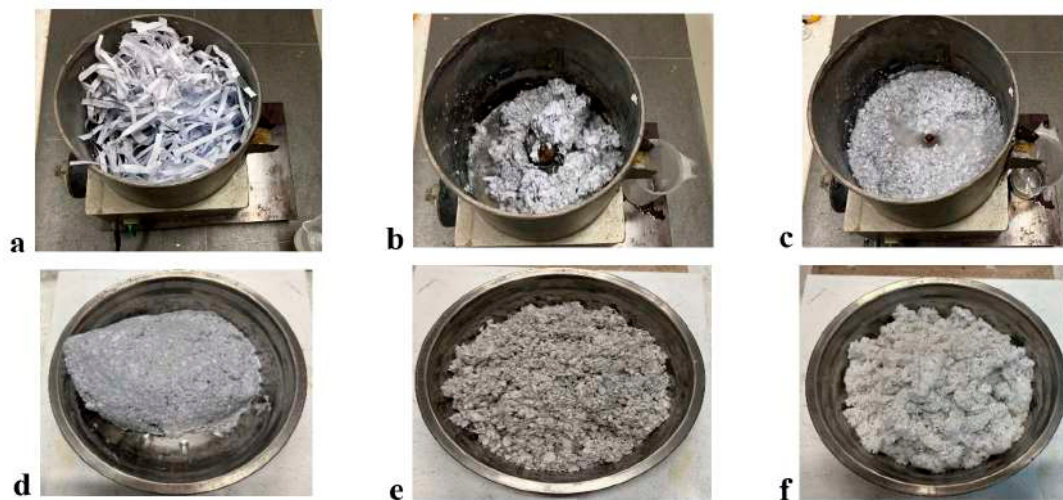


Figure 3. Steps in preparing the recyclable paper: (a) shredded paper; (b) water addition; (c) homogenizing with a blender; (d) paste sieving; (e) drying the paper paste; (f) grinding recyclable paper.

The green composites obtained after pouring the natural material blends onto the recyclable paper can be seen in Figure 4.

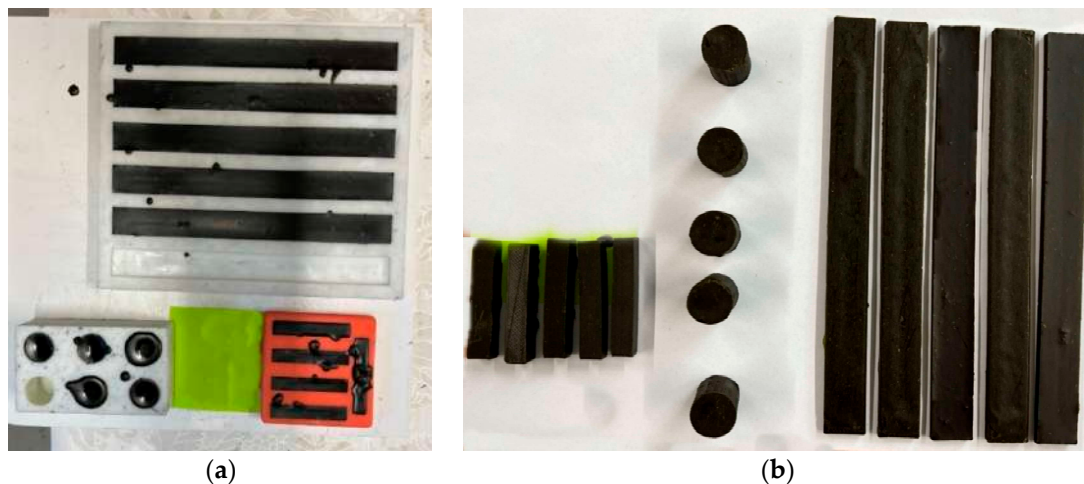


Figure 4. Green composites prepared for mechanical tests; (a) casting in the silicon rubber molds; (b) samples removed from the molds.

All the natural composition blends were poured onto recyclable paper in the PLA molds.

2.3. Characterization Techniques

2.3.1. Mechanical Tests

Bending and compression strength and Young's modulus (E) for the composite structures (sandwich structures and wing sections) were performed on the WDW-150S universal testing machine with a constant crosshead speed of 10 mm/min for all test (Jinan Testing Equipment IE Corporation, Jinan, China). The impact (resilience) strength of the green composites obtained was measured on a Galdabini Impact 25 equipment, Cardano al Campo, Italia, with 25 kJ maximum energy. Compression and bending tests were performed with a speed of 10 mm/s. The impact energy of the impact hammer was 5.5 J. Five samples were tested for each mechanical test property, and the average values are reported.

2.3.2. Surface Morphology Analysis

Micrographs were obtained by using a scanning electron microscope (SEM), Hitachi, Japan, S3400N, type II, and the images were taken from the impact-fractured composite surface.

2.3.3. Optical Microscope

Images of the fractured composite surfaces were taken using an optical microscope type Leica (Arnhem, The Netherlands), Emspira 3 model.

3. Results and Discussion

3.1. Mechanical Tests

The mechanical, thermal, and durability properties of a composite are largely determined by the interfacial adhesion zone in the composite system. The strength of this zone depends on several factors, including the physical–chemical properties of each composite component, their size and shape, mass ratio, dispersion grade of fillers into the matrix composite, preparation technique, and technological parameters used for composite preparation. In this study, we evaluated the mechanical properties of the green composites in terms of impact, compression, and bending maximum force, as shown in Figures 5–7.

Figure 5 shows the variation in impact resistance (resilience) for the natural composites. It is worth noting that the addition of the melted beeswax and fir resin positively influences the impact strength of the resulting composites (S2 and S3) compared to S1 (recyclable paper only). The addition of *Equisetum arvense* powder (S4) and ground rice (S5) negatively impacted the resilience value of the beeswax-based samples (S2), likely due to their higher modulus of elasticity, which includes silica-based compounds and unplasticized starch.

Conversely, the addition of fir needle powders (S6) and fir resin (S8) led to an increase in shock resistance or resilience. The best resilience value was achieved with the S6 composite, which was based on beeswax and fir resin. Additionally, improvements in impact strength were recorded for S2, S6, S7, and S8, with the highest values found in S6 and S8 at 19.42 and 19.32 kJ/m², respectively. These results can be assigned to the mechanical strength provided by fir resin, as well as the viscoelastic properties of the cellulosic fibers, as noted by Jakob et al. [40]. It is widely recognized that cellulosic fibers significantly contribute to the mechanical enhancement of fiber-based composites [40–44]. These findings are consistent with a study conducted by Butnaru et al. [44], which demonstrated the superior thermal and mechanical properties of fir needles compared to fir cone and bark. Furthermore, in addition to their remarkable mechanical and thermal strength, fir needles also exhibit antioxidant properties, which are of great importance in the development of natural composite materials [35].

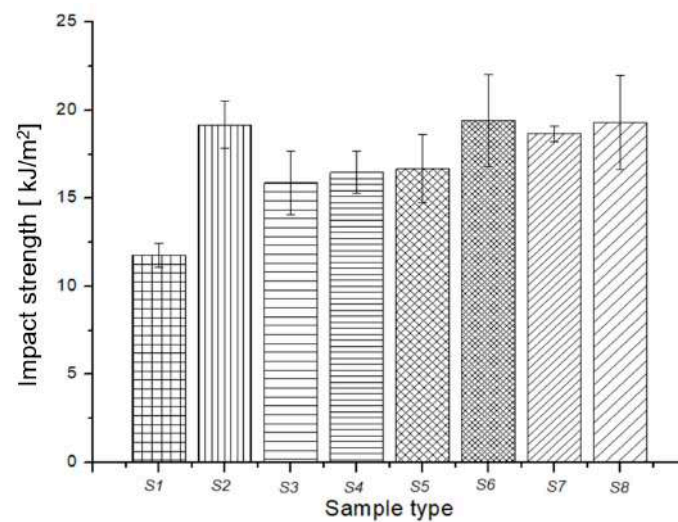


Figure 5. Impact strength variation for green composites.

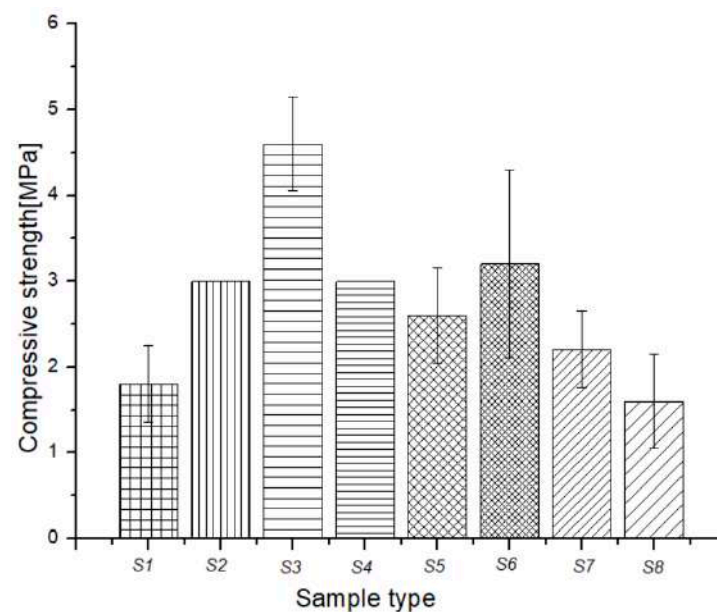


Figure 6. Compressive strength variation for green composites.

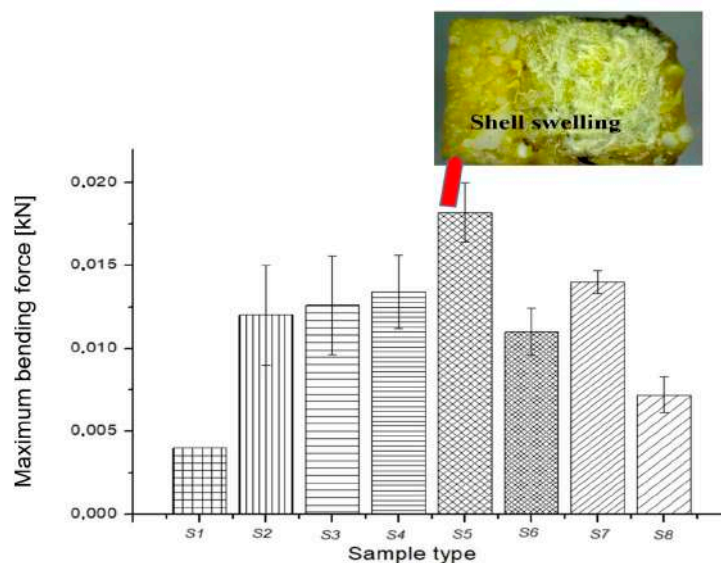


Figure 7. Maximum bending force variation for composites.

Figure 6 shows the compression strength of the natural blends poured onto recyclable paper. Sample S2, based on beeswax poured onto recyclable paper, exhibited a 66.6% increase in compression strength, while sample S3 showed a remarkable increase, exceeding 100%, from 1.8 MPa recorded for S1 (recyclable paper) to 4 MPa recorded for S3. This significant increase in compression strength can be attributed to the insertion of melted fir resin molecules through the paper fibers, as well as the formation of an ordered shell that covers the paper core, as observed in the next section using light microscopy. The hardened fir resin in S3 effectively reinforced the paper fibers, while the shell provided additional support, resulting in a remarkable increase in compression strength.

Ground rice addition caused a slight decrease in compressive strength for the S5 sample, while the addition of fir needle powder caused a slight increase in compressive strength for the S6 sample. The sample based on fir resin (S3) showed the best value for compressive strength. However, the addition of *Equisetum* powder and beeswax (S7) and beeswax alone (S8) had a strong negative effect on the compressive strength of sample S3.

In Figure 7, the maximum bending force of the composites is presented. The addition of ground fir needles to the S2 sample caused a decrease in the maximum bending force for the S6 composite. On the other hand, the addition of *Equisetum* powders (S4), ground rice (S5), and fir resin with *Equisetum* powders (S6) led to an increase in the maximum bending force for sample S2. Among all the samples, composite S5 based on beeswax and ground rice demonstrated the best value for maximum bending strength. This can be attributed to the swelling of the rice fibers, as can be observed in the inset surface fracture image of S5 in Figure 7. The rice fibers covered the paper core, resulting in higher bending force compared to other samples.

In this study, we compared the mechanical properties of the green composites, which were considered as the core materials for the final green products with those of similar commercial products from the automotive sector (see Table 1). We mechanically tested the commercial core product used as a sound-absorbing panel and found that its properties were inferior to those of the core material composites developed in this research. These results indicate that the green composites have the potential to be a superior alternative to the commercial products in terms of mechanical strength and could be applied in various fields, including automotive and sound-absorbing panels.

Table 1. Mechanical properties of the green composites compared to similar commercial products used in the automotive industry.

Mechanical Property/Commercial Automotive Sample/Green Composites	Impact Strength [kJ/m ²]	Compressive Strength [MPa]	Bending Force [N]
	11.41	<1	<3
	13.26	<1	<3
Green composites' mechanical properties			
	19.42	4.60	18.20

The results obtained from the mechanical tests on the proposed composites indicate that improvements and a different approach are necessary to further enhance these properties without sacrificing their advantages, such as being natural, ecological, recyclable, and sustainable. However, the improved physical–mechanical properties make these composites suitable for various applications beyond the automotive industry, including aeronautics and other fields where sound-absorbing panels are needed.

It was also observed that high mechanical properties are not always required for materials used in the automotive industry, particularly for the lining of the engine hood and linear luggage, where good sound-absorbing properties are more important. Overall, the use of natural, sustainable materials in these applications can provide a more environmentally friendly solution while maintaining or even improving performance.

3.2. Light Microscopy

To observe the effect of the natural material blend incorporation poured onto the recyclable paper matrix, optical images of the fractured green composites' surfaces were analyzed using light microscopy. Figure 8 displays representative images of all samples, where the lowest incorporation of natural material onto the recyclable paper matrix corresponds to sample S3, which was poured with fir resin. The rapid toughening of the fir resin forms a stiff shell that encapsulates the paper matrix, resulting in the highest compression strength of this sample compared to the others, as previously shown in the compression test with a recorded value of 4.6 MPa.

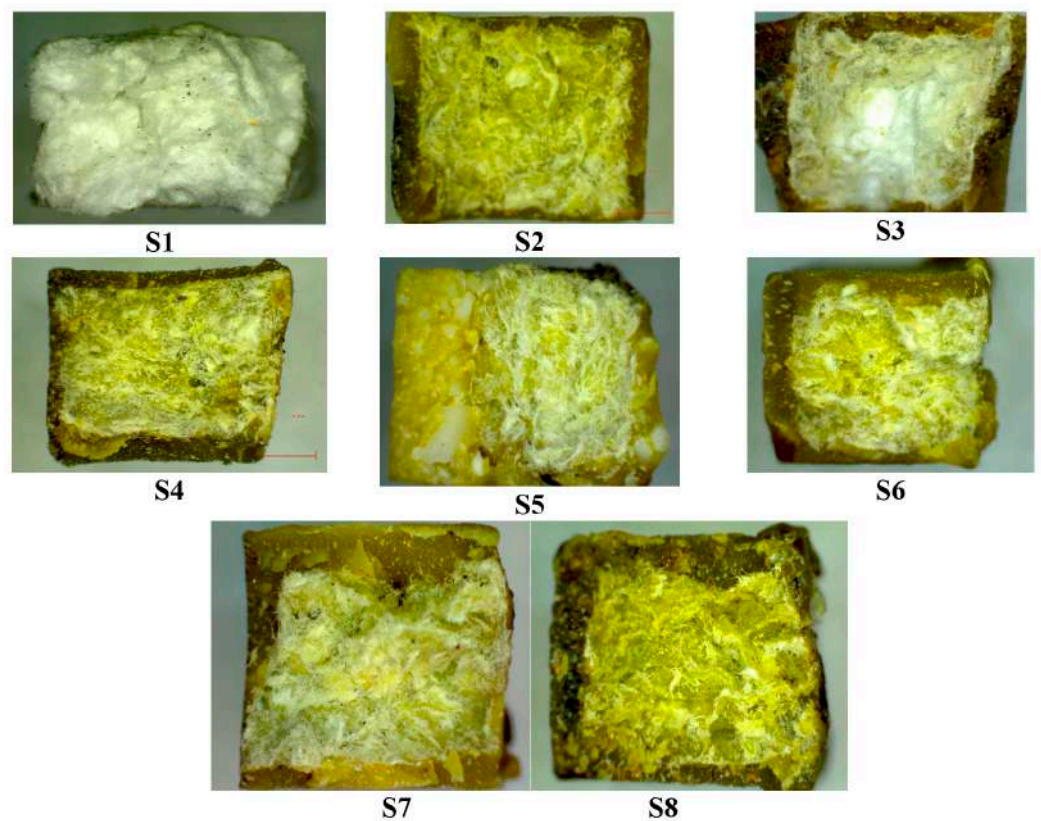


Figure 8. Fractured surfaces' microscope images of the green composites (30× magnification).

The observations from the light microscopy images show that the natural material blends were able to wet the paper core effectively. The dispersion of natural blends was remarkable for samples S2, S6, S7, and S8, with the blends encapsulating the paper core fibers, thereby adding mechanical strength to the resulting green composites. These findings confirm the results from the mechanical tests, particularly the high impact strength values of 19.16, 19.42, and 19.32 kJ/m² for the green composites denoted as S2, S6, and S8, respectively.

3.3. Surface Morphology and Internal Structure

Scanning electron microscopy was performed to investigate the surface morphology and interface structure of the impact-fractured composite samples with good mechanical strength (S2, S6, S7, and S8), as shown in Figure 9. The SEM images reveal a low-rugosity surface, indicating strong bonding between the composite components and reflecting good interface strength.

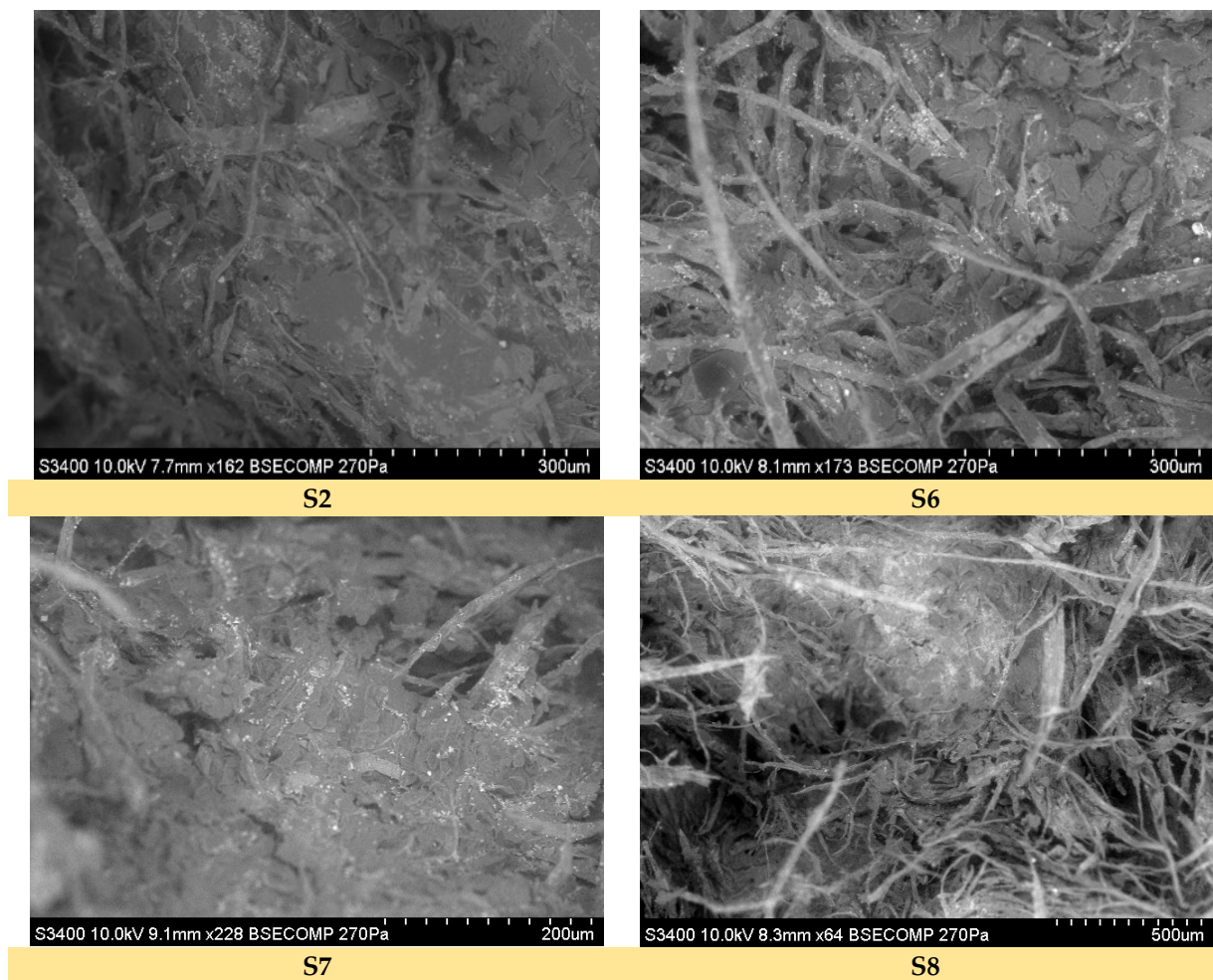


Figure 9. SEM images of fractured green composites' surfaces.

The SEM images obtained from the fractured S2, S6, and S7 samples demonstrate a uniform morphology, indicating a high dispersion of the melted natural materials (beeswax, fir resin with/without fir needles, and *Equisetum* fibers) throughout the internal structure of the paper fiber cores. This behavior, particularly in the case of the S2 sample, confirms its mechanical performance, as the mechanical tests showed an approximately doubled impact strength compared to the recyclable paper-only reference. The interface failure is observed as a matrix failure, with tearing and shearing of the matrix visible. The images in Figure 9 also show that even after composite fracture, the paper core fibers are still covered by the melted natural material blend.

4. Conclusions

- This paper presents the steps involved in obtaining 3D-printed PLA molds for natural composites made of recyclable paper, beeswax, fir resin, needles, rice, and *Equisetum arvense*, and it assesses the mechanical properties of the green composites;
- The highest impact strengths, provided mainly by fir resin and cellulose, were attributed to the samples with beeswax and fir needles S6 and beeswax fir resin and recyclable paper S8, 19.42 and 19.32 kJ/m², respectively, while the highest compressive strength was 4 MPa for the S3 sample. The rice fibers positively influenced the maximum bending for the S5 sample;
- The superiority of the green composites' mechanical properties was proved, considering the core materials for the final green products over similar commercial products from the automotive sector;

- The green composites exhibited over 60% higher mechanical properties compared to similar products from the market used as sound-absorbing core materials in the automotive industry;
- The physico-mechanical properties were directly influenced by the wetting degree of the powders for the beeswax and the fir resin and through the interaction between the complementary chemical groups from the fillers and the matrices (possibly silicates, phenolic carboxylic acids, resinic acids, and so on);
- Further research is ongoing to determine the thermal and sound-absorbing properties of these composites, as well as finding new solutions to enhance their physical-mechanical properties. One possible solution is combining the benefits of eco-friendly filament printing, such as polylactic acid, with the sound-absorbing properties of these new materials.

Author Contributions: Conceptualization, M.A.P. and M.C.; methodology, C.C., S.M.Z., M.A.P. and M.C.; software, S.M. and C.S.; validation, C.C., investigation, M.A.P., C.C., S.M.Z. and M.C.; writing—original draft preparation, M.C., M.A.P., S.M. and C.S.; project administration, M.A.P. All authors have read and agreed to the published version of the manuscript.

Funding: This work was supported by a grant from the Ministry of Research, Innovation and Digitization, CNCS-UEFISCDI, project number PN-III-P1-1.1-TE-2021-0294, within PNCDI III.

Institutional Review Board Statement: Not applicable.

Data Availability Statement: The data presented in this study are available on request from the corresponding author.

Acknowledgments: This work was supported by a grant from the Ministry of Research, Innovation and Digitization, CNCS-UEFISCDI, project number PN-III-P1-1.1-TE-2021-0294, within PNCDI III. We also acknowledge the structural funds project PRO-DD (POS-CCE O.2.2.1, ID 123, SMIS 2637, ctr. No 11/2009) for partially providing the infrastructure used in this work at the CDI Institute of Transilvania University of Brasov.

Conflicts of Interest: The authors declare no conflict of interest. The funders had no role in the design of the study; in the collection, analyses, or interpretation of data; in the writing of the manuscript; or in the decision to publish the results.

References

1. Hoang, A.T.; Varbanov, P.S.; Nižetić, S.; Sirohi, R.; Pandey, A.; Luque, R.; Ng, K.H.; Pham, V.V. Perspective review on Municipal Solid Waste-to-energy route: Characteristics, management strategy, and role in circular economy. *J. Clean. Prod.* **2022**, *359*, 131897. [[CrossRef](#)]
2. Isitman, N.A.; Kaynak, C. Nanoclay and carbon nanotubes as potential synergists of an organophosphorus flame-retardant in poly(methyl methacrylate). *Polym. Degrad. Stab.* **2010**, *95*, 1523–1532. [[CrossRef](#)]
3. Gay, D. *Matériaux Composites*; Hermes: Paris, France, 1991.
4. Stefanescu, F.; Neagu, G.; Mihai, A. *Materiale Composite*; Publishing house “Didactica si Pedagogica”: Bucuresti, Romania, 1996.
5. Abraham, T.; Bryant, R.W.; Mooney, P.J. The Prospects for Advanced Polymer-, Metal- and Ceramic-Matrix Composites. *JOM* **1988**, *40*, 46–48. [[CrossRef](#)]
6. Chawla, K.K. The high-temperature application of ceramic-matrix composites. *JOM* **1995**, *47*, 19–21. [[CrossRef](#)]
7. Baltas, L. *Materiale Amorse—Materiale Compozite*; Publishing House “Transilvania” University: Brasov, Romania, 2003.
8. Sumesh, G.; Mailadil, T.S. Three-phase polymer–ceramic–metal composite for embedded capacitor applications. *Compos. Sci. Technol.* **2009**, *69*, 1298–1302.
9. Usmani, Z.; Sharma, M.; Awasthi, A.K.; Sivakumar, N.; Lukk, T.; Pecoraro, L.; Thakur, V.K.; Roberts, D.; Newbold, J.; Gupta, V.K. Bioprocessing of waste biomass for sustainable product development and minimizing environmental impact. *Bioresour. Technol.* **2021**, *322*, 124548. [[CrossRef](#)]
10. Rajak, D.K.; Pagar, D.D.; Menezes, P.L.; Linul, E. Fiber-Reinforced Polymer Composites: Manufacturing, Properties, and Applications. *Polymers* **2019**, *11*, 1667. [[CrossRef](#)]
11. Ismail, S.O.; Akpan, E.; Dhakal, H.N. Review on natural plant fibres and their hybrid composites for structural applications: Recent trends and future perspectives. *Compos. Part C Open Access* **2022**, *9*, 100322. [[CrossRef](#)]
12. Mueller, D.H.; Krobjilowski, A. New Discovery in the Properties of Composites Reinforced with Natural Fibers. *J. Ind. Text.* **2003**, *33*, 111–130. [[CrossRef](#)]

13. Rodríguez, E.; Petrucci, R.; Puglia, D.; Kenny, J.M.; Vázquez, A. Characterization of Composites Based on Natural and Glass Fibers Obtained by Vacuum Infusion. *J. Compos. Mater.* **2005**, *39*, 265–282. [[CrossRef](#)]
14. Mann, G.S.; Singh, L.P.; Kumar, P.; Singh, S. Green composites: A review of processing technologies and recent applications. *J. Thermoplast. Compos. Mater.* **2018**, *33*, 1145–1171. [[CrossRef](#)]
15. Syduzzaman, M.; Al Faruque, M.A.; Bilisik, K.; Naebe, M. Plant-Based Natural Fibre Reinforced Composites: A Review on Fabrication, Properties and Applications. *Coatings* **2020**, *10*, 973. [[CrossRef](#)]
16. Faruk, O.; Bledzki, A.K.; Fink, H.-P.; Sain, M. Progress Report on Natural Fiber Reinforced Composites. *Macromol. Mater. Eng.* **2014**, *299*, 9–26. [[CrossRef](#)]
17. Ates, B.; Koytepe, S.; Ulu, A.; Gurses, C.; Thakur, V.K. Chemistry, Structures, and Advanced Applications of Nanocomposites from Biorenewable Resources. *Chem. Rev.* **2020**, *120*, 9304–9362. [[CrossRef](#)] [[PubMed](#)]
18. Sharath Shekar, H.S.; Ramachandra, M. Green Composites: A Review. *Mater. Today Proc.* **2018**, *5*, 2518–2526. [[CrossRef](#)]
19. Islam, M.Z.; Sarker, M.E.; Rahman, M.M.; Islam, M.R.; Ahmed, A.; Mahmud, M.S.; Syduzzaman, M. Green composites from natural fibers and biopolymers: A review on processing, properties, and applications. *J. Reinf. Plast. Compos.* **2022**, *41*, 526–557. [[CrossRef](#)]
20. Ntimugura, F.; Vinai, R.; Harper, A.; Walker, P. Mechanical, thermal, hygroscopic and acoustic properties of bio-aggregates—lime and alkali—Activated insulating composite materials: A review of current status and prospects for miscanthus as an innovative resource in the South West of England. *Sustain. Mater. Technol.* **2020**, *26*, e00211. [[CrossRef](#)]
21. Núñez-Decap, M.; Wechsler-Pizarro, A.; Vidal-Vega, M. Mechanical, physical, thermal and morphological properties of polypropylene composite materials developed with particles of peach and cherry stones. *Sustain. Mater. Technol.* **2021**, *29*, e00300. [[CrossRef](#)]
22. Kumar, A.; Gupta, V.; Singh, S.; Saini, S.; Gaikwad, K.K. Pine needles lignocellulosic ethylene scavenging paper impregnated with nanozeolite for active packaging applications. *Ind. Crop. Prod.* **2021**, *170*, 113752. [[CrossRef](#)]
23. Farid, M.; Purniawan, A.; Rasyida, A.; Ramadhani, M.; Komariyah, S. Improvement of acoustical characteristics: Wideband bamboo based polymer composite. *IOP Conf. Ser. Mater. Sci. Eng.* **2017**, *223*, 012021. [[CrossRef](#)]
24. Paul, P.; Ahirwar, M.; Behera, B.K. Acoustic behaviour of needle punched nonwoven structures produced from various natural and synthetic fibers. *Appl. Acoust.* **2022**, *199*, 109043. [[CrossRef](#)]
25. Atabani, A.; Ali, I.; Naqvi, S.R.; Badruddin, I.A.; Aslam, M.; Mahmoud, E.; Almomani, F.; Juchelková, D.; Atelge, M.; Khan, T.Y. A state-of-the-art review on spent coffee ground (SCG) pyrolysis for future biorefinery. *Chemosphere* **2022**, *286*, 131730. [[CrossRef](#)] [[PubMed](#)]
26. Bhatia, S.K.; Palai, A.K.; Kumar, A.; Bhatia, R.K.; Patel, A.K.; Thakur, V.K.; Yang, Y.-H. Trends in renewable energy production employing biomass-based biochar. *Bioresour. Technol.* **2021**, *340*, 125644. [[CrossRef](#)]
27. Moscardiello, C.; Matassa, S.; Pirozzi, F.; Esposito, G.; Papirio, S. Valorisation of industrial hemp (*Cannabis sativa* L.) biomass residues through acidogenic fermentation and co-fermentation for volatile fatty acids production. *Bioresour. Technol.* **2022**, *355*, 127289. [[CrossRef](#)]
28. Rana, A.K.; Guleria, S.; Gupta, V.K.; Thakur, V.K. Cellulosic pine needles-based biorefinery for a circular bioeconomy. *Bioresour. Technol.* **2023**, *367*, 128255. [[CrossRef](#)]
29. Sealy, C. Recyclable graphite-cellulose composite stronger than steel. *Mater. Today* **2019**, *28*, 7–8. [[CrossRef](#)]
30. Dong, C. Review of natural fibre-reinforced hybrid composites. *J. Reinf. Plast. Compos.* **2018**, *37*, 331–348. [[CrossRef](#)]
31. Khalid, M.Y.; Arif, Z.U.; Ahmed, W.; Arshad, H. Recent trends in recycling and reusing techniques of different plastic polymers and their composite materials. *Sustain. Mater. Technol.* **2022**, *31*, e00382. [[CrossRef](#)]
32. Angin, N.; Caylak, S.; Ertas, M.; Cavdar, A.D. Effect of alkyl ketene dimer on chemical and thermal properties of polylactic acid (PLA) hybrid composites. *Sustain. Mater. Technol.* **2022**, *32*, e00386. [[CrossRef](#)]
33. Patel, V.K.; Rawat, N. Physico-mechanical properties of sustainable Sagwan-Teak Wood Flour/Polyester Composites with/without gum rosin. *Sustain. Mater. Technol.* **2017**, *13*, 1–8. [[CrossRef](#)]
34. AL-Oqla, F.M.; Hayajneh, M.T.; Al-Shrida, M.M. Mechanical performance, thermal stability and morphological analysis of date palm fiber reinforced polypropylene composites toward functional bio-products. *Cellulose* **2022**, *29*, 3293–3309. [[CrossRef](#)]
35. Singh, M.K.; Tewari, R.; Zafar, S.; Rangappa, S.M.; Siengchin, S. A comprehensive review of various factors for application feasibility of natural fiber-reinforced polymer composites. *Results Mater.* **2023**, *17*, 100355. [[CrossRef](#)]
36. Zhang, J.; Khatibi, A.A.; Castanet, E.; Baum, T.; Komeily-Nia, Z.; Vroman, P.; Wang, X. Effect of natural fibre reinforcement on the sound and vibration damping properties of bio-composites compression moulded by nonwoven mats. *Compos. Commun.* **2019**, *13*, 12–17. [[CrossRef](#)]
37. Joseph-Leenose-Helen, J.; Noor, N.; Mushtaq, M.; Gani, A. Ultrasonics as a tool for development of pine-needle extract loaded bee wax edible packaging for value addition of Himalayan cheese. *Ultrason. Sonochem.* **2022**, *82*, 105914. [[CrossRef](#)]
38. Kajjari, P.B.; Manjeshwar, L.S.; Aminabhavi, T.M. Novel blend microspheres of cellulose triacetate and bee wax for the controlled release of nateglinide. *J. Ind. Eng. Chem.* **2014**, *20*, 397–404. [[CrossRef](#)]
39. Jakob, M.; Mahendran, A.R.; Gindl-Altmatter, W.; Bliem, P.; Konnerth, J.; Müller, U.; Veigel, S. The strength and stiffness of oriented wood and cellulose-fibre materials: A review. *Prog. Mater. Sci.* **2022**, *125*, 100916. [[CrossRef](#)]
40. Bazli, M.; Heitzmann, M.; Hernandez, B.V. Durability of fibre-reinforced polymer-wood composite members: An overview. *Compos. Struct.* **2022**, *295*, 115827. [[CrossRef](#)]

41. Taurino, R.; Bondioli, F.; Messori, M. Use of different kinds of waste in the construction of new polymer composites: Review. *Mater. Today Sustain.* **2023**, *21*, 100298. [[CrossRef](#)]
42. Cosnita, M.; Cazan, C.; Duta, A. The influence of inorganic additive on the water stability and mechanical properties of recycled rubber, polyethylene terephthalate, high density polyethylene and wood composites. *J. Clean. Prod.* **2017**, *165*, 630–636. [[CrossRef](#)]
43. Al-Oqla, F.M.; Sapuan, S.M. Natural fiber reinforced polymer composites in industrial applications: Feasibility of date palm fibers for sustainable automotive industry. *J. Clean. Prod.* **2014**, *66*, 347–354. [[CrossRef](#)]
44. Butnaru, E.; Brebu, M. The Thermochemical Conversion of Forestry Residues from Silver Fir (*Abies alba* Mill.) by Torrefaction and Pyrolysis. *Energies* **2022**, *15*, 3483. [[CrossRef](#)]

Disclaimer/Publisher's Note: The statements, opinions and data contained in all publications are solely those of the individual author(s) and contributor(s) and not of MDPI and/or the editor(s). MDPI and/or the editor(s) disclaim responsibility for any injury to people or property resulting from any ideas, methods, instructions or products referred to in the content.

Article

Design and Testing of Brushless DC Motor Components of A6 Steel Additively Manufactured by Selective Laser Sintering

Sebastian-Marian Zaharia ^{1,*}, Mihai Alin Pop ², George Razvan Buican ¹, Lucia-Antoneta Chicos ¹, Valentin Marian Stamate ¹, Ionut Stelian Pascariu ¹ and Camil Lancea ¹

¹ Department of Manufacturing Engineering, Transilvania University of Brasov, 500036 Brasov, Romania

² Department of Materials Science, Transilvania University of Brasov, 500036 Brasov, Romania

* Correspondence: zaharia_sebastian@unitbv.ro

Abstract: Metallic additive manufacturing technology is seeing increasing use from aviation companies manufacturing prototypes or components with complex geometric shapes, which are then tested and put into operation. This paper presents the design, fabrication via a selective laser sintering process, and testing of the mechanical performance by performing three-point bending and tensile tests on A6 steel specimens. After performing the mechanical tests on specimens made from A6 steel manufactured via the SLS process, the following performances were obtained: the maximum three-point bending strength was 983.6 MPa and the maximum tensile strength was 398.6 MPa. In the microscopic analysis of the specimens manufactured by the selective laser sintering process, a homogeneous structure with defects specific to additive processes (voids) was revealed. Additionally, the feasibility of designing, manufacturing through the selective laser sintering process and subsequent testing of some components (rotor, right case, left case and motor mount) from a brushless motor made from A6 steel material was demonstrated. After testing the brushless motor, the main performances showed stable behavior of the motor and a linear dependence with the increase in electronic speed control signal or motor electrical speed, resulting in a maximum thrust force of 4.68 kgf at 7800 RPM.

Keywords: brushless motor; performance analysis; selective laser sintering; mechanical testing



Citation: Zaharia, S.-M.; Pop, M.A.; Buican, G.R.; Chicos, L.-A.; Stamate, V.M.; Pascariu, I.S.; Lancea, C. Design and Testing of Brushless DC Motor Components of A6 Steel Additively Manufactured by Selective Laser Sintering. *Aerospace* **2023**, *10*, 60. <https://doi.org/10.3390/aerospace10010060>

Academic Editor: Kyriakos I. Kourousis

Received: 18 September 2022

Revised: 27 December 2022

Accepted: 5 January 2023

Published: 6 January 2023



Copyright: © 2023 by the authors. Licensee MDPI, Basel, Switzerland. This article is an open access article distributed under the terms and conditions of the Creative Commons Attribution (CC BY) license (<https://creativecommons.org/licenses/by/4.0/>).

1. Introduction

A brushless direct current (BLDC) motor is a synchronous motor that uses a direct current (DC) power supply. The BLDC motor uses an electronic closed-loop controller to switch DC currents to the motor windings, producing magnetic fields that actually rotate in space and which the permanent magnet rotor follows [1]. The controller adjusts the phase and amplitude of the DC pulses to control the speed and torque of the motor [2]. The main advantages of a brushless motor are long life, high power-to-weight ratio, high speed and efficiency, low manufacturing and maintenance costs, almost instantaneous speed and torque control and its compact structure [3]. In recent years, BLDC motors have seen frequent use in fields such as aerospace, automotive, robotics, household appliances, food and chemicals, medical equipment and computer peripherals [4,5]. Information on the performance of BLDC motors used in aviation to propel unmanned aerial vehicles (UAVs) is generally available from the suppliers of such propulsion systems. However, an accurate estimate of the performance of BLDC motors depends on the materials from which the stator and rotor cores are made, their geometry, the type and number of permanent magnets and the winding distribution. In order to determine the performance of BLDC motors, various studies were carried out using various techniques and methods. The behavior of BLDC motors was analyzed using two methods: Fast-Fourier Transform (FFT) and chaos analysis [6], and application of the cuckoo search (CS) algorithm in an attempt to minimize the commutation torque ripple in a brushless BLDC motor [7], improving the

efficiency and reducing the acoustic noise of BLDC motors by reducing current harmonics using a novel commutation method to generate a sinusoidal current waveform without requiring additional hardware [8]. Another study [9] investigates three BLDC motor control schemes analyzed under different operating conditions, including steady-state and transient operations. A comparative study based on qualitative, quantitative and electromagnetic analysis of BLDC motors was carried out using finite element analysis in order to optimize the designed models [10,11]. BLDC motors are intensively studied and used in various aerospace applications, such as analysis of the flight performance of drones [12–14] and UAVs [15,16], as well as various morphing wing models, actuated by actuator systems, increasing their span/chord during flight [17,18].

Currently, additive manufacturing technologies are successfully used in various fields, such as aviation, automotive, medicine, dentistry, architecture, various aircraft [19–21], functional components [22–24], models for assembly testing [25] and medical device prototypes [26–28]. Additive technology has represented and continues to represent a challenge, especially in the field of aviation where there is fierce competition in the market to produce aeronautical products, in the shortest possible time, that respect both aeronautical regulations and structural performances. Additive manufacturing technologies represent a current trend in the realization of electric machines or their components, offering a high degree of flexibility regarding the design of products in order to achieve performance parameters which are more difficult to achieve through conventional manufacturing techniques [29,30]. Manufacturing a BLDC motor, completely through additive manufacturing technologies remains a challenge for manufacturing and aviation engineers. Next, some studies on certain components of electric motors made using additive manufacturing technologies will be presented. In order to verify the design process, an initial study [31] was carried out regarding selective laser melting (SLM) manufacturing of three components from a synchronous reluctance motor (SynRM). One option for making BLDC motors is manufacturing through the fused filament fabrication (FFF) process. In this sense, an electric motor with permanent magnets was manufactured and tested using the FFF process from polylactic acid filament [32]. Of course, the design for additive manufacturing is also an important aspect that must be considered. In this sense, various models of spiderweb lattice structures used in a BLDC motor were designed and analyzed using the finite element method [33]. Garibaldi et al. [34] reported the successful manufacture, through the laser beam machining (LBM) process, of the rotor core made of FeSi6.9, for rotating electrical machinery. A recent study [35] demonstrated the feasibility of manufacturing concentrated windings through the laser powder bed fusion (LPBF) process of pure copper, with air between the flat layered turns. Another study [36] showed that that topology optimized soft magnetic core was successfully created using the selective laser melting process, from Fe-Co powder. Lancea et al. [37] manufactured the components (the rotor and the two housings right case and left case) via the FFF process, from LW-PLA filament, with the aim of verifying the assembly of the components and finding design problems.

Thus, this study is based on previous research [37], which expanded the manufacturing domain for a functional model of a BLDC motor made using the selective laser sintering (SLS) process. Starting from the initial model, by modifying and manufacturing the components (rotor, right case, left case and motor mount) using the SLS method, a functional BLDC motor was assembled and tested. Prior to the SLS manufacture of the BLDC motor components mentioned above, in this study, the A6 steel was tested (three-point bending and tensile) and microscopically analyzed.

2. Materials and Methods

2.1. Design of Specimens Used in Mechanical Tests

By using current standards ASTM E290-14 [38] and ASTM E8/E8M-16ae1 [39] applied to metal specimens manufactured via additive processes, and by using the SolidWorks 2021 software system (Dassault Systèmes SolidWorks Corporation, Waltham, MA, USA), the specific specimens for mechanical tests (three-point bending and tensile) were designed.

The specimens, manufactured by the SLS process, tested in three-point bending, have the dimensions shown in Table 1.

Table 1. The dimensions of specimens subjected to three-point bending.

Length L [mm]	Width w [mm]	Thickness t [mm]
130	19	3.2

The specimen dimensions used in the three-point bending and tensile tests were detailed in Table 2.

Table 2. The dimensions of specimens subjected to tensile testing.

Overall Length [mm]	Distance between Grips [mm]	Gauge Length [mm]	Width of Grip Section [mm]	Width [mm]	Thickness [mm]	Radius of Fillet [mm]
165	115	57	19	13	3.2	76

2.2. Component Design for BLDC Motor Model

The design of the BLDC motor components from the previous study [32] was optimized for a more appropriate additive manufacturing process. Thus, for easier manufacturing, the rotor and the right housing were designed as one piece (Figure 1a), to remove the need for assembly. This component (Figure 1a) has been provided with spacer surfaces for easy positioning of the magnets. The other two designed components of the BLDC motor were the left housing (Figure 1b) and the motor mount (Figure 1c). The rotor has a wall thickness of 2 mm, a length of 55 mm and an outer diameter of 49.8 mm. The left case (Figure 1b) has a diameter of 49.8 mm, a shell thickness of 2 mm and is provided with holes for ventilation. The motor mount component (Figure 1c) has four arms and a thickness of 4 mm.

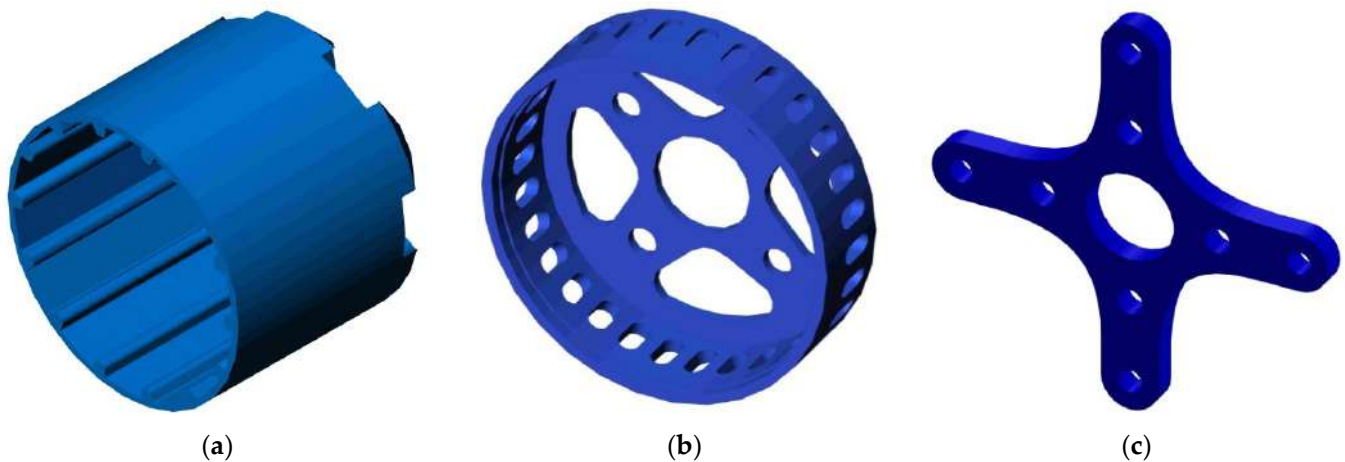


Figure 1. Designed components of BLDC motor: (a) rotor; (b) left case; (c) motor mount.

2.3. SLS Manufacturing of BLDC Motor Specimens and Components

After careful analysis of the design and operation of the electric motor, the following components (rotor and right housing, printed together, left housing and flange) are good candidates for additive manufacturing using the SLS process. The other components of the motor (stator with winding, shaft) were manufactured using classical manufacturing technologies. The 3D System sPRO 60 SD printer (sPRO 60, 3D Systems, Inc., Rock Hill, SC, USA) was used to manufacture the BLDC motor components. The 3D printing facility allows the creation of highly complex products, from a geometrical point of view, using

metal, ceramic, polymer and composite powders. The sintering furnace attached to the SLS printing plant ensures the sintering of ceramic and metal powders and infiltration with different metals.

If, in the case of using polymeric materials, the final component is obtained directly from the SLS process, without the need for other subsequent steps, in the case of using metal powder, after obtaining the desired components, an additional bronze infiltration step is required. This additional step is preceded by a weighing of the component and the establishment of the infiltrant proportion (65% of the mass of the component), according to the technical data sheet provided by the manufacturer. These bronze particles are placed in contact with the specimens to guarantee infiltration via capillary action once melting takes place in the furnace. Components and bronze are coated with alumina powder for homogeneous heat transfer and infiltration. Infiltration is a post-processing method [40] of components manufactured by the SLS process from metal powder. Infiltration is used in particular to densify and strengthen components when the required characteristics cannot be achieved through the main manufacturing process (SLS in this study).

The material used in the manufacture of the electric motor components, through the SLS process, was A6 steel, produced by the 3D Systems Company. LaserForm™ A6 steel powder is a magnetic material, used for rapid prototyping of molds and tools, which presents the following advantages: design flexibility, excellent machinability, good thermal conductivity and surface finish [41].

BLDC motor specimens and components, designed in SolidWorks 2021, were exported in .stl (stereolithography) format for manufacture using the 3D System sPRO 60 SD printer. The Vanguard software system was used to generate the machine code for the SLS manufacturing process of the components. In Table 3, the main manufacturing parameters used in the SLS process to make the BLDC motor components and the specimens are presented.

Table 3. Manufacturing parameters of BLDC motor components and specimens.

Process Parameter	Unit	Value
Fill laser power	W	15
Outline laser power	W	5
Layer thickness	µm	100
Scanning speed	m/s	5
Laser beam diameter	µm	60
Preheating temperature	°C	120

After manufacturing the components of the BLDC motor (Figure 2a–c), the next steps were to clean and weigh the parts, calculate the amount of infiltrate (Figure 2d) and place them in the heat-treatment furnace. The infiltration temperature was 1070 °C, according to the plant manufacturer’s specifications, in gaseous nitrogen atmosphere, and the total heating–holding–cooling cycle was 72 h. The last stage was the removal of the “tabs” (supports created intentionally for placing the bronze) and the turning process on a lathe. The results of the SLS additive process can be seen in Figure 2e (BLDC motor rotor) and in Figure 2f (specimens used in mechanical tests).

2.4. Test Conditions and Microscopic Analysis of Specimens

Three-point bending testing (Figure 3a) and tensile testing (Figure 3b) of the specimens, manufactured by the SLS process, was performed on a WDW-150S universal testing machine (Jinan Testing Equipment IE Corporation, Jinan, China). For testing, five specimens were manufactured for each type of test, according to standards for the testing of mechanical specimens. Three-point bending tests and tensile tests were carried out in order to determine the characteristics (bending strength, tensile strength and aspects related to the load–displacement characteristic curve) of the A6 steel material. This information was the basis for the use of A6 steel material in the manufacture of BLDC motor components. Both types of tests were carried out with a loading speed of 5 mm/min [42,43], until the

specimens broke. In order to assess the manufacturing method of the A6 steel material, microscopic analyses were performed using three sections (Figure 3c), with the help of a Nikon Eclipse MA 100 microscope (Nikon Corp., Tokyo, Japan). The specimens were polished and treated with aqua regia to reveal the internal structure of the A6 steel material.

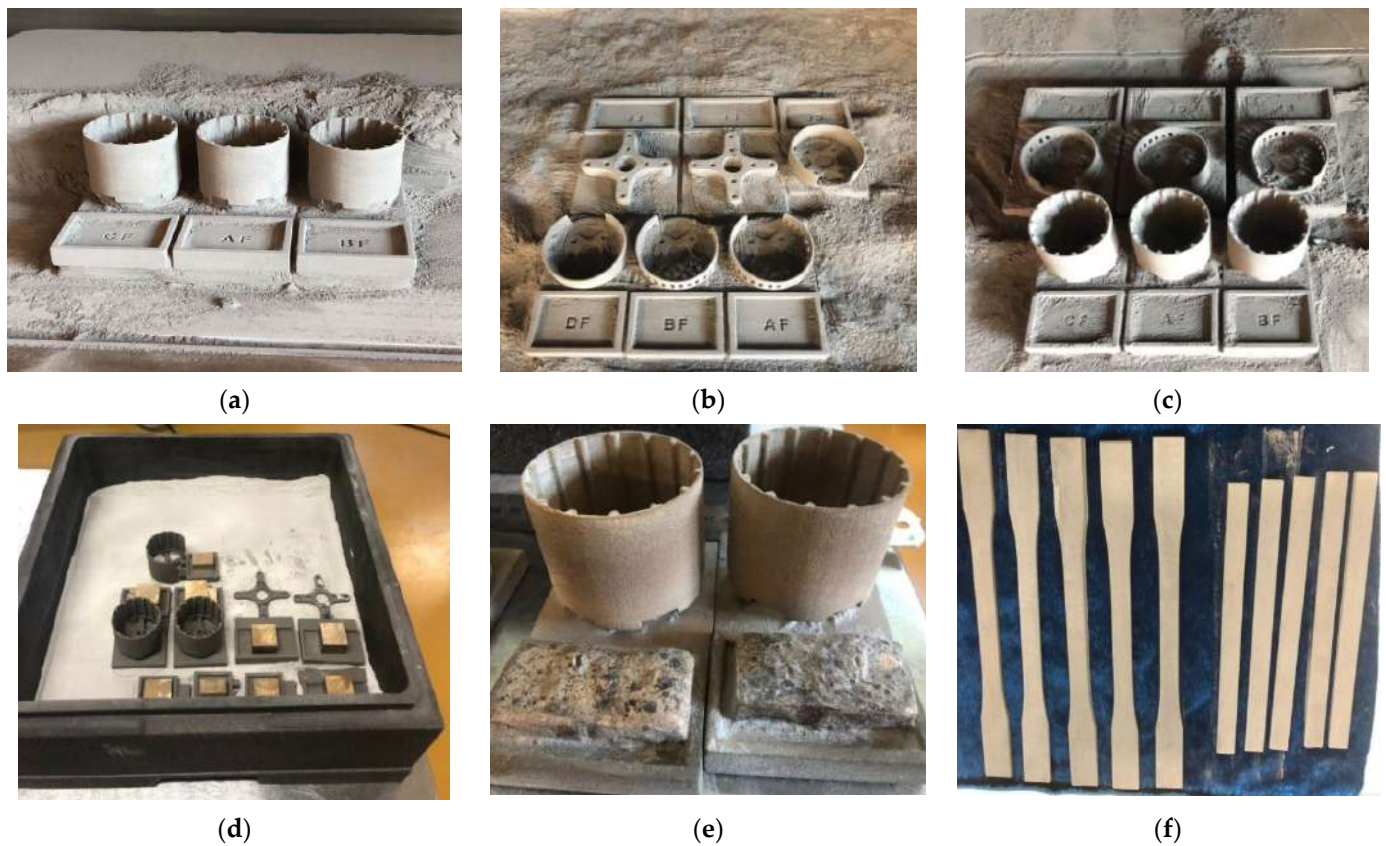


Figure 2. Additive manufacturing of BLDC motor components using the SLS process: (a) Parts cleaning; (b) left housing and motor mount; (c) rotor; (d) preparing the components for infiltration into the sintering furnace; (e) rotor obtained after infiltration; (f) specimens obtained after infiltration.

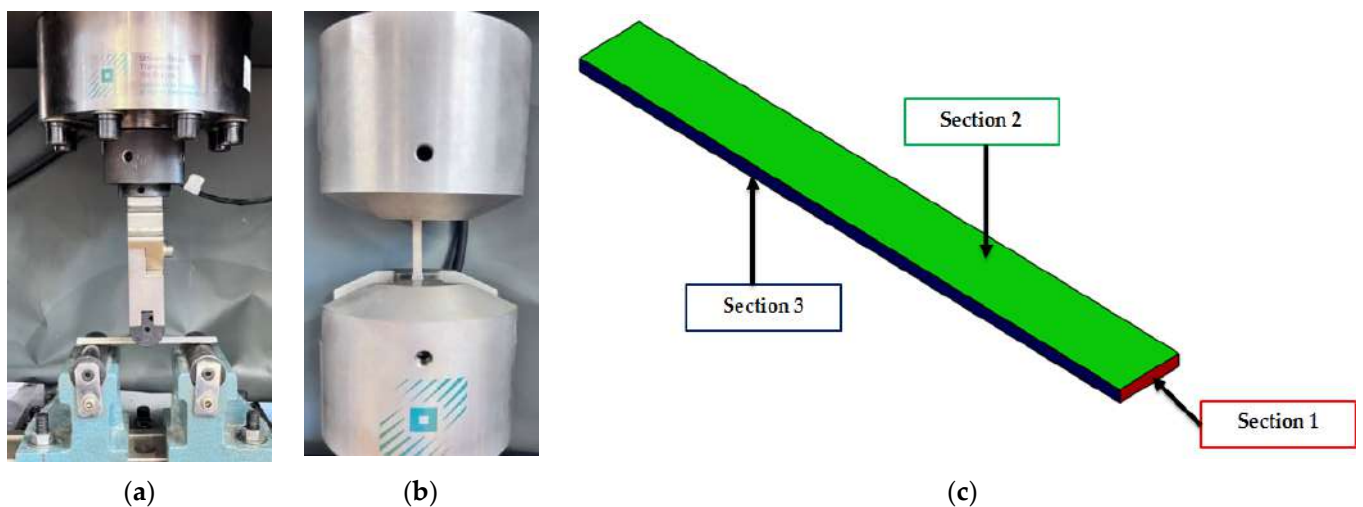


Figure 3. Testing and analysis of specimens: (a) three-point bending test; (b) tensile testing; (c) establishment sections for microscopic analysis.

2.5. Assembling BLDC Motor Components

In the first stage of the assembly of the BLDC motor manufactured via the SLS process, the centering and fixing of the rotor component on the motor shaft was considered in order to check the position of the shaft and the mode of operation of the rotor. Afterwards, the winding support was fixed on the shaft and two radial ball bearings were inserted in the specially created bearing housing from the right cover. Due to the high complexity and precision of the execution, it was decided that the stator and winding should be manufactured by a specialized manufacturer. This is because the manufacturing of magnets and copper windings by additive technologies has not reached the technological maturity and performance of the same products made using classical technologies.

The stator component contains 12 coils wrapped with 0.25 mm diameter copper wire. The 14 neodymium magnets were glued to the rotor housing with two-component epoxy adhesive using the spacer support (Figure 4a), made via the SLS process. The magnets have been considered to follow the configuration of a brushless electric motor, so the magnets inside the rotor are attached in alternating polarity and therefore attract and repel each other. For the dynamic balancing of the rotor, it required various machining operations: turning and internal/external grinding (Figure 4b).

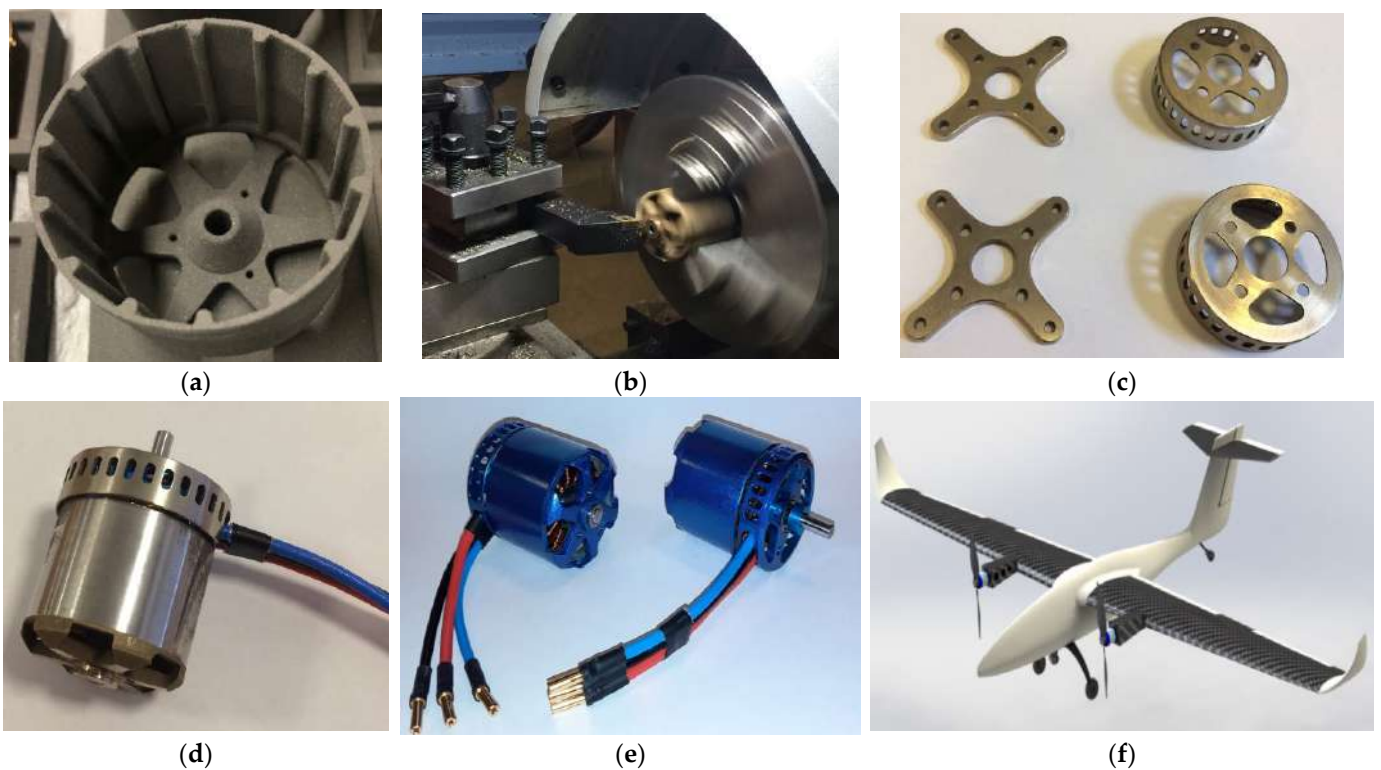


Figure 4. Assembling BLDC motor components: (a) rotor fitted with spacer; (b) rotor turning; (c) motor mount and left housing; (d) assembled motor; (e) electric motor prepared for testing; (f) the UAV aircraft on which the BLDC motors will be mounted.

Next came the assembly of the left cover equipped with a slot for removing the three wires. These wires were obtained from the pairing of four coils on the stator. The next step was to introduce the ball bearings on the stator mount, and they had to absorb all the forces from the BLDC motor (vibration, torque). After the ball bearings had been fully positioned, the shaft and rotor were reinstalled. For a more precise fixation of the ball bearings, a safety ring C was positioned on the shaft. This safety ring C and the step washer held the BLDC motor together. Because the BLDC motor operates at high speeds, for high operational safety, the motor shaft was held in place by two M4 grub screws.

On the left cover of the stator, in the four threaded holes, the motor mount (Figure 4c) is secured by screws, which allows the positioning of the electric motor on the aircraft structure. Once the electric motor was assembled (Figure 4d) the painting preparation followed. The outcome of all these steps was an electric motor with components manufactured using the SLS process (Figure 4e). The BLDC motor will be the propulsion system of a twin-motor airplane, from composite materials and composite sandwich structures [44], through the FFF process (Figure 4f). Table 4 shows the main characteristics of the assembled BLDC motor.

Table 4. BLDC motor characteristics.

Component	Unit	Value
Rotor diameter	mm	49.8
Stator diameter	mm	40.5
Number of poles stator	-	12
Number of magnets rotor	-	14
Neodymium magnet dimensions	mm	$30 \times 7.5 \times 2.5$
Length motor	mm	66
Shaft Diameter	mm	6.2
Weight	g	417

2.6. BLDC Motor Performance Testing

To test the performance of the BLDC motor, manufactured via the selective laser sintering process, the RCbenchmark Series 1585 traction stand [45] was used.

This test stand has the following characteristics: thrust: 5 kgf, torque: 2 Nm, voltage: 50 V, current: 55 A. In order to test the electric motor, we first need to calibrate the RCbenchmark Series 1585 experimental stand. Afterwards, the electric motor is fixed on the stand and first tested without the propeller. When the propeller is mounted, the motor is tested again, but first at low speeds (Figure 5a), and then the speed is increased. The following equipment was used to test the motor: RCbenchmark Series 1585 traction test stand, an ESC (Electronic Speed Controller) carrying a current of 60 A, 2 LiPo batteries with three cells connected in series (Figure 5b), a computer, a RCbenchmark GUI 1.2.0 software system and a 16×8 -inch propeller.

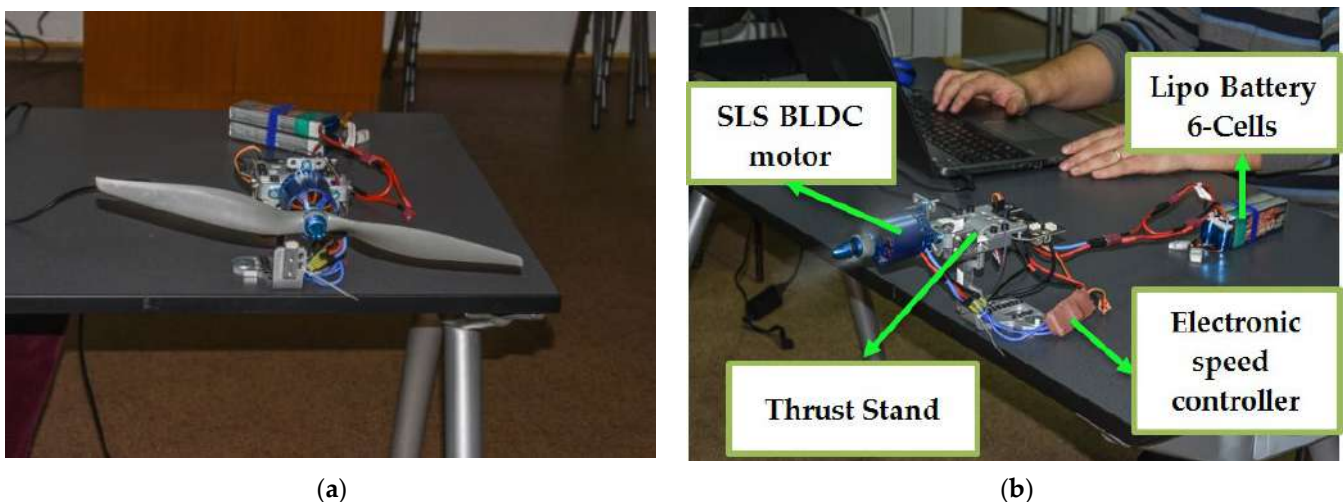


Figure 5. BLDC motor testing: (a) initial operation check of test stand; (b) BLDC motor performance testing.

3. Results and Discussion

3.1. Three-Point Bending Testing of Specimens Manufactured by the SLS Process

The tests in the static regime, for three-point bending, were carried out on five specimens manufactured by the SLS process from A6 steel, until their failure occurred. The load–displacement behavior for the 5 specimens (Figure 6a), tested in a static bending regime, shows two main stages: a linear increase obtained between the applied force and displacement, with some non-linear behavior, towards the maximum of the curve and then a sudden decrease, at maximum force, at the moment of specimen breakage. It can be seen that the maximum force, until the moment when the irreversible damage appeared in the A6 steel material, was about 0.8 kN. Additionally, the displacement of the specimens manufactured by the SLS process from the A6 steel material, at which the irreversible damage occurred, was 17.5 mm.

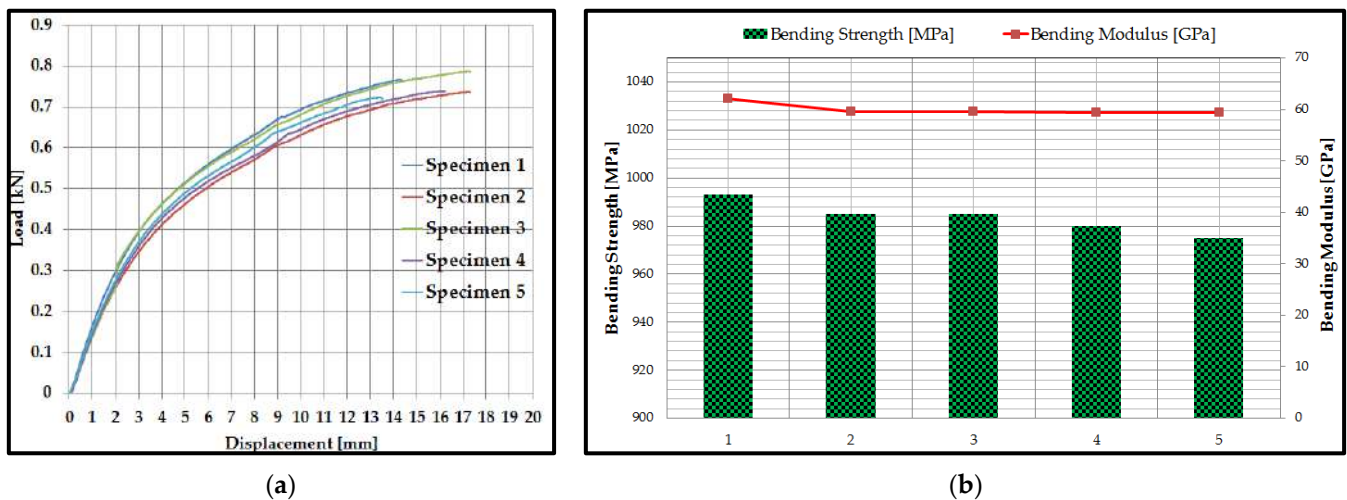


Figure 6. The results of three-point bending tests: (a) load–displacement curves of the specimens; (b) bending strength and bending modulus of specimens.

Using the software system of the WDW-150S testing machine, the main mechanical properties (bending strength and bending modulus) of the specimens manufactured by the SLS process from the A6 steel material were determined and graphically represented (Figure 6b). The bending performance of A6 steel specimens is higher or similar compared to the results obtained in other studies for different types of materials fabricated by additive manufacturing technologies [46,47] or traditional technologies [48–50]. The bending strength of tools' steel materials varies depending on the manufacturing technology and the heat treatment applied. In the case of steel alloys manufactured by additive technologies, the following values were obtained: the bending strength of steel 316 L manufactured by extrusion was 426.6 MPa [46], and for a deposition layer of 0.1 mm by the extrusion process of the 316 L material [47], it was 914.4 MPa (flatwise) and 792.2 MPa (edgewise). A6 tool steel and alloy steel manufactured by traditional technologies showed a bending strength in the range of 500 MPa and 990 MPa [41,48,49].

The main statistical indicators (mean, standard deviation, coefficient of variation) were calculated for the values of the bending strength and the bending modulus for the specimens manufactured using the SLS process from the A6 steel material (Table 5). For the data series above (the values of the bending strength and the bending modulus), the coefficient of variation was determined, in order to obtain an image of the homogeneity of the experimental data. From the results described in Table 5, it can be seen that the value of the maximum coefficient of variation is 1.8%. If the coefficient of variation (CV) is close to zero ($CV < 30\%$), then the statistically processed data (the value of the coefficient of variation CV is between 0.6–1.8%) are homogeneous and the calculated mean is representative for these sets of values.

Table 5. The statistical indicators determined after the three-point bending tests of the A6 steel specimens.

	Mean (m)	Standard Deviation (s)	Coefficient of Variation (CV)%
Bending strength [MPa]	983.6	6.6	0.6
Bending modulus [GPa]	59.9	1.1	1.8

3.2. Tensile Behavior of Specimens Manufactured by the SLS Process

Static tensile tests were carried out on five specimens manufactured via the SLS process from A6 steel, until their breakage occurred. The load–displacement curves (Figure 7a) followed the same pattern for the specimens tested in bending, manufactured by the SLS process from A6 steel. From the graphic representations of the load–displacement curves, it can be seen that the maximum force (approximately 17 kN), at a displacement of 3.3 mm. Additionally, in the case of tensile tests, the behavior, from the point of view of the load–displacement curves, of the 5 specimens (Figure 7a), presents two main stages: linear growth, between the applied force and displacement, with some nonlinear behavior, towards the maximum curves and then a sudden decrease, at maximum force, at the moment of breaking the specimens.

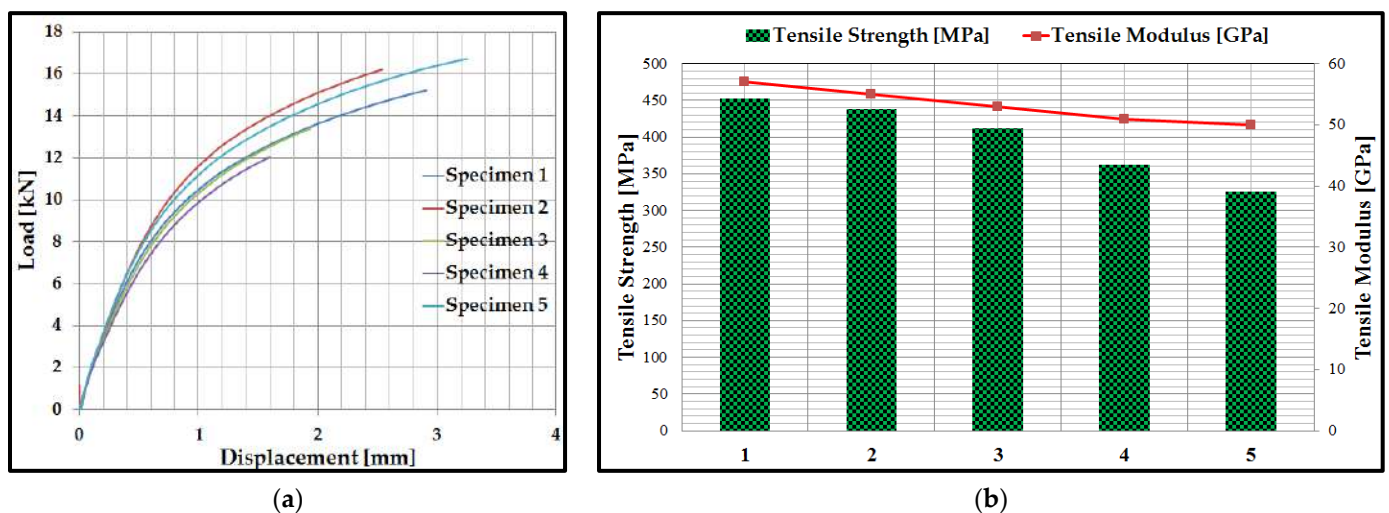


Figure 7. The results of tensile tests: (a) load–displacement curves of the specimens; (b) Tensile strength and tensile modulus of specimens.

This test method is used to investigate the mechanical performance (tensile strength, tensile modulus and behavior analysis resulting from the load–displacement curve) of specimens manufactured by the SLS process, from A6 steel. For the specimens manufactured by the SLS process from A6 steel, the software system of the machine allows the calculation of the following characteristics: tensile strength and tensile modulus of elasticity (Figure 7b). As can be seen from Figure 7b, the tensile strength varies between 326 MPa and 453 MPa, and the tensile modulus is in the range of 50 GPa and 57 GPa. This large variation can be caused by several factors, including positioning on the table or control over the infiltration process. The SLS additive manufacturing process is not 100% controllable and this is where these differences may arise. However, these differences are also found in other studies looking at the additive manufacturing process [50,51]. The tensile performance of A6 steel specimens is similar compared to the results obtained in other studies for different types of materials fabricated by additive manufacturing technologies [50,51] or traditional technologies [52,53]. The mechanical characteristics of the tool steels vary by the type of heat treatment applied and by the manufacturing process used to produce the specimens. Aluminum alloys manufactured by additive technologies presented the following perfor-

mances [50,51]: the tensile strength for 316 L manufactured by the SLM process indicated values between 510 MPa and 570 MPa, on the other hand, by the FFF process the tensile strength values were lower (between 300 MPa and 480 MPa). The tensile strength values for A6 steel tools [52] and aluminum alloys [53] are between 400 MPa and 520 MPa.

The values of the coefficient of variation (Table 6), for the obtained experimental data (tensile strength and tensile modulus), are relatively low. The maximum coefficient of variation for the tensile strength was 13.3%, and for the tensile modulus it was 5.4%. Thus, it can be appreciated that the experimental data are homogeneous and the mean is representative for the specimens manufactured via the SLS process using the A6 steel material.

Table 6. Statistical indicators determined from tensile tests of A6 steel specimens.

	Mean (m)	Standard Deviation (s)	Coefficient of Variation (CV)%
Tensile strength [MPa]	398.6	53.1	13.3
Tensile modulus [GPa]	53.2	2.8	5.4

3.3. Microscopic Analysis of Specimens

The microscopic analysis of the specimens was carried out after the three sections established in Section 2.4. From the microscopic analysis of the three sections of the specimens, it can be seen that the specific process of obtaining metal parts with the help of the SLS process proceeded in good conditions, highlighting minor defects such as voids [54–56] of small sizes. The capillary infiltration process took place according to the technical conditions of the material and equipment used and at the optimal temperature, as proven by the micrographs analyzed (Figure 8), as well as the results obtained during the three-point bending and tensile testing of the specimens manufactured via the SLS process using A6 steel.

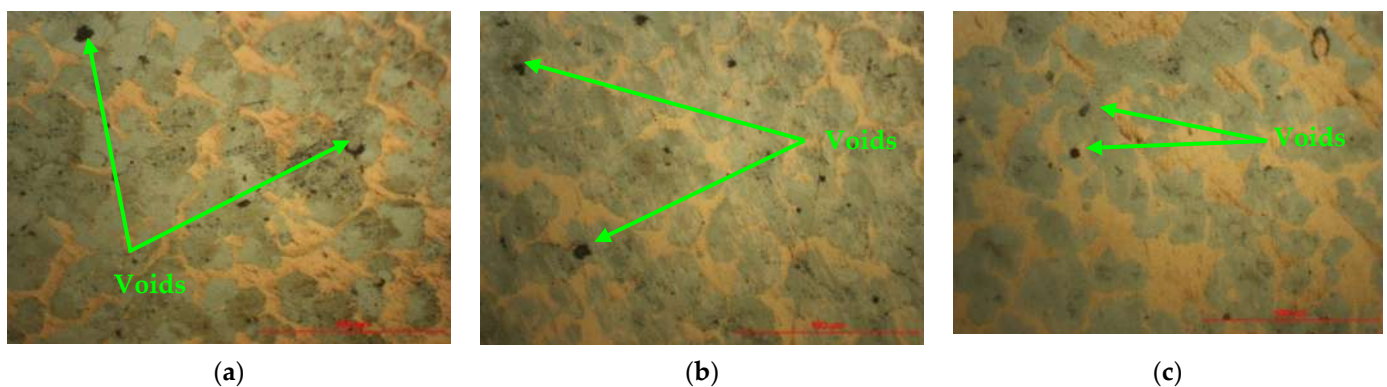


Figure 8. Microscopic analysis of specimens manufactured by the SLS process: (a) Section 1; (b) Section 2; (c) Section 3.

3.4. BLDC Motor Performance Analysis

The main motor characteristics were determined using the RCbenchmark 1585 test stand and the RCbenchmark GUI 1.2.0 software, namely: ESC signal [μ s], torque [Nm], thrust [kgf], voltage [V], current [A], electric motor speed [RPM], electrical power [W], mechanical power [W], motor efficiency [%] and propeller mechanical efficiency [kgf/W]. To test the motor, a set of instructions was created to test automation, where the following modifications were made: the minimum and maximum values that the ESC signal can take; the number of steps and their duration; the number of repetition cycles.

What can be noted after testing the BLDC motor, with components manufactured by the SLS process, is that it shows high performance determined primarily by the most important result (thrust force). The maximum thrust force obtained during the tests was

4.68 kgf. This parameter was limited by the performance of the stand; thus, the motors functioned at approximately 75% of the thrust capacity. The results of the electric motor testing were analyzed by the outlier analysis methods (Grubbs test). Following the statistical processing, it can be concluded that no outliers were identified in the results of the electric motor testing. Using the Minitab 19 software system, the mean of the main performances of the BLDC motor was plotted. The performances of the BLDC motor were represented graphically, as follows: thrust—signal ESC (Figure 9a), torque—signal ESC (Figure 9b), current—signal ESC (Figure 9c), electrical power—signal ESC (Figure 9d), electrical speed and ESC signal (Figure 9e), mechanical power and ESC signal (Figure 9f), motor efficiency and ESC signal (Figure 9g), propeller mechanical efficiency and ESC signal (Figure 9h). It can be seen that all eight parameters analyzed in Figure 9 have a linear dependence that varies according to the ESC signal [57,58]. Additionally, the efficiency of the BLDC motor, defined as the ratio between the electric power and the mechanical power, shows an increase (up to about 90%) with the increase in the ESC signal (Figure 9f).

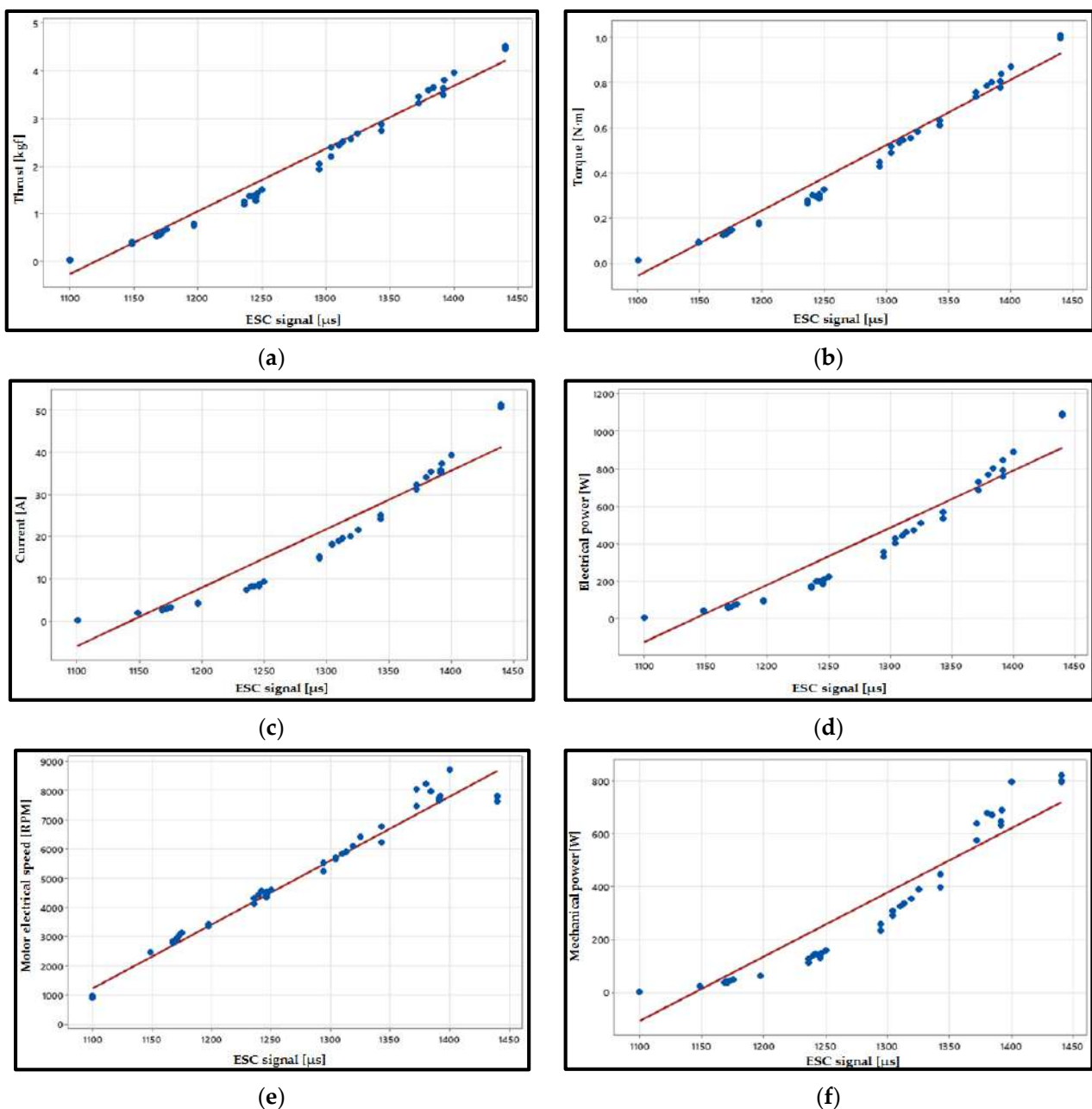


Figure 9. Cont.

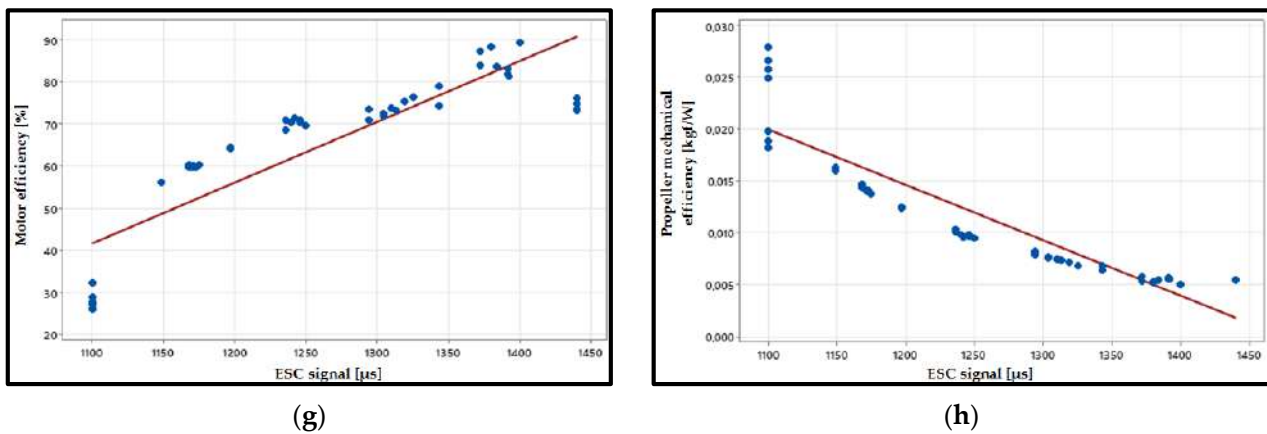


Figure 9. BLDC motor test results: (a) Dependence between thrust and ESC signal; (b) dependence between torque and ESC signal; (c) dependence between current and ESC signal; (d) dependence between electrical power and ESC signal; (e) dependence between motor electrical speed and ESC signal; (f) dependence between motor mechanical power and ESC signal; (g) dependence between motor efficiency and ESC signal; (h) dependence between propeller mechanical efficiency and ESC signal.

The force generated by the BLDC motor, manufactured using the SLS process from A6 steel, at different rotation speeds is presented in Figure 10a. The maximum thrust generated by the BLDC motor was 4.68 kgf at 7800 RPM. Thrust force and torque are directly proportional to the square of the propeller rotation speed [57,58], as can be seen in Figure 10a,b.

The maximum torque generated by the propeller equipped BLDC motor is approximately 1 Nm at 8000 RPM, as indicated in Figure 10b. The efficiency of the BLDC motor (Figure 10c) is an important factor in determining whether the SLS motor and the ESC signal work well together. In general, the efficiency of the motor shows an increase with the increase in motor electrical speed, as can be seen in Figure 10c. The efficiency of the propeller is equal to the ratio between the output quantity—in the analyzed case, the thrust force—and the input quantity, which is mechanical power. As can be seen from Figure 10d, the propeller efficiency has a clear trend and relationship with the motor electrical speed parameter. Unlike thrust force, torque and motor efficiency, the propeller efficiency showed an inversely proportional dependence in relation to the motor electrical speed parameter.

The analyzed motors that were manufactured using classic technologies [59–61] have mass and dimensions approximately equal to those of the motor manufactured using additive technologies. Additionally, their performances (thrust force and motor efficiency) are similar to those of the motor manufactured via the SLS process. For these reasons, it can be concluded that there is similar behavior between the performance of the BLDC motor manufactured by the SLS process and the performance of the motors manufactured by classical technologies [59–61], conclusions which result from the comparative analysis carried out on the results of the testing of the two types of motors.

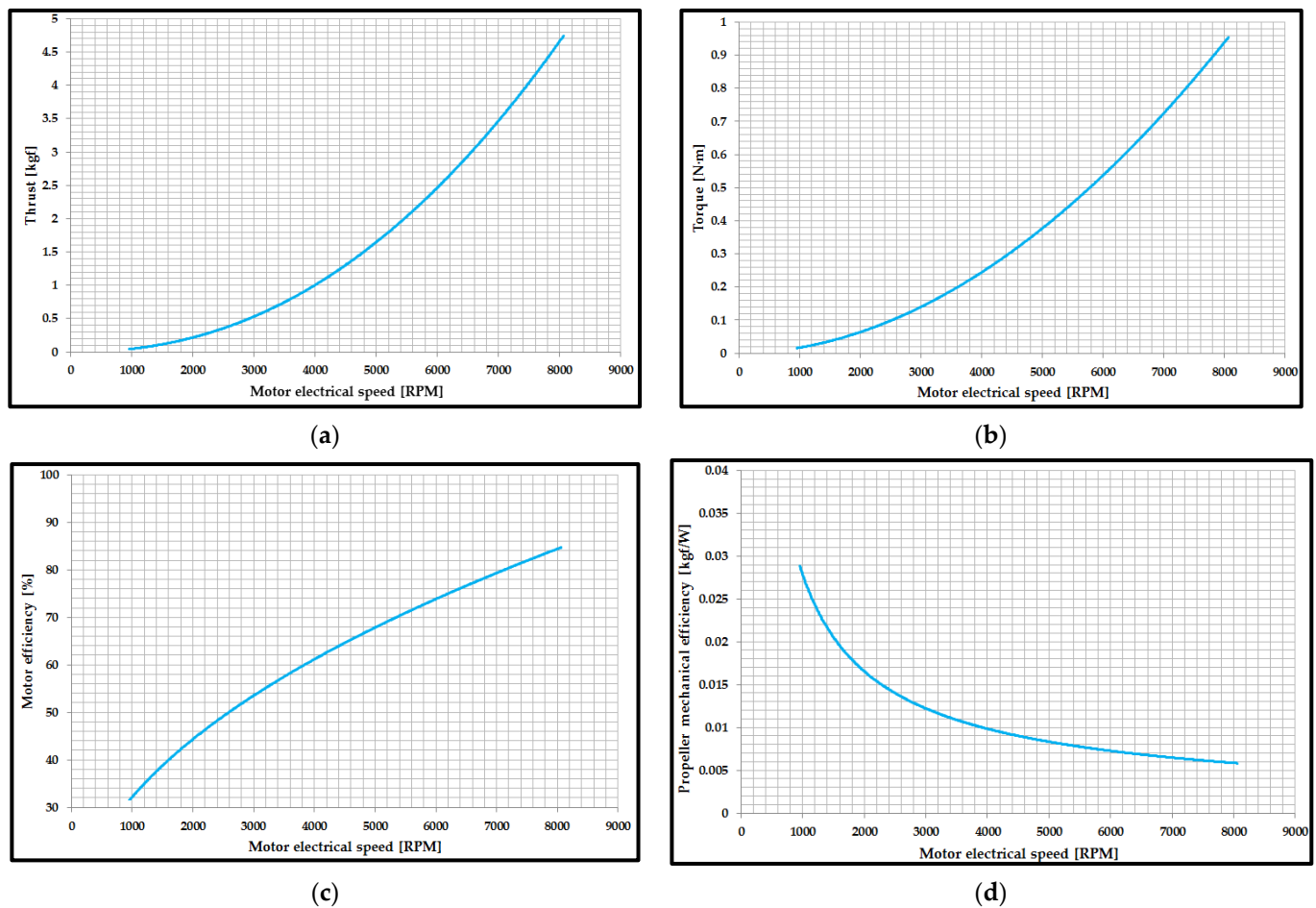


Figure 10. The performances of the BLDC motor manufactured via the SLS process: (a) thrust variation according to motor electrical speed; (b) variation of torque according to motor electrical speed; (c) motor efficiency variation according to motor electrical speed; (d) variation of propeller mechanical efficiency according to motor electrical speed.

4. Conclusions

Through metal additive manufacturing technology, more and more aerospace products can be made faster than ever before, which means that 3D metal powder prototyping is becoming a real and viable option for aircraft manufacturers. In the framework of this paper, the mechanical characteristics of the A6 steel material, manufactured via the SLS process, were studied, using three-point bending tests and tensile tests. The determination of the mechanical performances (three-point bending and tensile) of the specimens manufactured by the SLS process represented the first step in the manufacture of metal components for a BLDC motor. The mechanical characteristics of the A6 steel material, manufactured by the SLS process, had tensile strength (398.6 MPa) and bending strength (983.6 MPa) values close to those of the materials obtained by additive processes. The microscopic analysis of the material again revealed its good homogeneity after infiltration, with small defects (voids) specific to additive manufacturing processes.

After testing the BLDC motor, it can be highlighted that the main performances of the motor showed stable behavior and have a linear dependence with the increase in the ESC signal or motor electrical speed. Additionally, the most important parameter required for the use of this motor to power an UAV was determined, namely the thrust force having the value of 4.68 kgf. In conclusion, the SLS process can be successfully used to manufacture components from a BLDC motor prototype, and the advantages that this process confers are obvious: short time to build the components for the BLDC motor prototype, good

accuracy of the manufactured component (post processing of the parts required small-scale machining), and the manufactured BLDC motor components have high strength, which provides the possibility of manufacturing the BLDC motor components with complex geometries, followed by the testing and use of these motors to power an UAV in flight.

Author Contributions: Conceptualization, S.-M.Z., G.R.B. and L.-A.C.; methodology, S.-M.Z., M.A.P., L.-A.C. and V.M.S.; software, G.R.B. and C.L.; validation, S.-M.Z., G.R.B. and V.M.S.; investigation, S.-M.Z., M.A.P., G.R.B., V.M.S. and I.S.P.; writing—original draft preparation, S.-M.Z., G.R.B. and L.-A.C.; project administration, S.-M.Z. All authors have read and agreed to the published version of the manuscript.

Funding: This work was supported by a grant of the Ministry of Research, Innovation and Digitization, CNCS/CCCDI—UEFISCDI, project number PN-III-P2-2.1-PED-2019-0739, within PNCIDI III.

Data Availability Statement: Not applicable.

Acknowledgments: We also acknowledge PRO-DD Structural Funds Project (POS-CCE, O.2.2.1., ID 123, SMIS 2637, ctr. No. 11/2009) for providing the infrastructure used in this work.

Conflicts of Interest: The authors declare no conflict of interest.

References

1. Xia, C.L. *Permanent Magnet Brushless DC Motor Drives and Controls*; John Wiley & Sons: Hoboken, NJ, USA, 2012.
2. Krishnan, R. *Permanent Magnet Synchronous and Brushless DC Motor Drives*; CRC Press: Boca Raton, FL, USA, 2009.
3. Carev, V.; Roháč, J.; Šipoš, M.; Schmirler, M. A Multilayer Brushless DC Motor for Heavy Lift Drones. *Energies* **2021**, *14*, 2504. [[CrossRef](#)]
4. Hubik, V.; Sveda, M.; Singule, V. On the Development of BLDC Motor Control Run-Up Algorithms for Aerospace Application. In Proceedings of the 13th Power Electronics and Motion Control Conference (EPE-PEMC2008), Poznan, Poland, 1–3 September 2008; pp. 1620–1624.
5. Guoyuan, Q. Energy cycle of brushless DC motor chaotic system. *Appl. Math. Model.* **2017**, *51*, 686–697.
6. V. Medeiros, R.L.; G. S. Ramos, J.G.; Nascimento, T.P.; C. Lima Filho, A.; Brito, A.V. A Novel Approach for Brushless DC Motors Characterization in Drones Based on Chaos. *Drones* **2018**, *2*, 14. [[CrossRef](#)]
7. Knypiński, Ł.; Kuroczycki, S.; Márquez, F.P.G. Minimization of Torque Ripple in the Brushless DC Motor Using Constrained Cuckoo Search Algorithm. *Electronics* **2021**, *10*, 2299. [[CrossRef](#)]
8. Jin, C.-S.; Kim, C.-M.; Kim, I.-J.; Jang, I. Proposed Commutation Method for Performance Improvement of Brushless DC Motor. *Energies* **2021**, *14*, 6023. [[CrossRef](#)]
9. Azab, M. Comparative Study of BLDC Motor Drives with Different Approaches: FCS-Model Predictive Control and Hysteresis Current Control. *World Electr. Veh. J.* **2022**, *13*, 112. [[CrossRef](#)]
10. Jo, S.-T.; Shin, H.-S.; Lee, Y.-G.; Lee, J.-H.; Choi, J.-Y. Optimal Design of a BLDC Motor Considering Three-Dimensional Structures Using the Response Surface Methodology. *Energies* **2022**, *15*, 461. [[CrossRef](#)]
11. Lee, H.-Y.; Yoon, S.-Y.; Kwon, S.-O.; Shin, J.-Y.; Park, S.-H.; Lim, M.-S. A Study on a Slotless Brushless DC Motor with Toroidal Winding. *Processes* **2021**, *9*, 1881. [[CrossRef](#)]
12. Sato, M.; Nirei, M.; Yamanaka, Y.; Suzuki, T.; Bu, Y.; Mizuno, T. Increasing the efficiency of a drone motor by arranging magnetic sheets to winding. *Energy Rep.* **2020**, *6*, 439–446. [[CrossRef](#)]
13. Hu, J.; Lanzon, A. An innovative tri-rotor drone and associated distributed aerial drone swarm control. *Robot. Auton. Syst.* **2018**, *103*, 162–174. [[CrossRef](#)]
14. Biczyski, M.; Sehab, R.; Whidborne, J.F.; Krebs, G.; Luk, P. Multicopter Sizing Methodology with Flight Time Estimation. *J. Adv. Transp.* **2020**, *2020*, 9689604. [[CrossRef](#)]
15. Zhang, B.; Song, Z.; Zhao, F.; Liu, C. Overview of Propulsion Systems for Unmanned Aerial Vehicles. *Energies* **2022**, *15*, 455. [[CrossRef](#)]
16. Boukoberine, M.N.; Zhou, Z.; Benbouzid, M. A critical review on unmanned aerial vehicles power supply and energy management: Solutions, strategies, and prospects. *Appl. Energy* **2019**, *255*, 113823. [[CrossRef](#)]
17. Khan, S.; Grigorie, T.L.; Botez, R.M.; Mamou, M.; Mébarki, Y. Fuzzy Logic-Based Control for a Morphing Wing Tip Actuation System: Design, Numerical Simulation, and Wind Tunnel Experimental Testing. *Biomimetics* **2019**, *4*, 65. [[CrossRef](#)]
18. Rea, F.; Amoroso, F.; Pecora, R.; Moens, F. Exploitation of a Multifunctional Twistable Wing Trailing-Edge for Performance Improvement of a Turboprop 90-Seats Regional Aircraft. *Aerospace* **2018**, *5*, 122. [[CrossRef](#)]
19. Pascariu, I.S.; Zaharia, S.M. Design and testing of an unmanned aerial vehicle manufactured by fused deposition modeling. *J. Aerosp. Eng.* **2020**, *33*, 06020002. [[CrossRef](#)]
20. Azarov, A.; Antonov, F.; Golubev, M.; Khaziev, A.; Ushanov, S. Composite 3-D Printing for the Small Size Unmanned Aerial Vehicle Structure. *Compos. Part B Eng.* **2019**, *169*, 157–163. [[CrossRef](#)]

21. Skawiński, I.; Goetzendorf-Grabowski, T. FDM 3D printing method utility assessment in small RC aircraft design. *Aircr. Eng. Aerosp. Technol.* **2019**, *91*, 865–872. [CrossRef]
22. Childerhouse, T.; Jackson, M. Near Net Shape Manufacture of Titanium Alloy Components from Powder and Wire: A Review of State-of-the-Art Process Routes. *Metals* **2019**, *9*, 689. [CrossRef]
23. Barroqueiro, B.; Andrade-Campos, A.; Valente, R.A.F.; Neto, V. Metal Additive Manufacturing Cycle in Aerospace Industry: A Comprehensive Review. *J. Manuf. Mater. Process.* **2019**, *3*, 52. [CrossRef]
24. Vafadar, A.; Guzzomi, F.; Rassau, A.; Hayward, K. Advances in Metal Additive Manufacturing: A Review of Common Processes, Industrial Applications, and Current Challenges. *Appl. Sci.* **2021**, *11*, 1213. [CrossRef]
25. Rupal, B.S.; Anwer, N.; Secanell, M.; Qureshi, A.J. Geometric tolerance and manufacturing assemblability estimation of metal additive manufacturing (AM) processes. *Mater. Des.* **2020**, *194*, 108842. [CrossRef]
26. Auriemma, G.; Tommasino, C.; Falcone, G.; Esposito, T.; Sardo, C.; Aquino, R.P. Additive Manufacturing Strategies for Personalized Drug Delivery Systems and Medical Devices: Fused Filament Fabrication and Semi Solid Extrusion. *Molecules* **2022**, *27*, 2784. [CrossRef] [PubMed]
27. Weisman, J.A.; Jammalamadaka, U.; Tappa, K.; Mills, D.K. Doped halloysite nanotubes for use in the 3D printing of medical devices. *Bioengineering* **2017**, *4*, 96. [CrossRef] [PubMed]
28. Wang, Z.; Yang, Y. Application of 3D Printing in Implantable Medical Devices. *BioMed Res. Int.* **2021**, *2021*, 6653967. [CrossRef]
29. Naseer, M.U.; Kallaste, A.; Asad, B.; Vaimann, T.; Rassölkin, A. A Review on Additive Manufacturing Possibilities for Electrical Machines. *Energies* **2021**, *14*, 1940. [CrossRef]
30. Szabó, L.; Fodor, D. The Key Role of 3D Printing Technologies in the Further Development of Electrical Machines. *Machines* **2022**, *10*, 330. [CrossRef]
31. Zhang, Z.-Y.; Jhong, K.J.; Cheng, C.-W.; Huang, P.-W.; Tsai, M.-C.; Lee, W.-H. Metal 3D printing of synchronous reluctance motor. In Proceedings of the 2016 IEEE International Conference on Industrial Technology (ICIT), Taipei, Taiwan, 14–17 March 2016; Institute of Electrical and Electronics Engineers (IEEE): Taipei, Taiwan, 2016; pp. 1125–1128.
32. Stakhiv, H.; Solomchak, O.; Stepien, M.; Lasek, P. Analysis and experimental investigation of 3D printed electric motor with permanent magnets. In Proceedings of the XI International Conference on Electrical Power Drive Systems (ICEPDS), Saint Petersburg, Russia, 4–7 October 2020; pp. 1–5.
33. Bari, K.; Bollenbach, L. Spiderweb Cellular Structures Manufactured via Additive Layer Manufacturing for Aerospace Application. *J. Compos. Sci.* **2022**, *6*, 133. [CrossRef]
34. Garibaldi, M. Laser Additive Manufacturing of Soft Magnetic Cores for Rotating Electrical Machinery: Materials Development and Part Design. Ph.D. Thesis, University of Nottingham, Nottingham, UK, 2018.
35. Silbernagel, C. Investigation of the Design, Manufacture and Testing of Additively Manufactured Coils for Electric Motor Applications. Ph.D. Thesis, University of Nottingham, Nottingham, UK, 2019.
36. Metsä-Kortelainen, S.; Lindroos, T.; Savolainen, M.; Jokinen, A.; Revuelta, A.; Pasanen, A.; Ruusuvoori, K.; Pippuri, J. Manufacturing of topology optimized soft magnetic core through 3D printing. In Proceedings of the NAFEMS Exploring the Design Freedom of Additive Manufacturing through Simulation, Helsinki, Finland, 22–23 November 2016.
37. Lancea, C.; Stamate, V.M.; Chicoş, L.A.; Zaharia, S.M.; Pop, A.M.; Pascariu, I.S.; Buican, G.R. Design and additive manufacturing of brushless electric motor components. In Proceedings of the MATEC Web Conference, Sibiu, Romania, 2–4 June 2021.
38. *ASTM E290-14*; Standard Test Methods for Bend Testing of Material for Ductility. ASTM International: West Conshohocken, PA, USA, 2014.
39. *ASTM E8/E8M-16ae1*; Standard Test Methods for Tension Testing of Metallic Materials. ASTM International: West Conshohocken, PA, USA, 2016.
40. Kumar, S.; Kruth, J.P. Effect of bronze infiltration into laser sintered metallic parts. *Mater. Des.* **2007**, *28*, 400–407. [CrossRef]
41. Jeon, G.; Ha, D.; Park, Y.; Jeong, C. Three-Point Bending Properties of Hybrid Multi-Materials Using Adhesive Bonding Dependent on Strength Difference between Steel and Aluminum. *Materials* **2022**, *15*, 3328. [CrossRef]
42. Sánchez, M.; Cicero, S.; Arroyo, B.; Álvarez, J.A. Coupling Finite Element Analysis and the Theory of Critical Distances to Estimate Critical Loads in Al6060-T66 Tubular Beams Containing Notches. *Metals* **2020**, *10*, 1395. [CrossRef]
43. Acanfora, V.; Zarrelli, M.; Riccio, A. Experimental and numerical assessment of the impact behaviour of a composite sandwich panel with a polymeric honeycomb core. *Int. J. Impact Eng.* **2022**, *171*, 104392. [CrossRef]
44. 3D Systems LaserForm™ A6 Tool Steel Powder for Rapid Tooling and Rapid Manufacturing. Available online: <http://www.lookpolymers.com/pdf/3D-Systems-LaserForm-A6-Tool-Steel-Powder-for-Rapid-Tooling-and-Rapid-Manufacturing.pdf> (accessed on 3 August 2022).
45. RCbenchmark. Thrust Stand and Dynamometer. Available online: https://cdn.rcbenchmark.com/landing_pages/Manuals/Series%201585%20Datashet.pdf (accessed on 20 July 2022).
46. Kasha, A.; Obadimu, S.O.; Kourousis, K.I. Flexural characteristics of material extrusion steel 316L: Influence of manufacturing parameters. *Addit. Manuf. Lett.* **2022**, *3*, 100087. [CrossRef]
47. Carminati, M.; Quarto, M.; D’Urso, G.; Giardini, C.; Maccarini, G. Mechanical Characterization of AISI 316L Samples Printed Using Material Extrusion. *Appl. Sci.* **2022**, *12*, 1433. [CrossRef]

48. Alhassan, E.A.; Olasehinde, D.A.; Musonda, A.; Odeniyi, O.M. *Tensile and Flexural Behaviour of Steel Materials Used in the Construction of Crop Processing Machines*; IOP Conference Series Earth and Environmental Science; IOP Publishing: Lagos, Nigeria, 2020.
49. Charif, A.; Mourad, S.M.; Khan, M.I. Flexural Behavior of Beams Reinforced with Steel Bars Exceeding the Nominal Yield Strength. *Lat. Am. J. Solids Struct.* **2016**, *13*, 945–963. [[CrossRef](#)]
50. Kedziora, S.; Decker, T.; Museyibov, E.; Morbach, J.; Hohmann, S.; Huwer, A.; Wahl, M. Strength Properties of 316L and 17-4 PH Stainless Steel Produced with Additive Manufacturing. *Materials* **2022**, *15*, 6278. [[CrossRef](#)]
51. Li, Z.; Kuai, Z.; Bai, P.; Nie, Y.; Fu, G.; Liu, W.; Yang, S. Microstructure and Tensile Properties of AlSi10Mg Alloy Manufactured by Multi-Laser Beam Selective Laser Melting (SLM). *Metals* **2019**, *9*, 1337. [[CrossRef](#)]
52. *A 6/A 6M-07*; Standard Specification for General Requirements for Rolled Structural Steel Bars, Plates, Shapes, and Sheet Piling. ASTM International: West Conshohocken, PA, USA, 2007.
53. Paik, J.; Branner, K.; Choo, J.; Czujko, J.; Fujikubo, M.; Gordo, J.M.; Parmentier, G.; Iaccarino, R.; O’Neil, S.; Pasqualino, I.; et al. Committee III. 1 Ultimate Strength. In *17th International Ship and Offshore Structures Congress (ISSC2009)*; Jang, C., Hong, S., Eds.; University of Seoul: Seoul, Korea, 2009; pp. 375–475.
54. Brennan, M.; Keist, J.; Palmer, T. Defects in Metal Additive Manufacturing Processes. *Addit. Manuf. Processes* **2020**, *24*, 277–286.
55. Castellano, A.; Mazzarisi, M.; Campanelli, S.L.; Angelastro, A.; Fraddosio, A.; Piccioni, M.D. Ultrasonic Characterization of Components Manufactured by Direct Laser Metal Deposition. *Materials* **2020**, *13*, 2658. [[CrossRef](#)]
56. Hu, Y.N.; Wu, S.C.; Withers, P.J.; Zhang, J.; Bao, H.Y.X.; Fu, Y.N.; Kang, G.Z. The effect of manufacturing defects on the fatigue life of selective laser melted Ti-6Al-4V structures. *Mater. Des.* **2020**, *192*, 108708. [[CrossRef](#)]
57. Pérez Gordillo, A.M.; Villegas Santos, J.S.; Lopez Mejia, O.D.; Suárez Collazos, L.J.; Escobar, J.A. Numerical and Experimental Estimation of the Efficiency of a Quadcopter Rotor Operating at Hover. *Energies* **2019**, *12*, 261.
58. Callender, M.N. UAS propeller/rotor sound pressure level reduction through leading edge modification. *J. Appl. Mech. Eng.* **2017**, *6*, 254.
59. Brushless Outrunner Motor PROPDRIVE 5060. Available online: https://hobbyking.com/en_us/propdrive-v2-5060-270kv-brushless-outrunner-motor.html?__store=en_us (accessed on 22 December 2022).
60. Brushless Motor Mitoot SS Series A4130. Available online: <https://www.amazon.co.uk/brushless-Brushless-Aircraft-Multi-copter-Outrunner/dp/B09Z82X26P?th=1> (accessed on 22 December 2022).
61. Brushless Outrunner Motor Turnigy Aerodrive SK3. Available online: https://hobbyking.com/en_us/turnigy-aerodrive-sk3-5055-320kv-brushless-outrunner-motor.html (accessed on 22 December 2022).

Disclaimer/Publisher’s Note: The statements, opinions and data contained in all publications are solely those of the individual author(s) and contributor(s) and not of MDPI and/or the editor(s). MDPI and/or the editor(s) disclaim responsibility for any injury to people or property resulting from any ideas, methods, instructions or products referred to in the content.

Article

The Influence of Solar Sintering on Copper Heat Exchanger Parts with Controlled 3D-Printed Morphology

Mihai Alin Pop ¹, Cătălin Croitoru ^{2,*}, Tibor Bedo ¹, Virgil Geamăn ¹, Irinel Radomir ³, Aurel Crișan ¹, Emmanuel Guillot ⁴, Ioan Miloșan ¹, Sebastian Marian Zaharia ⁵ and Lucia Antoaneta Chicos ⁵

- ¹ Materials Science Department, Transilvania University of Brasov, 29 Eroilor Ave., 500484 Brasov, Romania; mihai.pop@unitbv.ro (M.A.P.); bedo.tibor@unitbv.ro (T.B.); geaman.v@unitbv.ro (V.G.); crisan.a@unitbv.ro (A.C.); milosan@unitbv.ro (I.M.)
- ² Materials Engineering and Welding Department, Transilvania University of Brasov, 29 Eroilor Ave., 500484 Brasov, Romania
- ³ Mathematics and Informatics Department, Transilvania University of Brasov, 29 Eroilor Ave., 500484 Brasov, Romania; i.radomir@unitbv.ro
- ⁴ PROMES-CNRS Laboratory, Processes, Materials and Solar Energy, 7 Rue du Four Solaire, F-66120 Font Romeu Odeillo, France; emmanuel.guillot@promes.cnrs.fr
- ⁵ Manufacturing Engineering Department, Faculty of Technological Engineering and Industrial Management, Transilvania University of Brasov, 29 Eroilor Ave., 500484 Brasov, Romania; zaharia_sebastian@unitbv.ro (S.M.Z.); l.chicos@unitbv.ro (L.A.C.)
- * Correspondence: c.croitoru@unitbv.ro; Tel.: +40-748126598

Abstract: From a scientific point of view, heat transfer is different in solar furnaces compared with classical ones and the influence of direct concentrated solar radiation on sintered parts needs to be studied in detail to determine the feasibility of solar furnaces in manufacturing small workpieces. This study was performed on cylindrical samples with controlled morphology obtained by a powder metallurgy 3D printing technique. All samples were heated with a heating rate of 120 ± 10 °C/minute, with 0, 1, 2, 3, 4 and 5 min holding times at 900 °C and 930 °C. The morphology of the samples was analyzed microscopically, the microhardness was determined before and after sintering, and the results were correlated with the sintering parameters (temperature, heating rate and holding time). The best results were obtained at 930 °C with 5 min holding time from the microhardness value and microstructure point of view.

Keywords: powder metallurgy; 3D printing; concentrated solar energy



Citation: Pop, M.A.; Croitoru, C.; Bedo, T.; Geamăn, V.; Radomir, I.; Crișan, A.; Guillot, E.; Miloșan, I.; Zaharia, S.M.; Chicos, L.A. The Influence of Solar Sintering on Copper Heat Exchanger Parts with Controlled 3D-Printed Morphology. *Materials* **2022**, *15*, 3324. <https://doi.org/10.3390/ma15093324>

Academic Editors: Evgeny Levashov and Dina Dudina

Received: 27 February 2022

Accepted: 3 May 2022

Published: 5 May 2022

Publisher's Note: MDPI stays neutral with regard to jurisdictional claims in published maps and institutional affiliations.



Copyright: © 2022 by the authors. Licensee MDPI, Basel, Switzerland. This article is an open access article distributed under the terms and conditions of the Creative Commons Attribution (CC BY) license (<https://creativecommons.org/licenses/by/4.0/>).

1. Introduction

Three-dimensional printing is a unique technology that offers a high degree of freedom for customizing practical products in a short time at an acceptable price. In recent years, the improved and reliable 3D printers and 3D scanners custom-made for additive manufacturing technology are becoming an increasingly viable and cost-effective option for high-mix–low-volume manufacturing of customized parts and prototypes [1–3].

These new technologies have been collectively classified as additive manufacturing (AM), which seems to be the most commonly used name, and as rapid prototyping (RP) technologies and solid freeform fabrication (SFF) techniques. These techniques with reproducible and mathematically predictable physical properties have become a fast-developing research area [4,5].

Computer-aided designs are applied to obtain precise geometries, with the possibility to obtain different shapes.

The design is imported into a software, which mathematically slices the conceptual model into horizontal layers. Toolpaths are generated before the data are downloaded to the Filament Fused Fabrication (FFF) hardware. The FFF extrusion head operates in the

X and Y axes while the platform is lowered in the Z-axis in order to form each new layer. Practically, the process draws the designed model one layer at a time [1–5].

The focus of the present paper is to investigate how solar energy can be used to sinter copper parts with internal controlled geometry via powder metallurgy. These parts are obtained by using a negative 3D model, which is printed using polyvinyl alcohol (PVA)-based resin filament and filled with different metallic powders. Before sintering, the support material must be removed (PVA) by immersing it in water until it is totally eliminated, and then, the part is dried and sintered in the furnace. By sintering, the resulting part will have a special internal architecture given by the 3D-printed model.

A cellular architecture with deterministic 3D morphology was developed by our research group in recent years for different prototypes to create precise models with well-defined architectures [6,7].

On the other hand, powder metallurgy is also an evolving technology, using a wide variety of metallic and alloy materials [8–10].

By producing parts using the PM process, we can obtain a homogeneous structure, with controlled porosity and special properties such as hardness and wear resistance, for a wide range of applications, especially for the automotive industry [11–14].

The action of concentrating the solar energy on small surfaces offers the possibility of local heating necessary for obtaining these types of metallic parts. Besides obtaining the proposed features for these types of materials, the exploitation of advantages given by using solar energy compared with the classical ones is taken into consideration [15,16]. Environmental protection by reducing the pollution level while exploiting the technical availabilities of using solar energy is also desirable.

The compaction of powders (semi-finished products) subjected to sintering for the models obtained by 3D printing have the advantage that by 3D printing, parts (shapes, molds and models) with any configuration (with complex surfaces) without the need for further machining or raw models can be obtained directly from a computer drawing and in a very short time. This considerably reduces the execution time of the profiled molds used for compacting the powders and, finally, the time for obtaining the sintered parts. Sintering in solar ovens in turn reduces the time; energy consumption; labor; and therefore, the costs of the final parts.

Starting from these premises, we researched how to obtain parts made from Cu (99.6% powder purity), “full” parts (without internal gaps) and parts with thin walls (with internal gaps) by solar sintering.

The concrete objectives of the research were to obtain and establish the working parameters for the sintering in solar ovens with concentrated energy for copper parts with or without internal gaps and the analysis of the factors that influence their structure and properties.

Numerous researches have been found in the literature regarding the classical sintering of Cu or Cu matrix composite materials where the optimal temperature was determined to be 900 °C, coupled with a holding time of 120 min [17]. Additionally, it has been found that the relative density and hardness of sintered parts increase with the sintering temperature [10].

The values of the micro hardness for conventionally furnace-sintered pure Cu are 43 ± 2.6 HV₁₀₀, and by microwave sintering at 900 °C, it is 46 ± 2.8 HV₁₀₀ with a holding time of 60 min [12,18–22].

The main objectives of this paper are to establish technological parameters for sintering Cu metallic powders for the manufacture of prototypes with internal morphology using 3D printing technology under concentrated solar energy (CSE) action in relation to the pre-established properties.

2. Experimental

2.1. Materials and Equipment

The research was carried out on cylindrical specimens (samples) with dimensions $D \times H = 16 \text{ mm} \times 30 \text{ mm}$ (Figure 1). The metal powder is Cu > 99% (purchased from Alfa Aesar, Thermo Fisher Scientific, Shore Road, Port of Heysham Industrial Park Lancashire, LA3 2XY, Heysham, Lancashire, UK) with size of $<63 \mu\text{m}$ [23].

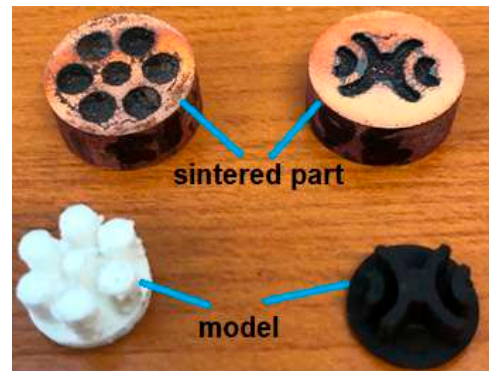


Figure 1. Different internal sample architectures.

A CreatBot (Henan Creatbot Technology Limited 6#, Chaoya Industry Park, Hanghai Road, No.13 Ave., Eco-Tech Development Zone, Zhengzhou City, Henan Province, China) DX—a 3D double-nozzle printer—was used to obtain models with a 0.2 mm layer thickness and PVA material (Filament AquaSolve™—PVA Natural) from Form Futura Company (Tarweweg 3, 6534 AM Nijmegen, The Netherlands) [24]. The printing temperature for the filament (measured at the extrusion head) was 200 °C and a bed temperature of 50 °C with a printing speed of 40 mm/s, as recommended by the manufacturer.

For pressing, a universal testing machine, a type WDW-150S (Jinan Testing Equipment IE Corporation, Jinan, China) was used, and for drying, a Nabertherm furnace (Nabertherm GmbH, Bahnhofstr. 20, 28865, Lilienthal, Germany) was used.

A Delta Wasp 2040 Clay 3D printer (Via Castelletto, 104, 48024 Massa Lombarda RA, Italy) with a 0.5 mm layer thickness was used to manufacture a ceramic crucible starting from a ceramic slurry, followed by sintering at 1350 °C in the Nabertherm furnace.

Solar sintering was performed at Odeillo-Font Romeu (PROMES-CNRS, 7, rue du Four Solaire, 66120 Font Romeu Odeillo, France) using MSSFs furnace with a diameter of 16 mm of the concentrated solar energy focused beam.

A FM-700 AHOTEC tester (Future-Tech Corp, Talkpier Kawasaki, Kanagawa, Japan) was used to determine the microhardness with 100 gf for 10 s.

2.2. Technological Stages of Obtaining the Copper Parts

The copper-sintered parts were obtained following the six-step protocol mentioned below:

1. The CAD model (SolidWorks 2016 software) was designed, and a mold (negative part) was printed by 3D printing using FFF technology (PVA material).

2. The cavity die of this mold (the negative part) was filled gravimetrically with metallic powder.

3. The powder was pressed unidirectional in the die at a force of $F = 90 \text{ kN}$. The pressing aimed to obtain a sufficient mechanical strength for the next three steps.

4. The support material (PVA) was removed by immersion in water until complete dissolution for different time periods, depending on the amount, size of the sample and water temperature (roughly 48 h).

5. The drying process was performed in the Nabertherm furnace at 120 °C with a holding time of 2 h.

6. The dried parts were sintered in the CSE furnace and purged with N₂. The N₂ flow was 5 L/min to prevent oxidation of the samples.

The sintering process was performed in a 3D-printed ceramic crucible (Materials Science Department from Transilvania University of Brasov), provided with a hole for gas purging and holes for fixing of thermocouple for measuring the temperature during sintering (Figure 2).

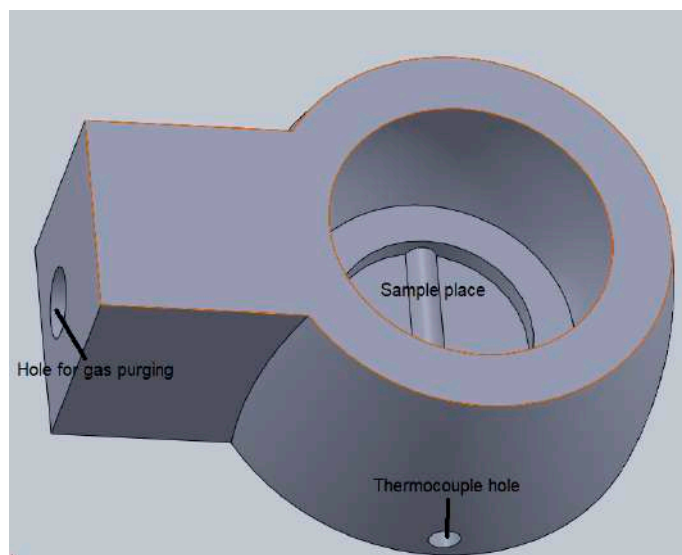


Figure 2. Ceramic crucible for sintering.

2.3. Materials Properties and Manufacturing Conditions

The theoretical heating rate was $V_{\text{het}} = 120 \pm 10$ °C/min, but the real heating rate for each sample (depending on solar flux incident on the sample) is presented in Table 1. The practical sintering diagrams are presented in Figures 3 and 4 for each sintering temperature.

Table 1. The sintering parameters.

No. Crt.	Temperature (°C)	Holding Time (min)	Theoretical Heating Rate (°C/min)	Practical Heating Rate (°C/min)
1	900	0	120 ± 10	112.24
2		1		125.6
3		2		126.3
4		3		116.7
5		4		122.6
6		5		110.8
7	930	0	120 ± 10	111.7
8		1		115.4
9		2		119.9
10		3		113.87
11		4		118.2
12		5		117.1

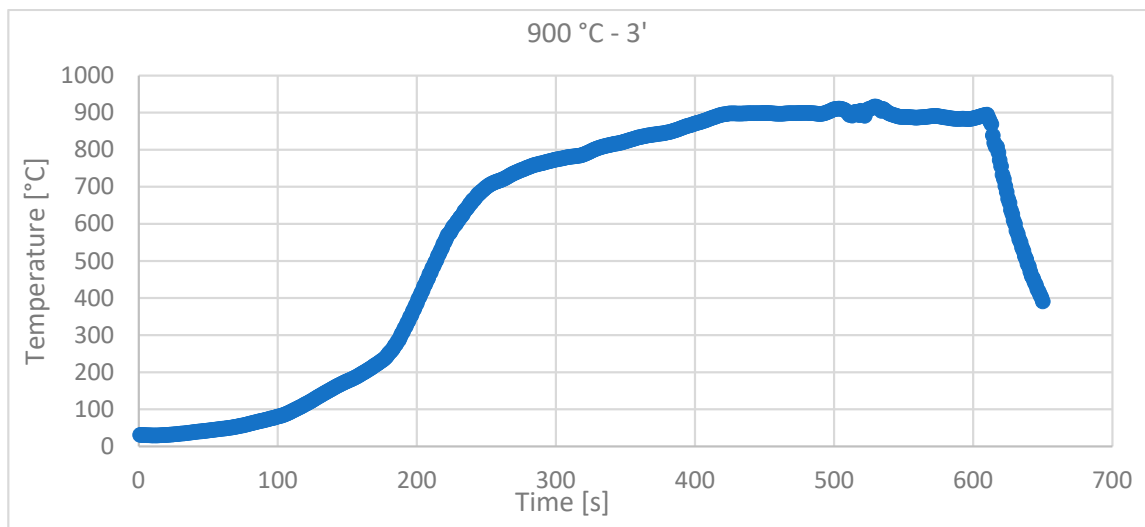


Figure 3. Solar sintering diagram at 900 °C, with 3 min holding time and with a 116.7 °C/min heating rate.

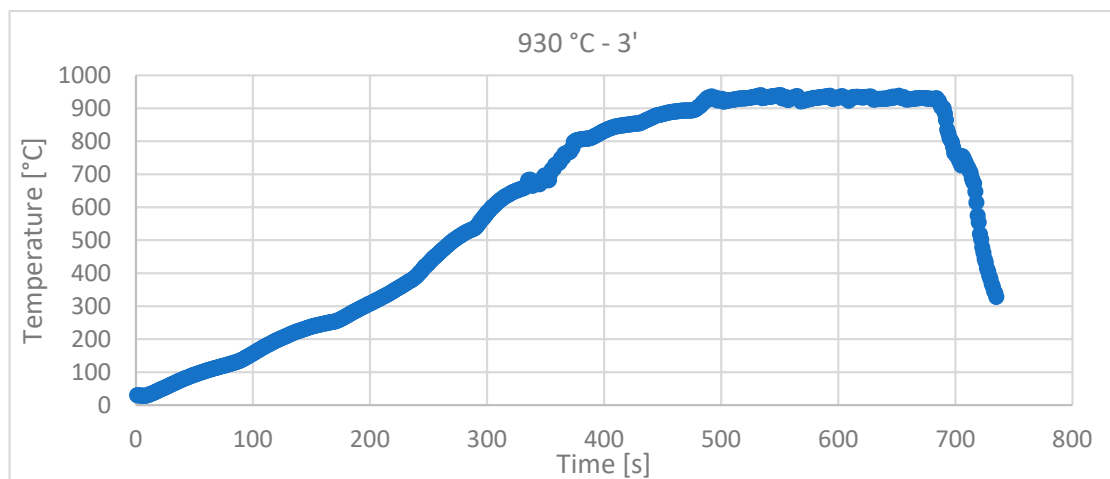


Figure 4. Solar sintering diagram at 930 °C, with 3 min holding time and with a 113.87 °C/min heating rate.

Cylindrical specimens with dimensions $D \times H = 16 \text{ mm} \times 30 \text{ mm}$ were used and uniaxially pressed with a force of $F = 90 \text{ kN}$ in a metallic die.

Figures 3 and 4 show the recordings made during the sintering with CSE of the samples, using Data Logger recorder—Pyro Tracer (model C.A. 650) and Type K thermocouples (maximum temperature—1300 °C).

Even though there were sometimes variations in the light intensity/wind that moved the reflecting mirrors, the temperature control with a variation of $\pm 10 \text{ °C}$ was achieved for all of the samples.

3. Results and Discussion

3.1. Microhardness

The microhardness was measured in nine points; the minimum and maximum values were eliminated; and from the remaining seven measurements, the arithmetic mean was calculated.

The study was conducted in the “filled” area—the area with thick walls—and in the “hollow” areas—that is, in the areas with thin copper walls resulting from the dissolution of the PVA model.

Figures 5 and 6 show the values of HV microhardness measured in the upper part of the sample (where the solar radiation was direct) and in the lower part (where the heat was transmitted through conductivity) in comparison with the solid and thin-walled samples.

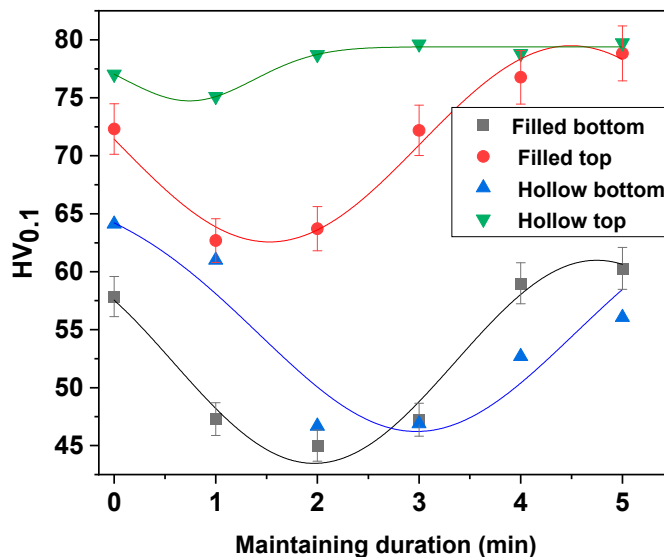


Figure 5. The microhardness obtained in the case of the sintering heat treatment at 900 °C.

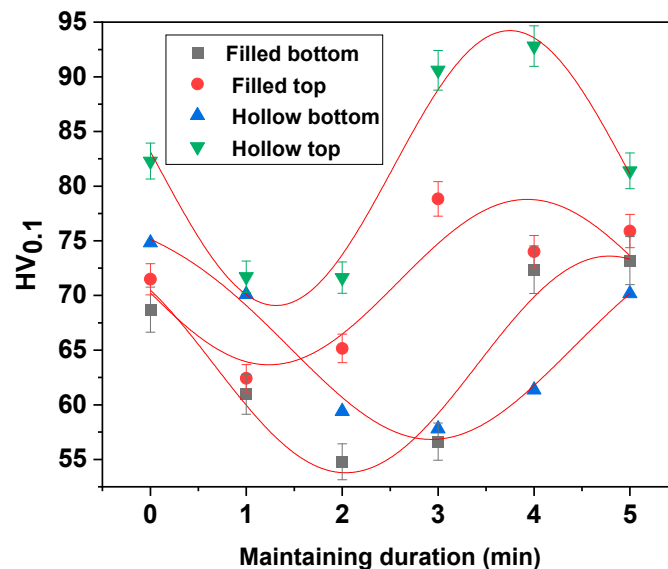


Figure 6. The microhardness obtained in the case of the sintering heat treatment at 930 °C.

Under normal conditions, copper as a metal presents a hardness of 50–110 HV [21–23]. When obtaining samples by pressing, a cold plastic deformation of the powder granules occurs, having the characteristic appearance of twins. Twinning is usually associated with internal tensions, and for this reason, the pressed samples have a higher hardness, with an average of 119.9 HV.

When samples are sintered, there is an ongoing relief in the internal stresses due to annealing [23].

Following the sintering process, the hardness of the samples presents different values as a function of different processes that occur in their obtaining:

- A uniform structure in the samples is realized through the disappearance of the boundaries between the metal granules.
- The remaining gaps from the stage when the samples are obtained by pressing participate in this process.
- In the case of all samples, a mechanical binding of the metal granules is noticed due to the pressing, which leads to an increase in the hardness, while in the heat-treated samples at 930 °C a bonding is produced due to the temperature.
- Even if the hardness variations are higher in the case of sintered samples at 930 °C, they are the highest.

3.2. Microscopic Analysis

The microscopic analysis was performed with a Nikon Eclipse MA 100 metallographic microscope (Nikon Corp., Tokyo, Japan). For the structure and morphology analysis, the next samples have been embedded into acrylic resin and leveled using an automatic metallographic Phoenix Beta polishing device from Buehler (with Al₂O₃ suspension and 0.05 μm grit).

3.2.1. NS—Non-Sintered Sample

From the analysis of the microstructure in Figure 7, a plastic deformation can be observed, which appeared at the moment during pressing in the mold. Due to the different internal energies resulting from the plastic deformations as well as the different reaction to the reagent, there are minor differences in the microstructure.

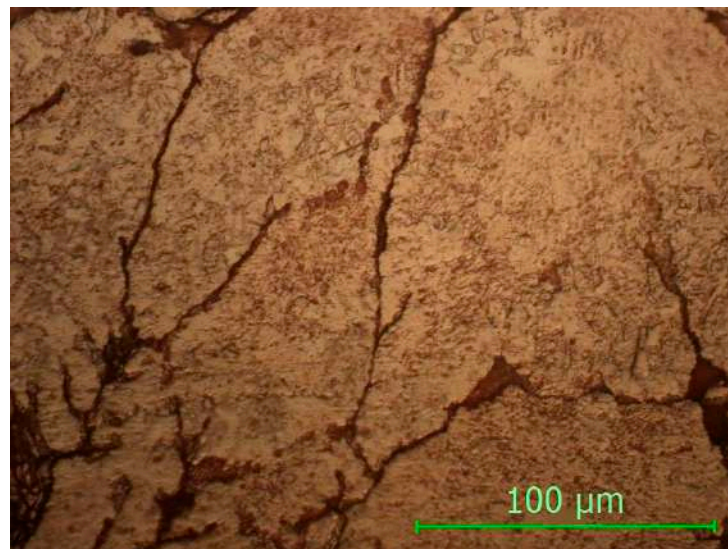
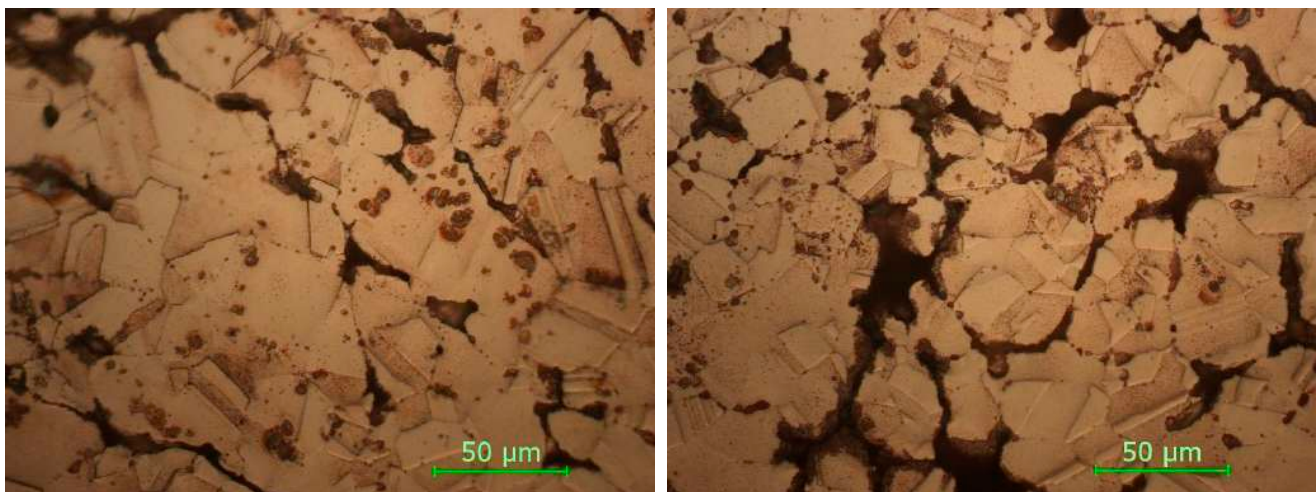


Figure 7. Non-sintered sample, magnification 500×.

The spaces and the limits between the copper particles are small due to the pressing, with the mechanical binding appearing, which gives it a good mechanical resistance to the sample as well as a high microhardness.

3.2.2. STW₉₀₀

In Figure 8 are presented the microstructures in the case of the sample with thin walls sintered at 900 °C.



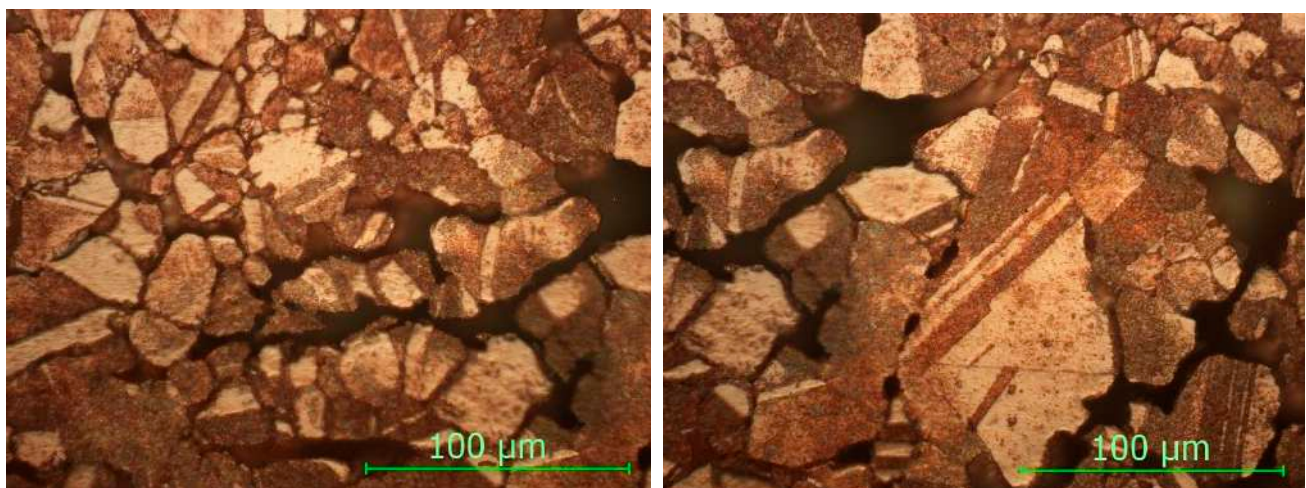
(a)

(b)

Figure 8. Sample STW900: (a) upper side; (b) bottom side (magnification 500×).

3.2.3. SFW900

In Figure 9 are presented the micrographs for the sample with fully walls sintered at 900 °C, with a holding time of 5 min.



(a)

(b)

Figure 9. Sample SFW900: (a) upper side; (b) bottom side (magnification 500×).

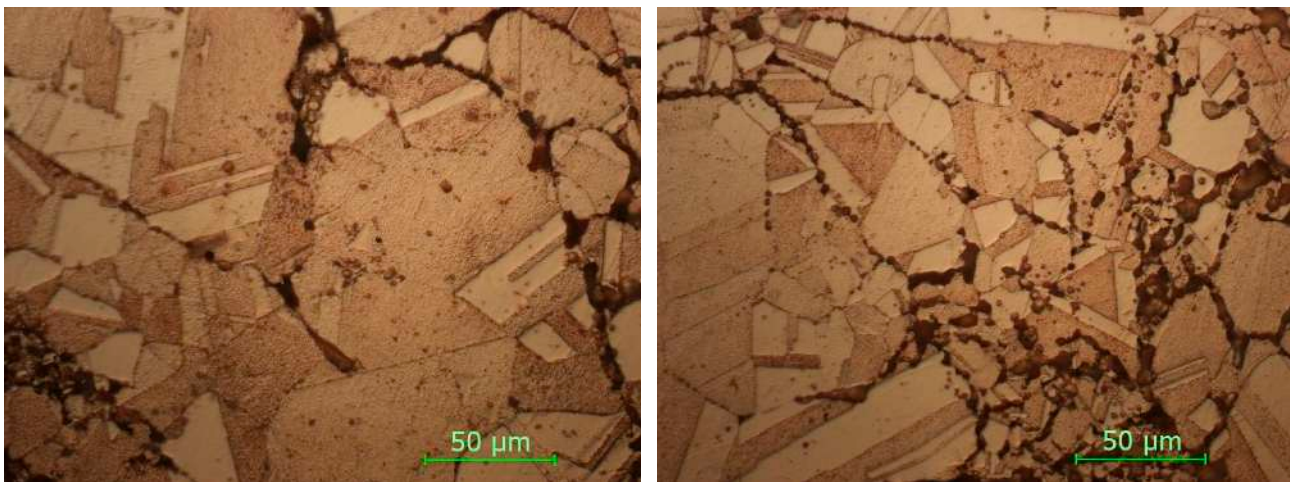
As it can be seen from the micrographs presented in Figures 8 and 9 and corroborating the values of HV microhardness presented in Figure 5, the following influencing factors could be found:

- The direct radiation facilitates the binding at certain temperatures and thus the sintering of the material takes place, resulting in a hardness close to the maximum hardness of Cu.
- In the case of samples with thin walls, the same amount of heat is transmitted in the mass of the part much more easily than in solid parts, with the results being decreases in the size, and number of defects and gaps and an increase in microhardness.
- Even if Cu is a good thermal conductor when full parts are concerned, the sintering process is affected, resulting in parts with a lower hardness.
- The variation in the microhardness is uniform and similar in the case of solid samples in the upper part and in the lower part.

- By applying the heating process, slightly larger gaps can be observed in the samples due to uneven expansion so that, locally, the effect of mechanical bonding is canceled and, for thermal bonding, the temperature/time of treatment is insufficient.

3.2.4. STW930

In Figure 10 are presented the micrographs for the sample with thin walls sintered at 930 °C, with a holding time of 5 min.



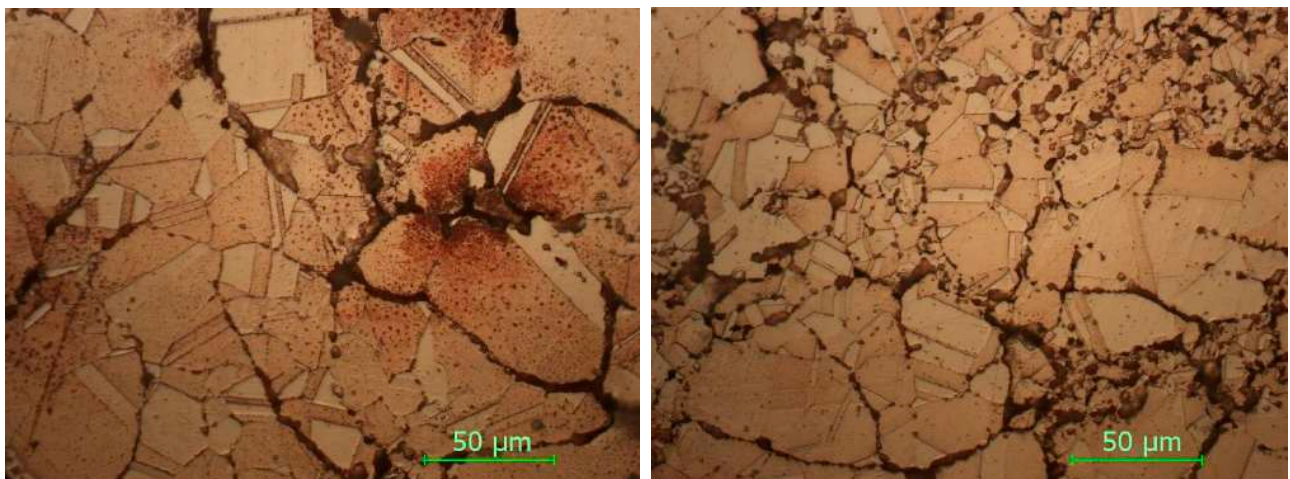
(a)

(b)

Figure 10. Sample SFW930: (a) upper side; (b) bottom side (magnification 500×).

3.2.5. SFW930

In Figure 11 are presented the micrographs for the sample with fully walls sintered at 930 °C, with a holding time of 5 min.



(a)

(b)

Figure 11. Sample SFW930: (a) upper side; (b) bottom side (magnification 500×).

As it can be seen from the micrographs presented in Figures 10 and 11 and corroborating the values of microhardness presented in Figure 6, the following influencing factors were found to take place:

- Direct radiation facilitates the binding at temperature (as in the case of sintering at 900 °C), and thus, the material is sintered, resulting in a high hardness.
- It is possible to observe the disappearance of the boundaries between the grains, a phenomenon characteristic of the thermal treatments with maintenance at high temperatures.
- The results of the microhardness in the case of the heat treatment at 930 °C do not vary much, being close both to the solid/thin-walled samples and to the surface where direct radiation was employed and to the lower part where the heat propagated through thermal conductivity.
- Maintaining a higher temperature can cause an increase in the size of the crystals, resulting in polyhedral crystals with twin boundaries and orientation in bands.
- In the case of heat treatments performed at 930 °C, the clear influence of the increase in the temperature and in the holding time can be observed by decreasing the defects in the microstructures as well as by increasing the microhardness.
- By comparing the micrographs obtained at the sintered samples at 900 °C and 930 °C, a clear improvement in the microstructures can be seen by decreasing the number of defects and increasing the number of polyhedral crystals, which leads to an increase in the microhardness.

4. Conclusions

Solar sintered parts with controlled internal geometry were obtained in this study via the negative part method, achieved through 3D printing and powder metallurgy. This approach has not been used until now, and it can be considered an innovation in the field. The proposed configuration of the copper parts is difficult to achieve using other technologies.

- Generally, due to higher production costs, professional 3D printing technologies are not suitable for mass production. Instead, due to the short time frame from designing to obtaining the physical product, they are more suitable for prototypes and it is the best solution for checking/validating the changes made to parts before their mass production. In this way, small series or prototypes can be obtained.
- With an increase in the temperature from 900 °C to 930 °C, the particles practically bind better and the gaps (pores) disappear.
- The contours of the grains are noticeable at 900 °C, even if the adhesion of the particles is more obvious at 930 °C, a fact confirmed by the microhardness values.
- In the case of heat treatment at 930 °C, a stronger finishing of the structure was obtained.
- By comparison, the solid sample/the sample with gaps at the same temperature and holding time shows a reduction in the gaps (porosities), a good compaction and embedding of the particles clearly superior to the samples with thin walls.
- Internal microporosity is random due to the technological process specific to powder metallurgy and is dictated by the distribution of granules upon pressing.
- Using 3D printing technology with the powder processing technology and solar sintering shows combined benefits.
- The 5 min holding time for these samples at 930 °C proved to be the best after we analyzed and compared all of the microstructures made and the values of the microhardness. Additionally, 5 min was proven to be the average holding time based on the experiments.
- Using solar energy in the sintering process is feasible because of its advantages: clean energy, inexhaustible energy, environmentally friendly, and shorter heat treatment durations.
- The results presented in this paper have determined that concentrated solar energy sintering can be successfully applied to sinter copper heat exchanger parts with a controlled 3D-printed morphology.

Author Contributions: Conceptualization, M.A.P., C.C. and V.G.; methodology, M.A.P., C.C., E.G., T.B., V.G. and A.C.; software, I.R., I.M., S.M.Z. and L.A.C.; validation, E.G., S.M.Z. and L.A.C.; formal analysis, M.A.P., T.B., C.C., V.G. and I.R.; investigation, M.A.P., C.C., T.B., A.C. and I.M.; resources, M.A.P., E.G., S.M.Z. and L.A.C.; data curation, C.C., I.R., I.M. and S.M.Z.; writing—original draft preparation, M.A.P., C.C., S.M.Z. and E.G.; writing—review and editing, M.A.P., V.G., T.B., C.C. and E.G.; visualization, C.C.; supervision, M.A.P., V.G. and E.G.; project administration, M.A.P. and V.G.; funding acquisition, M.A.P. and E.G. All authors have read and agreed to the published version of the manuscript.

Funding: This research was funded by SFERA-III project—grant agreement No 823802.

Institutional Review Board Statement: Not applicable.

Informed Consent Statement: Not applicable.

Data Availability Statement: Not applicable.

Acknowledgments: We hereby acknowledge the structural funds project PRO-DD (POS-CCE, O.2.2.1., ID 123, SMIS 2637, ctr. No 11/2009) for partly providing the infrastructure used in this work, and we thank the CNRS-PROMES for providing access to its installations, the support of its scientific and technical staff and the financial support of the SFERA-III project (grant agreement No 823802).

Conflicts of Interest: The authors declare no conflict of interest.

References

1. Dizon, J.R.C.; Espera, A.H., Jr.; Chen, Q.; Advincola, R.C. Mechanical characterization of 3D-printed polymers. *Addit. Manuf.* **2018**, *20*, 44–67. [[CrossRef](#)]
2. Wang, X.; Jiang, M.; Zhou, Z.W.; Gou, J.H.; Hui, D. 3D printing of polymer matrix composites: A review and prospective. *Compos. Part B Eng.* **2017**, *110*, 442–458. [[CrossRef](#)]
3. Lim, L.-T.; Auras, R.; Rubino, M. Processing technologies for poly(lactic acid). *Prog. Polym. Sci.* **2008**, *33*, 820–852. [[CrossRef](#)]
4. Angjellari, M.; Tamburri, E.; Montaina, L.; Natali, M.; Passeri, D.; Rossi, M.; Terranova, M.L. Beyond the concepts of nanocomposite and 3D printing: PVA and nanodiamonds for layer-by-layer additive manufacturing. *Mater. Des.* **2017**, *119*, 12–21. [[CrossRef](#)]
5. Duran, C.; Subbian, V.; Giovanetti, M.T.; Simkins, J.R.; Beyette, F.R., Jr. Experimental desktop 3D printing using dual extrusion and water-soluble polyvinyl alcohol. *Rapid Prototyp. J.* **2015**, *21*, 528–534. [[CrossRef](#)]
6. Pop, M.A.; Croitoru, C.; Bedó, T.; Geaman, V.; Radomir, I.; Cosnită, M.; Zaharia, S.M.; Chicos, L.A.; Milosan, I. Structural changes during 3D printing of bioderived and synthetic thermoplastic materials. *J. Appl. Polym. Sci.* **2019**, *136*, 47382. [[CrossRef](#)]
7. Zaharia, S.M.; Enescu, L.A.; Pop, M.A. Mechanical Performances of Lightweight Sandwich Structures Produced by Material Extrusion-Based Additive Manufacturing. *Polymers* **2020**, *12*, 1740. [[CrossRef](#)]
8. Fujiki, A. Present state and future prospects of powder metallurgy parts for automotive applications. *Mater. Chem. Phys.* **2001**, *67*, 298–306. [[CrossRef](#)]
9. Sedlak, J.; Rican, D.; Piska, M.; Rozkosny, L. Study of Materials Produced by Powder Metallurgy Using Classical and Modern Additive Laser Technology. *Procedia Eng.* **2015**, *100*, 1232–1241. [[CrossRef](#)]
10. Dutta, G.; Bose, D. Effect of sintering temperature on density, porosity and hardness of a powder metallurgy component. *Int. J. Emerg. Technol. Adv. Eng.* **2012**, *2*, 121–123.
11. Wong-Ángel, W.D.; Téllez-Jurado, L.; Chávez-Alcalá, J.F.; Chavira-Martínez, E.; Verduzco-Cedeño, V.F. Effect of copper on the mechanical properties of alloys formed by powder metallurgy. *Mater. Des.* **2014**, *58*, 12–18. [[CrossRef](#)]
12. Ayyappadas, C.; Muthuchamy, A.; Annamalai, A.R.; Agrawal, D.K. An investigation on the effect of sintering mode on various properties of copper-graphene metal matrix composite. *Adv. Powder Technol.* **2017**, *28*, 1760–1768. [[CrossRef](#)]
13. Mishra, R.R.; Rajesha, S.; Sharma, A.K. Microwave sintering of pure metal powders—A review. *Int. J. Adv. Mech. Eng.* **2017**, *4*, 2250–3234.
14. Ritasalo, R.; Cura, M.; Liu, X.; Söderberg, O.; Ritvonon, T.; Hannula, S.-P. Spark plasma sintering of submicron-sized Cu-powder—Influence of processing parameters and powder oxidization on microstructure and mechanical properties. *Mater. Sci. Eng. A* **2010**, *527*, 2733–2737. [[CrossRef](#)]
15. Chicos, L.-A.; Zaharia, S.M.; Lancea, C.; Pop, M.A.; Cañadas, I.; Rodríguez, J.; Galindo, J. Concentrated solar energy used for heat treatment of Ti6Al4V alloy manufactured by selective laser melting. *Sol. Energy* **2018**, *173*, 76–88. [[CrossRef](#)]
16. Chicos, L.-A.; Zaharia, S.M.; Cempura, G.; Kruk, A.; Lech, S.; Kryshstal, O.; Ziętara, M.; Michta, G.; Rodríguez, J.; Cosnita, M.; et al. Effect of concentrated solar energy on microstructure evolution of selective laser melted Ti-6Al-4V alloy. *Int. J. Adv. Manuf. Technol.* **2021**, *118*, 3183–3207. [[CrossRef](#)]
17. Efe, G.C.; Yener, T.; Altinsoy, I.; Ipek, M.; Zeytin, S.; Bindal, C. The effect of sintering temperature on some properties of Cu–SiC composite. *J. Alloys Compd.* **2011**, *509*, 6036–6042. [[CrossRef](#)]
18. Torabi, H.; Arghavanian, R. Investigations on the corrosion resistance and microhardness of Cu–10Sn/SiC composite manufactured by powder metallurgy process. *J. Alloys Compd.* **2019**, *806*, 99–105. [[CrossRef](#)]

19. Horita, Z.; Langdon, T.G. Microstructures and microhardness of an aluminum alloy and pure copper after processing by high-pressure torsion. *Mater. Sci. Eng. A* **2005**, *410–411*, 422–425. [[CrossRef](#)]
20. Ren, C.; Wang, Q.; Hou, J.; Zhang, Z.; Yang, H. Revealing the maximum microhardness and thickness of hardened layers for copper with various grain sizes. *Mater. Sci. Eng. A* **2020**, *778*, 139113. [[CrossRef](#)]
21. Pan, M.; Gupta, M.; Tay, A.; Vaidyanathan, K. Development of bulk nanostructured copper with superior hardness for use as an interconnect material in electronic packaging. *Microelectron. Reliab.* **2006**, *46*, 763–767. [[CrossRef](#)]
22. Ledbetter, H.M.; Naimon, E.R. Elastic properties of metals and alloys. II. Copper. *J. Phys. Chem. Ref. Data* **1974**, *3*, 897–935. [[CrossRef](#)]
23. Available online: <https://www.alfa.com/en/catalog/010161/> (accessed on 8 January 2022).
24. Available online: <https://www.filamente3d.ro/filamente/filament-aquasolve%E2%84%A2-pva-natural-solubil-in-apa-300g> (accessed on 19 December 2021).

Structural changes during 3D printing of bioderived and synthetic thermoplastic materials

Mihai Alin Pop ¹, Cătălin Croitoru ², Tibor Bedő ¹, Virgil Geamăn,¹ Irinel Radomir,³ Mihaela Coșniță,⁴ Sebastian Marian Zaharia ⁵, Lucia Antoaneta Chicoș,⁵ Ioan Miloșan¹

¹Transilvania University of Brasov, Faculty of Materials Science and Engineering, Department of Materials Science, Colina Universitatii Street, no. 1, 500084, Brasov, Romania

²Department of Materials Engineering and Welding, Transilvania University of Brasov, Faculty of Materials Science and Engineering, Colina Universitatii Street, no. 1, 500084, Brasov, Romania

³Department of Mathematics and Informatics, Transilvania University of Brasov, Faculty of Mathematics and Informatics, 29 Eroilor Avenue, 500036, Brasov, Romania

⁴Department of Product Design, Mechatronics and Environment, Transilvania University of Brasov, Faculty of Product Design and Environment, Colina Universitatii Street, no. 1, 500068, Brasov, Romania

⁵Department of Manufacturing Engineering, Transilvania University of Brasov, Faculty of Technological Engineering and Industrial Management, Mihai Viteazu Street, no. 5, 500174, Brasov, Romania

Correspondence to: C. Croitoru (E-mail: c.croitoru@unitbv.ro)

ABSTRACT: Three-dimensional (3D) printing processes are nowadays leading the charge in transforming traditional art, engineering, and manufacturing processes. In this study, the structural and thermal behavior of commercially available filaments composed of synthetic poly(acrylonitrile-*co*-butadiene-*co*-styrene) thermoplastic as well as poly(lactic acid) and poly(lactic acid)/polyhydroxyalcanoate reinforced with bamboo (*Bambusa sp.*) wood flour composite biothermoplastics were assessed by differential scanning calorimetry and infrared spectroscopy, aiming to understand the modifications that occur at the molecular level during their 3D printing. It has been determined that the biothermoplastic materials undergo both molecular reorientations related to tacticity increase and crystallinity decrease when submitted to 3D printing extrusion, while the synthetic thermoplastic undergoes crosslinking due to its butadiene component. All of the studied materials present good water stability (with water uptake values between 0.8% and 24%), and the water absorption follows a pseudo-Fickian mechanism. © 2019 Wiley Periodicals, Inc. *J. Appl. Polym. Sci.* **2019**.

KEYWORDS: biopolymers and renewable polymers; cellulose and other wood products; extrusion; morphology; thermoplastics

Received 2 July 2018; accepted 11 November 2018

DOI: 10.1002/app.47382

INTRODUCTION

In recent years, three-dimensional (3D) printing has become a robust, standalone additive manufacturing technology due to its almost linear design-to-object workflow.^{1,2} It allows the printing of complex products and easily reproducible pieces at high speed, with low environmental impact, material losses, and production costs compared to conventional methods (drilling, milling, extrusion, injection, and so forth).^{2,3} The 3D printing technique has an extensive application palette, ranging from typical consumer goods to specialized applications such as microelectronic and microfluidic devices and electrodes.⁴

The most widely used 3D printing method utilizes material extrusion, which deposits molten material (usually in the form of a filament), layer by layer, through a nozzle head onto a platform.¹

One of the most frequent components in filament manufacturing is thermoplastic polymers, among which poly(lactic acid) (PLA),⁵ acrylonitrile-butadiene-styrene copolymers (ABS),⁶ polycarbonates (PC),¹ polyhydroxyalkanoates (PHA),⁷ polyurethanes (PU), glycol-modified poly(ethylene terephthalate) (PETG), and polyamides (nylon) are most often used.¹

To overcome the relatively poor mechanical properties of the 3D printed polymers, a relatively wide selection of commercial filaments are already available or under development, which make use of several types of polymer blends (PLA/PHA,⁸ PC/ABS,⁹ PU/PLA,¹⁰ and so on) and composite formulations (polymer-carbon nanotubes,¹¹ polymer-ceramic,¹² polymer-metal¹³). Further introduction of additives into the filament recipe (coupling agents, plasticizers, stabilizers, and so on) can fine-tune the stability and mechanical response to several degradative factors of the

final 3D printed polymer, as well as improve the stability of the polymer melt during extrusion.¹⁴ To minimize the environmental footprint of the 3D printing process, biodegradable polymer formulations [based on aliphatic polyesters such as PLA or PHA and polyols (PEG)^{8,15–17}] or composite formulations filled with plant-derived materials are already available.^{18,19}

An understanding of the structural aspects and thermal behavior of both the filament and 3D prints is of utmost importance in designing functional products with improved properties. There are many studies to date concerning the mechanical behavior of 3D printed structures originating from several types of filaments (standalone polymers, polymer blends, or composites),^{13,20} but only a few deal with the structural and thermal behavior of both filament and corresponding 3D print.^{21,22} Furthermore, among these, most of the studies deal with custom-made filaments, which may have limited practical applicability to mass production of 3D printed objects. Study of the behavior of commercial filament types is of utmost importance, especially considering some limitations and inconsistencies of 3D printing technology at this stage, which are manifested in the insufficient quality of the printed items due to their internal structural defects (high porosity or low layer adhesion).^{2,13}

This paper aims to apply the already available structural and thermal characterization of bulk polymer materials, blends, and composites to the 3D printing filaments and to the materials obtained through 3D printing. The polymer and composite filaments are typically obtained through extrusion. The 3D printing process is in its essence an extrusion process, so the structural and morphological properties of both filaments and prints may have unique features not otherwise found in conventional bulk materials.²²

Two types of commercial polymer filaments, composed of PLA and ABS, and a composite mixture of PLA, PHA, and bamboo (*Bambusa sp.*) wood flour (PLA/PHA/BambooFill) have been used in this study. The differences in morphology, structure, thermal behavior, and stability at water immersion between these filaments and their corresponding 3D prints have been comparatively assessed.

EXPERIMENTAL

Materials

PLA and ABS filaments designed for fused deposition modeling were bought from Verbatim (Eschborn, Germany). A PLA/PHA/BambooFill filament that is a composite mixture of PLA, PHA, and bamboo (*Bambusa sp.*) wood flour (PLA/PHA/BambooFill) at 20 wt % loading was bought from ColorFabb (Belfeld, The Netherlands). The diameter of each type of filament, as specified by the producer, is 2.85 ± 0.03 mm. These materials were chosen based on their abundant availability, good extrusion properties, good postprinting ability, and tunable texture.

A CreatBot (Zhengzhou, China) DX-3D double-nozzle printer was used to obtain cylindrical prints 10 ± 0.1 mm in diameter and 2 ± 0.1 mm thick and having a 0.4 mm layer thickness.

The printing temperatures for the filaments (measured at the extrusion head) were 220 °C for the PLA and PLA/PHA/BambooFill filaments and 275 °C for ABS. The bed temperature for

the PLA and PLA/PHA/BambooFill filaments was 60 °C and for ABS 90 °C, as recommended by the manufacturer.

For each type of material, five prints were obtained at a printing speed of 30 mm/s for ABS and PLA/PHA BambooFill, and 40 mm/s for PLA, according to the manufacturer's specifications. The same printing path was used for each printed material type.

Characterization Methods

Optical Microscopy. For the structure and morphology analysis, representative samples including both neat filaments and prints were cross-sectioned with a microtome blade perpendicular to the original printing direction, embedded into an acrylic resin, and leveled using an automatic metallographic polishing device (Al_2O_3 suspension 0.05 μm grit). For each sample, five different micrographs from different regions of the cross section were acquired with three different magnifications (10 \times , 25 \times , and 100 \times) using a Nikon OMNIMET-BUEHLER microscope (Tokyo, Japan). No significant differences in morphology were detected in the micrographs at each magnification level between various regions located on the same sample. Only the images acquired at 25 \times magnification have been presented in this paper.

Water Stability and Wetting Behavior. The filaments and the prints were immersed in distilled water (50 mL) for predetermined time intervals, taken out and placed on filter paper (5 s on each side) to eliminate excess water, and weighed. This procedure was repeated until water absorption equilibrium was reached. A RADWAG (Radom, Poland) analytical balance model AS 60/220. X2 with an accuracy of 10^{-4} g was used to weigh the samples.

The relative water uptake Δm (%) of the filaments and prints was calculated using eq. (1):

$$\Delta m = \frac{m_t - m_0}{m_0} \cdot 100(\%) \quad (1)$$

where m_t is the mass of the materials immersed in water at time t , and m_0 is the initial mass of the materials before immersion in water. Five samples from each type of filament and its corresponding printed material were taken into the analysis, and the average values are presented in this paper.

Thermal Analysis. Differential scanning calorimetry (DSC) analysis of the filaments and printed samples was performed in the $[(-100) \div (+450)]$ °C domain under a nitrogen atmosphere, with 10 °C/min cooling/heating rate (DSC-200 F3 Maia/STA 449F3 Jupiter, Netzsch, Selb, Germany).

Spectral Analysis. The infrared spectra of the filaments and corresponding prints were acquired with a Bruker Vertex70 Fourier transform infrared (FTIR) spectrometer (Karlsruhe, Germany) in the 4000–550 cm^{-1} interval [4 cm^{-1} resolution, attenuated total reflectance (ATR) mode, 10 scans per spectrum].

RESULTS AND DISCUSSION

As can be seen in the micrographs shown in Figure 1(a,c), the PLA and ABS filaments exhibit a compact mass without any macrostructural defects. The PLA/PHA/BambooFill [Figure 1(e)] presents an uneven distribution of wood particles (average

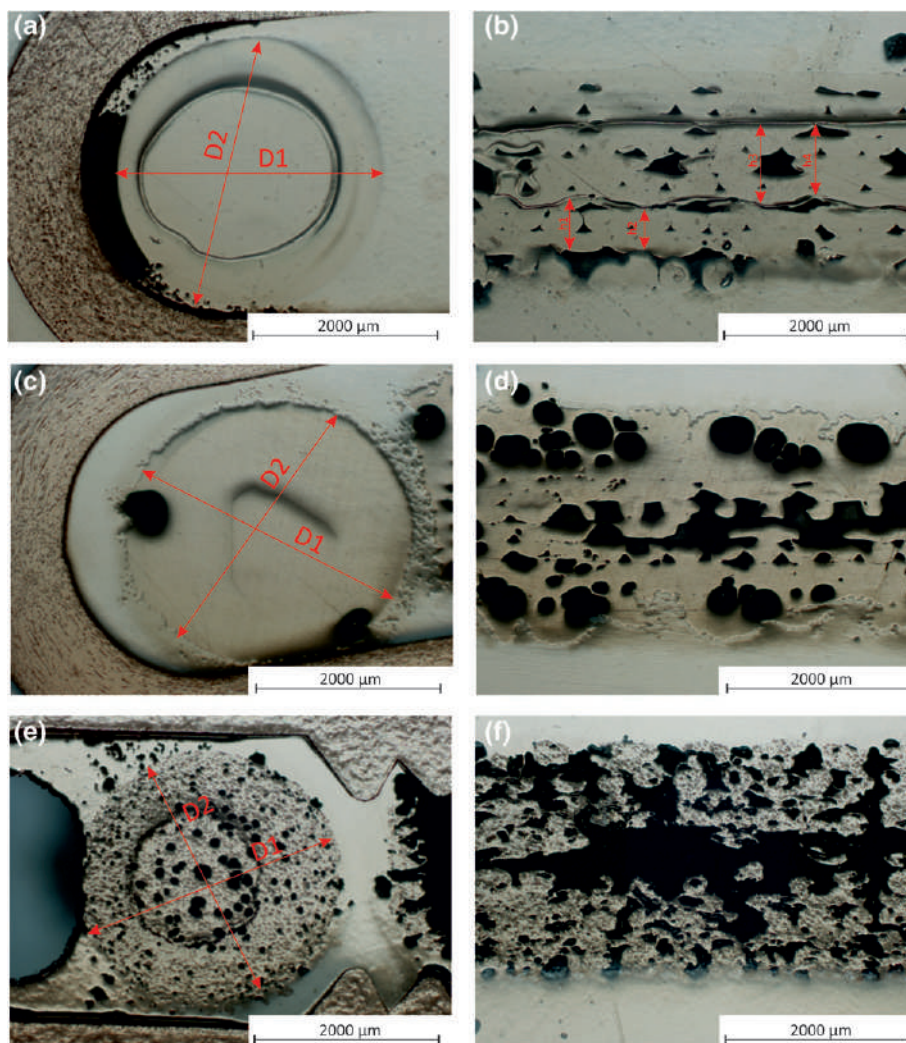


Figure 1. Cross-sectional optical micrographs of (a) PLA filament, (b) PLA print, (c) ABS filament, (d) ABS print, (e) PLA/PHA/BambooFill filament, and (f) PLA/PHA/BambooFill print at 25 \times magnification. [Color figure can be viewed at wileyonlinelibrary.com]

diameter 49.4 μm), with clustering near the center of the filament. Since all three types of filament are coextruded, this setup is best for high-resolution microprinting.²³ The diameters of the filaments, as measured from the optical micrographs of their cross sections, are 2.90 ± 0.02 mm for PLA, 2.59 ± 0.15 mm for ABS, and 2.55 ± 0.11 mm for PLA/PHA BambooFill.

In Figure 1(b), for the PLA print, the minimum and maximum thicknesses of an individual layer were determined as $h_1 = 0.57$ mm and $h_2 = 0.44$ mm. A fusion of two adjacent layers can also occur such that the layers are interwoven and no longer distinguishable ($h_3 = 0.87$ mm and $h_4 = 0.77$ mm).

In the case of the ABS print [Figure 1(d)], because of the higher printing temperature, the layers are merged and cannot be distinguished individually. In the case of PLA/PHA BambooFill [Figure 1(e)], due to bamboo sawdust, the layers have many gaps or agglomerations and also cannot be individually distinguished.

The cross sections of the printed samples present several defects (interlayer pores), with regular triangular patterns in the case of PLA [Figure 1(b)] and irregular patterns in the case of ABS

[Figure 1(d)] and PLA/PHA/BambooFill [Figure 1(f)], caused by the inclusion of small air bubbles and otherwise indiscernible filament defects fusing during the extrusion through the heated nozzle of the filament in the molten state.²⁴ The fewest defects occur in the case of the PLA printed sample, where the deposited filament can merge better into coalesced layers, due to the low value of the PLA melt/air interfacial tension and due to the higher printing speed.²⁵ In contrast with PLA, in the PLA/PHA/BambooFill, the density of defects is the highest, due to the localized influence of the wood particles on the polymer layer distribution and adhesion. The higher printing speed (40 mm/s) could explain the regular shape of the defects in the case of the PLA [Figure 1(b)] print for this type of filament, which causes a reduction in the pressure-forced outgassing during extrusion; the combination of the solidification rate of the melted polymer and the elimination of gases results in smaller, closed pores of more regular shape. At lower printing speeds, the emergence of perforated pores could be observed [Figure 1(d,f)].

Another factor that causes defects is the temperature of the build platform (printing bed). At a lower temperature (such as for PLA

and PLA/PHA/BambooFill), the bonding between layers is faulty due to the solidification of the previously deposited layers, resulting in voids, pores, and poor adhesion between layers (exfoliation). At higher temperatures (for ABS), the previously deposited layers remain in a softened state, which leads to an inhomogeneity in the thickness of the layers as well as a diminution of the dimensional precision.

The average roughness (Ra) and skewness (Rsk) values for the filaments and prints cross sections, expressed in μm , computed with the help of the ImageJ software (Roughness calculation plugin,²⁶ are depicted in Table I. The roughness values were directly computed/displayed by the software on the preloading of each micrograph image into the software. As a general trend, the average roughness of the filaments is slightly higher than that of the prints, as also found in other research.²⁴

The highest average roughness values are registered for the PLA and ABS filaments, for which the extrusion process causes a uniform melting of the polymer, contributing to the coalescence of individual 3D printed tracks and to lowering of the individual Ra values for the prints.²⁷ A profile with a higher Rsk value tends to be peaky (high-frequency occurrence of high asperities and deep valleys);²⁷ this is recorded for the PLA/PHA/BambooFill filament and prints, due to the embedded wood particles.

Besides roughness, ImageJ software was used to determine a percent average filament density based on the cross-sectional optical micrographs from Figure 1, through the Filament-Analysis plugin,²⁸ as well as to color map the interconnected areas in the same cross sections, through the Find-Connected-Regions plugin.²⁹ The interconnected areas were mapped to assess the compactness of the 3D prints, based on the fact that a more monochrome surface presents a high amount of interconnected areas and is more compact. The density profiles are illustrated in Figure 2, and the corresponding values for the average filament densities are given in Table I.

It can be seen, in agreement with the roughness values, that a higher filament density determines a lower average surface roughness and lower density of microdefects in the prints. For the PLA/PHA/BambooFill sample, the filament density presents lower values because the wood particles act as local "disruptors" for the fusion of melted tracks. Also, the highest compactness could be seen for the ABS and PLA prints, in contrast with PLA/PHA/BambooFill.

Table I. Roughness and Filament Density Values Computed with ImageJ Software

Material		Ra (μm)	Rsk (μm)	Filament density (%)
Filament	PLA	63.38	0.51	—
	PLA/PHA/ BambooFill	57.89	0.55	—
	ABS	61.75	0.50	—
Print	PLA	61.92	0.54	49.99
	PLA/PHA/ BambooFill	53.57	0.65	42.47
	ABS	55.68	0.60	47.94

The water uptake kinetics for the filaments and prints are illustrated in Figure 3.

As a general trend, it can be seen that the prints show higher relative mass-uptake values than their corresponding printed filaments, which could be due to slight modification in the architecture of the polymeric chains at the molecular level on one hand, and to modifications in surface Rsk values on the other hand (the roughness profile peaks act as local water sorption concentrators).

The highest equilibrium uptake value is registered for the PLA/PHA/BambooFill prints, followed by the corresponding filament, due to the hydrophilic nature of the embedded wood particles and to the presence of defects in the structure of the prints (interconnected pores), which act as pathways for water penetration into the bulk of the material. The Δm values for ABS and PLA are the lowest, due to their lower hydrophilicity and compactness (lower porosity).

To model the mass-uptake kinetics of the filaments and the corresponding printed composites, eq. (2) was used:³⁰

$$\frac{\Delta m_t}{\Delta m_{eq}} = k \cdot t^n \quad (2)$$

where Δm_t is the relative mass uptake of the samples at time t , Δm_{eq} is the mass uptake at equilibrium, k (min^{-n}) is the water uptake rate, and n is the power-law diffusion exponent describing the solvent transport mechanism in or through the filaments and printed composites.

Based on the values of n , four types of water diffusion can be described: Fickian diffusion ($n = 0.5$), non-Fickian or Case II transport mode when $n = 1$, anomalous or Case III ($0.5 < n < 1$), and pseudo-Fickian, when $n < 0.5$.³⁰

The results obtained for k and n and the R^2 values obtained by fitting eq. (2) against the experimental data are expressed in Table II. The water uptake rates are higher for the prints than for the filaments, due to their higher Rsk values and also due to possible structural changes in the material during printing, the highest values being recorded firstly for PLA, followed by PLA/PHA/BambooFill and finally ABS, for which the lowest k values have been determined. Interestingly, PLA/PHA/BambooFill does not present the highest uptake rate, due to the impeding effect of the wood particles (which act as water adsorption centers) on water transport into the bulk of the material.

By plotting the relative mass uptake of the filaments and printed composites, Δm_t , as a function of $t^{1/2}$, the slope of the resulting linear dependency, for $\Delta m_t < 0.2\Delta m_{eq}$, is represented by the parameter p . This parameter can be used to determine the value for the apparent diffusion coefficient, D_{app} , by using eq. (3) (Table II):³¹

$$D_{app} = \pi \cdot \left(\frac{h \cdot p}{4 \cdot \Delta m_{eq}} \right)^2 \quad (3)$$

where h is the thickness of the material.

In all cases, except for the PLA filament, for which the model described by eq. (2) does not apply, the water diffusion mechanism into the mass of the material is pseudo-Fickian (i.e., it occurs with a

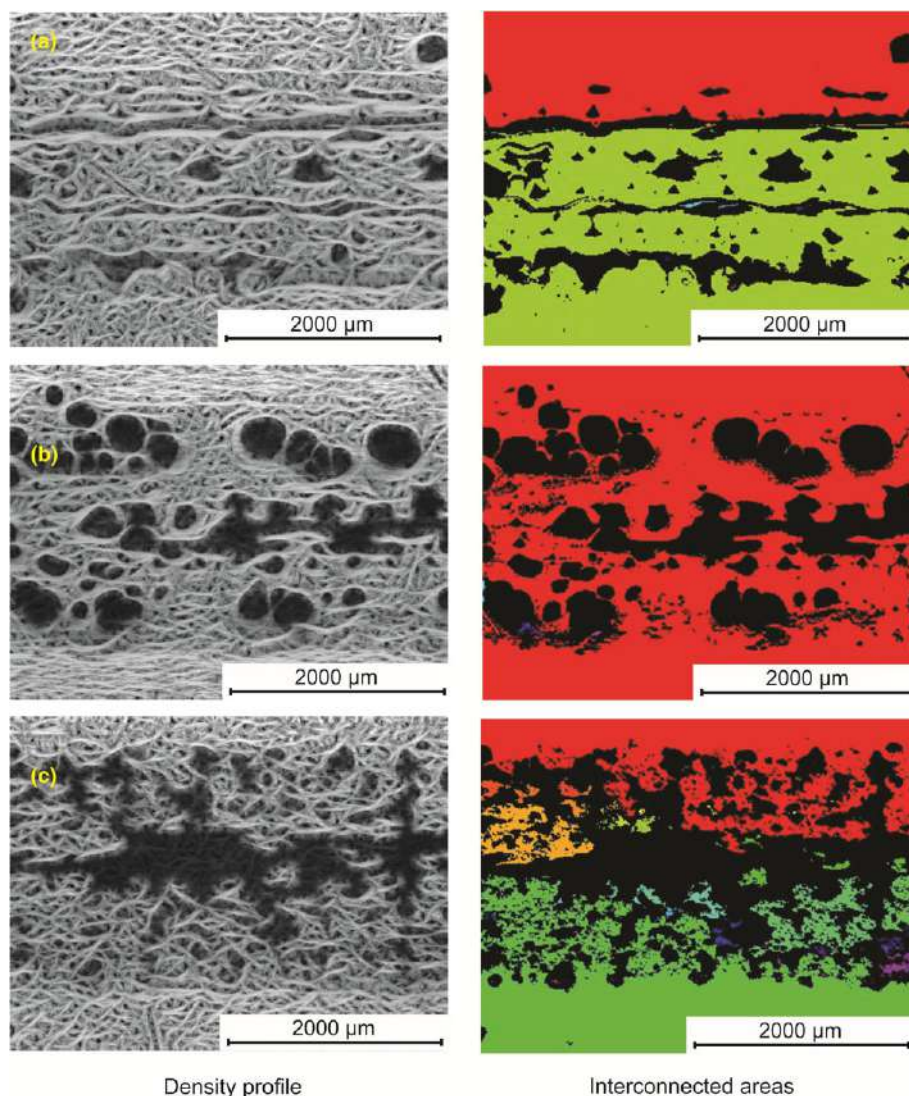


Figure 2. Filament density profiles and interconnected areas computed with ImageJ software for (a) PLA, (b) ABS, and (c) PLA/PHA/BambooFill (25× magnification). [Color figure can be viewed at wileyonlinelibrary.com]

slower onset than in ideal Fickian behavior), in accordance with other thermoplastic polymer systems at temperatures below their corresponding glass-transition temperatures (T_g).^{31,32}

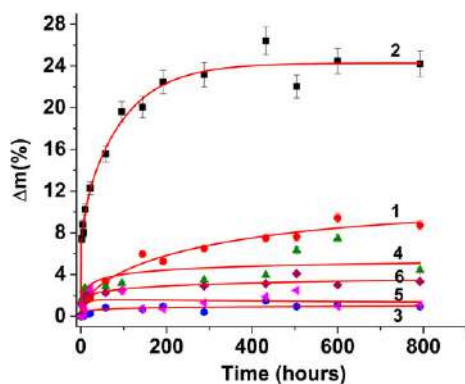


Figure 3. Water uptake kinetics of (1) PLA/PHA/BambooFill filament, (2) PLA/PHA/BambooFill print, (3) ABS filament, (4) ABS print, (5) PLA filament, and (6) PLA print. [Color figure can be viewed at wileyonlinelibrary.com]

The diffusion coefficients for the prints present lower values than for the corresponding filaments, due to tighter packing of the macromolecular polymer assembly during extrusion and later cooling of the materials. The PLA/PHA/BambooFill print presents the lowest diffusion coefficient among the prints, confirming that the wood particles may act as local sorption concentrators, which has also been found in other research on wood–plastic composites.³¹ The different behavior of the PLA print (the lowest R^2 value from fitting against eq. (2) among all prints) could be due to the different pattern of pores (smaller size, triangular-shaped, with low interconnection), which may impede steady-state Fickian diffusion. Also, water diffusion into the PLA filament could not be described by steady-state Fickian diffusion. As the T_g of the PLA filament is 67 °C (Figure 4), it is expected that at room temperature, the mobility of the PLA phase will be increased more, as compared to the PLA print and to the other types of polymers/blends, which have a much higher T_g value. This increase in the macromolecular chain mobility allows for different water penetration regimes into this type of

Table II. Kinetics Values for Water Uptake

Material		<i>k</i>	<i>n</i>	<i>R</i> ²	<i>D</i> _{app} (10 ⁻⁵ mm ² /min)
Print	PLA	0.455	0.113	0.949	1.020
	PLA/PHA/BambooFill	0.233	0.253	0.980	0.143
	ABS	0.216	0.145	0.902	2.730
Filament	PLA	0.933	0.016	0.002	—
	PLA/PHA/BambooFill	0.156	0.454	0.982	6.466
	ABS	0.128	0.392	0.842	5.089

matrix over time, contrasting with the more rigid matrix of ABS and PLA/PHA/BambooFill, where the water flux into the polymer matrix can reach a steady state with a higher probability.

The glass transition, cold crystallization, melting, and degradation onsets for the filaments and the prints (where applicable) have been qualitatively (through the peak temperature values, T_g , T_{CC} , T_m , and T_{degr}) and quantitatively (through the enthalpies) assessed from the DSC thermograms, presented in Figures IV–VI. The DSC heating curve for PLA presents some well-documented features, summarized in Figure 3. Cold crystallization of PLA occurs as an exothermic process, from $T_{CC} = 107.5$ °C for the filament to 122.8 °C for the print, followed by a sizable endothermic peak ascribed to melting of PLA, occurring at $T_m = 172$ for the filament and 172.1 °C for the print, in accordance with the values presented in the literature.^{33,34}

During extrusion, the molten material originating from the filament cools rapidly, resulting in the development of irregular crystal aggregates, which means that the printed material is found in a quenched state.³⁵ The rearrangement of the irregular crystal aggregates into new crystalline regions above T_g occurs at a higher temperature for the PLA print ($T_{CC} = 122.8$ °C) than for the PLA filament ($T_{CC} = 107.5$ °C), as also found in other research.³⁶

The crystallinity degree of the PLA samples was calculated using eq. (4):³⁴

$$\chi_C = \frac{|\Delta H_m| - |\Delta H_{CC}|}{w_{PLA} \cdot \Delta H_m^0} \cdot 100(\%) \quad (4)$$

where ΔH_m is the melting enthalpy, ΔH_{CC} is the cold crystallization enthalpy of the filament/print, ΔH_m^0 is the melting enthalpy of 100% crystalline PLA (93.1 J/g),³⁷ and w_{PLA} is the weight fraction of PLA (1 for neat PLA).

The crystallinity of the PLA filament is 24.37%, and it decreases to 18.98% for the print, showing that the latter does not have enough time to crystallize in a more ordered manner, given the rapid cooling gradient of the molten extruded material.

An endothermic peak, centered at $T_g = 67$ °C for the filament and 80.4 °C for the print, could be ascribed to the PLA glass transition.³³ The presence of only a single (not split) T_g -related peak could imply that all of the PLA is kept in its α' anomer form, due to the high cooling gradient, which impedes molecular reorientation in this case.³⁷

Regarding the amorphous PLA fraction, the mobile amorphous (X_{MA}) and rigid amorphous phases (X_{RA}) were determined using

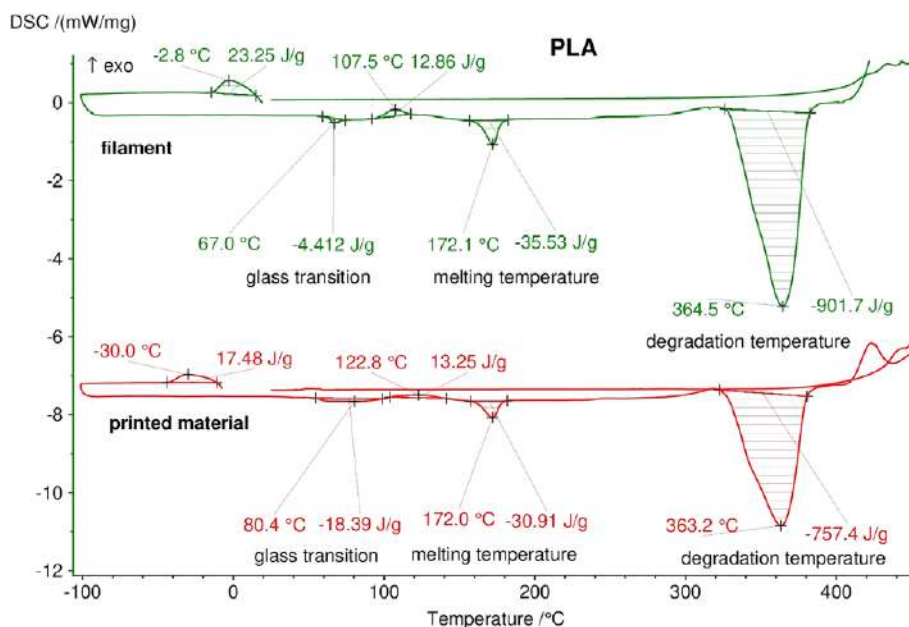


Figure 4. DSC thermograms for PLA filament and print samples. [Color figure can be viewed at wileyonlinelibrary.com]

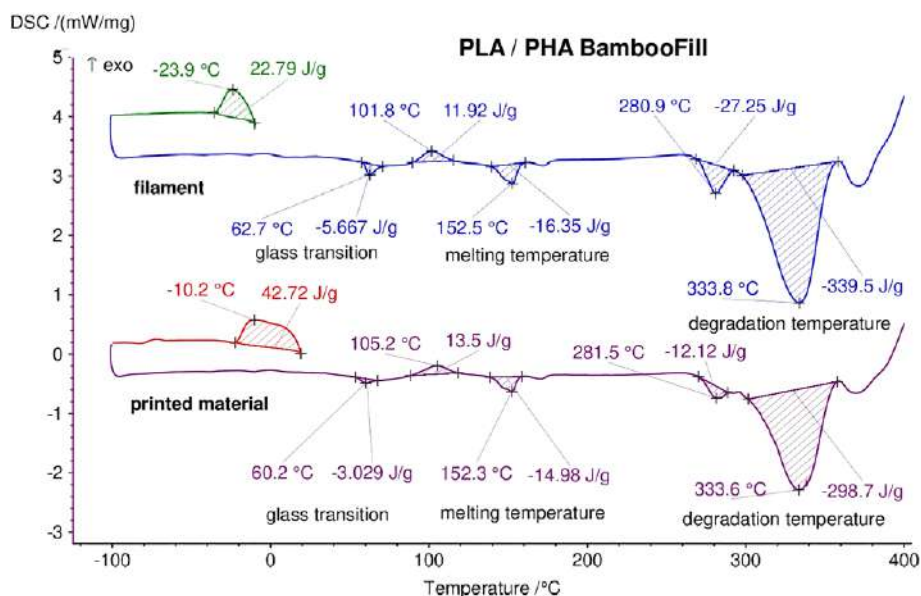


Figure 5. DSC thermograms for PLA/PHA/BambooFill filament and print samples. [Color figure can be viewed at wileyonlinelibrary.com]

eq. (5) and eq. (6) based on the specific heat capacities of the PLA materials at T_g :³⁶

$$X_{MA} = \frac{\Delta C_p}{\Delta C_p^0} \cdot 100(\%) \quad (5)$$

where ΔC_p and ΔC_p^0 represent the measured specific heat changes at T_g of the PLA sample and 100% amorphous PLA, respectively [$\Delta C_p^0 = 0.693 \text{ J/(g K)}$]:³⁸

$$X_{RA} = 1 - \chi_C - X_{MA} \quad (6)$$

The mobile amorphous phases X_{MA} decrease from 54.30% in the case of the filament to 33.50% for the print, while the rigid amorphous phase increases from 21.33% (filament) to 52.48% (print), which means that in the printed material, there is a more substantial fraction of rigidly confined macromolecules. The increase

of this fraction in the print leads to an increase in the T_g values for PLA, even though the overall crystallinity decreases, which has also been found in other research.^{36,39}

The decrease in crystallinity, also associated with the macromolecular chains reorienting, may be responsible for a slight decrease in the resistance of the material to thermal degradation, because for the prints T_{degr} is lower than for the filament.

In the case of the PLA/PHA blend with embedded bamboo wood particles, Figure 5 reveals the main patterns that could be found also for pure PLA, namely the $T_g = 62.7 \text{ °C}$ (filament) and 60.2 °C (print) and T_{CC} for the PLA fraction (101.8 °C for the filament and 105.2 °C for the print). The endothermic melting peaks for PLA (centered at $T_m = 152.5 \text{ °C}$ for the filament and

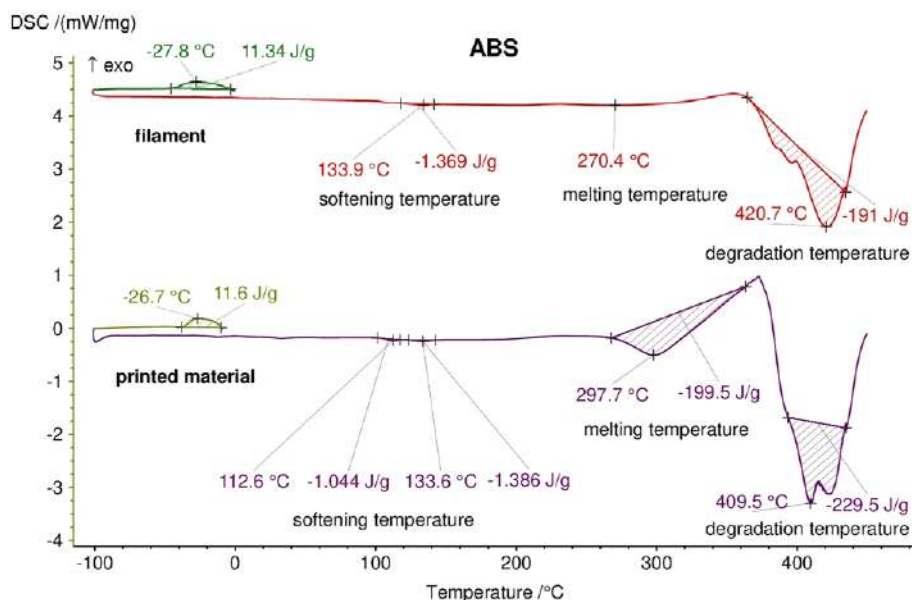


Figure 6. DSC thermograms for ABS filament and print samples. [Color figure can be viewed at wileyonlinelibrary.com]

152.3 °C for the print) occur at a much lower temperature compared to pure PLA.⁴⁰ The differences between PLA/PHA/BambooFill and neat PLA also reside in the slightly lower thermal degradation temperature onset of the former compared to the latter (due to more degradation-susceptible components of wood.^{41,42}) In this respect, an endothermic peak between 282 °C and 289 °C could be found in the thermograms from Figure 5, possibly ascribed to the onset of hemicellulose degradation.^{41,43}

Also, two endothermic peaks, centered at 169 °C for PLA/PHA/BambooFill filament and 172 °C for the PLA/PHA/BambooFill print, could be ascribed to the PHA melting transition⁴⁰ (not marked in Figure 5), which is an indication that the two polymers in the blend respond independently to the heating regime; that is, the two polymers (PLA and PHA) are not entirely miscible.⁴⁴

The PHA and wood particles could act as disruptors of the orderly chain alignment of PLA macromolecules, leading to practically the same first-order transition temperatures for both filament and prints, as has also been found in other research.^{40,42,44}

Considering the melting enthalpy for PLA [Figure 4, $\Delta H_{m,PLA} = -35.53$ J/g (filament) and -30.91 J/g (print)] and the melting enthalpy corresponding to PLA in PLA/PHA/BambooFill determined from the DSC thermogram in Figure 5, the relative fraction of PLA (w_{PLA}) can be found using eq. (7):

$$w_{PLA} = \text{Average} \left[\left(\frac{\Delta H_{m,PLA/PHA}}{\Delta H_{m,PLA}} \right)_{\text{filament}} ; \left(\frac{\Delta H_{m,PLA/PHA}}{\Delta H_{m,PLA}} \right)_{\text{print}} \right] \quad (7)$$

The calculated w_{PLA} value is 0.47, and based on eq. (4), the calculated crystallinity degree for the PLA in the filament material is 6.38%, while in the print it decreases to 2.25%. These crystallinity values are like that found in other research on PLA/PHA blends.⁴⁰

This decrease in crystallinity for PLA could account for the higher water-uptake values registered in Figure 3 and for the lower thermal-degradation onset for PLA/PHA/BambooFill.

For ABS, the thermogram in Figure 6 registers a “softening” temperature, related to the endothermic styrene glass transition at ~ 112 °C (observed only for the printed sample), and an

endothermic acrylonitrile glass-transition temperature at 133–134 °C, while melting occurs at 270–297 °C.^{45,46}

In general, the prints present higher transition temperatures than the filament. Since the rubber (butadiene) phase of ABS is susceptible to thermal degradation, crosslink points are formed between the macromolecular chains,⁴⁵ which lead to a decreased chain mobility, and an increase in the melting temperature is expected for the heat-processed (extruded) print. The supplementary crosslinking could also contribute, besides ABS low polarity, to the low water-uptake values (Figure 3).

The print is more prone to thermal degradation, as seen from the ~ 11 °C lower degradation onset (409–421 °C).

The ATR-FTIR spectra of PLAs from Figure 7 present an overall aspect characteristic of semicrystalline PLA, including several well-documented absorption features, such as the —C—H stretching modes at 2998–2847 cm^{-1} , the —C—O stretching band at ~ 1745 cm^{-1} , the ester —C—O— symmetric stretch at 1187 cm^{-1} , and the —C—O—C— asymmetric stretch at ~ 1072 cm^{-1} .⁴⁷ The two bands at ~ 861 cm^{-1} and ~ 756 cm^{-1} can be ascribed to the amorphous and crystalline phases of PLA, respectively.⁴⁸ The crystallinity index of PLA can be calculated as the ratio between the two band areas A_{756}/A_{861} , and it decreases from 3.095 for the filament to 1.763 for the print, in accordance with the DSC results.

The —C—O stretching band in PLA is sensitive to morphology modifications, increasing proportionally to the amount of syndiotactic polylactide.⁴⁹ It can be seen that the absorbance of this band increases from 0.03 in the filament to 0.15 in the print, implying chain restructuring of PLA during 3D printing.

The slight redshifting of the absorption band maxima to lower wave-number values in the print compared to the filament could be an indicator of polymer phase flexibilization.⁴⁸ A flexibilization of the polymer matrix along with a crystallinity decrease could also be responsible for the higher water-uptake values registered in Figure 3 for the prints.

The FTIR spectra for the PLA/PHA/BambooFill materials in Figure 8 suggest the overall appearance of a polyester blend. The

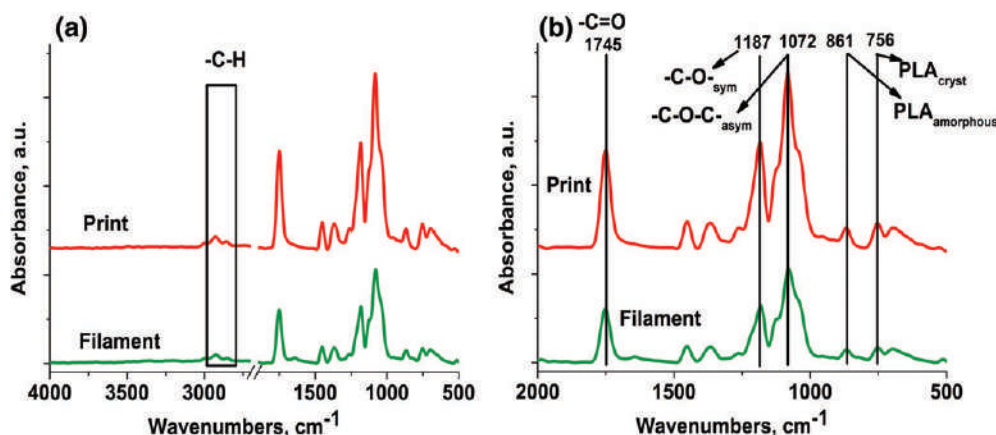


Figure 7. ATR-FTIR spectra of the PLA filament and print samples: (a) whole spectrum; (b) detail of 2000–500 cm^{-1} region. [Color figure can be viewed at wileyonlinelibrary.com]

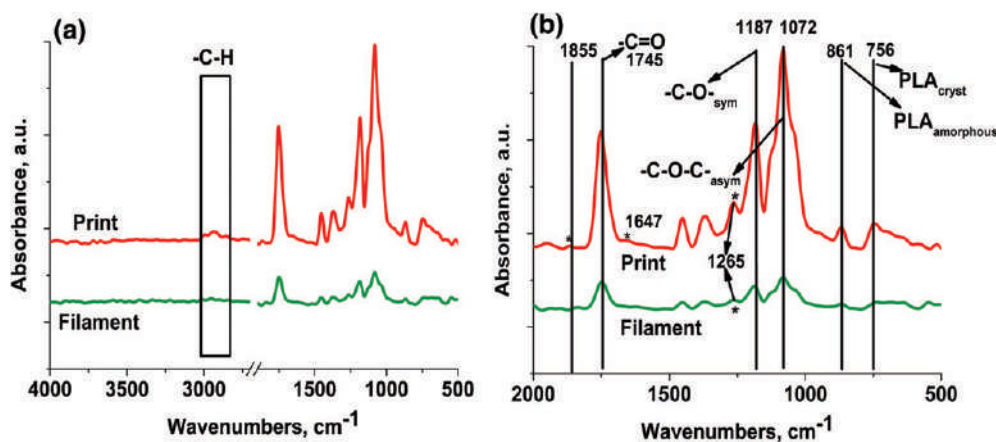


Figure 8. ATR-FTIR spectra of the PLA/PHA/BambooFill filament and print samples: (a) whole spectrum; (b) detail of 2000–550 cm^{-1} region. [Color figure can be viewed at wileyonlinelibrary.com]

absorption features of wood could not be well discerned, implying that it may be well embedded in the polymer matrix.

Most of the absorption bands from Figure 8 are like those from Figure 7, because PLA is the main component and both polymers are polyesters. It can be seen that the intensity of the band at $\sim 1265 \text{ cm}^{-1}$ ascribed to the crystalline phase of PHA⁴⁰ is increased in the printed sample by about five times compared to the filament, implying an increased ordering in the PHA phase during the melt-extrusion printing process. This fact is also supported by the presence of a weak shoulder at $\sim 1647 \text{ cm}^{-1}$ in the printed sample, related to a crystal defect in polyhydroxyalkanoates that occurs during melt crystallization.⁵⁰

Based on the fourfold increase in the intensity of the band at $\sim 867 \text{ cm}^{-1}$ ascribed to the amorphous PLA contributions in the printed sample as compared to the filament, a decrease in PLA crystallinity is expected, as also found in the DSC data.

A weak band appears at $\sim 1855 \text{ cm}^{-1}$ in the printed sample, ascribed to the weak —C—O— antisymmetric stretch in anhydrides,⁵¹ implying that the PLA/PHA/BambooFill material may be additivated (a fraction of PLA may be grafted with maleic anhydride to improve coupling with the wood phase).

The FTIR spectra of ABS in Figure 9 reveal some general features, such as the absorption bands at 3057–3047 cm^{-1} ascribed to the C—H stretching in the aromatic styrene rings, the absorptions between 2916 and 2851 cm^{-1} ascribed to C—H stretching modes in the aliphatic segments of ABS, and the weak band at 2230 cm^{-1} ascribed to the —C—N— vibration in acrylonitrile.^{52,53} The bands at 1602–1598 cm^{-1} and 1455 cm^{-1} are ascribed to the aromatic styrene ring vibration modes, while the bands at 964 cm^{-1} and 911 cm^{-1} are characteristic of the 1,4-butadiene and 1,2-butadiene components, respectively.

No significant changes occur in the FTIR spectra of ABS after printing, except for the increase in the absorbance values ascribed to the styrene rings and butadiene vibration modes and the shifting of their absorption maxima to lower wave numbers, due to the higher mobility and molecular contact of the polymer chains during the 3D printing extrusion process.^{52,54} This could also be related to the results regarding the weak crosslinking of the ABS macromolecular assembly, as observed in the DSC analysis. The general preservation of the surface chemistry, in this case, handles the low water absorption coefficient for this type of sample.

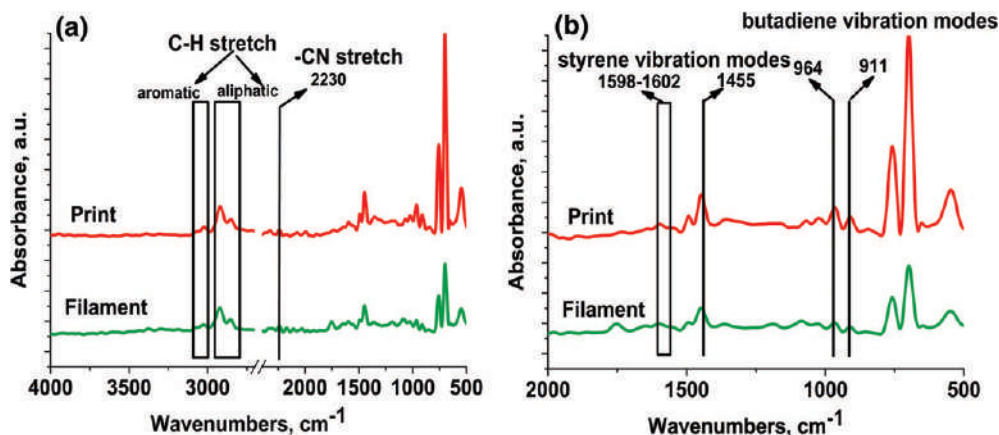


Figure 9. ATR-FTIR spectra of ABS filament and print samples: (a) whole spectrum; (b) detail of 2000–550 cm^{-1} region. [Color figure can be viewed at wileyonlinelibrary.com]

CONCLUSIONS

Both the filaments and their corresponding prints present good water stabilities, the water sorption uptakes being higher for the prints than for the filaments. The increase in water uptake values followed the order ABS < PLA < PLA/PHA/BambooFill for each material type (filament, print).

The DSC analysis has proven that all of the studied materials present good thermal stability, with low degradation of the polymer phase, which may account for the slight decrease in the degradation-onset temperature for the prints, in comparison with the filaments. The lowest resistance to thermal degradation was recorded for the PLA/PHA/BambooFill material, due to the presence of the thermally labile wood phase.

The ATR-FTIR results showed that no significant changes occur in the surface chemistry of the biothermoplastic filaments during 3D printing, except for molecular reorientations (in the case of PLA and the PLA/PHA blend with embedded wood particles) and crystallinity decrease, which could account for the high water-uptake values and implicitly lower dimensional stability of the prints. Also, due to molecular reorientations, several new bands appear in the FTIR spectra of the PLA/PHA/BambooFill material, indicating additivation with a coupling agent, such as maleic anhydride. In the case of ABS, weak crosslinks can occur, related to the increase in molecular mobility during melting.

ACKNOWLEDGMENTS

We hereby acknowledge the structural funds project European Commission (<GN>POS-CCE, O.2.2.1., ID 123, SMIS 2637, ctr. No 11/2009</GN>) for partly providing the infrastructure used in this work.

REFERENCES

- Dizon, J. R. C.; Espera, A. H.; Chen, Q.; Advincola, R. C. *Addit. Manuf.* **2018**, *20*, 44.
- Manzanas-Palenzuela, C. L.; Martín-Clemente, J. P.; Lobo-Castañón, M. J.; López-Ruiz, B. *Talanta*. **2017**, *164*, 261.
- Wang, X.; Jiang, M.; Zhou, Z.; Gou, J.; Hui, D. *Composites, Part B*. **2017**, *110*, 442.
- Berman, B. *Business Horizons*. **2012**, *55*(2), 155.
- Lim, L. T.; Auras, R.; Rubino, M. *Prog. Polym. Sci.* **2008**, *33*(8), 820.
- Cole, D. P.; Riddick, J. C.; Iftekhar Jaim, H. M.; Strawhecker, K. E. *Zander, N. E. J. Appl. Polym. Sci.* **2016**, *133*(30), 43671.
- Junyu, Z.; Shishatskaya, E. I.; Volova, T. G.; da Silva, L. F.; Chen, G. Q. *Mater. Sci. Eng., C*. **2018**, *86*, 144.
- Szuman, K.; Krucińska, I.; Boguń, M.; Draczyński, Z. *Autex Res. J.* **2016**, *16*(3), 119.
- Lee, J. Y.; An, J.; Chua, C. K. *Appl. Mater. Today*. **2017**, *7*, 120.
- Hung, K. C.; Tseng, C. S.; Hsu, S. H. *Adv. Healthcare Mater.* **2014**, *3*(10), 1578.
- Gnanasekaran, K.; Heijmans, T.; van Bennekom, S.; Woldhuis, H.; Wijnia, S.; Friedrich, H. *Appl. Mater. Today* **2017**, *9*, 21.
- Weng, Z.; Wang, J.; Senthil, T.; Wu, L. *Mater. Des.* **2016**, *102*, 276.
- Hwang, S.; Reyes, E. I.; Moon, K. S.; Rumpf, R. C.; Kim, N. S. *J. Electron. Mater.* **2015**, *44*(3), 771.
- Ngo, T. D.; Kashani, A.; Imbalzano, G.; Nguyen, K. T.; Hui, D. *Composites, Part B*. **2018**, *143*(15), 172.
- Serra, T.; Ortiz-Hernandez, M.; Engel, E.; Planell, J. A.; Navarro, M. *Mater. Sci. Eng., C*. **2014**, *38*, 55.
- Zeidler, H.; Klemm, D.; Böttger-Hiller, F.; Fritsch, S.; Le Guen, M. J.; Singamneni, S. *Procedia Manuf.* **2018**, *21*, 117.
- Serra, T.; Planell, J. A.; Navarro, M. *Acta Biomater.* **2013**, *9*(3), 5521.
- Frone, A. N.; Berlioz, S.; Chailan, J. F.; Panaitescu, D. M. *Carbohydr. Polym.* **2013**, *91*(1), 377.
- Le Duigou, A.; Castro, M.; Bevan, R.; Martin, N. *Mater. Des.* **2016**, *96*, 106.
- Senatov, F. S.; Niaza, K. V.; Zadorozhnyy, M. Y.; Maksimkin, A. V.; Kaloshkin, S. D.; Estrin, Y. Z. *J. Mech. Behav. Biomed. Mater.* **2016**, *57*, 139.
- Feng, X.; Yang, Z.; Rostom, S. S.; Dadmun, M.; Xie, Y.; Wang, S. *J. Appl. Polym. Sci.* **2017**, *134*(31), 45082.
- Cuiffo, M. A.; Snyder, J.; Elliott, A. M.; Romero, N.; Kannan, S. *Halada, G. P. Appl. Sci.* **2017**, *7*(6), 579.
- Weimer, C. U. S. *Pat. Appl.* **2016**, *14/927*, 588.
- Wu, Y.; Isakov, D.; Grant, P. S. *Materials*. **2017**, *10*(10), 1218.
- Sarikhani, K.; Jeddi, K.; Thompson, R. B.; Park, C. B.; Chen, P. *Thermochim. Acta*. **2015**, *609*, 1.
- Croitoru, C.; Patachia, S.; Doroftei, F.; Parparita, E.; Vasile, C. *Appl. Surf. Sci.* **2014**, *314*, 956.
- Townsend, A.; Senin, N.; Blunt, L.; Leach, R. K.; Taylor, J. S. *Precis. Eng.* **2016**, *46*, 34.
- Jacques, E.; Buytaert, J.; Wells, D. M.; Lewandowski, M.; Bennett, M. J.; Dirckx, J.; Verbelen, J.-P.; Vissenberg, K. *Plant J.* **2013**, *74*(6), 1045.
- Wagner, T.; Lipinski, H. G. *J. Open Res. Software*. **2013**, *1*(1), 6.
- Bajpai, A. K.; Saini, R. J. *Mater. Sci.: Mater. Med.* **2009**, *20*(10), 2063.
- Kaboorani, A. *Construct. Build. Mater.* **2017**, *136*, 164.
- Dhakal, H. N.; Zhang, Z. Y.; Richardson, M. O. W. *Compos. Sci. Technol.* **2007**, *67*(7–8), 1674.
- Lee, S. T.; Kareko, L.; Jun, J. J. *Cell. Plast.* **2008**, *44*(4), 293.
- Song, Y.; Li, Y.; Song, W.; Yee, K.; Lee, K. Y.; Tagarielli, V. L. *Mater. Des.* **2017**, *123*, 154.
- Tsuji, H.; Miyase, T.; Tezuka, Y.; Saha, S. K. *Biomacromolecules*. **2005**, *6*(1), 244.
- Lizundia, E.; Petisco, S.; Sarasua, J. R. *J. Mech. Behav. Biomed. Mater.* **2013**, *17*, 242.

37. Sarasua, J. R.; Arraiza, A. L.; Balerdi, P.; Maiza, I. *J. Mater. Sci.* **2005**, *40*(8), 1855.
38. Pyda, M.; Bopp, R. C.; Wunderlich, B. *J. Chem. Thermodyn.* **2004**, *36*(9), 731.
39. Zuza, E.; Ugartemendia, J. M.; Lopez, A.; Meaurio, E.; Lejardi, A.; Sarasua, J. R. *Polymer*. **2008**, *49*(20), 4427.
40. Lai, S. M.; Liu, Y. H.; Huang, C. T.; Don, T. M. *J. Polym. Res.* **2017**, *24*(7), 102.
41. Croitoru, C.; Spirchez, C.; Cristea, D.; Lunguleasa, A.; Pop, M. A.; Bedo, T.; Roata, I. C.; Luca, M. A. *J. Appl. Polym. Sci.* **2018**, *135*(22), 46317. <https://doi.org/10.1002/app.46317>.
42. Yao, L.; Wang, Y.; Li, Y.; Duan, J. *Iran. Polym. J.* **2017**, *26*(2), 161.
43. Croitoru, C.; Spirchez, C.; Lunguleasa, A.; Cristea, D.; Roata, I. C.; Pop, M. A.; Bedo, T.; Stanciu, E. M.; Pascu, A. *Appl. Surface Sci.* **2018**, *438*, 114.
44. Cao, X.; Mohamed, A.; Gordon, S. H.; Willett, J. L.; Sessa, D. J. *Thermochim. Acta.* **2003**, *406*(1–2), 115.
45. Blom, H.; Yeh, R.; Wojnarowski, R.; Ling, M. *J. Therm. Anal. Calorim.* **2006**, *83*(1), 113.
46. Ghaemy, M.; Scott, G. *Polym. Degrad. Stab.* **1981**, *3*(3), 233.
47. Riba, J. R.; Cailloux, J.; Cantero, R.; Canals, T.; MasPOCH, M. L. *Polym. Test.* **2018**, *65*, 264.
48. Xu, R.; Xie, J.; Lei, C. *RSC Adv.* **2017**, *7*(63), 39914.
49. Kister, G.; Cassanas, G.; Vert, M. *Polymer*. **1998**, *39*(2), 267.
50. Kanna, Y.; Shurgalinb, M.; Krishnaswamy, R. K. *Polym. Test.* **2014**, *40*, 218.
51. Tsou, C. Y.; Wu, C. L.; Tsou, C. H.; Chiu, S. H.; Suen, M. C.; Hung, W. S. *Polym. Sci. Ser. B.* **2015**, *57*(5), 473.
52. Kamelian, F. S.; Mousavi, S. M.; Ahmadvpour, A.; Ghaffarian, V. *Korean J. Chem. Eng.* **2014**, *31*(8), 1399.
53. Cañavate, J.; Pages, P.; Saurina, J.; Colom, X.; Carrasco, F. *Polym. Bull.* **2000**, *44*(3), 293.
54. Li, J.; Chen, F.; Yang, L.; Jiang, L.; Dan, Y. *Spectrochim. Acta, Part A.* **2017**, *184*, 361.

Studies regarding simulation process to static loading of the structures obtained from polylactic acid, 3D printed

Dorin Catana¹  | Mihai-Alin Pop²

¹Department of Materials Engineering and Welding, Transilvania University of Brasov, Brasov, Romania

²Department of Materials Science, Transilvania University of Brasov, Brasov, Romania

Correspondence

Dorin Catana, Department of Materials Engineering and Welding, Transilvania University of Brasov, Brasov 500036, Romania.

Email: catana.dorin@unitbv.ro

Abstract

Being a relatively new process, additive manufacturing needs many studies to be able to produce parts with the required properties. The aim of the paper is to establish whether, based on the physical and mechanical properties determined by tensile testing and by applying finite element analysis (FEA), viable results can be obtained regarding the behavior of the 3D printed structures at the different, static loading. The application of FEA for the tensile testing of 3D specimens led to the results close to those obtained by the tests. The values of the results obtained by simulation are higher by up to 7.2% compared with those recorded by tests. The simulation was applied both for the printed specimens from a single material and from two materials (multi-material). Regardless of the materials used in printing and the simulation method, the results of applying FEA are close to those recorded by testing.

KEYWORDS

additive manufacturing, biodegradable, finite element analysis, mechanical properties, polyesters

1 | INTRODUCTION

For thousands of years, technological processes for the manufacturing metallic or non-metallic materials have been based on subtractive methods (by material removal). Whether it is the Stone Age, Bronze Age, or the Iron Age, methods based on the removal of the material to be processed represented the largest weight. Also, currently the weight of the subtractive methods is still majority, although lately the manufacturing processes have diversified. For several decades the methods of additive manufacturing (by adding material) have been developed and started to be implemented in the production process, actually, these are continuously expanding. It is clear, that additive manufacturing still has many aspects that need to be improved, tested, and verified in order to reach a high degree of reproducibility of 3D printed structures (products, manufactured article). This is also the reason why many current researches aim to improve the performance of additive processing and increase the

quality of manufactured products. The new research also, verifies whether certain concepts applicable to structures manufactured by subtractive methods are also valid for the structures (parts) obtained by additive processing. The researches presented in the paper aims to understand and thorough study the possible connections between the processing parameters and the properties of the structures obtained by the additive manufacturing.

A material often used in 3D printing is polylactic acid (PLA), which is a thermoplastic aliphatic polyester produced from renewable resources. Being biodegradable, it is used for the manufacture of various products and is a sustainable solution for the products derived from the petrochemical industry. Regarding the recycling of polylactic acid, technologies have already been developed for this operation, which shows that there are technologies available for each stage of the life cycle of products made of PLA. Frequent uses of polylactic acid are, among other things, packaging material and disposable items (food packaging, cutlery). Under certain conditions

(the presence of oxygen) it is biodegradable, which is why it can be used in medical applications. In the medical field, polylactic acid is used for stents, post-surgery stitches, and the medical implants in the form of anchors, screws, rod, pins, and plates. PLA medical implants disintegrate (break down) in the human body in a period of 6 months–2 years, depending on where they were used. Gradual degradation is beneficial for a supporting structure, as the weight is gradually transferred to the bone structure during the healing of that area. Information on polylactic acid and the 3D printed parts of it has been the subject of numerous scientific articles, from the study of which the following ideas emerge.

Farah et al¹ shows that polylactic acid is one of the most researched studied and utilized bio degradable aliphatic polyester in human history. For its properties, PLA has numerous applications in medicine as well as in replacing conventional petrochemical-based polymers. The manufacturing of PLA has some advantages, including eco-friendly, renewable resources, biodegradable recyclable, compostable. Therefore, of the global level, it is a major interest for the utilization of this type of bio polyester and the prediction shows a rapid growth of the PLA global production capacities, to about 800 kilo tone per year in 2020 from under 200 kilo tone per year in 2011.² Blending PLA with other polymers offers a convenient option to enhance its properties or generate novel properties for target applications without the need developed new materials. Biocompatibility and superior mechanical properties PLA and its blends with other have been explored to develop porous scaffold using different techniques.³ The experimental trials show that, there are reasons as PLA to be assimilated as a homogenous, isotropic, and linear-elastic material.⁴ Some studies try to find if exist connection between the ultimate tensile strength and the nominal strain at break for the printed parts made from polylactic acid. The study shows the relations among the main process parameters and the stiffness and strength of fused deposition modeling-printed parts, made from PLA.⁵ Other researchers show that the elastic response of the 3D-printed material is transversely isotropic, although the anisotropy is mild; also, both axial and transverse stiffness are similar to that of injection-molded PLA. The tests show that 3D printing does not affect material elasticity substantially. Also, study shows that PLA material displays a pronounced tension/compression asymmetry.⁶

Also, study shows that under tensile cycle loading the favorable results were obtained for the parts in 45° build orientation, for the fatigue tests. The parts in X and Y build orientation had a short fatigue life. Paper shows that the ultimate tensile stress for the sample build in X

direction is higher up to 64% of raw PLA material. For the sample build in Y and 45° orientation the values of ultimate tensile stress were lower than raw PLA material.⁷ Some researches show that, of an engineering point of view, the influence of the deposition angle on the overall strength/fracture resistance of additively manufactured PLA can be neglected with little loss of accuracy.⁸ Other tests reveal that the mechanical properties increase as the layer thickness increase. For infill, the mechanical behavior was different. Also, the paper shows, that it can be found valid relationships between mechanical properties and printing parameters.⁹ For the 3D printed PLA specimens, in the case of landfill test it was observed positive signs of degradation of PLA under standard atmospheric conditions. Also, the paper shows that PLA can be further used in any biomedical components.¹⁰ Other researches show that the structural arrangement design in 3D printing for two materials can affect the mechanical properties. With the optimized arrangement of material layers can be enhanced in terms of mechanical properties even with some ratio of materials.¹¹ In case of mixing PLA with other biomaterials (amorphous polyhydroxyalkanoate–PHA) copolymer it is obtained the improvement of the mechanical properties of printed PLA parts. It is possible as notched impact strength value of PLA/PHA 3D printed parts to increase by 90%, compared with pure PLA.¹² The researchers demonstrated that mixing of PLA with 15% HA (hydroxyapatite) permitted the manufacturing of porous scaffolds by 3D-printing with 98% recovery of the shape. Also, they have the capacity to be used as self-fitting implants, for the bone replacement.¹³ Wang et al¹⁴ shows when PLA is reinforced with glass fiber, the positive effects appear in the composite behavior. The tensile strength, impact strength, and tensile modulus increase with enlargement of glass fiber percent.

Numerous tests must be performed to study the behavior of the 3D printed structures from polylactic acid, at different static loadings. Research shows that there are significant differences between the mechanical properties of the PLA filament and those of the products obtained by additive manufacturing process from the respectively filament. Moreover, using the same filament and the same printing parameters, the mechanical properties of the 3D printed products also depend of the equipment, which was performed in the additive manufacturing.

2 | EXPERIMENTAL

The studies presented in the paper were performed on the following filament types: PLA and PLA-Glass. The

PLA filament (product code PLA-S3 DPLA 01–285-1000) has the following mechanical properties:

- impact resistance 7.5 kJ m^{-2} (ISO 180/A);
- tensile strength 1100 MPa (ASTM D882);
- modulus of elasticity 3310 MPa (AST MD882);
- bending modulus of elasticity 2392.5 MPa;
- printing speed $40\text{--}80 \text{ mm s}^{-1}$;
- printing temperature $190\text{--}225^\circ\text{C}$.

For the PLA-Glass filament (product code PLA-Glass 041–285-750), the mechanical properties are:

- maximum tensile strength 57 MPa (ASTM D638);
- tensile strength at yield 46 MPa (ASTM D638);
- tensile modulus 4.0 GPA (ASTM D638);
- tensile elongation 3.4% (ASTM D638);
- notched impact 29 J m^{-1} (ASTM D256);
- printing speed $50\text{--}120 \text{ mm s}^{-1}$;
- printing temperature $190\text{--}220^\circ\text{C}$.

From the two types of filaments, 3D printed specimens were used in the study. The additive manufacturing process was performed with a Creat Bot DX-3D double-nozzle printer. The parameters of the printing process were:

- layer height -0.2 mm ;
- printing temperature -210°C ;
- bed temperature -61°C ;
- print speed $-30, 50, \text{ or } 70 \text{ mm s}^{-1}$;
- printing angle (overhang angle for support) $-0, 30 \text{ or } 45^\circ$;
- infill -100% (the internal structure is solid); also, solid infill at top and bottom;
- infill overlap -10% ;
- infill flow -110% .

The number of perimeter's shell is 2 and has 1 mm thickness (in total) on horizontal and on top and bottom each has the thickness of 0.8 mm (4 layers).

From these filaments were made by 3D printing, the specimens used later in the tensile tests. The geometry of the 3D printed specimens is presented in Figure 1.

The specimens were printed in different variants, the modified parameters were material filament, printing speed, and printing angle. Regarding the material filament used, the content of the 3D printed specimens, was obtained by:

- using only the PLA filament (100% PLA);
- using only the PLA-Glass filament (100% PLA-Glass);
- using the PLA and PLA-Glass filament in proportion of 50% each, more precisely from the thickness of 4 mm, 2 mm were from PLA and 2 mm from PLA-Glass;

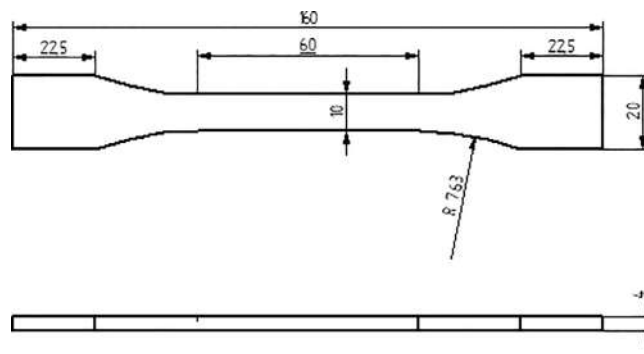


FIGURE 1 Geometry and dimensions of the specimen

- using 50% PLA and PLA-Glass filament each; the materials were arranged in 3 superimposed packages, as follows: PLA-PLA-Glass-PLA with their thickness of 1–2–1 mm, or PLA-Glass-PLA-PLA-Glass with the thickness of the packages of 1–2–1 mm.

For all 3D printed specimens, their geometric dimensions were identical. The printing of the specimens in the different variants has allowed to obtaining the specimens presented in Table 1.

For simplification of notations and removal of errors in Table 1 and further on, the PLA-glass filament will simply be called glass. Also, the 3D printing of the specimens obtained by combining the filaments was done as shown in the Figure 2. The printing of the specimens was done using speeds of 30, 50, and 70 mm s^{-1} , which are located toward the lower part of the recommended speed range. From the point of view of the printing angle, it had an inclination of $0^\circ, 30^\circ, \text{ and } 45^\circ$, relative to the longitudinal axis of the specimen.

The tensile testing was performed for the 3D printed specimens. The tensile tests were performed on WDW-150S universal testing machine (the applied test force varied between 0.1 and 150 kN). The test conditions were:

- tighten speed 5 mm min^{-1} ;
- stress speed 10 MPa s^{-1} .

The tensile test allowed the following parameters to be established for each 3D printed specimen, based on the recordings made during it (see Figure 3):

- applied force and maximum force F_m (kN);
- extension at break (mm);
- proportionality limit F_p (kN);
- modulus of elasticity (GPa);
- ultimate tensile strength (MPa);
- yield strength (MPa);
- strain at break (%).

TABLE 1 Printing parameters of the specimens

Filament type	Printing speed (mm s ⁻¹)	Printing angle (°)	Specimen code
PLA	30	45	P30_45
PLA-Glass	30	45	G30_45
PLA	50	0	P50_0
PLA-Glass	50	0	G50_0
PLA	50	30	P50_30
PLA-Glass	50	30	G50_30
PLA + Glass	50	30	PG50_30
PLA + Glass+PLA	50	30	PGP50_30
Glass+PLA + Glass	50	30	GPG50_30
PLA	50	45	P50_45
PLA-Glass	50	45	G50_45
PLA + Glass	50	45	PG50_45
PLA + Glass+PLA	50	45	PGP50_45
Glass+PLA + Glass	50	45	GPG50_45
PLA	70	45	P70_45
PLA-Glass	70	45	G70_45

3 | RESULTS AND DISCUSSION

The results of the tensile tests performed were processed and analyzed. Figure 4 shows the evolution according to the printing speed of the values for the yield strength (YS) and ultimate tensile strength (US). The analysis shows that for 3D printed specimens of PLA (P) the highest value for ultimate tensile strength is obtained for the printing speed of 50 mm s⁻¹.

For the printed specimens of PLA-Glass (G) the highest value for ultimate tensile strength was obtained for the printing speed of 30 mm s⁻¹. Also, the tests performed show that for the other printing speeds, the decreases of the analyzed values are not significant. The analysis of the strain (St) and extension (Ex) to break values (see Figure 5) shows that the highest values were obtained for the printing speed of 30 mm s⁻¹.

The analysis of the two figures shows that the printing speed has an influence on the analyzed values, but this is not very high and the recorded differences are not significant. The specimens obtained by the additive manufacturing of PLA have better mechanical characteristics than those printed of PLA-Glass.

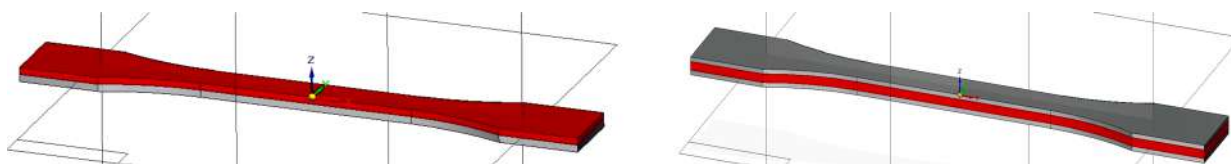


FIGURE 2 Specimen with multi-package of materials (left-2 material packages and right-3 material packages) [Color figure can be viewed at [wileyonlinelibrary.com](https://onlinelibrary.wiley.com/doi/10.1002/app.50036)]

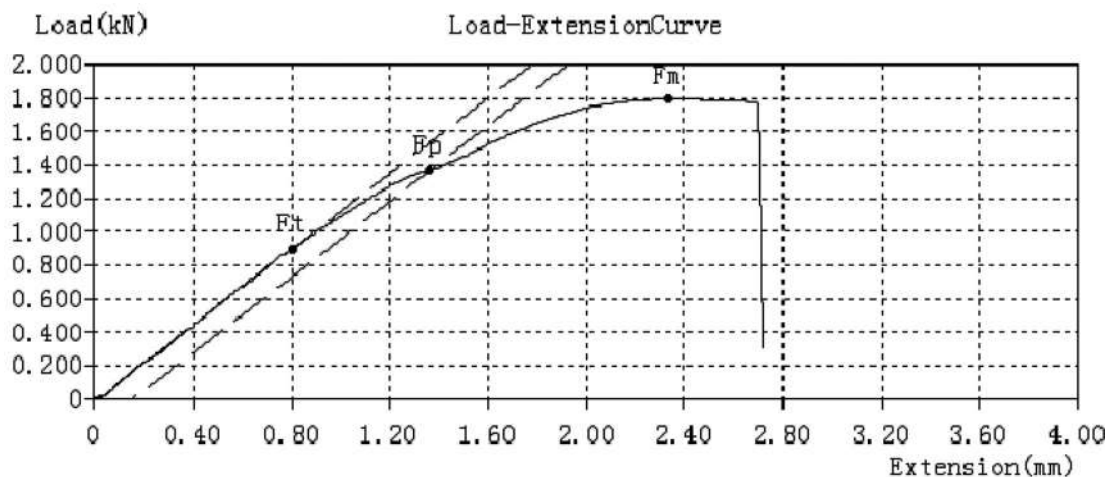


FIGURE 3 Load-extension curve obtained during tensile test (G30_45 specimen)

FIGURE 4 Evolution of yield strength and ultimate tensile strength depending on printing speed [Color figure can be viewed at wileyonlinelibrary.com]

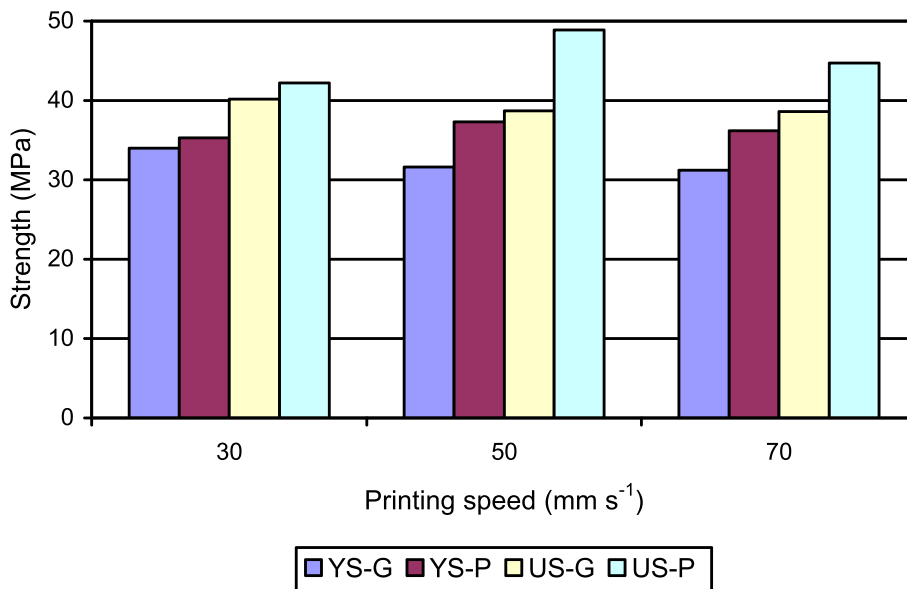
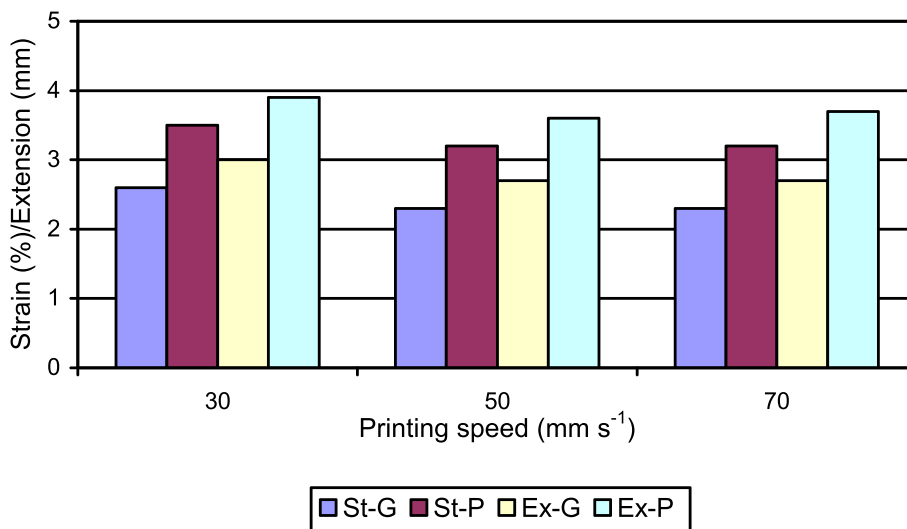


FIGURE 5 Evolution of strain and extension depending on printing speed [Color figure can be viewed at wileyonlinelibrary.com]



The Figure 6 shows the evolution of yield strength and ultimate tensile strength values for the printed specimens with a speed of 50 mm s^{-1} and a printing angle of 45° , for the different combinations of the two analyzed materials. Thus, by combining in proportion of 50%–50% of the two analyzed materials, it is found that ultimate tensile strength is placed between the values of that property, when the materials are not combined. In terms of value for the yield strength, its evolution is similar to that of the ultimate tensile strength.

Also, the strain at break and the extension (see Figure 7) of the tested specimens show an evolution similar to that of the values for engineering stress (ultimate tensile strength and yield strength).

For the printing speed of 50 mm s^{-1} , the Figure 8 shows the evolution of the engineering stress according to

the printing angle (G mean PLA-Glass and P mean PLA). The figure shows that both for ultimate tensile strength and for yield strength the printing angle of 30° allows the obtaining the higher values for the examined properties. But, for the strain at break and extension (see Figure 9) the evolution is changed because for these, better results were obtained when printing angle was of 45° .

After the tests and performed analyses, enough information was accumulated and it can proceed to the next stage of the study. In this stage, it is tried as on the basis of the obtained information to appeal to the finite element analysis (FEA or FEM) to verify if the application of the method provides (offers) viable results. In other words, whether by using the FEA method there is the possibility of predictability of the behavior for the ultimate tensile stress of 3D printed structures from PLA and

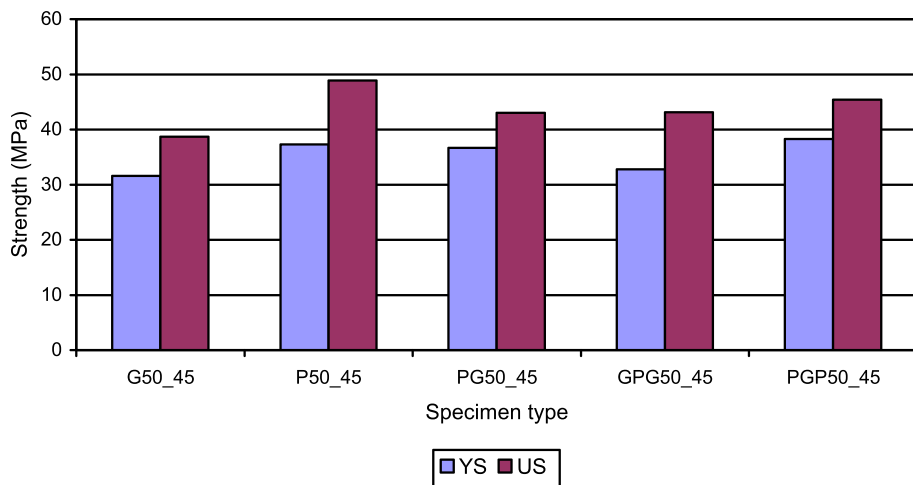


FIGURE 6 Evolution of yield strength and ultimate tensile strength depending on printed filament [Color figure can be viewed at wileyonlinelibrary.com]

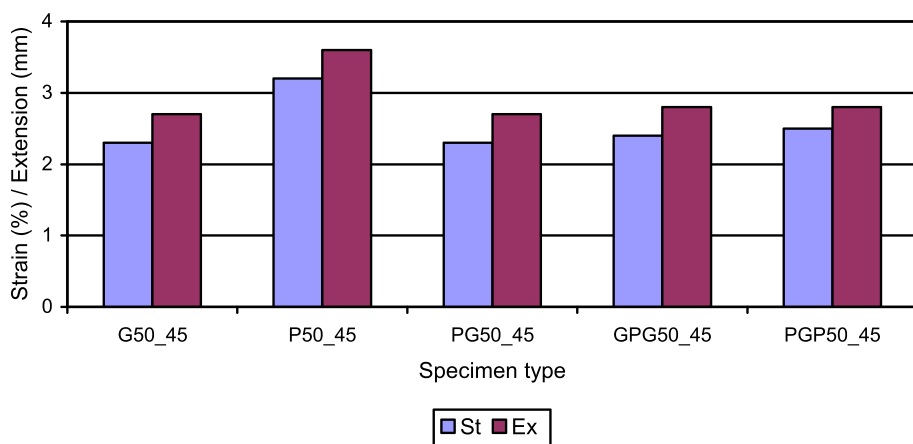


FIGURE 7 Evolution of strain and extension depending on printed filament [Color figure can be viewed at wileyonlinelibrary.com]

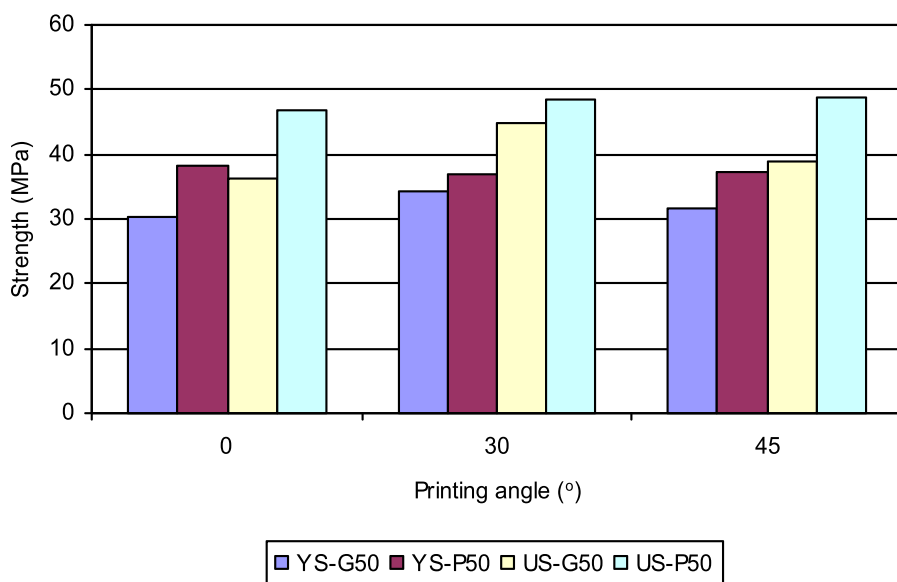


FIGURE 8 Evolution of yield strength and ultimate tensile strength depending on printing angle [Color figure can be viewed at wileyonlinelibrary.com]

PLA-Glass filaments. To perform the simulation process are required information about the physical and mechanical properties of 3D printed specimens. Thus, for 3D printed specimens, depending of the filament material or

combination of filament materials used, their density was determined. The density of the specimens obtained by additive manufacturing is totally different of the filament density, used for their printing. Another characteristic of

FIGURE 9 Evolution of strain and extension depending on printing angle [Color figure can be viewed at wileyonlinelibrary.com]

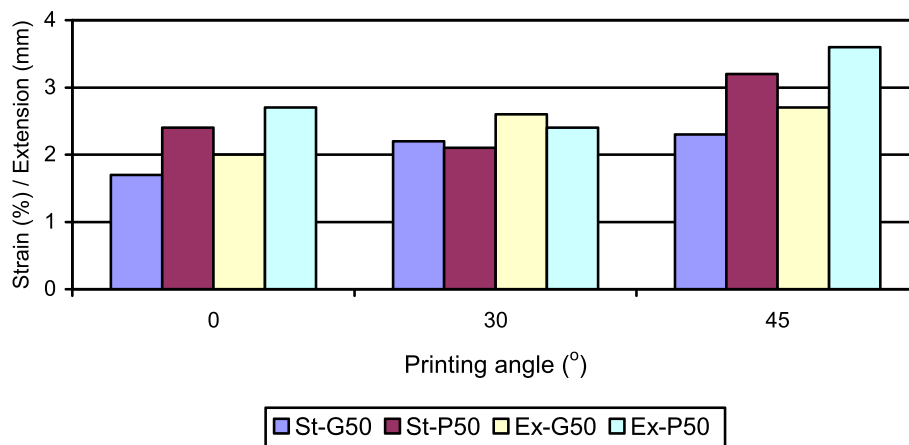
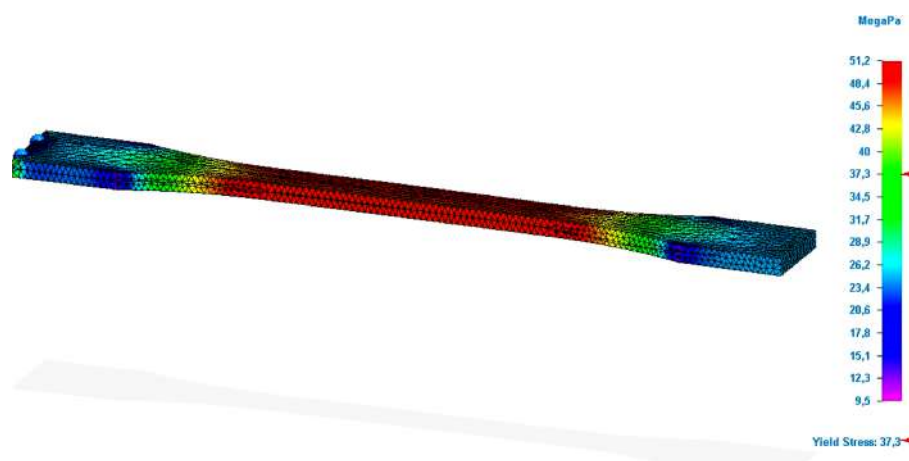


FIGURE 10 Result of simulation process for P50_45 specimen [Color figure can be viewed at wileyonlinelibrary.com]



the material required for the simulation is the value of the Poisson's ratio. According to the publications, the value of the Poisson's ratio for the printed parts of PLA is between 0.33 and 0.36.¹⁵ For the simulation processes presented in the paper, the value of 0.35 was used for the Poisson's ratio. Another characteristic of the material required for the simulation process is the value of the modulus of elasticity. Its value is that determined during the tensile test, because among the properties determined during that test is the value of the modulus of elasticity. Also, for the simulation it is necessary the value for yield strength. This characteristic is obtained, as a result of tensile tests performed on 3D printed specimens. The development of the simulation process requires the values for thermal conductivity and specific heat, but these are irrelevant for the results of the tensile simulation. Those characteristics are obtained from the filament manufacturers.

Knowing the physical and mechanical characteristics of 3D printed structures, it can begin the simulation process when the specimens are loaded with the pre-established forces. For each specimen and its filament, the simulation process is performed by applying at the

end of the specimen a force equal to the maximum force recorded during the tensile test. The other end of the samples is locked. By the simulation were determined the values for Von Mises stresses that were developed in the specimens, during static loading of these, to tensile (see Figure 10).

The simulation was performed under the following conditions: linear static study, tetrahedral mesh type, and mesh size of 1.25 mm. Because, in the specimen's shell manufacturing the infill value is 100%, in the FEA analysis it was considered that specimen working like a single block and has the same properties, in the entire volume. The maximum value obtained for Von Mises stress (noted VM) was compared with the value of the ultimate tensile strength (noted US) recorded during the tensile test, for the same type of specimen (material, speed, printing angle). Also, the specimen zone where this maximum value of stress appears was checked (see Figure 11). The figure shows specimen zone where this will break when loading is equal with ultimate tensile strength. The simulation result corresponds with zone where the specimen broke during tensile test.



FIGURE 11 Specimen zone where stress value is equal with ultimate tensile strength (P50_45 specimen) [Color figure can be viewed at wileyonlinelibrary.com]

TABLE 2 Results of tensile tests and simulation process for 3D printed specimens

Specimen code	Maximum force [N]	Modulus of elasticity [GPa]	YS [MPa]	US [MPa]	VM by SIM [MPa]	VM by ROM [MPa]
P30_45	1688.00	4.00	35.30	42.20	44.20	NA
G30_45	1607.80	3.80	34.00	40.20	42.10	NA
P50_0	1869.20	4.20	38.40	46.20	48.90	NA
G50_0	1457.00	4.00	30.20	36.40	38.10	NA
P50_30	1941.80	4.20	37.00	48.50	50.80	NA
G50_30	1791.80	4.80	34.40	44.80	46.90	NA
PG50_30	1993.40	4.40	36.20	49.80	53.40	52.20
PGP50_30	2011.00	4.00	34.80	50.30	52.10	52.60
GPG50_30	1944.20	4.20	35.00	48.60	52.10	50.90
P50_45	1954.00	3.50	37.30	48.90	51.20	NA
G50_45	1545.00	3.60	31.60	38.70	40.40	NA
PG50_45	1721.00	3.20	36.70	43.00	46.00	45.80
PGP50_45	1815.00	3.80	38.30	45.40	48.20	47.50
GPG50_45	1724.00	4.00	32.80	43.10	45.70	45.10
P70_45	1788.80	4.00	36.20	44.70	46.80	NA
G70_45	1544.60	4.00	31.20	38.60	40.40	NA

Abbreviations: NA, not applicable; US, ultimate tensile strength; VM, Von Mises stress; YS, yield strength.

Table 2 shows the results obtained in the tensile test as well as those obtained by applying the simulation process (SIM column). Also, table shows the column (ROM) in which the results of the simulation process are introduced (entered) but when the rules of mixture (ROM) were applied. The rule of mixtures (ROM) method is frequently used to estimate the tensile strength of fiber reinforced polymers (FRPs) reinforcing bars (rebars). Generally, the ROM method predicts the FRP rebars' modulus of elasticity adequately but overestimates their tensile strength. The possibility of use modified rule of mixture is adequate and offers the better results (closer to the tests results).¹⁶ Many studies use in their researches the basic rule of mixture to solve different problems for the composite materials. The rules of mixture are applied

for determine Young's modulus, Poisson's ratio, mass density and not only.^{17,18} This type of simulation was applied in the case of specimens obtained by combining the studied materials (PLA and PLA-Glass). For these specimens, the two studied materials are arranged in alternative packages (2 or 3, see Figure 2). For the case with two packages the specimen consists of a package with a thickness of 2 mm of PLA and another package also of 2 mm of PLA-Glass. Basically, the proportion in the specimen is 50% PLA and 50% PLA-Glass.

For specimens consisting of three packages, there is a 2 mm thick PLA-Glass package arranged between two PLA packages, with 1 mm thick each. And in this case, the proportion is also 50% PLA and 50% PLA-Glass. There is also the situation when a PLA package is

between two PLA-Glass packages. For this type of specimens (obtained by combining the two materials in the described variants) rule of mixtures was applied to calculate the mechanical properties of the specimens.¹⁹ These laws have the possibility to establish (predict) the properties of the combination of materials. To establish the properties of the composite, the relation is:

$$P_c = P_m \cdot V_m + P_p \cdot V_p. \quad (1)$$

In the relation (1) $P_{c,m,p}$ is property value, $V_{m,p}$ is volume fraction, and c, m, p represents composite, matrix and phase. This relationship was applied to determine the density, modulus of elasticity, yield strength for specimens that have combination of materials (multi-package). Also, the maximum force for the specimens with multi-package was also calculated based on the relation (1). In the simulation process of the multi-package specimens, one of simulation applied method was those who for each material package of the composition were assigned the properties of the respective material (density, modulus of elasticity, yield strength, Poisson's ratio). In these cases the specimens consist of 2 or 3 thinner specimens (mini specimens), which by overlap form the standard specimen. The package of 2 or 3 mini specimens is thought that forming a single specimen (a block) and on this block was applied the simulation process. The force applied to the multi-package specimen was also calculated with the relation (1), where the values of the force are those obtained at the tensile test for the materials from the composition of the respective specimen. The Figure 12 shows the comparison between the ultimate tensile strength values determined by the tensile test and those for Von Mises stress determined by

simulation for the speeds used in 3D printing. For those three speeds analyzed, the values obtained by simulation are higher than those obtained during the tensile test. By simulation, higher values are obtained up to 4.7% than those obtained by testing.

Figure 13 shows the comparison between the ultimate tensile strength values determined by the tensile test and those for Von Mises stress determined by simulation for the different printing angles. The simulation provided values up to 5.8% higher than those determined by the tensile test.

The Figure 14 shows the comparison between the ultimate tensile strength values determined by the tensile test and those for Von Mises stress determined by simulation or by applying the rule of mixtures for multi-material specimens. In the case of simulation, the values are up to 7.2% higher than those determined by tensile tests. In the case of ROM application, the values are higher by up to 6.5% compared to those obtained by tensile tests. The comparison between the two simulation processes shows that the ROM-based simulation is more accurate (see Figure 15), in other words the values determined are closer to those obtained by the tensile test.

To verify whether the application of the simulation process provides the expected results, three sets of specimens were 3D printed. Thus, for printing speed of 50 mm s^{-1} and the printing angle of 30° by 3D printing were manufactured multi-material specimens (with 2 packages of material). The proportion was 80% PLA and 20% PLA-Glass (3.2 mm thick for PLA and 0.8 mm thick for PLA-Glass). The value determined for Von Mises stress by applying the simulation was 7.5% higher than that recorded by the tensile test. In the case of applying the simulation based on the rule of mixtures,

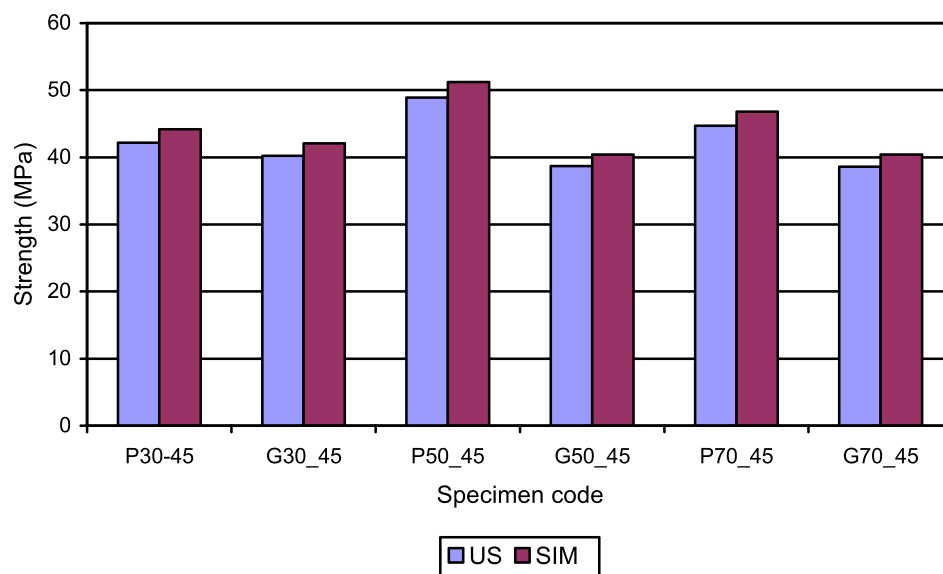


FIGURE 12 Comparison between results of the tensile test and simulation process for used printing speed [Color figure can be viewed at wileyonlinelibrary.com]

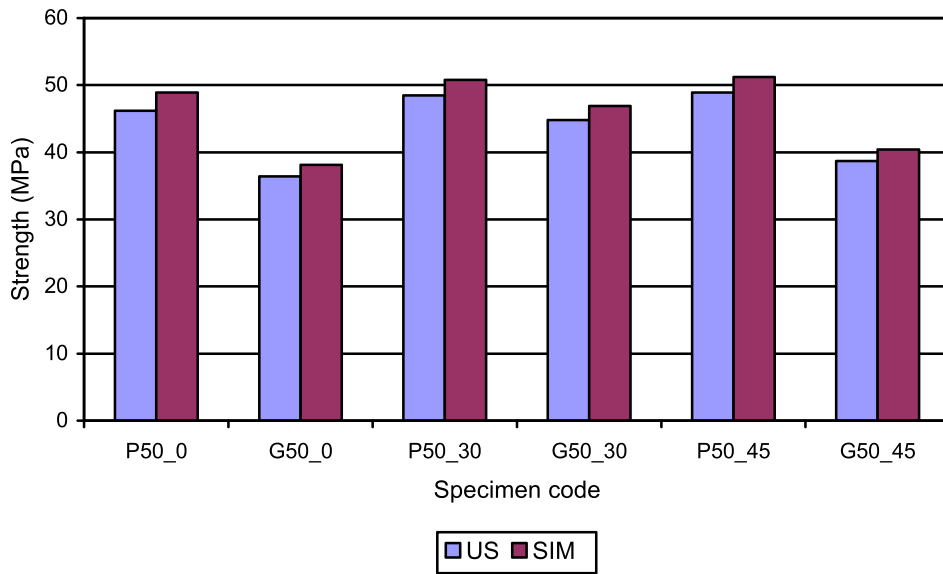


FIGURE 13 Comparison between results of the tensile test and simulation process for used printing angle [Color figure can be viewed at wileyonlinelibrary.com]

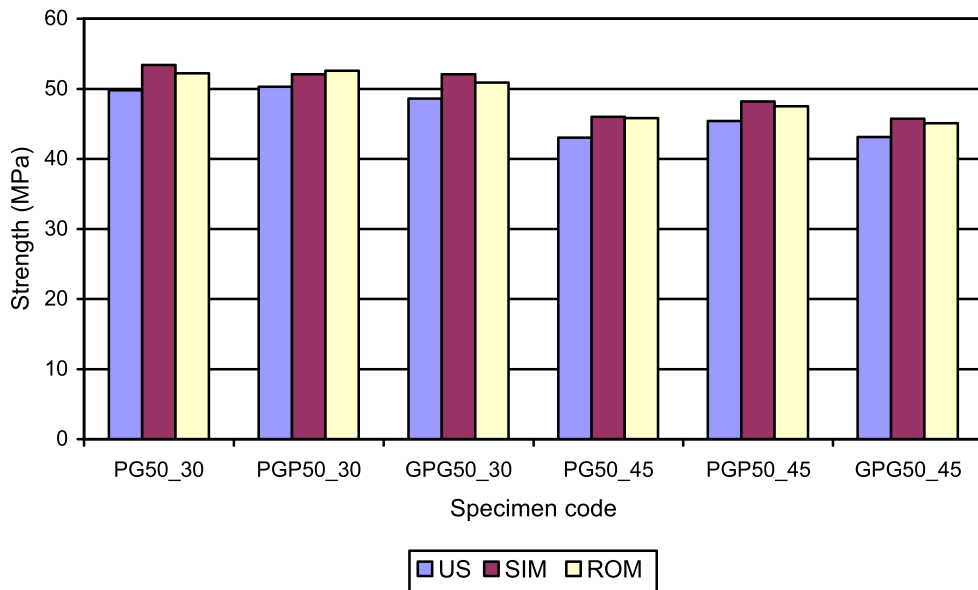


FIGURE 14 Comparison between results of the tensile test and simulation process in case of multi-package specimens (printing speed of 50 mm s^{-1}) [Color figure can be viewed at wileyonlinelibrary.com]

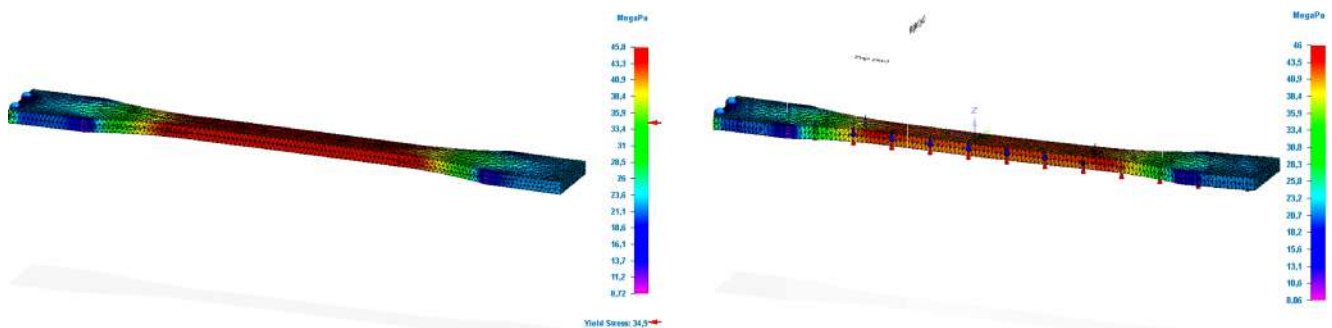
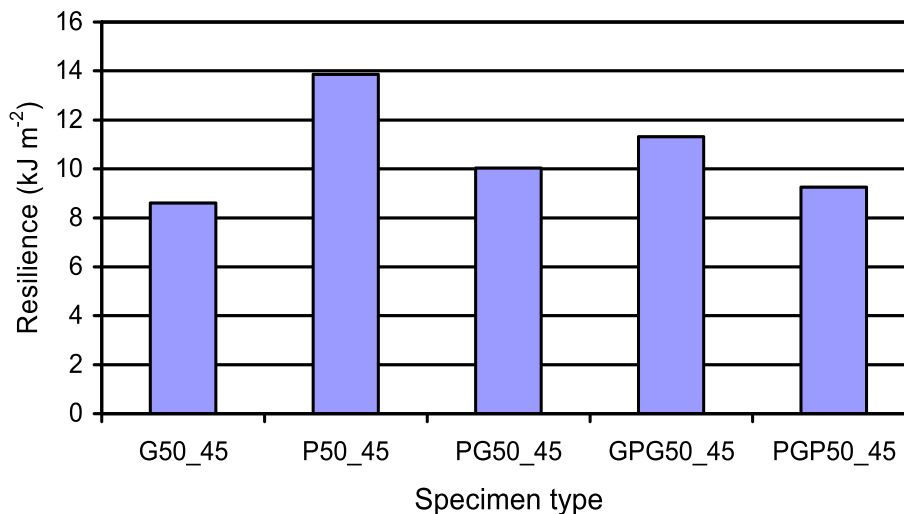


FIGURE 15 Results of simulation process for PG50_45 specimen (left-by ROM and right-by SIM) [Color figure can be viewed at wileyonlinelibrary.com]

FIGURE 16 Evolution of resilience for 3D printed specimens (printing speed of 50 mm s^{-1} , printing angle 45°) [Color figure can be viewed at wileyonlinelibrary.com]



the value determined for Von Mises stress was 3.7% lower than that recorded by the tensile test. Also, the specimens were printed with 3 packages of material. A set of specimens had a proportion of 75% PLA and 25% PLA-Glass (2 packages of PLA with a thickness of 1.5 mm each, and between them a pack of PLA-Glass with a thickness of 1 mm). For this configuration, the value determined for Von Mises stress by applying the simulation was 4.5% higher than that recorded by the tensile test. In the case of applying the simulation based on the rule of mixtures, the value determined for Von Mises stress was 5.3% lower than that recorded by the tensile test. Another set of specimens have had a proportion of 65% PLA and 35% PLA-Glass (2 packages of PLA-Glass with a thickness of 0.7 mm each, and between them a pack of PLA with a thickness of 2.6 mm). For this configuration, the value determined for Von Mises stress by applying the simulation was 2% higher than that recorded by the tensile test. In the case of applying the simulation based on the rule of mixtures, the value determined for Von Mises stress was 6.3% lower than that recorded by the tensile test.

Figure 16 shows the resilience (impact resistance) evolution depending on the material used in 3D printing of the specimens. The specimens used to determine the resilience were U-notched, with dimensions $55 \times 10 \times 10 \text{ mm}$. In the case of the multi-package specimens, the thickness of the material package was 5–5 mm for the PG type material combination and 3–4–3 mm for PGP or GPG type material combinations. The resilience study shows that for the 3D printed specimens from PLA, the resilience registers the highest values. PLA-Glass specimens have lower values, which mean that this type of material is more fragile than PLA. Also, for multi-package specimens (GPG50_45) high values are recorded compared to the other values recorded by multi-package specimens. The alternation of the materials in the structure (part) allows

the improvement of their behavior to resilience, especially to those in which the materials alternate of three times.

4 | CONCLUSIONS

The presented study was applied on two materials commonly used in 3D printing, called PLA and PLA-Glass. The materials being used in different applications, it was tried that based on the physical and mechanical properties established by tests for the 3D printed structures (parts) these can be used successfully in the FEA. The possibility of applying the FEA with good results will allow the optimization of the geometry for the 3D printed structures but also the shortening of their design time. The simulation process was based on information acquired during testing. The analysis of the test results performed on the 3D printed structures shows that the determined values have depended on the following parameters of the printing process: material and the printing speed and angle. The study shows that changing parameters of the printing process leads to a change in the value of the determined properties, but these differences are not large. The application of the simulation process allows obtaining of results comparable to those measured in the tests. The use of two simulation processes allowed a comparison to be made between the results provided, by their application. Thus, the simulation allows obtaining results close to those obtained by the tensile test. For the printing speeds used in the study, the error is not higher than 5%, compared with that determined by tests. In the case of printing angles, the application of the simulation generated an error of maximum 6%, compared with the test results. The study also shows that the simulation can be applied with good results in the case of 3D printed structures that are obtained by combining two materials (multi-material). For

the combination of analyzed materials, in the case of FEA by applying rule of mixtures the error does not exceed 6.5% compared with the test results. By applying the simulation (assigning for each material of composition its mechanical properties), the error is higher than in the case of using ROM, but even in this case does not exceed the value of 7.2%. Also, the paper shows the resilience's evolution for the utilized materials. By the materials combination it is possible to improve the resilience.

Because the results of the simulation process do not concur with those of the tensile tests, the future studies will be concentrated on the reduction of these. A possible source of the errors is the multi-material specimen dimensions (package thickness) that have deviation in comparison with the dimension established by design. Thus, the accuracy of the measured dimensions for the 3D printed specimens will increase. Whether it is considered that the specimen's shell has other properties than those of central area, then, through tests, they must be established. In this case, it will be considered that the specimen is composed of two or more zones (entities) depending on printing parameters, and the simulation process will be performed in the same way as for the multi-material specimens. Also, the researchers will try to improve the mathematical model of the simulation process for the increasing the predictability of this and to decrease the errors value. The use of the simulation process in the design of 3D printed structures allows their optimization, because the studies presented in the paper show that the simulation results are close to those of tensile tests. Simulation can also be applied with acceptable results in the case of multi-material structures. The simulation process is based on the physical and mechanical properties obtained by performing various tests on 3D printed structures. The simulation will not be able to be applied if the mechanical characteristics of the 3D structures are not known. The study shows that these characteristics depend on the material and the printing speed and angle. Also, the paper shows that FEA applied to the structures (parts) design for 3D printing can be used with good results, but also, it can save time, in comparison with classical methods.

ORCID

Dorin Catana  <https://orcid.org/0000-0001-7554-0720>

REFERENCES

- [1] S. Farah, D. G. Anderson, R. Langer, *Adv. Drug Delivery Rev.* **2016**, *107*, 367.
- [2] M. Murariu, P. Dubois, *Adv. Drug Delivery Rev.* **2016**, *107*, 17.
- [3] P. Saini, M. Arora, M. N. V. R. Kumar, *Adv. Drug Delivery Rev.* **2016**, *107*, 47.
- [4] O. H. Ezeh, L. Susmel, *Procedia Struct. Integr.* **2018**, *9*, 29.
- [5] M. Grasso, M. Martorelli, A. Lanzotti, G. Staiano, *Rapid Prototyping J.* **2015**, *21*, 604.
- [6] Y. Song, Y. Li, W. Song, K. Yee, K. Y. Lee, V. L. Tagarielli, *Mater. Des.* **2017**, *123*, 154.
- [7] M. F. Afrose, S. H. Masood, P. Iovenitti, M. Nikzad, I. Sbarski, *Prog. Addit. Manuf.* **2016**, *1*, 21.
- [8] A. A. Ahmed, L. Susmel, *Procedia Struct. Integr.* **2017**, *3*, 498.
- [9] J. C. Camargo, Á. R. Machado, E. C. Almeida, E. F. M. S. Silva, *The Int. J. Adv. Manuf. Technol.* **2019**, *103*, 2423.
- [10] S. A. Raj, E. Muthukumar, K. Jayakrishna, *Mater. Today: Proc.* **2018**, *5*, 11219.
- [11] H. Kim, E. Park, S. Kim, B. Park, N. Kim, S. Lee, *Procedia Manuf.* **2017**, *10*, 887.
- [12] J. V. Ecker, I. Burzic, A. Haider, S. Hild, H. Renhofer, *Polym. Test.* **2019**, *78*, 105929.
- [13] F. S. Senatov, K. V. Niaza, M. Y. Zadorozhnyy, A. V. Maksimkin, S. D. Kaloshkin, Y. Z. Estrin, *J. Mech. Behavior Biomed. Mater.* **2016**, *57*, 139.
- [14] G. Wang, D. Zhang, G. Wan, B. Li, G. Zhao, *Polymer* **2019**, *181*, 121803.
- [15] L. Kuentz, A. Salem, M. Singh, M. R. Halbig, J. A. Salem, *Additive manufacturing and characterization of polylactic acid (PLA) composites containing metal reinforcements*. pp. 17. <https://ntrs.nasa.gov/archive/nasa/casi.ntrs.nasa.gov/20160010284.pdf> (accessed March 1, 2020).
- [16] Y.-J. You, J. J.-H. Kim, K.-T. Park, D.-W. Seo, T.-H. Lee, *Polymer* **2017**, *9*, 682.
- [17] L.-L. Ke, J. Yang, S. Kitipornchai, *Compos. Struct.* **2010**, *92*, 676.
- [18] A. Alibeigloo, *Compos. Struct.* **2013**, *95*, 612.
- [19] R. Flinn, P. Trojan, *Engineering Materials and their Application*, 2nd ed., John Wiley and Sons Ltd, New Jersey **1992**, p. 123.

How to cite this article: Catana D, Pop M-A. Studies regarding simulation process to static loading of the structures obtained from polylactic acid, 3D printed. *J Appl Polym Sci.* 2021;138: e50036. <https://doi.org/10.1002/app.50036>